

**NASA CONTRACTOR
REPORT**



NASA CR-1866
C.1

0061020

TECH LIBRARY KAFB, NM

NASA CR-1866

LOAN COPY: RETURN TO
AFWL (DOUL)
KIRTLAND AFB, N. M.

**POTASSIUM RANKINE CYCLE
VAPOR CHAMBER (HEAT PIPE)
RADIATOR STUDY**

by Ellsworth E. Gerrels and Robert E. Killen

Prepared by

GENERAL ELECTRIC COMPANY

Philadelphia, Pa. 19101

for Lewis Research Center



0061020

1. Report No. NASA CR-1866	2. Government Accession No.	3. Recipient's Catalog No.	
4. Title and Subtitle POTASSIUM RANKINE CYCLE VAPOR CHAMBER (HEAT PIPE) RADIATOR STUDY		5. Report Date September 1971	
		6. Performing Organization Code	
7. Author(s) Ellsworth E. Gerrels and Robert E. Killen		8. Performing Organization Report No. GESP-7047	
		10. Work Unit No.	
9. Performing Organization Name and Address General Electric Company Philadelphia, Pennsylvania 19101		11. Contract or Grant No. NAS 3-10615	
		13. Type of Report and Period Covered Contractor Report	
12. Sponsoring Agency Name and Address National Aeronautics and Space Administration Washington, D. C. 20546		14. Sponsoring Agency Code	
		15. Supplementary Notes	
16. Abstract A structurally integrated vapor chamber fin (heat pipe) radiator is defined and evaluated as a potential candidate for rejecting waste heat from the potassium Rankine cycle powerplant. Several vapor chamber fin geometries, using stainless steel construction, are evaluated and an optimum is selected. A comparison is made with an operationally equivalent conduction fin radiator. Both radiators employ NaK-78 in the primary coolant loop. In addition, the Vapor Chamber Fin (VCF) radiator utilizes sodium in the vapor chambers. Preliminary designs are developed for the conduction fin and VCF concepts. Performance tests on a single vapor chamber were conducted to verify the VCF design. A comparison shows the conduction fin radiator easier to fabricate, but heavier in weight, particularly as meteoroid protection requirements become more stringent. While the analysis was performed assuming the potassium Rankine cycle powerplant, the results are equally applicable to any system radiating heat to space in the 900 ^o to 1400 ^o F temperature range.			
17. Key Words (Suggested by Author(s)) Nuclear space power system Rankine cycle Radiators Heat pipe		18. Distribution Statement Unclassified - unlimited	
19. Security Classif. (of this report) Unclassified	20. Security Classif. (of this page) Unclassified	21. No. of Pages 230	22. Price* \$3.00



FOREWORD

The research described in this report was conducted by the General Electric Company under NASA contract NAS 3-10615. Mr. James P. Couch of the Lewis Research Center Space Power Systems Division was the NASA Project Manager. The report was originally issued as General Electric report GESP-7047.



TABLE OF CONTENTS

<u>Section</u>		<u>Page</u>
1	INTRODUCTION.	1
	1.1 Study objective	1
	1.2 Report Contents.	3
2	SUMMARY	4
	2.1 Introduction	4
	2.2 Selection of Candidate Vapor Chamber Fin Geometries.	6
	2.3 Optimization of Candidate Concepts	7
	2.4 Testing of Rectangular Vapor Chamber Fin Geometry	8
	2.5 Vapor Chamber Fin Radiator Design.	12
	2.6 Conduction Fin Radiator Design	12
	2.7 Comparison of the Vapor Chamber and Conduction Fin Radiators	12
	2.8 Conclusion	15
3	RADIATOR DESIGN REQUIREMENTS	17
	3.1 General Discussion	17
	3-2 System Specification	17
	3-3 Meteoroid Criteria	20
	3-4 Structural Criteria	22
	3-5 Operational Criteria	23
	3-6 Vehicle Integration	23
	3-7 Fabrication	24
4	VAPOR CHAMBER CONCEPT DEVELOPMENT	25
5	VAPOR CHAMBER ANALYSIS	28
	5.1 Condenser Evaluation	28
	5.1.1 Vapor Chamber Analytical Considerations	30
	5.1.2 Concept Parametric Analysis	43
	5.2 Vapor Chamber Fin Integration Evaluation.	77
	5.3 Vapor Chamber Fin Concept/Radiator Structural Evaluation	86
	5.3.1 General	86
	5.3.2 Loads	86
	5.3.3 Assumptions.	87
	5.3.4 Analysis	90
	5.3.5 Summary of Results	101

TABLE OF CONTENTS (Cont'd)

<u>Section</u>	<u>Page</u>
5.4	Fabrication Evaluation 101
5.4.1	General 101
5.4.2	Fabrication Techniques 103
5.5	Vapor Chamber Fin Design Conclusions 109
6	VAPOR CHAMBER (HEAT PIPE) TEST PROGRAM 113
6.1	Test Objectives and Requirements 113
6.2	Test Approach. 114
6.2.1	Vapor Chamber Orientation 114
6.2.2	Test Vapor Chamber Design and Fabrication 114
6.2.3	Heat and Calorimeter Design and Fabrication 118
6.2.4	Test Unit Insulation 120
6.2.5	Tilt Adjustment 123
6.2.6	Test Unit Setup 123
6.3	Vapor Chamber Instrumentation 127
6.3.1	General 127
6.3.2	Thermocouple Location 128
6.3.3	Thermocouple Attachment 128
6.4	Vapor Chamber Test Assembly Evaluation 131
6.4.1	Heat Flux Measurement 131
6.4.2	Temperature Drop (ΔT) Measurement 137
6.5	Test Description and Results 138
6.5.1	Calibration Test 138
6.5.2	Heat Flux and ΔT Measurements (Phase 2) 139
6.5.3	Tilting Test (Phase 3) 147
6.5.4	Limiting Heat Flux Test (Phase 4) 148
6.5.5	Additional Investigations of the Condensing Temperature Drop 148
6.5.6	Discussion of Test Results. 150
7	RADIATOR DESIGN, ANALYSIS AND FABRICATION 154
7.1	General Discussion 154
7.2	Conduction Fin Radiator 154
7.2.1	Conduction Fin Radiator Analysis 154
7.2.2	Conduction Fin Radiator Design 164
7.2.3	Fabrication and Assembly 168
7.3	Vapor Chamber Fin Radiator 174
7.3.1	Vapor Chamber Fin Radiator Analysis 174
7.3.2	Vapor Chamber Fin Radiator Design 181
7.3.3	Fabrication and Assembly 184

TABLE OF CONTENTS (Cont'd)

<u>Section</u>	<u>Page</u>
7.4	Startup Considerations 192
7.4.1	General 192
7.4.2	Type of Fluid in System 193
7.4.3	Total Fluid Inventory 194
7.4.4	Fluid Location and Disbursement 196
7.4.5	System/Mission Considerations 198
8	RADIATOR COMPARISON AND CONCLUSIONS 199
8.1	General 199
8.2	Performance (Weight/Area) 199
8.3	Fabrication Feasibility 203
8.4	Required Development Effort 203
8.5	Operational Comparison 204
8.6	Conclusions. 204
9	REFERENCES 207
APPENDIX A:	NOMENCLATURE 209
APPENDIX B:	TEST PLAN FOR VAPOR CHAMBER RADIATOR 212

LIST OF ILLUSTRATIONS

<u>Figure</u>		<u>Page</u>
1-1	Simplified Potassium Rankine Cycle	2
1-2	Representative Vapor Chamber Fin Radiator Panel	2
2-1	Simplified Potassium Rankine Cycle	4
2-2	Vapor Chamber Concept Alternatives	7
2-3	Vapor Chamber Geometry Evaluation Summary	9
2-4	Vapor Chamber Fin Test Schematic	10
2-5	Vapor Chamber Fin Used in Test	11
2-6	Vapor Chamber Fin Radiator Design	13
2-7	Conduction Fin Radiator Design	14
2-8	Total Radiator Weight versus Area for Vapor Chamber and Conduction Fin Radiators	16
3-1	Advanced Rankine Power System (Nominal 300 kWe)	18
3-2	Trend in Launch Vehicle Dynamic Loads	23
4-1	Vapor Chamber Concept Alternatives	26
4-2	Concepts Selected for Further Investigation	27
5-1	Concept Parameters Evaluated	29
5-2	Relationship Between the Overall and Individual Survival Probabilities (as determined by the binomial distribution for 75 percent chamber survivability)	35
5-3	Relationship Between the Overall and Individual Survival Probability (as determined by the binomial distribution for 85 percent chamber survivability)	36
5-4	Basic Heat Pipe	37
5-5	Heat Pipe Limitations	38
5-6	Required Armor Thickness versus Vapor Chamber Consensing Length at Various Chamber Diameters	45
5-7	Fin Efficiency versus Fin Length for Various Thickness Stainless Steel	46
5-8	Variation of Radiating Effectiveness with Fin Plate Length (Reference)	46
5-9	Geometry 1 Specific Weight versus Fin Length ($T_F = 0.010$ in.)	49
5-10	Geometry 1 Specific Weight versus Fin Length ($T_F = 0.020$ in.)	50
5-11	Geometry 1 Specific Weight versus Fin Length ($T_F = 0.040$ in.)	51
5-12	Geometry 1 Specific Weight versus Fin Length (Sodium)	52
5-13	Geometry 1 Specific Weight versus Fin Length (Cesium)	53
5-14	Geometry 1 Specific Weight versus Channel Width (Potassium)	55

LIST OF ILLUSTRATIONS (Cont'd)

<u>Figure</u>		<u>Page</u>
5-15	Geometrical Relationships Used for Geometry 2	56
5-16	Geometry 2 Specific Weight versus Channel Width (Sodium)	57
5-17	Geometry 4 Specific Weight versus Fin Length ($T_F = 0.010$ in.)	58
5-18	Geometry 4 Specific Weight versus Fin Length ($T_F = 0.020$ in.)	59
5-19	Geometry 4 Specific Weight versus Fin Length ($T_F = 0.040$ in.)	60
5-20	Hexagonal Geometry Computer Code Model	62
5-21	Geometry 3 Hexagonal Fin Temperature Profiles (Fin Length = 6 in.) . .	64
5-22	Geometry 3 Hexagonal Fin Temperature Profiles (Fin Length = 12 in.) .	65
5-23	Geometry 3 Hexagonal Fin Temperature Profiles (Fin Length = 18 in.) .	66
5-24	Geometry 3 Effect on Specific Weight with Core Height of 0.250 inches .	68
5-25	Geometry 3 Effect on Specific Weight with Core Height of 0.50 inches .	69
5-26	Geometry 3 Effect on Specific Weight with Core Height of 0.750 inches .	70
5-27	Geometry 3 Effect on Specific Weight with Facing Thickness of 0.010 inches	71
5-28	Geometry 3 Effect on Specific Weight with Facing Thickness of 0.020 inches	72
5-29	Geometry 3 Effect on Specific Weight with Facing Thickness of 0.010 inches and Core Height of 0.5 inches	73
5-30	Geometry 3 Effect on Specific Weight with Facing Thickness of 0.020 inches and Core Height of 0.5 inches	74
5-31	Geometry 3 Minimum Weight Hexagonal Fins for Core Height of 0.25 and 0.50 inches.	75
5-32	Axial Vapor Temperature Drop for Hexagonal Configuration with Holes	76
5-33	Primary Duct Concepts Heat Transfer-Both Sides (Penetrating and Nonpenetrating)	78
5-34	Primary Duct Concepts Heat Transfer-One Side (Nonpenetrating) . . .	79
5-35	Flow Chart for Computer Program to Evaluate Primary Fluid Duct System Weight Penalty	80
5-36	Effect of Flow Velocity and Variable Condensing Length on Primary Duct Weight	82
5-37	Variation of Primary Fluid Duct Weight as a Function of Duct Width and Vapor Chamber Length	82
5-38	Radiator Weight as a Function of Vapor Chamber Fin Length and Primary Duct Width	83
5-39	Variation of Radiator Weight with Condensing Length (Geometry 1) . .	83
5-40	Vapor Chamber Fin Concepts	86
5-41	Aerodynamic Loads Imposed by Two Stage Saturn V	88
5-42	Acceleration Loads Imposed by Two Stage Saturn V	89
5-43	Equivalent Axial Load-Saturn V Launch Vehicle (Two Stage)	89

LIST OF ILLUSTRATIONS (Cont'd)

<u>Figure</u>		<u>Page</u>
5-44	Mode Shapes for Panel and General Instability of Stiffened Cylinders in Bending	91
5-45	Local Failure Modes	94
5-46	Allowable Load on Tubes	95
5-47	Fin Critical Buckling Stress versus Panel Thickness Length and Size	95
5-48	Intercell Buckling Stress versus Facing Thickness and Cell Size	96
5-49	Equivalent Load to Cause Intercell Buckling	97
5-50	Stainless Steel Honeycomb Core Density.	98
5-51	Face Sheet Loading.	99
5-52	Stress Relationships of Radiator Panel Face Sheets	100
5-53	Fabrication Processes for Vapor Chamber Geometries	104
5-54	Geometry 1 Fabrication Techniques	107
5-55	Geometry 2 Fabrication Techniques	107
5-56	Geometry 3 Fabrication Techniques	108
5-57	Geometry 4 Fabrication Techniques	108
5-58	Vapor Chamber Geometry Evaluation Summary	110
5-59	Fluid Comparison Finned Cylinder Geometry 1	112
6-1	Vapor Chamber Thermal Orientation on Spacecraft	115
6-2	Vapor Chamber Test Orientation	115
6-3	Vapor Chamber (Heat Pipe) Design	116
6-4	Disassembled Vapor Chamber (Heat Pipe)	117
6-5	Close-up View of Vapor Chamber Wick	117
6-6	Assembled Vapor Chamber	118
6-7	Unside Electron Bombardment Heater	119
6-8	Calorimeter	122
6-9	Unassembled Test Block Hardware	122
6-10	Multifoil Insulation Around Vapor Chamber.	123
6-11	Assembled Insulation Test Block on Tilt Stand	124
6-12	System Block Diagram Vapor Chamber (Heat Pipe) Test	125
6-13	Vapor Chamber Test Setup	126
6-14	Thermocouple Calibration	127
6-15	Thermocouple Locations	129
6-16	Arrangement of Thermocouple 1 and Heat Input Surface (to Scale)	130
6-17	Thermocouple Attachment	130
6-18	Thermocouple Test Configuration	131
6-19	Insulation Block (1.90 in.) Temperature Distribution	134
6-20	Insulation Block (1.50 in.) Temperature Distribution	134
6-21	Temperature Data for Heat Flux versus ΔT Tests	141
6-22	Startup Data from VCF No. 2	142

LIST OF ILLUSTRATIONS (Con)

<u>Figure</u>		<u>Page</u>
6-23	Vapor Pressure of Sodium	142
6-24	Evaporative and Vapor Temperature Drop as a Function of Evaporative Heat Flux	143
6-25	Sum of Evaporative and Vapor Temperature Drops as a Function of Evaporator Temperature	143
6-26	Axial Vapor Temperature Drop as a Function of Evaporator Temperature	145
6-27	Maximum Axial Vapor Velocity and Vapor Temperature Drop with Respect to Evaporator Heat Flux	145
6-28	Condenser Temperature Drop versus Evaporator Temperature	145
6-29	Comparison of Calculated Interfacial Resistance with Observed Thermal Resistance	148
6-30	Temperature Data for Tilt Test (10 degrees).	149
6-31	Deformation of Heat Pipe After Limiting Heat Flux Test.	150
6-32	Temperature Data for Limiting Heat Flux Test	151
6-33	Condenser Test Results of VCF No. 2	152
7-1	Offset Fin Tube Geometry	155
7-2	Header/Flow Tube Orientation	156
7-3	Fluid Look Configuration	157
7-4	Conduction Fin Radiator System Weight versus Percent Copper in Fins	159
7-5	Conduction Fin Radiator System Weight versus Heat Rejection Area	159
7-6	Conduction Fin Radiator Weight/Area Relationship ($P_o = 0.990$)	160
7-7	Conduction Fin Radiator Weight/Area Relationship ($P_o = 0.999$)	161
7-8	Radiator System Weight versus Heat Rejection Area ($\gamma = 2.62$)	161
7-9	Conduction Fin Radiator Design Layout	166
7-10	Conduction Fin Radiator Design Details	167
7-11	Flow Tube/Fin Assembly (Step 1)	170
7-12	Conduction Fin Panel Assembly (Step 2)	170
7-13	Assembly of Z Rings and Mating Rings on Fixture (Step 3)	171
7-14	Radiator Bay Assembly (Steps 4 and 5)	172
7-15	Mating of Upper and Lower Bays (Step 7)	173
7-16	Header, Primary Duct, Vapor Chamber Orientation	175
7-17	Vapor Chamber Fin Radiator Optimization Results	176
7-18	Effect of Extended Surfaces in Primary Fluid Duct on Vapor Chamber Fin Radiator Weight.	178
7-19	Vapor Chamber Fin Radiator Weight/Area with Optimum Number of Primary Duct Fins	178
7-20	Vapor Chamber Fin Radiator Weights Including Structure	179

LIST OF ILLUSTRATIONS (Cont'd)

<u>Figure</u>		<u>Page</u>
7-21	Vapor Chamber Radiator Design Layout	182
7-22	Vapor Chamber Radiator Design Details.	183
7-23	Primary Coolant Duct Fabrication and Assembly (Step 1)	185
7-24	Vapor Chamber Panel Subassembly - Alternative 1 (Step 2)	185
7-25	Vapor Chamber Panel Subassembly - Alternative 2 (Step 2)	186
7-26	Vapor Chamber Panel Subassembly - Alternative 2 (Step 3)	187
7-27	Panel Assembly (Step 4)	190
7-28	Final Assembly (Step 5 and 6)	191
7-29	Ascent Temperature of Outer Skin	194
7-30	Effect of Radiator Surface Properties on Effective Sink Temperature for 100 n.m. Earth Orbit	195
7-31	Vapor Chamber Fin Radiator in Standby Condition	197
8-1	Total Radiator Weight versus area for Vapor Chamber and Conduction Fin Radiators	200

SECTION 1

INTRODUCTION

This study was performed by the General Electric Space Division's Isotope Power Systems Operation in partial fulfillment of Contract NAS3-10615, "Vapor Chamber Radiator Study," directed by the NASA Lewis Research Center. The major emphasis of the program was directed towards the development of a vapor chamber fin (heat pipe) radiator for application in the potassium Rankine cycle.

The heat rejection system for large unmanned nuclear powerplants constitutes a significant portion of the overall weight and area of the system. In addition, definite advantages exist in integrating the radiator design with the launch vehicle. These factors necessitate a detailed analysis of the radiator system so as to achieve an attractive power system size and weight.

1.1 STUDY OBJECTIVE

The primary purpose of this study was to assess the incentives for developing the Vapor Chamber Fin (VCF) radiator for the potassium Rankine cycle. The alternative is the use of a conduction fin radiator which is simpler in design and operational characteristics.

The potassium Rankine cycle space powerplant, under development at the Lewis Research Center, uses an indirect heat rejection process with a heat rejection rate of 1500 kW. A heat exchanger, shown in Figure 1-1, transfers waste heat from the power conversion loop to the primary coolant. The primary coolant is circulated through the main radiator where waste heat is rejected.

The present configuration visualized for the main radiator is an array of tubes through which coolant flows and to which are attached solid, conducting fins. The vapor chamber fin concept, under investigation in this study, operates in a different manner. Primary coolant enters the fluid passages and transfers heat to the vapor chamber evaporator sections by convection and conduction. As the evaporator increases in temperature,

the vapor chamber working fluid vaporizes and flows along the condenser vapor passage. As energy is radiated to space, condensation of the vapor chamber fluid occurs and the condensate is returned to the evaporator by the capillary pump action of the internal vapor chamber design. These processes are pictured in Figure 1-2.

In order to reach meaningful conclusions, the study consisted of both detailed analytical and experimental segments. The contents of the report are provided below.

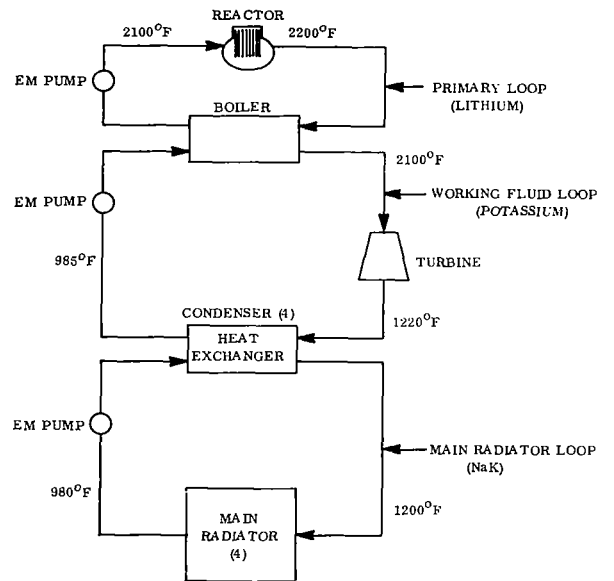


Figure 1-1. Simplified Potassium Rankine Cycle

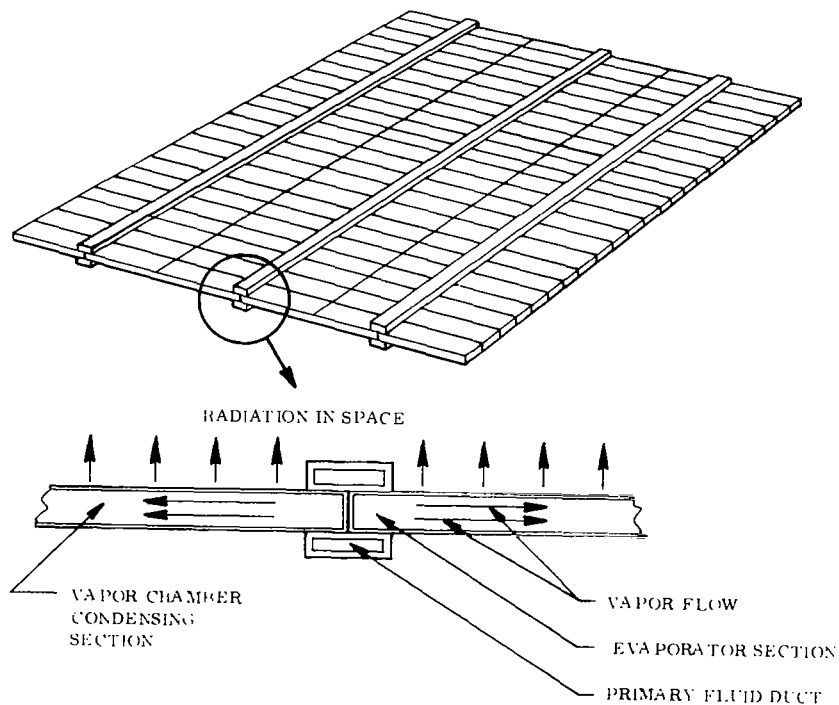


Figure 1-2. Representative Vapor Chamber Fin Radiator Panel

1.2 REPORT CONTENTS

Section 2 of this report contains a summary of the work performed, results obtained, and conclusions to be made.

Radiator and potassium Rankine cycle powerplant system specifications submitted by NASA Lewis were used as a design criteria. Design requirements used for the conduction fin and vapor chamber fin radiators are contained in Section 3.

Section 4 describes the various vapor chamber fin concepts considered for the radiator and identifies four basic geometries selected for further evaluation.

The thermal, integration, structural and fabrication evaluation of the four selected geometries is contained in Section 5. Conclusions and a selection of the preferred vapor chamber geometry are made.

Section 6 presents the vapor chamber test program performed on the selected geometry. A test description, test data and conclusions are provided.

The preliminary vapor chamber fin and comparable conduction fin radiator design are presented in Section 7. Weight, area, performance and fabrication comparisons are made.

The overall study evaluation of results and conclusions are contained in Section 8.

References are tabulated in order of appearance in Section 9. A list of numerical terms is included in Appendix A. The vapor chamber test plan followed in the program is included in Appendix B.

SECTION 2

SUMMARY

2.1 INTRODUCTION

The purpose of this study was to identify an optimum vapor chamber fin (heat pipe) radiator for the potassium Rankine cycle. It was anticipated that this approach would result in significant weight and area savings over the conduction fin radiator presently considered for this application.

The specifications on which the radiator analyses and final design are based were provided by NASA. These ground rules, listed in Table 2-1, reflect the current definition of the potassium Rankine cycle operating conditions for an unmanned mission.

The reference potassium Rankine cycle consists of three fluid loops; a simplified cycle diagram is shown in Figure 2-1. Liquid NaK (78 wt %K) condenses the potassium vapor exiting from the turbine in a heat exchanger and subsequently rejects the waste heat to space in the primary radiator. In this investigation the radiator was also designed to provide the main structural support for the power system during launch. Additional system radiators for the shield, pumps and electrical equipment were not a prime consideration in this analysis.

This study consisted of both analytical and experimental efforts. The program was divided in the following manner:

1. Selection of candidate vapor chamber fin geometries
2. Optimization of each candidate vapor chamber fin and working fluid

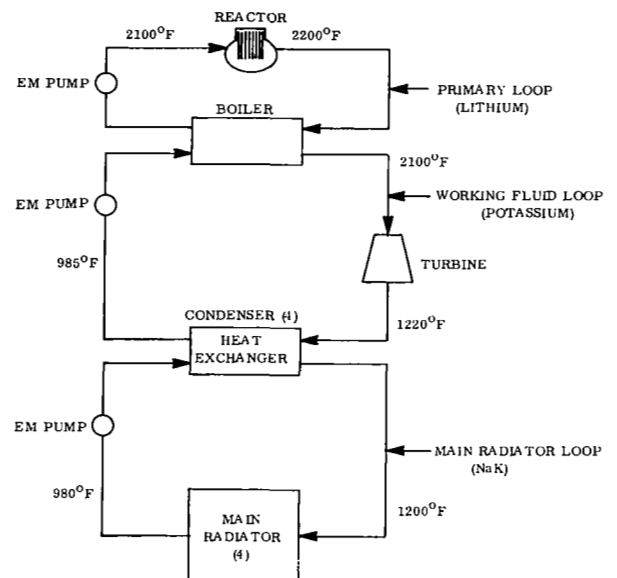
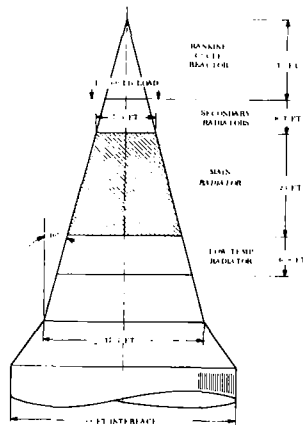


Figure 2-1. Simplified Potassium Rankine Cycle

Table 2-1. Specifications for the Potassium Rankine Radiator System (Unmanned)

Heat Rejection Rate (initial)	1536 kWt
Radiator Fluid	NaK - 78
Fluid Inlet Temperature	1200 ^o F
Fluid Outlet Temperature	980 ^o F
Redundancy	4 panel groups 3 survive
Heat Rejection Rate (end-of-life)	75% of initial
Radiator Meteoroid Survival Probability	0.99 0.999
Radiator Lifetime	20,000 hours 5 years
Materials	Stainless steel tube and armor; stainless steel clad copper or stainless steel fins; iron titanate coating.
Radiator Sink Temperatures	300nm equatorial orbit; radiator axis parallel to earth's surface; sun at zenith.
Launch Vehicle	2-stage Saturn V (10 degree half cone angle)
Supported Load	15,000 pounds on 10 degree half cone angle



3. Selection of optimum vapor chamber fin and working fluid
4. Testing of vapor chamber fin concept
5. Design and optimization of a vapor chamber fin radiator
6. Design and optimization of a conventional conduction fin radiator
7. Comparison between a vapor chamber fin and a conduction fin radiator.

Each of these tasks are summarized in the following paragraphs.

2.2 SELECTION OF CANDIDATE VAPOR CHAMBER FIN GEOMETRIES

The intent of this task was to define a number of attractive vapor chamber fin concepts from which an optimum configuration could be selected. This initial screening was primarily qualitative in nature.

Thermal efficiency, structural rigidity, sensitivity to meteoroid damage, heat pipe hydraulic considerations and fabricability were among the main factors governing the selection of four candidate designs. These are shown in Figure 2-2 in addition to other concepts which were reviewed.

Geometry 1 was selected because of the thermal and hydraulic efficiency offered by the cylindrical design. The presence of the conduction fin, separating the chambers, added a degree of flexibility to this design.

The rectangular cross section geometry was chosen as a candidate because it appeared to offer a sound structure having reasonable fabrication possibilities. At the same time, this concept would possess acceptable thermal and hydraulic characteristics.

The hexagonal honeycomb configuration was chosen solely for its load carrying capability. Each hexagon is pictured as operating as a separate vapor chamber which transfers energy to adjoining vapor chambers by the condensation process. The magnitude of the thermal

disadvantage presented by the interior walls could not be easily assessed without the support of a detailed analytical investigation.

Geometry 4 is easily fabricated and thermally efficient. The unknown quantity in this particular design (and Geometry 1) was the structural problems associated with a large thin sheet area.

2.3 OPTIMIZATION OF CANDIDATE CONCEPTS

The four concepts described in the preceding paragraph were examined parametrically to assess the optimum geometric values for each design. The evaluation was based on pounds of radiator per kilowatt of heat rejected. This optimization included the effects of the primary fluid ducts and vehicle structural considerations as well as the more obvious thermal, meteoroid protection and fluid flow requirements.

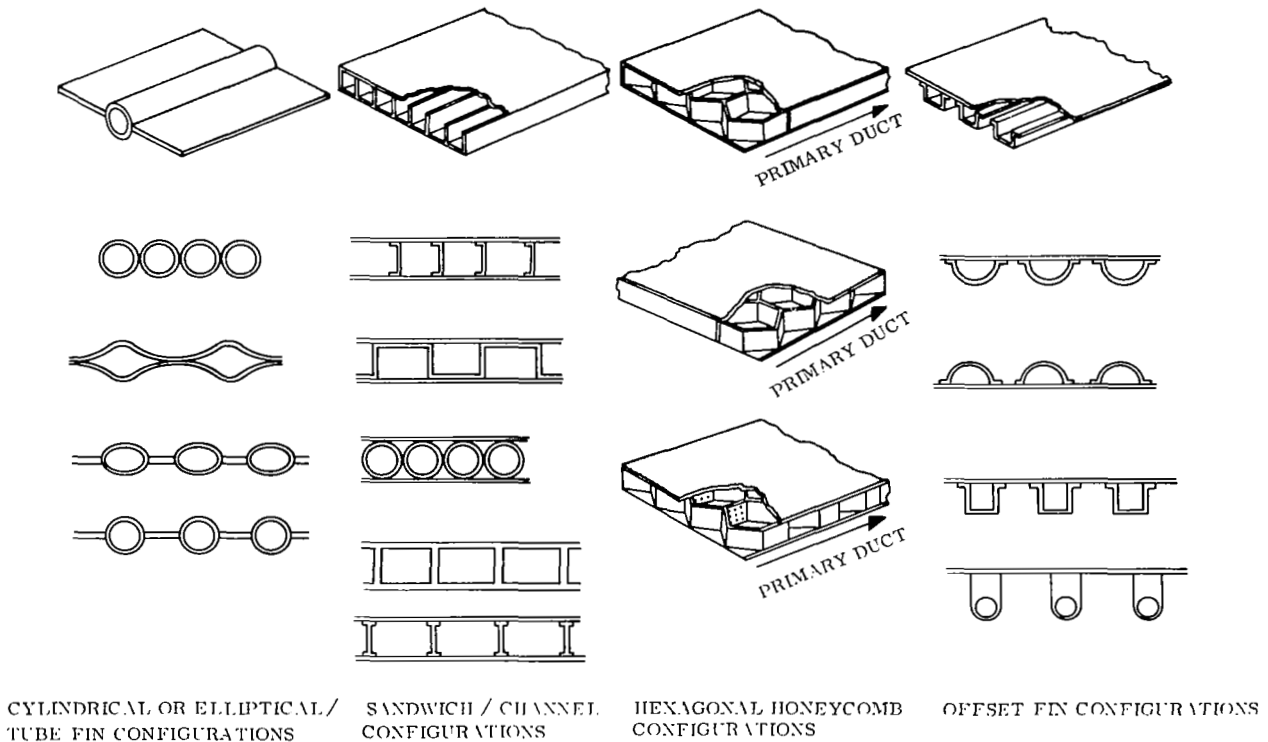


Figure 2-2. Vapor Chamber Concept Alternatives

The optimization procedure used a computer program to calculate required wick thickness, temperature distributions and heat rejection rates. Three working fluids were considered: cesium, potassium and sodium.

Geometry 2, the rectangular vapor chamber fin concept, was chosen as the most attractive concept. This decision was based on the low radiator system weight obtainable while working within the framework of reasonable fabrication techniques. A summary of the geometry evaluation is shown in Figure 2-3.

Sodium demonstrated superiority over cesium and potassium primarily due to its high surface tension and latent heat of vaporization. Cesium was found to constitute a poor fluid choice for this application (900° - 1200° F range).

2.4 TESTING OF THE RECTANGULAR VAPOR CHAMBER FIN GEOMETRY

The objective of this portion of the program was to obtain accurate operational data on the vapor chamber fin design defined by the optimization procedure. A single vapor chamber fin, which represented the basic building block of a panel, was fabricated. Using sodium as the working fluid, with a composite wick design, tests were conducted between 825° and 1600° F. The vapor chamber performed satisfactorily in this regime. The test setup and vapor chamber design employed is shown in Figures 2-4 and 2-5.

The observed evaporative and axial vapor temperature drops agreed reasonably well with predicted values.

The overall condensing temperature drop existing between the condenser vapor space and heat rejection surface exhibited values substantially higher than predicted by theory. Subsequent testing with a second vapor chamber showed this temperature drop to be time dependent. Using the same test facility and identical instrumentation, the condensing ΔT decreased from 54° to 18° F at 1300° F over a 10 week period. No positive explanation

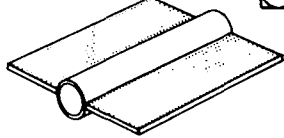
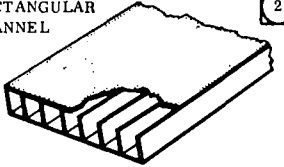
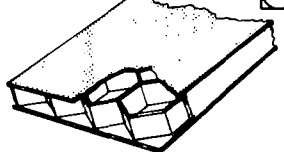
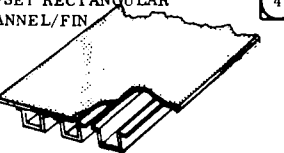
GEOMETRY CONFIGURATION	THERMAL	INTEGRATION	STRUCTURAL	FABRICATION
CYLINDRICAL TUBE/FIN 	HIGH RATIO OF FLOW AREA TO HEAT PIPE CIRCUM-FERENCE MINIMUM WEIGHT	MORE DIFFICULT TO INTEGRATE WITH PRIMARY DUCT THAN GEOMETRY 2 & 3 - HIGHER EVAPORATOR ΔT	SUSCEPTIBLE TO FIN BUCKLING AND TUBE CRUSHING	CONSIDERED ON A PAR WITH 4 IF EXTRUSION IS USED
RECTANGULAR CHANNEL 	HIGH EFFECTIVE RADIATOR TEMP. GOOD EVAPORATOR INTERFACE MINIMUM RADIATOR AREA	PROVIDES TWO FLAT SURFACES FOR GOOD ATTACHMENT TO PRIMARY DUCT AND SPLICE PLATES	LOW LOCAL AND PANEL STABILITY REQUIREMENTS. SMALL RADIATOR AREA PROVIDES STIFFER STRUCTURE DUE TO SMALLER BENDING MOMENT	SOMEWHAT MORE DIFFICULT THAN 1 OR 4 BUT USE OF FLANGES PERMITS GOOD BRAZE OR WELD.
HEXAGONAL HONEYCOMB 	GOOD EVAPORATOR INTERFACE POOR HEAT TRANSFER	PROVIDES TWO FLAT SURFACES FOR GOOD ATTACHMENT TO PRIMARY DUCT AND SPLICE PLATES	POOR THERMAL PERFORMANCE RESULTS IN LARGER RADIATOR AREA HAVING GREATER STRUCTURAL REQUIREMENTS	CONSIDERED VERY DIFFICULT IN THE CHARGING & SEALING OF CHAMBERS
OFFSET RECTANGULAR CHANNEL/FIN 	GOOD METEOROID RESISTANCE AREA COMPARABLE TO 1, HIGHER WEIGHT	ONE FLAT SURFACE. DOES NOT PRESENT EFFICIENT THERMAL INTEGRATION WITH PRIMARY DUCT	SUSCEPTIBLE TO FIN BUCKLING. SMALL RADIUS OF GYRATION PROVIDED BY PRIMARY DUCT DESIGN CAUSES LOCAL AND PANEL INSTABILITIES	CONSIDERED TO BE SIMPLE TO FABRICATE BY WELDING OR BRAZING

Figure 2-3. Vapor Chamber Geometry Evaluation Summary

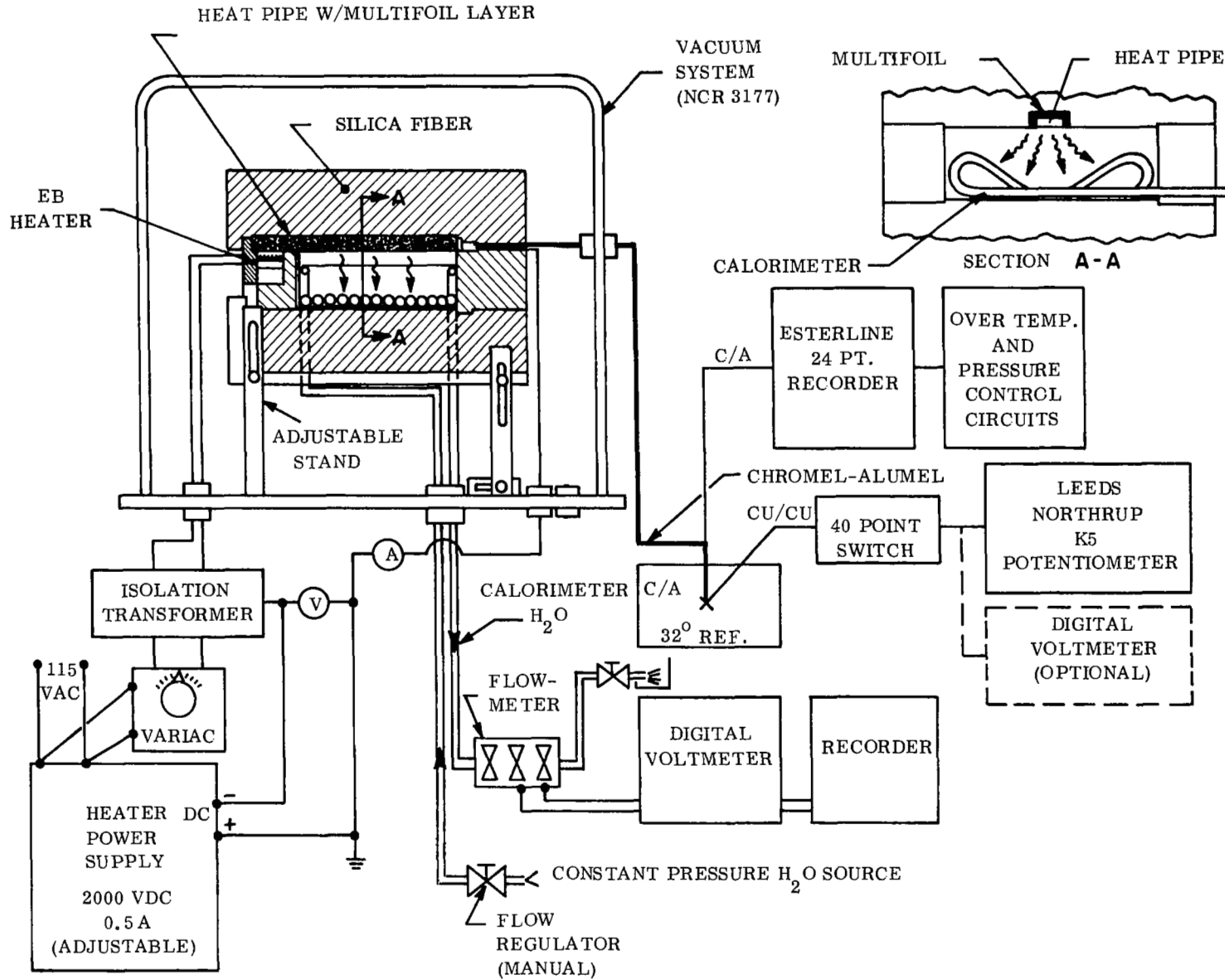


Figure 2-4. Vapor Chamber Fin Test Schematic

can be offered for this behavior, however, it appears that some conditioning process occurring between the fluid and stainless steel enabled the sodium to achieve a more complete filling of the fluid return annulus. Using the poorest operational data obtained, the vapor chamber fin efficiency was calculated to be 80 percent. The latter tests indicated a vapor chamber fin efficiency of 96 percent.

A tilt test was performed to ensure that the capillary in the evaporator was pumping the sodium. If the vapor chamber fin can operate in a tilted position in a one g environment, adequate capillary pumping can be assumed in zero g. The data from this series of tests agreed closely with the values obtained during the horizontal experiments. This result verified the effectiveness of the evaporator capillary pump.

An investigation of the evaporative heat flux limitation was also performed. The vapor chamber fin operated satisfactorily, with no evidence of burnout, at temperatures of 1600°F and evaporative heat fluxes of $1.46 \times 10^5 \frac{\text{BTU}}{\text{hr-ft}^2}$. Higher evaporative heat fluxes were precluded by the stainless steel strength limitations at higher temperatures.

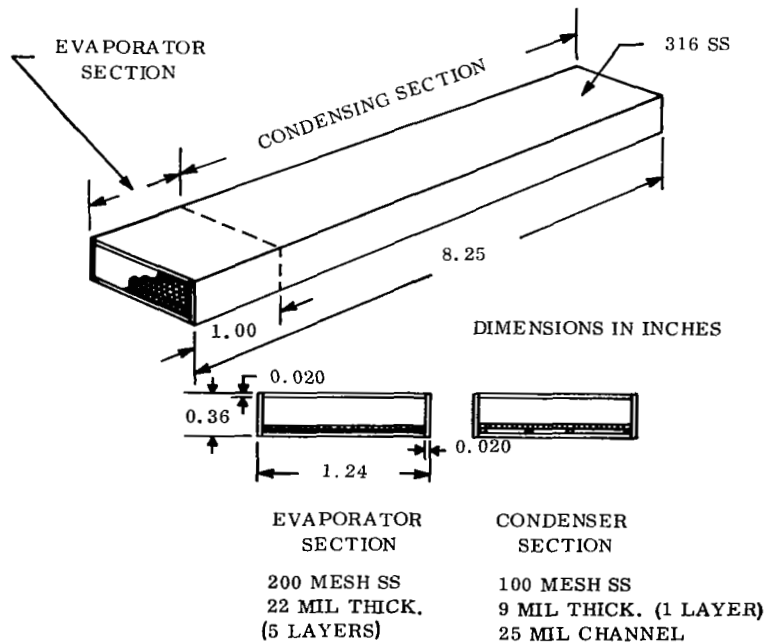


Figure 2-5. Vapor Chamber Fin Used in Test

2.5 VAPOR CHAMBER FIN RADIATOR DESIGN

The vapor chamber fin radiator design was optimized from a system standpoint by a large scale computer code especially designed for this purpose. Using the rectangular channel vapor chamber fin geometry, sodium working fluid and stainless steel construction, a series of minimum weight radiators was designed for meteoroid survival probabilities of 0.99 and 0.999 over lifetimes up to five years.

As part of this analysis several primary fluid duct (NaK-78) configurations were examined. The concept which was selected, shown in Figure 2-6, provided the minimum radiator weight design as well as a relatively easy panel unit to fabricate.

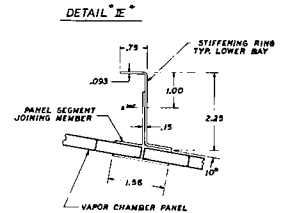
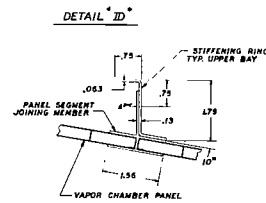
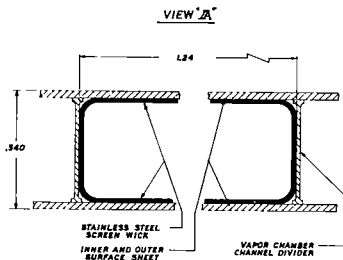
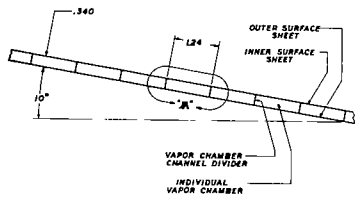
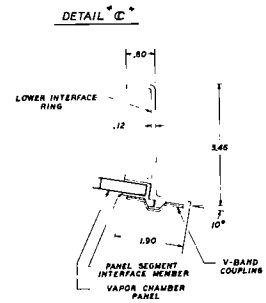
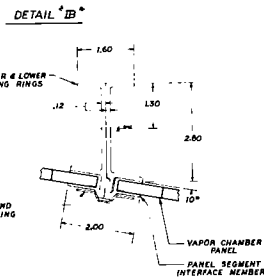
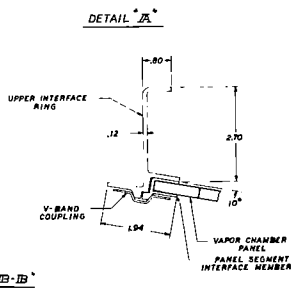
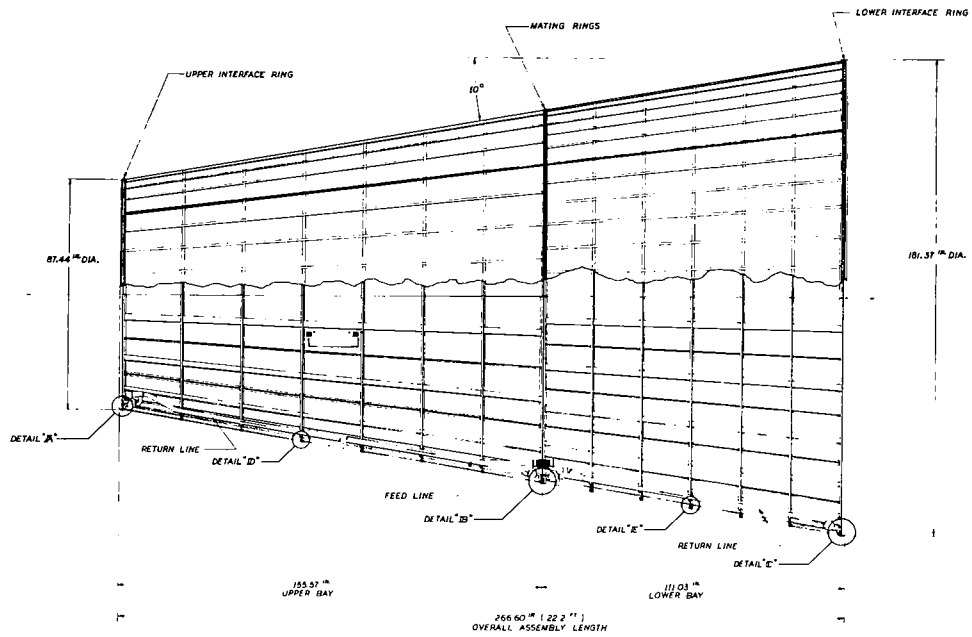
2.6 CONDUCTION FIN RADIATOR DESIGN

The concept presently considered for the potassium Rankine cycle heat rejection system is a conduction fin radiator having the offset fin/tube geometry. Stainless steel has been identified as the radiator tube and armor material; the fin is a stainless steel/copper laminate.

A complete radiator analysis and design was performed using a large scale computer code to integrate the heat transfer, fluid flow and meteoroid protection requirements into a minimum system weight design. The optimized design also reflected the secondary requirements of the radiator to support the power system and to act as the aerodynamic shroud during launch. Radiator system weights were determined for two meteoroid survival probabilities: 0.99 probability of survival for 20,000 hours and 0.999 probability of survival for five years (43,800 hours) where 3 of 4 panel groups survive the entire mission. Essential features of the conduction fin radiator design are shown in Figure 2-7.

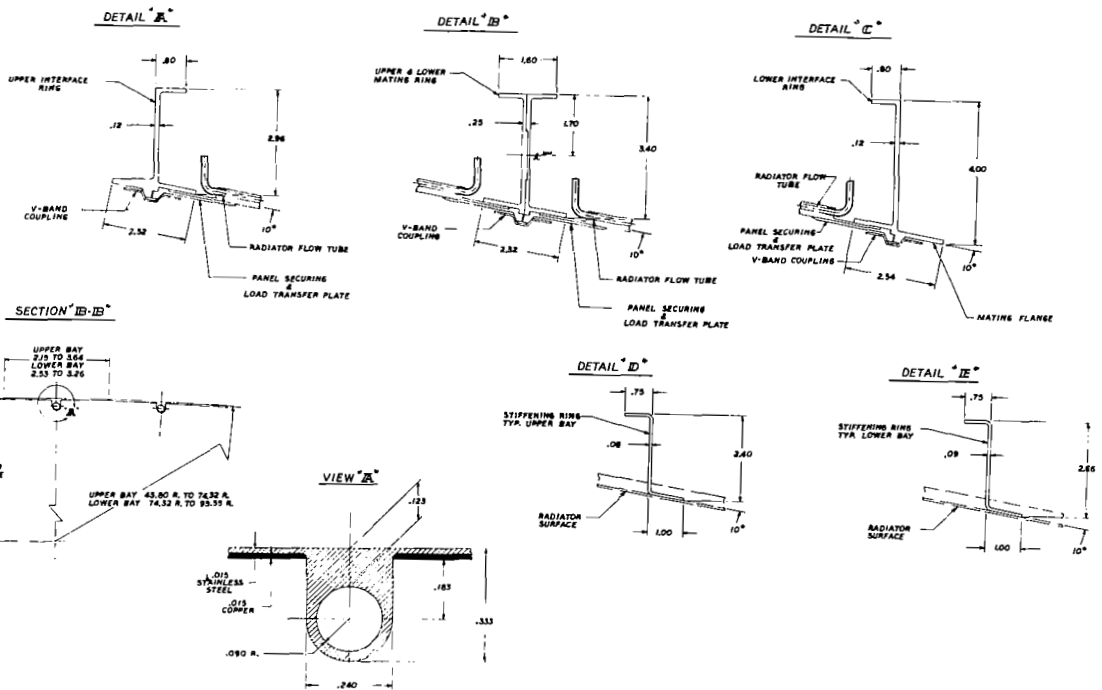
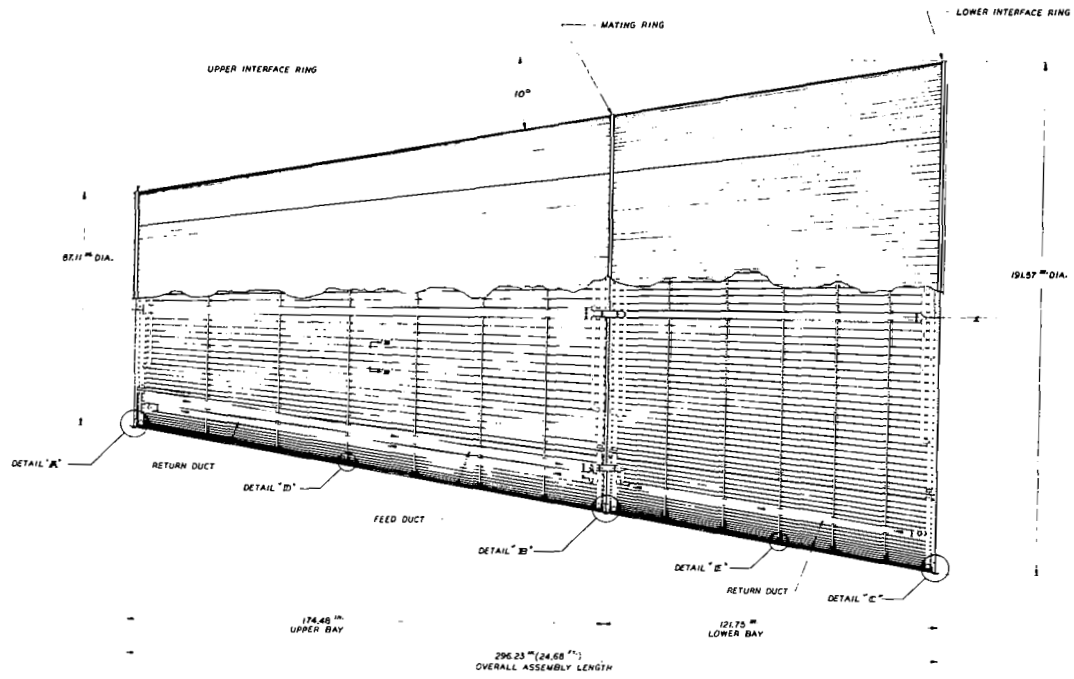
2.7 COMPARISON OF THE VAPOR CHAMBER AND CONDUCTION FIN RADIATORS

A comprehensive comparison of the vapor chamber fin and conduction fin concepts must include several factors including feasibility, development time and cost, fabrication difficulty, weight, area and special operational problems such as startup and transient response.



NOTE: ALL DIMENSIONS IN INCHES UNLESS OTHERWISE SPECIFIED

Figure 2-6. Vapor Chamber Fin Radiator Design



NOTE: ALL DIMENSIONS IN INCHES UNLESS OTHERWISE SPECIFIED

Figure 2-7. Conduction Fin Radiator Design

Both heat rejection concepts considered are well within the realm of feasibility, however, the conduction fin radiator can be considered to be at a more advanced stage of development. Although a stainless steel radiator with stainless steel/copper fins has never been fabricated, the composite fin material does not appear to entail an exceptional development effort. With respect to the vapor chamber fin radiator, more experience with heat pipe operation in a zero g environment is desirable, especially in the related areas of wick design and fluid inventory.

The vapor chamber fin radiator design is considerably more complex than the conduction fin radiator. Therefore, the fabrication of the vapor chamber fin radiator can be expected to be the costlier of the two. The requirement to fill thousands of individually sealed chambers under stringent purity conditions with alkali metal is of particular concern.

Weight versus area characteristics for both the conduction fin and vapor chamber fin designs are shown in Figure 2-8 for meteoroid survival probabilities of 0.99 for 20,000 hours and 0.999 for five years. The vapor chamber fin radiator system is lighter in weight and smaller under all of the conditions investigated. The redundant characteristics of the individual vapor chambers enables the vapor chamber fin radiator weight to remain fairly insensitive to large changes in the meteoroid protection requirements. For missions where high reliability against meteoroid damage is needed, the vapor chamber fin radiator may become more attractive.

2.8 CONCLUSION

The major conclusions drawn from this program are listed below:

1. The VCF radiator is a feasible heat rejection concept for use in the potassium Rankine cycle or any system radiating in the 900^o to 1400^o F range.
2. A comparison of the fabrication problems associated with the VCF and conduction fin radiator indicates that the VCF is considerably more difficult to fabricate. This is largely due to the requirement to individually fill and seal about 10,000 vapor chambers. Obviously, the entire reliability of the VCF radiator is dependent upon the quality of the filling and sealing techniques.

- The attractiveness of the VCF radiator as compared to the conduction fin concept on a system weight basis becomes significant as the meteoroid protection requirements become more severe. At a survival probability of 0.999 for 5 years the VCF design exhibited a 30 percent weight advantage over the conduction fin design.

For manned missions, where the shield weight dominates the powerplant weight, this weight advantage is probably insignificant.

- Sodium was identified as an excellent vapor chamber fluid for this application.

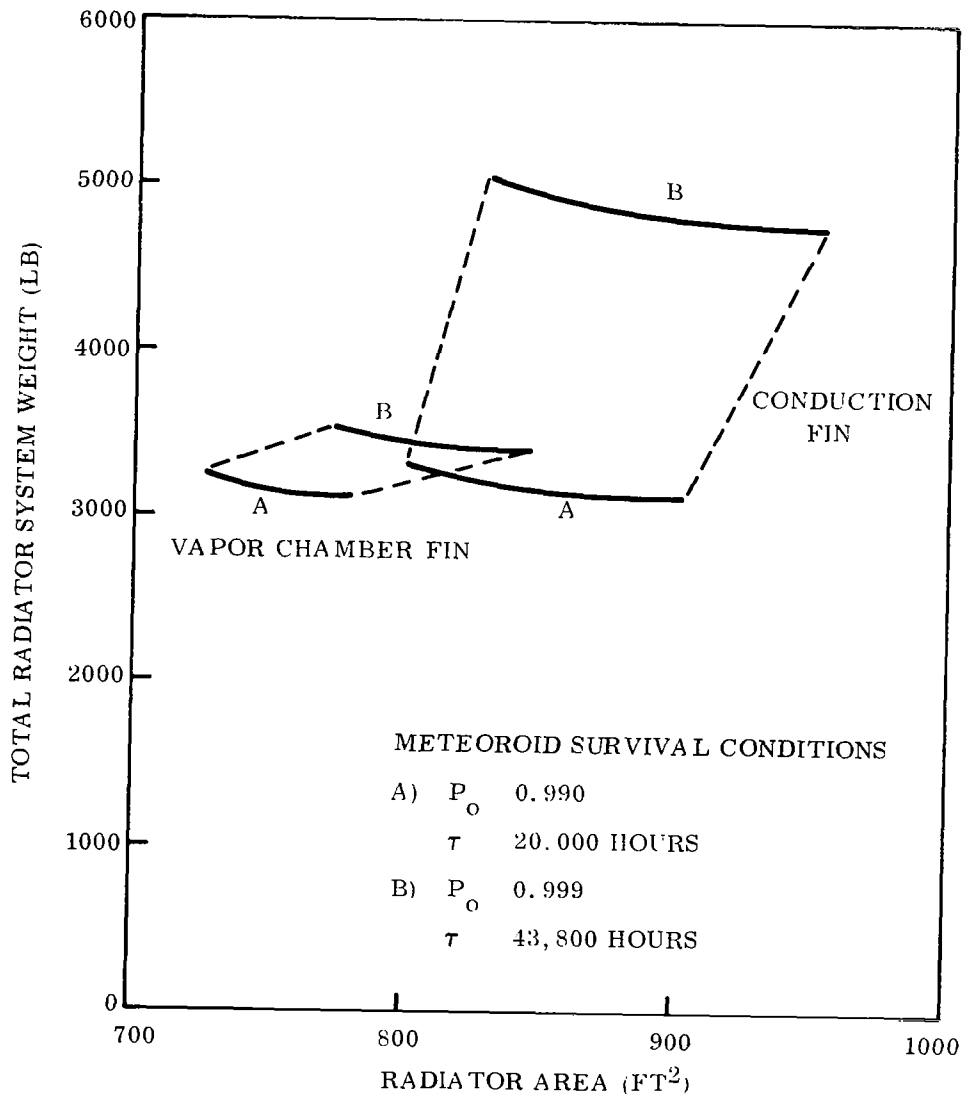


Figure 2-8. Total Radiator Weight vs Area for Vapor Chamber and Conduction Fin Radiator

SECTION 3

RADIATOR DESIGN REQUIREMENTS

3.1 GENERAL DISCUSSION

The potassium Rankine cycle powerplant, under development at the NASA-Lewis Research Center, transfers waste heat from the condensing fluid, potassium, to the primary liquid coolant, NaK-78. The primary coolant rejects the waste heat from the system by means of the main radiator. Other system radiators for the pumps, shield and electrical equipment were not examined in this study.

The basic requirements of the radiator can be divided into several categories including thermal performance, structural performance, integration, reliability and fabrication feasibility. These requirements must be satisfied within the framework of achieving an attractive weight, area and pumping power penalty.

3.2 SYSTEM SPECIFICATION

Design requirements for the main radiator were determined by the cycle conditions of the 300 kWe potassium Rankine cycle as presently conceived by NASA-Lewis. A schematic drawing of this system is shown in Figure 3-1.

Specific design specifications, pertinent to the radiator analyses are shown in Table 3-1. The main radiator is pictured as a cone cylinder and comprises a section of the aerodynamic fairing, atop a two stage Saturn V. In addition, the radiator and associated structure provides structural support for the nuclear powerplant during the launch sequence.

Four independent loops are currently defined for the primary coolant. Ground rules for this study allowed the failure of one loop due to meteoroid damage over the mission lifetime. Two meteoroid survival design conditions were investigated: a 0.99 probability of survival for 20,000 hours and a 0.999 probability of survival for 43,800 hours (5 years).

Stainless steel was stipulated as the radiator material of construction due to its compatibility with liquid metals, fabricability and high strength-to-weight ratio at launch conditions. The

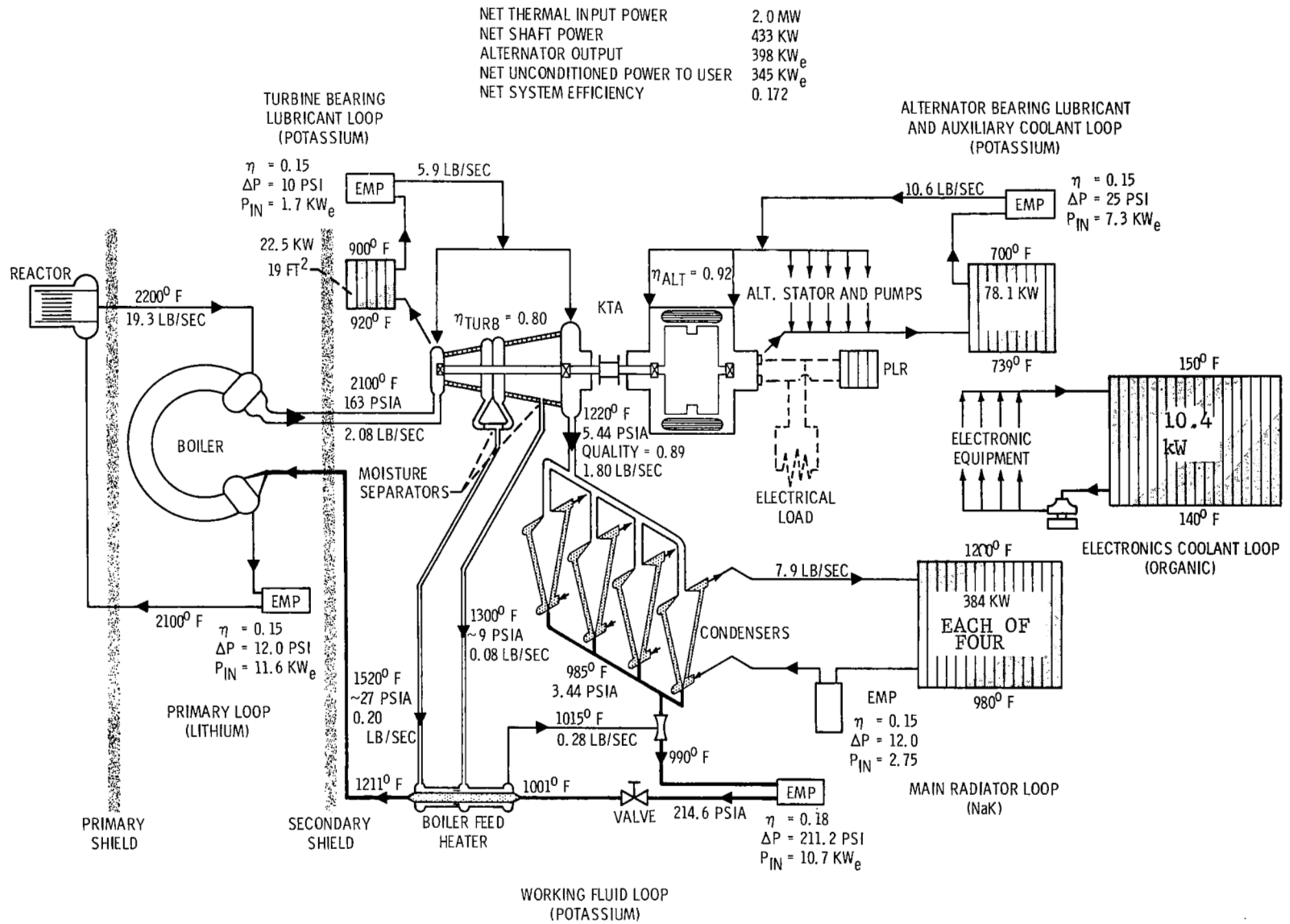
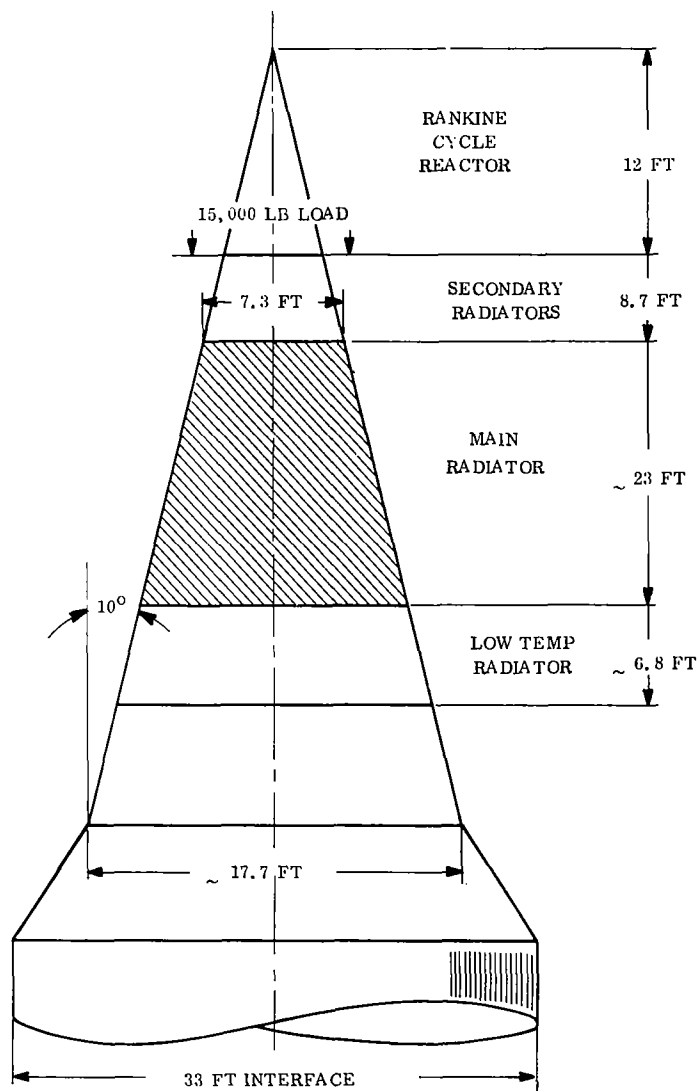


Figure 3-1. Potassium Rankine Power System (Nominal 300 kW_e)

Table 3-1. Reference Conditions and Specifications for the Potassium Rankine Main Radiator

Thermal Heat Rejection, Initial	1536 kWt
Radiator Fluid	NaK-78
Radiator Fluid Flow Rate/loop	7.9 lb/sec
Radiator Fluid Inlet Temperature	1200 ^o F
Radiator Fluid Outlet Temperature	980 ^o F
Redundancy	4 panel/loop segments 3 loops survive
Heat Rejection Rate (end-of-life)	75% of initial
Radiator Meteoroid Survival Probability	0.99 0.999
Radiator Lifetime	20,000 hrs. 43,800 hrs (5 years)
Radiator Materials	Stainless steel tube and armour; stainless steel clad copper or stainless steel fins; iron titanate coating
Radiator Sink Temperatures	300 nm equatorial orbit; radiator axis parallel to earth's surface; sun at zenith
Meteoroid criteria	Environment: Whipple 1963A Flux density Model (Reference 1) Damage Criteria: Loeffler (Reference 2)
Launch Vehicle	Two-stage Saturn V Interface diameter 33 feet
Structure/Supported Load	15,000 lbs 10 degree half-cone angle



conduction fin radiator, however, utilized a copper/stainless steel bimetallic fin in order to raise the fin thermal conductivity.

Also specified was the consideration of three fluids for use in the vapor chambers: cesium, potassium and sodium. While it is desirable to limit the choice to one fluid, the possibility of using two fluids, one in the high and one in the lower temperature section, was considered.

3.3 METEOROID CRITERIA

The meteoroid criteria used in this study reflected current recommendations of NASA-Lewis at that time. The meteoroid environment assumed is the Whipple 1963A flux density model (Reference 1) with an average meteoroid velocity of 20 km/sec and a meteoroid density of 0.5g/cc. Many of the previous radiator studies at General Electric assumed an average velocity of 30 km/sec and a meteoroid density of 0.44g/cc. The estimates specified for this study result in a 22 percent reduction in armor thickness. The use of estimates of near earth environment may be conservative for an outward bound interplanetary probe mission, since the flux is generally considered to decrease with heliocentric distance. Loeffler, Lieblein and Clough (Reference 2), suggest a flux density decreasing at the rate $(R)^{-1.5}$, where R is the heliocentric distance. If the flux is integrated between Earth and Jupiter, assuming a constant velocity and an $(R)^{-1.5}$ relation, the average flux is only 29 percent of the near Earth flux. However, the flux intensities in the asteroid belt and near Jupiter are anomalous, possibly comparable in intensity to the near Earth environment. Estimates of the flux in traversing the asteroid belt vary by an order of magnitude on either side of the near Earth environment, and the near Jupiter environment is as yet unexplored. A study of Jupiter flyby missions (Reference 3) assumes a Jupiter environment three times more severe than Earth's. Volkoff, (Reference 4) estimates a protection requirement ratio relative to near Earth of 0.432 for a Jupiter orbit mission based on a time integrated environment. In the absence of reliable experimental data, the more conservative estimates of near Earth environment are used in this study. The damage criteria used in determining meteoroid protection requirements is that proposed by Loeffler (Reference 2),

$$t_a = a \gamma \left(\frac{\rho_{mp}}{\rho_t} \right)^{1/2} \left(\frac{v_{mp}}{C_t} \right)^{2/3} \left(\frac{6}{\pi \rho_{mp}} \right)^{1/3} \left[\frac{\alpha A_v \tau}{-\log_e P_{ND}} \right]^{1/3\beta} \left(\frac{1}{\beta + 1} \right)^{1/3\beta} \quad (3-1)$$

where

t_a = required armor thickness

a = damage thickness factor

γ = materials cratering coefficient

ρ_{mp} = meteoroid density (0.5 gm/cm³)

ρ_t = armor material density

v_{mp} = meteoroid velocity (25 km/sec)

C_t = sonic velocity in armor

A_v = vulnerable area

τ = mission time

$\alpha = 10^{-14.41} \frac{\text{gm}^{1.22}}{\text{m}^2 \text{-sec}}$

$\beta = 1.22$

P_{ND} = design probability of no critical damage

The constants a and γ vary from material to material and with damage mode. The cratering coefficient γ for a wide range of materials has been determined experimentally. Lieblein and Diedrich (Reference 5) report a rear surface damage factor, for dimpling, of 2.4 and a cratering coefficient of 1.67 for 316 stainless steel. These values were used in the VCF and conduction fin reference design analyses.

During the course of this study a report issued by NASA-Lewis (Reference 6) indicated a room temperature cratering coefficient cratering coefficient for 316 stainless steel of 2.19. The following correlation was proposed for higher operating temperatures:

$$\gamma = \gamma_R \left(\frac{T}{T_R} \right)^{1/6}$$

At 1200^o F the value of γ is calculated to be 2.62; designs based on this value are presented for the conduction fin radiator. However, due to the relative insensitivity of the VCF radiator design to changes in meteoroid protection requirements, a similar analysis was not performed for this concept.

3.4 STRUCTURAL CRITERIA

The reference launch vehicle to be utilized with the potassium Rankine cycle is the two stage Saturn V. The position of the main radiator on the vehicle is shown in Table 3-1.

As listed in Table 3-1, the load supported by the radiator is 15,000 pounds. This includes the reactor, shield, power conversion equipment and associated piping.

The maximum loads occurring on the radiator will result from launch conditions. During launch maximum $q\alpha$ and maximum axial acceleration conditions exist giving equivalent axial loads approaching 500,000 pounds. Maximum bending loads occur when the product of dynamic pressure and angle of attack $q\alpha$ reach a maximum, and the maximum axial loads occur the instant of first stage engine cutoff. If the launch structure were designed to an axial load condition only, an unrealistic result would be obtained, since it is obvious that the structure must also have some lateral stiffness. A difficulty arises in attempting to specify a realistic load condition for lateral stiffness since it is known that static lateral accelerations during launch are generally low. One approach is to design to an artificial but conservative condition such as 12 g axial combined with 5 g lateral. This approach may be reasonable for small payloads, but excessively conservative and possibly prohibitive for a payload whose size and mass are no longer insignificant compared with the launch vehicle. The load factor must decrease as the payload size increases, as evidenced by the trend shown in Figure 3-2.

At the maximum $q\alpha$ condition, the two stage Saturn V has an axial acceleration of 2.0 g and a lateral acceleration of 0.2 g. These conditions are to be utilized in the study.

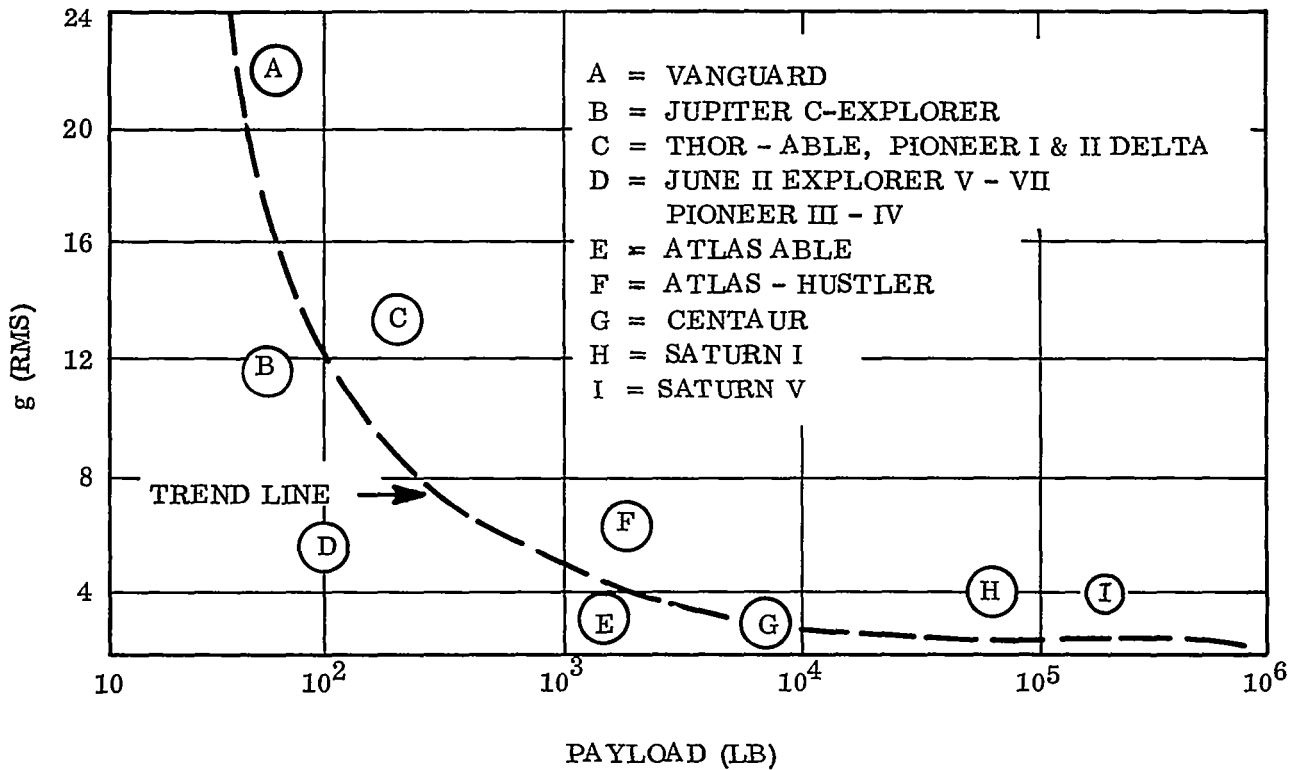


Figure 3-2. Trend in Launch Vehicle Dynamic Loads

3.5 OPERATIONAL CRITERIA

The radiator shall be capable of operating in a one g environment for purposes of establishing ground test performance predictions. Consideration should also be given to devising a radiator geometry capable of operating in any orientation in a zero g environment. Techniques and configuration schemes to provide radiator startup from a frozen state shall be evaluated.

3.6 VEHICLE INTEGRATION

The overall radiator design must be compatible with the remainder of the powerplant system and also reflect the requirement for the radiator to be used as the flight fairing. A relatively smooth heat rejection surface is consistent with the structural, thermal and aerodynamic functions of the radiator. Attention must also be given to the design of radiator interfaces with other portions of the system where thermal stresses could be a problem. The problem of efficient transfer of flight loads is also a consideration in this area. Fluid feed lines extending between the power conversion units and the radiator must also be considered in the overall design, since these require a considerable volume and are subjected to flight loads and thermal stresses.

3.7 FABRICATION

The radiator design shall be consistent with accepted NASA design practices. Insofar as possible fabrication practices should be within the present state-of-art. Projections of the state-of-art should be made with a high degree of confidence within the time frame of the projected applications.

SECTION 4

VAPOR CHAMBER CONCEPT DEVELOPMENT

The purpose of this effort was to select the candidate conceptual designs to be used as a basis in determining the most attractive vapor chamber radiator configuration. Three candidate working fluids were considered for use within the vapor chamber radiator: cesium, sodium and potassium. The vapor chamber radiator would consist of an upper and lower bay with radiation from the outer surface only. A distinct effort was made to include a wide spectrum of vapor chamber designs as well as the more familiar; an example of some of the configurations which were considered is provided in Figure 4-1. Since it would be impractical to thoroughly investigate each design, it was necessary to eliminate many of these concepts on the basis of engineering judgment. In addition, it became obvious that some of the more similar designs would be reduced to the same configuration due to fabrication considerations.

The primary factors which guided the selection of the basic geometries are:

1. Weight - Ability to be manufactured as a light-weight structure
2. Area - Maximum exposure of the condensing surfaces to the sink
3. Meteoroid Survivability - Ability to afford a high reliability against excessive meteoroid damage
4. Structural - Ability to be used as the aerodynamic fairing during launch and to support the power system during this period
5. Fabrication - Ease of fabrication into the complete radiator
6. Integration with Primary Duct - Vapor chamber fin must be able to accept heat from the primary duct without involved fabrication techniques or a large ΔT .

Of the concepts examined, four were deemed to be of sufficient interest to be included in the final comparative evaluation. These are presented in Figure 4-2. Geometry 1 represents a design which is easy to manufacture and is amenable to light-weight construction. The

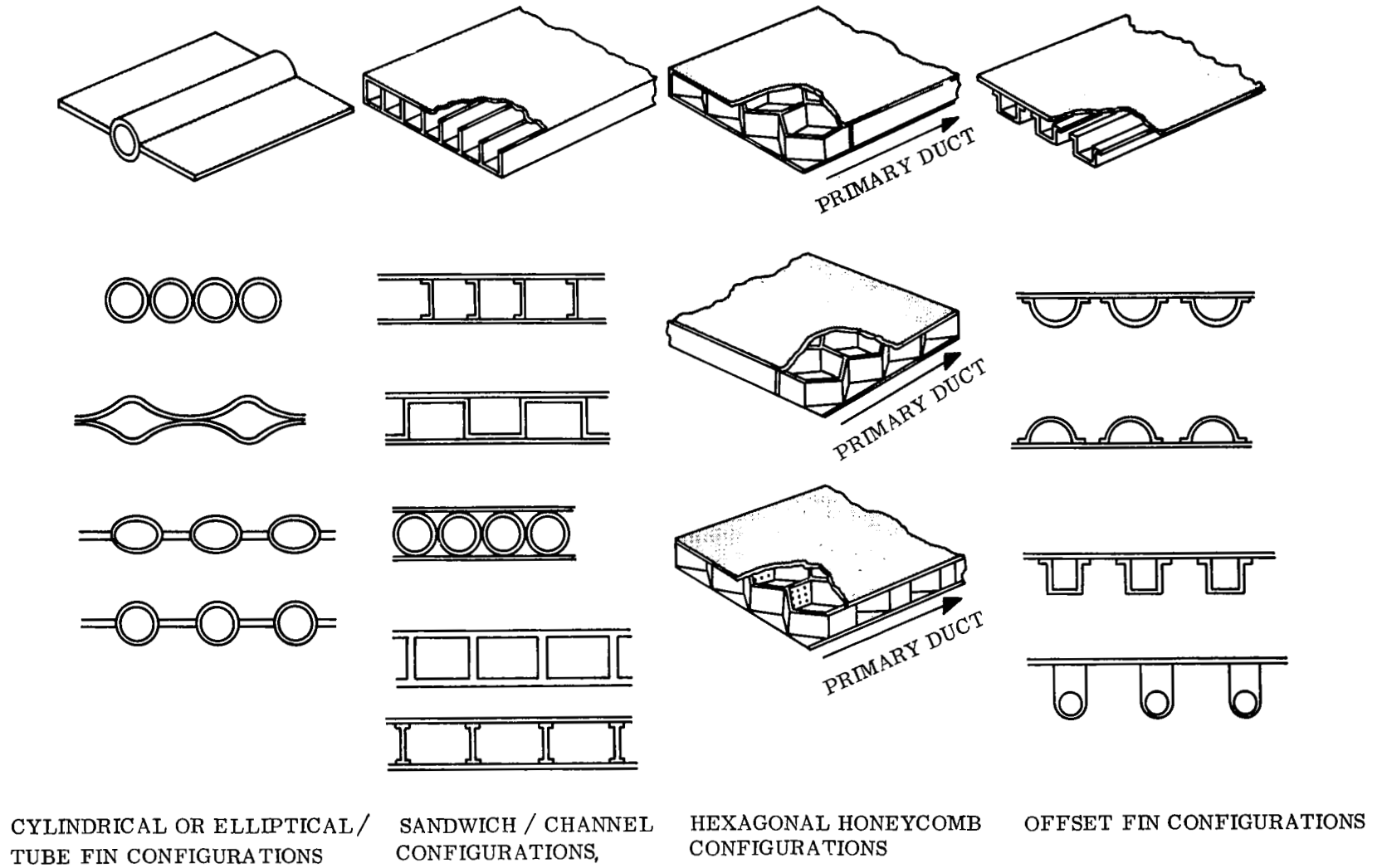


Figure 4-1. Vapor Chamber Concept Alternatives

round flow passage is ideal for all aspects of heat pipe operation, while the conduction fins are a light weight means of providing radiating area.

Geometry 2 is a design which would operate at a uniform surface temperature, thus reducing the overall radiator area. In addition, this design provides for a simple interface with the primary duct.

The obvious advantages of Geometry 3 are its structural rigidity and, due to the large number of cells, its exceptional resistance to significant meteoroid damage. Each hexagonal cell, however, has its own evaporator and condenser section resulting in several thermal resistances along the length of the fin. Since each cell must be a self-contained unit, fabrication of this system can be expected to be difficult.

Geometry 4 is similar in some respects to 1, but, has certain structural and fabrication advantages. The ability of the conduction fins to act as an efficient means of heat transfer in a vapor chamber radiator is of interest in both of these concepts.

The four geometries chosen for investigation were felt to represent a varied array of possible design alternatives. Each geometry has its particular advantages and disadvantages which justified a thorough study in order to choose the optimum design.

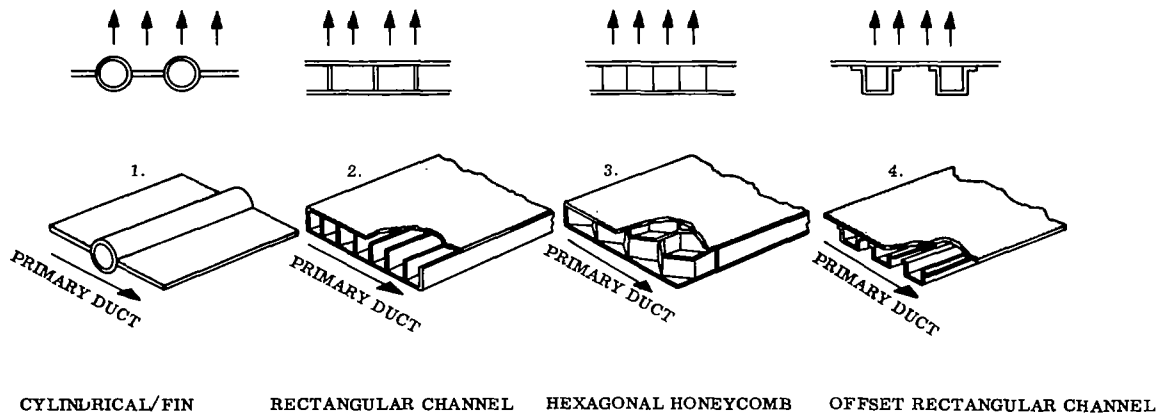


Figure 4-2. Concepts Selected for Further Investigation

SECTION 5

VAPOR CHAMBER ANALYSIS

The analysis for each geometry was divided into two parts: first, an evaluation of the condenser section, and secondly, the evaluation of the entire radiator including the primary fluid ducts, evaporator and condenser sections. In order to make a valid comparison between concepts, each geometry must be investigated thoroughly over a range of parameters so as to find the region of attractive design points. Principal areas of investigation and selected characteristics for final evaluation and comparison were:

1. Thermal performance (weight, area and reliability)
2. Integration with primary duct and radiator interfaces
3. Structural performance
4. Fabrication capability

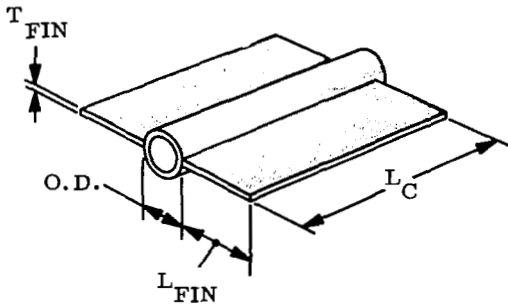
5.1 CONDENSER EVALUATION

In the first part of the analysis, each condenser geometry was evaluated over the range of variables shown in Figure 5-1. The criteria used as a basis of evaluation was weight per kilowatt of heat rejected. In this phase of the study, all system considerations such as total radiator area, system pumping power and vapor chamber fin/duct interface were temporarily neglected in order to focus attention on the condenser section weight calculations. The considerations which were factored into this analysis were:

1. Meteoroid criteria
2. Thermal performance in terms of fluid flow and heat transfer characteristics
3. Structural integrity under thermal and launch loads.

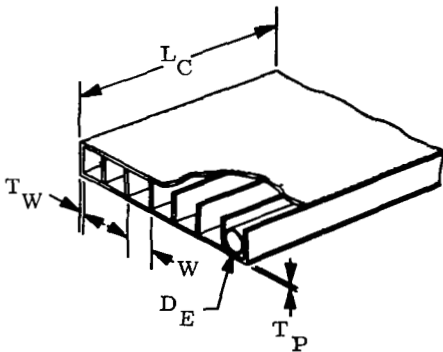
These subjects are treated individually in the following paragraphs.

GEOMETRY 1



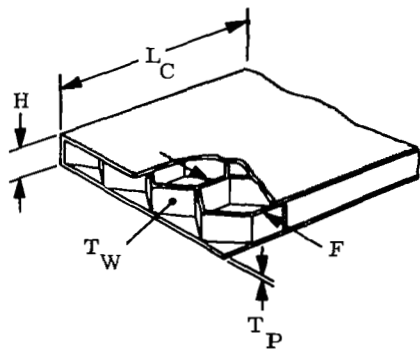
LENGTH (L) = 0.5, 1.0, 1.5, 2.0 (FEET)
 O. DIAMETER (O.D.) = 0.50, 0.75, 1.00 (INCHES)
 FIN THICKNESS (T_{FIN}) = 0.010, 0.020, 0.040 (INCHES)
 FIN LENGTH (L_{FIN}) = 0.000, 0.125, 0.250, 0.500 (INCHES)
 TUBE THICKNESS = 0.015 (INCHES)

GEOMETRY 2



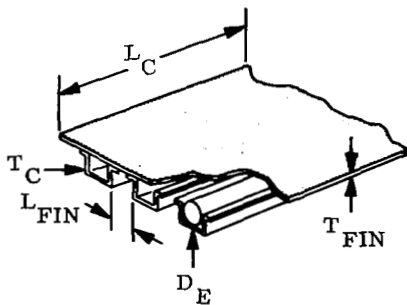
LENGTH (L) = 0.5, 1.0, 1.5, 2.0 (FEET)
 EQUIV. DIA. (D_E) = 0.25, 0.50, 0.75 (INCHES)
 CHANNEL WIDTH (W) = 0.250, 0.375, 0.500, 0.750,
 1.000, 1.500 (INCHES)
 PLATE THICKNESS (T_P) = 0.015 → 0.023 (INCHES)
 INNER WALL THICKNESS (T_W) = 0.010 (INCHES)

GEOMETRY 3



LENGTH (L) = 0.5, 1.0, 1.5, 2.0 (FEET)
 DISTANCE ACROSS
 FLATS (F) = 0.25, 0.50, 1.00, 2.00, 3.00 (INCHES)
 HEXAGON HEIGHT (H) = 0.25, 0.50, 0.75 (INCHES)
 PLATE THICKNESS (T_P) = 0.005, 0.010, 0.020 (INCHES)
 INNER WALL THICKNESS (T_W) = 0.005, 0.010, 0.020 (INCHES)

GEOMETRY 4



LENGTH (L) = 0.5, 1.0, 1.5, 2.0 (FEET)
 EQUIV. DIA. (D_E) = 0.50, 0.75, 1.00 (INCHES)
 FIN THICKNESS (T_{FIN}) = 0.01, 0.02, 0.04 (INCHES)
 FIN LENGTH (L_{FIN}) = 0.000, 0.125, 0.250, 0.500 (INCHES)
 CHANNEL THICKNESS (T_C) = 0.015 (INCHES)

Figure 5-1. Concept Parameters Evaluated

5.1.1 VAPOR CHAMBER ANALYTICAL CONSIDERATIONS

5.1.1.1 Meteoroid Criteria

A major factor in the design of any active space heat rejection system is consideration of possible meteoroid damage. The vapor chamber fin approach to radiator design can limit the amount of meteoroid armor required due to the fact that the number of primary fluid ducts can be reduced. Puncture of individual vapor chambers is not serious due to the redundant characteristics of this design.

In a conduction fin radiator, operating at relatively high temperatures, tube spacings greater than a few inches cannot be tolerated due to the low fin efficiencies incurred. This condition increases the amount of tubes and required meteoroid armor as compared to the vapor chamber fin concept. Although the vapor chamber fin radiator is less susceptible to critical meteoroid damage than the conduction fin radiator, the effect of the meteoroid environment must still be considered in the design.

Several difficulties are apparent in the selection of a design criterion to minimize the probability of meteoroid penetration. The data obtained from satellite experiments by various impact sensors and of indirect measurements from zodiacal light and radar photographic observation of meteors show various discrepancies. Secondly, simulation of the available data by hypervelocity impact tests is impossible due to the inability of experimenters to duplicate observed meteoroid velocities. Meteoroid velocities are reported to average 17 to 20 km/sec while projectile velocities in the order of only 8 km/sec can be achieved in the laboratory. The third problem becomes one of interpreting and modeling the observed meteoroid flux and hypervelocity impact data into an analytical expression which can be used for a reliable radiator design. The sporadic nature of meteoroid events, the uncertainty involved in the hypervelocity impact testing and the variation of damage mode with respect to tube and tube liner materials and thicknesses combine to further complicate the situation.

The damage criteria generally used and widely accepted for calculating meteoroid armor protection requirements is that proposed by Loeffler, et al (Reference 2) where:

$$t_a = a \gamma \left(\frac{\rho_{mp}}{\rho_t} \right)^{1/2} \left(\frac{v_{mp}}{C_t} \right)^{2/3} \left(\frac{6}{\pi \rho_{mp}} \right)^{1/3} \left[\frac{\alpha A_v \tau}{-\log_e P_{ND}} \right]^{1/3\beta} \left(\frac{1}{\beta+1} \right)^{1/3\beta} \quad (5-1)$$

where

- t_a = required armor thickness
- a = damage thickness factor
- γ = materials cratering coefficient
- ρ_{mp} = meteoroid density (0.5 gm/cm³)
- ρ_t = armor material density
- v_{mp} = meteoroid velocity (25 km/sec)
- C_t = sonic velocity in armor
- A_v = vulnerable area
- τ = mission time
- $\alpha = 10^{-14.41} \frac{\text{gm}^{1.22}}{\text{m}^2 \text{-sec}}$
- $\beta = 1.22$
- P_{ND} = design probability of no critical damage

The constants a and γ vary from material to material and with damage mode. The values utilized for the rear surface dimpling damage factor, a , and the cratering coefficient, γ , were 2.40 and 1.67, respectively, as cited for stainless steel in Reference 5. A more recent study, Reference 6, determined the cratering coefficient for several materials as a function of temperature. For 316 stainless steel, the cratering coefficient was estimated to be:

$$\gamma = \gamma_R \left(\frac{T}{T_R} \right)^{1/6} \quad (5-2)$$

where:

γ_R = room temperature cratering coefficient, 2.19

T_R = room temperature (absolute)

T = target temperature (absolute)

At 1100° F, this relation yields a value of 2.62 for the cratering coefficient. The discrepancy between the two values of γ is substantial and efforts to show the effects of this difference on radiator weight are presented in Section 7.2.

The value of P_{ND} utilized in Equation 5-1 refers to the probability of no critical damage, however, in the vapor chamber radiator, critical damage to a percentage of the vapor chambers is acceptable. Therefore, it is necessary to calculate the probability of no critical damage to the vapor chamber based on an overall probability of mission survival. Obviously, since a percentage of vapor chambers will be allowed to fail, the value of P_{ND} will be a small number.

The fundamental expression which describes the frequency of random events is the binomial distribution:

$$P_n = \frac{N_T!}{n! (N_T - n)!} p^n (1 - p)^{(N_T - n)} \quad (5-3)$$

where:

p = probability of a single event occurring

N_T = total number of independent trials

n = number of events occurring

P_n = probability that the event will occur n times.

If this expression is applied to the vapor chamber fin radiator, the following analogies are apparent:

$P \sim$ the probability of a single chamber surviving

$N_T \sim$ the total number of chambers

$n \sim$ the number of chambers which will survive

$P_n \sim$ the probability of n chambers surviving

By summing the expression between $n = N_S$ and $n = N_T$, the overall probability, P_o of N_S , or more chambers surviving can be obtained:

$$P_o = \sum_{n=N_S}^{N_T} \frac{N_T!}{n! (N_T - n)!} p^n (1 - p)^{(N_T - n)} \quad (5-4)$$

By putting the desired probability of mission success, P_o , total number of chambers, N_T and the number of chambers surviving, N_S , it is possible to solve for the individual survival probability, p . The value of P_{ND} input into Equation 5.1 is the overall probability of no critical damage. This is obtained by raising the individual survival probability to the N_T power. Therefore,

$$P_{ND} = p^{N_T} \quad (5-5)$$

The vulnerable area of the vapor chambers was assumed to be the entire vapor chamber surface area. The area and survival probability term in Equation 5-1 reduces to the following:

$$\left[\frac{A_v}{-\log_e P_{ND}} \right]^{1/3\beta} = \left[\frac{(N_T) (A_c)}{N_T [-\log_e (p)]} \right]^{1/3\beta} = \left[\frac{A_c}{-\log_e (p)} \right]^{1/3\beta} \quad (5-6)$$

where

$A_c =$ vulnerable area of a single chamber

An investigation was performed with the RSURV computer program to determine the relationship between p , the individual survival probability, and P_o , the overall survival probability, for varying survival percentages. Typical results of these studies are illustrated in Figures 5-2 and 5-3 for various values of N_S/N_T . These curves illustrate two important facts:

1. When large numbers of chambers are present, small changes in the individual survival probability create large changes in the overall survival probability.
2. The value of the individual survival probability required to obtain a large overall survival probability is one or two percent higher than the fraction of chambers which survive.

Previous work has indicated that the optimum fraction of chambers which are allowed to survive is dependent upon the temperature and design of the radiator; values between 0.8 and 0.9 have been found to be the most advantageous. Due to the low thermal conductivity of stainless steel and the relatively high operating temperatures, a value of 0.9 was selected for this study.

5.1.1.2 Vapor Chamber Relationships

The heat pipe (or vapor chamber) is a closed system containing a two-phase fluid and porous material which makes use of the physical phenomena of evaporation, condensation and capillary action. With proper design, it is able to transport large quantities of heat energy over relatively long distances, through small cross sections, with only a modest temperature drop. Figure 5-4 shows a heat pipe as a closed container, lined with a wick saturated with liquid; the remaining volume is filled with vapor of the same fluid. Heat input at the evaporator causes liquid to vaporize resulting in a local pressure increase. The induced pressure gradient causes the vapor to flow towards the condenser section where energy is being transferred to the environment. The vapor condenses and fills the wick; condensate is returned to the evaporator by capillary action. The internal fluid loop resulting from these processes will continue to function as long as the sum of the pressure drops incurred in the vapor flow and liquid return is less than the capillary pump pressure

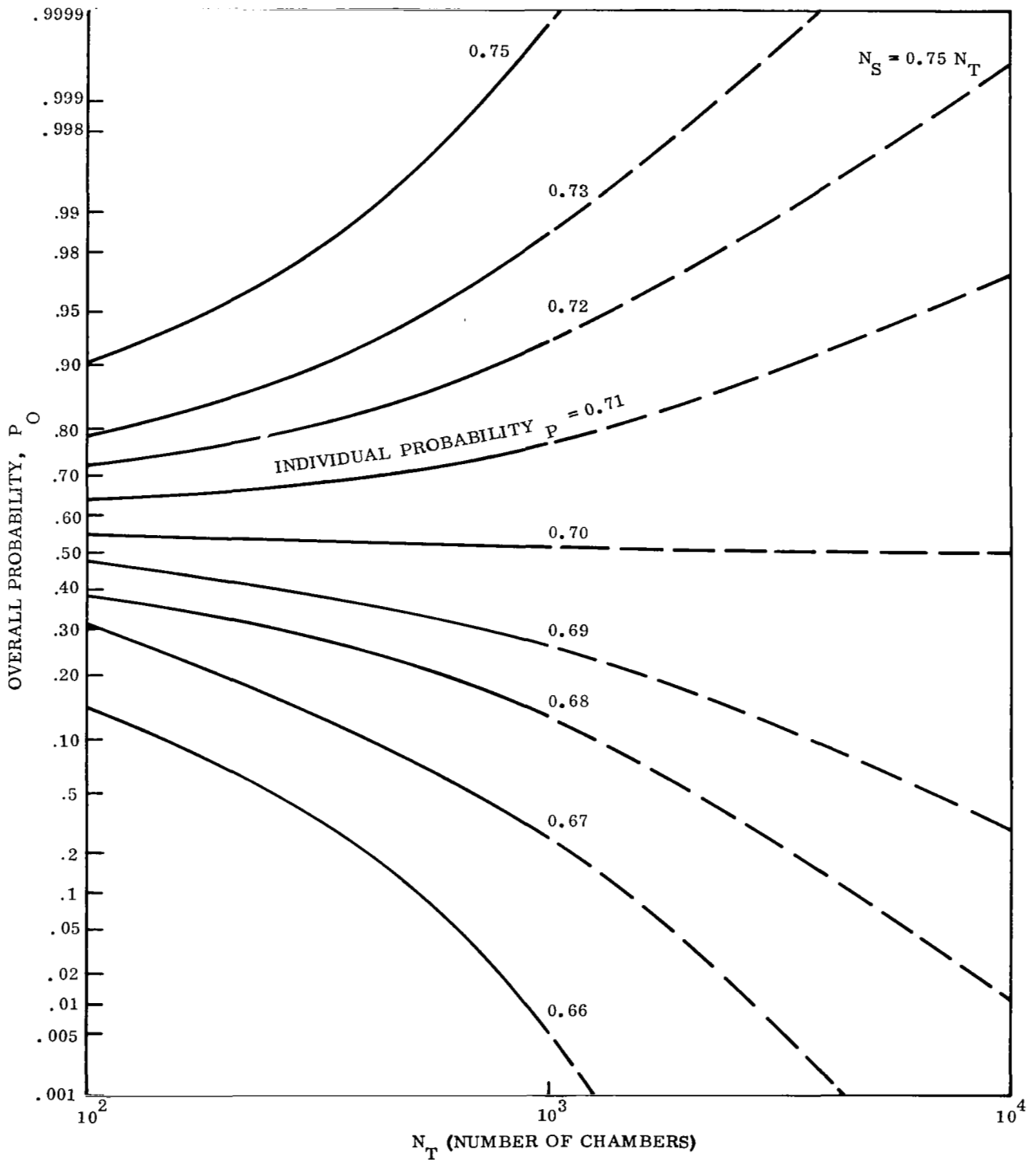


Figure 5-2. Relationship Between the Overall and Individual Survival Probabilities (as determined by the binomial distribution for 75 percent chamber survivability)

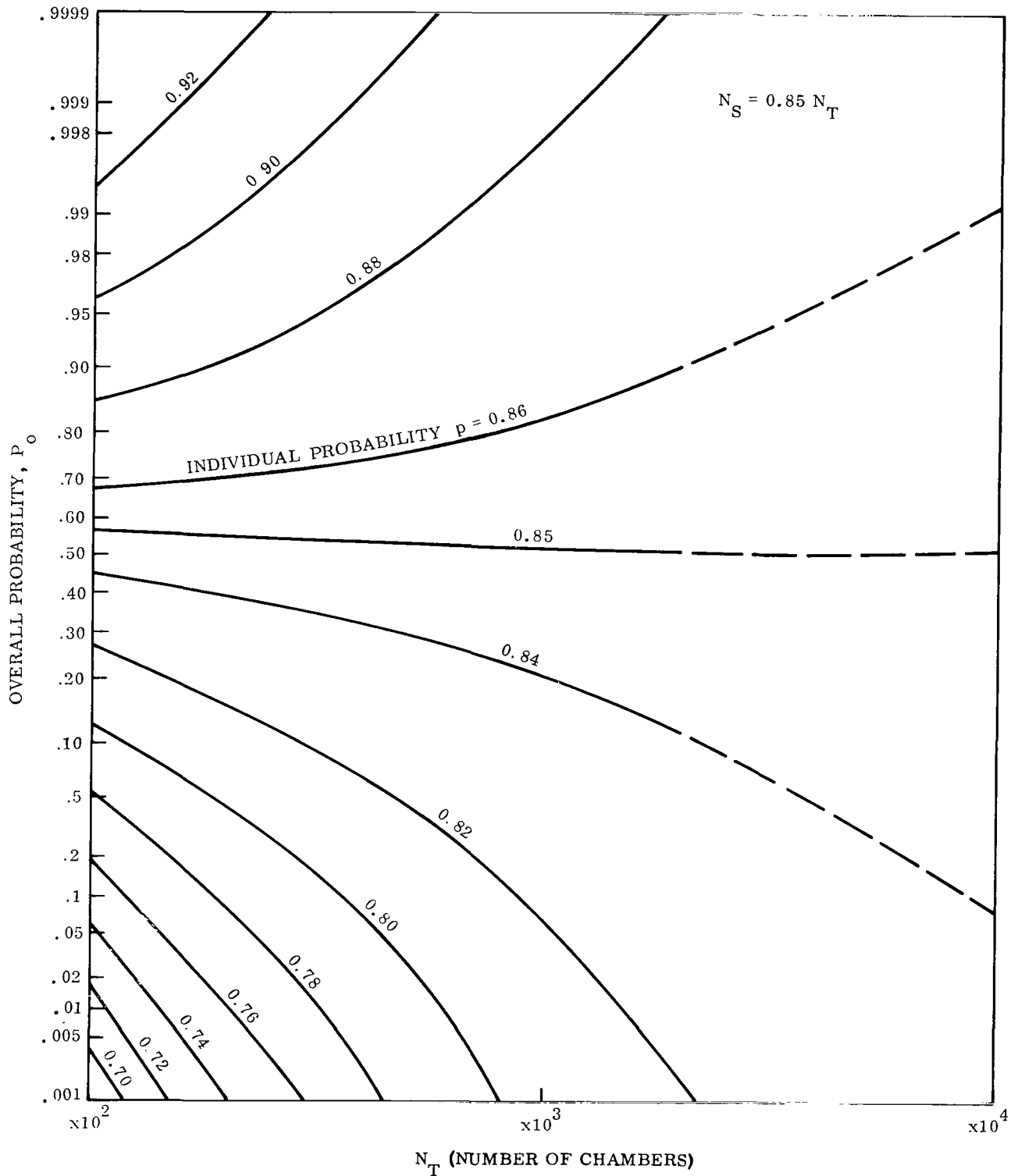


Figure 5-3. Relationship Between the Overall and Individual Survival Probability (as determined by the binomial distribution for 85 percent chamber survivability)

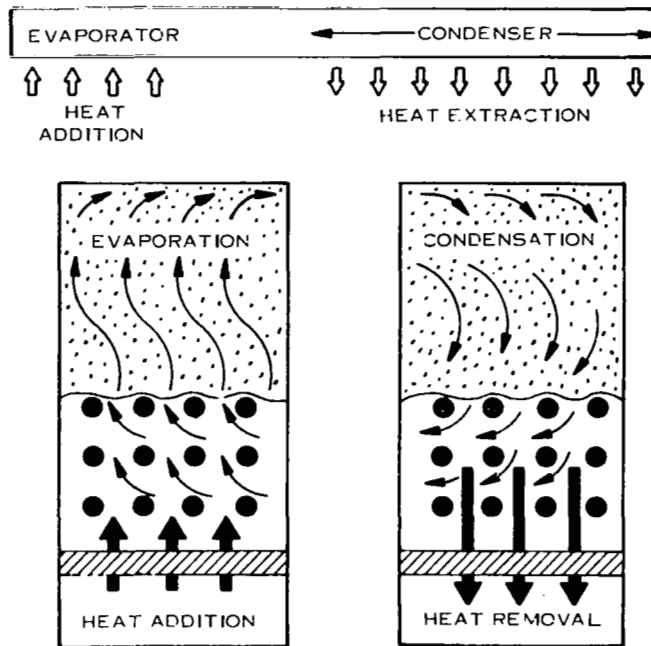


Figure 5-4. Basic Heat Pipe

rise at the evaporator. The high effectiveness of the heat pipe is due primarily to the fact that the energy transfer is accomplished in the form of the latent heat of vaporization.

5.1.1.2.1 Vapor Chamber Design

The four basic areas of design of a heat pipe are the vapor flow passage, the capillary structure and the evaporator and condenser areas. All of these depend to some extent upon the properties of the working fluid being considered. The selection of the working fluid is extremely important if the heat pipe is to be utilized to its fullest extent. The main physical properties of interest in a heat pipe fluid are as follows:

1. Vapor pressure - the vapor pressure should be low enough so as to be easily contained at the operating temperature
2. Vapor density - a high vapor density is desirable in order to reduce the required vapor passage flow area.

3. Latent heat of vaporization - a high latent heat of vaporization reduces the mass flow requirement.
4. Surface tension - the capillary pump pressure rise is directly proportional to the surface tension. A high surface tension allows for longer heat pipes.
5. Vapor viscosity - a low vapor viscosity minimizes the vapor pressure drop.
6. Liquid viscosity - a low value enables a finer capillary structure to be used as well as a longer heat pipe.
7. Thermal conductivity - a high thermal conductivity minimizes the evaporative and condensing temperature drops.
8. Liquid density - the density of the liquid phase should be high to reduce the flow rate of the liquid through the capillary structure.

5.1.1.2.2 Vapor Chamber Performance Limitations

In general, heat pipes are subject to four heat transfer limitations which will impair their operation. These constraints, pictured in Figure 5-5 are: sonic velocity, entrainment, boiling and wicking.

The sonic velocity limitation occurs when the vapor velocity at the evaporator exit attains sonic velocity, thereby limiting the pressure and temperature in the condenser with an end result of reduced heat rejection capability.

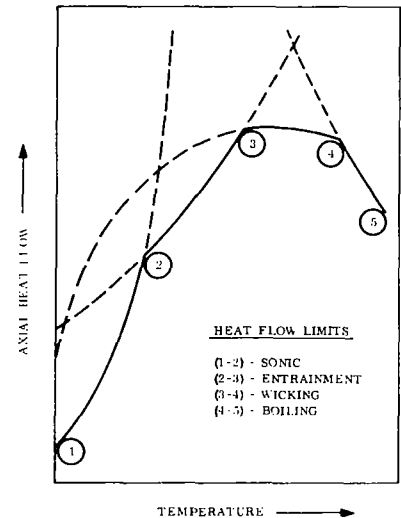


Figure 5-5. Heat Pipe Limitations

When the vapor velocity and density are sufficiently high, entrainment of the liquid return in the vapor is possible. This process can result in a depletion of fluid at the evaporator. The conditions which determine the severity of the entrainment are dependent upon the condenser wick pore size, vapor density and velocity and the fluid surface tension. The ratio of the vapor inertial forces to liquid surface tension forces can be expressed in terms of the Weber number:

$$W = \frac{\rho_v V^2 d}{2 \pi \sigma g_c} \quad (5-7)$$

where

ρ_v = vapor density

V = vapor velocity

d = a characteristic length dependent upon the wick pore size

σ = surface tension

g_c = force-mass conversion constant

When this ratio exceeds 1.0, entrainment is probable.

Boiling in the heat input section of a heat pipe is undesirable since it interferes with the capillary action occurring in the wick. Therefore, in a zero g environment, liquid from the condenser could be prevented from entering the heat input section by the presence of vapor bubbles in the wick. The onset of boiling is difficult to predict because of the sensitivity of this phenomena with the surface finish of the container and wick. Experimental work has shown that the alkali metals require heat fluxes in excess of 10^5 BTU/hr-ft² to nucleate. Analytical studies, discussed in Section 7 indicate that evaporator heat fluxes above 10^5 are not advantageous in a vapor chamber fin radiator, regardless of nucleate boiling considerations.

The three limitations discussed above can be regarded as constraints which must be considered during the design of a heat pipe. The wicking limitation, which relates directly to the pressure drop balance in the heat pipe, is generally used as a design criteria in order to minimize the heat pipe weight. The capillary pressure rise is determined by the choice of wick and fluid. It is then necessary to minimize the vapor passage flow area, the condenser wick weight and fluid inventory without imposing an excessive pressure drop.

From a quantitative standpoint, the following expression must be satisfied:

$$\Delta P_c \geq \Delta P_w + \Delta P_v \quad (5-8)$$

where:

ΔP_c = capillary pressure rise

ΔP_w = wick frictional pressure drop

ΔP_v = vapor pressure drop

The capillary pressure rise can be evaluated by the following relationship:

$$\Delta P_c = \frac{2 \sigma}{r_p \cos \theta} \quad (5-9)$$

where:

σ = surface tension of the fluid

r_p = equivalent pore radius

$\cos \theta$ = angle of contact between fluid and pore surface

The pressure drop through the wick can be estimated by means of the treatment outlined below. The pressure gradient within the wick can be written as:

$$\text{grad } P_w = K \mu \langle \vec{v} \rangle \quad (5-10)$$

where:

P_w = pressure within the wick

K = wick friction factor

μ = liquid viscosity

$\langle \vec{v} \rangle$ = local average liquid velocity

Integration of Equation 5-10 to obtain the fluid pressure drop within the wick is dependent upon the geometry of the wicked section. The problem can be approximated to be uniform one dimensional flow through the wick.

Integration of Equation 5-10 gives

$$\Delta P_w = K \mu \langle v \rangle t_w \quad (5-11)$$

where t_w is the wick thickness along the direction of flow.

The average flow velocity can be related to the total heat transfer rate between the potassium working fluid and the radiator fluid in the following manner. The energy transferred can be expressed in terms of its latent heat of vaporization.

$$Q = \dot{m} \lambda \quad (5-12)$$

where:

Q = heat transfer rate

\dot{m} = mass transfer rate

λ = fluid latent heat of vaporization

The mass flow rate can be expressed as

$$\dot{m} = \rho \langle \vec{v} \rangle A \quad (5-13)$$

where:

ρ = fluid density

A = flow cross sectional area

Finally, the pressure drop within the wick can now be written as:

$$\Delta P_w = \frac{K \mu t w Q}{\rho A \lambda} \quad (5-13a)$$

The pressure change in the condenser section may be either a drop or rise, depending upon the relative magnitude of the frictional losses as compared to the dynamic energy contributed by the decelerating condensing vapor. The expression used to calculate the vapor pressure drop is:

$$\Delta P_v = \frac{4 \mu_v Q \ell_c}{\pi \rho_v \lambda r_v^4} \quad \text{if } R_c < 1.0 \quad (5-14)$$

or

$$\Delta P_v = \frac{Q^2}{2 \pi^2 \lambda^2 \rho_v r_v^4 g} \quad \text{if } R_c > 1.0 \quad (5-14a)$$

where:

ℓ_c = condenser length

Q = condenser heat load (defined as a negative quantity)

r_v = vapor space radius

R_c = radiator Reynolds number

ρ_v = vapor density

μ_v = vapor viscosity

and

$$R_c = \frac{Q}{2 \pi \mu_v \lambda \ell_c} \quad (5-15)$$

5.1.1.3 Structural Considerations

The heat rejection system for the advanced Rankine cycle may be designed as an active load-bearing member attached to some type of supporting substructure. Previous studies (References 7 and 8) have shown that a more effective arrangement of the heat rejection system and launch vehicle structure can be achieved by utilizing the radiator system as a load-bearing aerodynamic fairing. The principal reason for the effectiveness of this approach is the fact that a substantial amount of structure must be incorporated into the design of the radiator, in any event, to provide the necessary meteoroid protection and heat conductive paths to its surfaces. Therefore, a basic ground rule of this study was the requirement of the radiator to support a 15,000 pound load during launch.

5.1.2 CONCEPT PARAMETRIC ANALYSIS

The fundamental fluid flow and thermodynamic expressions described above are contained within the HPIPE computer program. This code was utilized in the analysis of Geometries 1, 2 and 4 to obtain weight and pressure drop data. Due to the basic differences between Geometry 3 and the remaining concepts, a separate analysis, discussed in Section 5.1.2.4 was performed for this design.

The criteria used in determining the design values was weight; area was not a consideration at this particular time. Attention was centered on the condensing portion of the vapor chambers since a primary duct interface configuration had not been selected. However, an assumption that the evaporator section was one-fourth the length of the condenser section was made at this time to obtain effects associated with the evaporative ΔT and wick thickness.

The utilization of the HPIPE computer program proceeded in the following manner:

1. The values of the geometric parameters were input into HPIPE in accordance with the ranges shown in Figure 5-1. Since HPIPE was originally designed for circular geometry, appropriate changes were made in the input values for hydraulic pipe radius and wall thickness so that proper pressure drops and weights could be calculated.

2. Wall thickness of the vapor chambers were determined by the meteoroid protection requirements. The relationship between vapor chamber length, diameter and required armor thickness is shown in Figure 5-6. This analysis was performed under the ground rule that 90 percent of the vapor chambers survived.
3. The wicking material was assumed to be a 100 x 100 mesh sintered screen which has a friction factor, K, of $6.1 \times 10^8 \text{ ft}^{-2}$ and a porosity of 63 percent as reported in Reference 9. A list of other candidate screen sizes is provided in Table 5-1.

Table 5-1. SS Sintered Screen Characteristics
(From Reference 9)

Mesh Size (wires/inch)	Wire Diameter (inches)	Porosity (percent)	Wick Friction Factor $K_1 \times 10^{-8}, 1/\text{ft}^2$
30	0.0090	62.5	1.4
100	0.0045	67.9	6.1
150	0.0030	67.8	-
200	0.0022	67.6	12.0

In order to limit the number of cases to be studied, all investigations took place at a condenser surface temperature of 1100°F which corresponds closely to the average temperature of the radiator under consideration. Heat loads for each pipe were calculated on the basis of the chamber surface temperature and the fin efficiencies provided in Figure 5-7. These fin efficiencies were obtained from Figure 5-8, Reference 10, where fin efficiency is plotted against a generalized length parameter, L. The expression for L is:

$$L = \ell_f \left[\frac{\sigma (\epsilon_1 F_1 + \epsilon_2 F_2) T^3}{kt_f} \right]^{0.5} \quad (5-16)$$

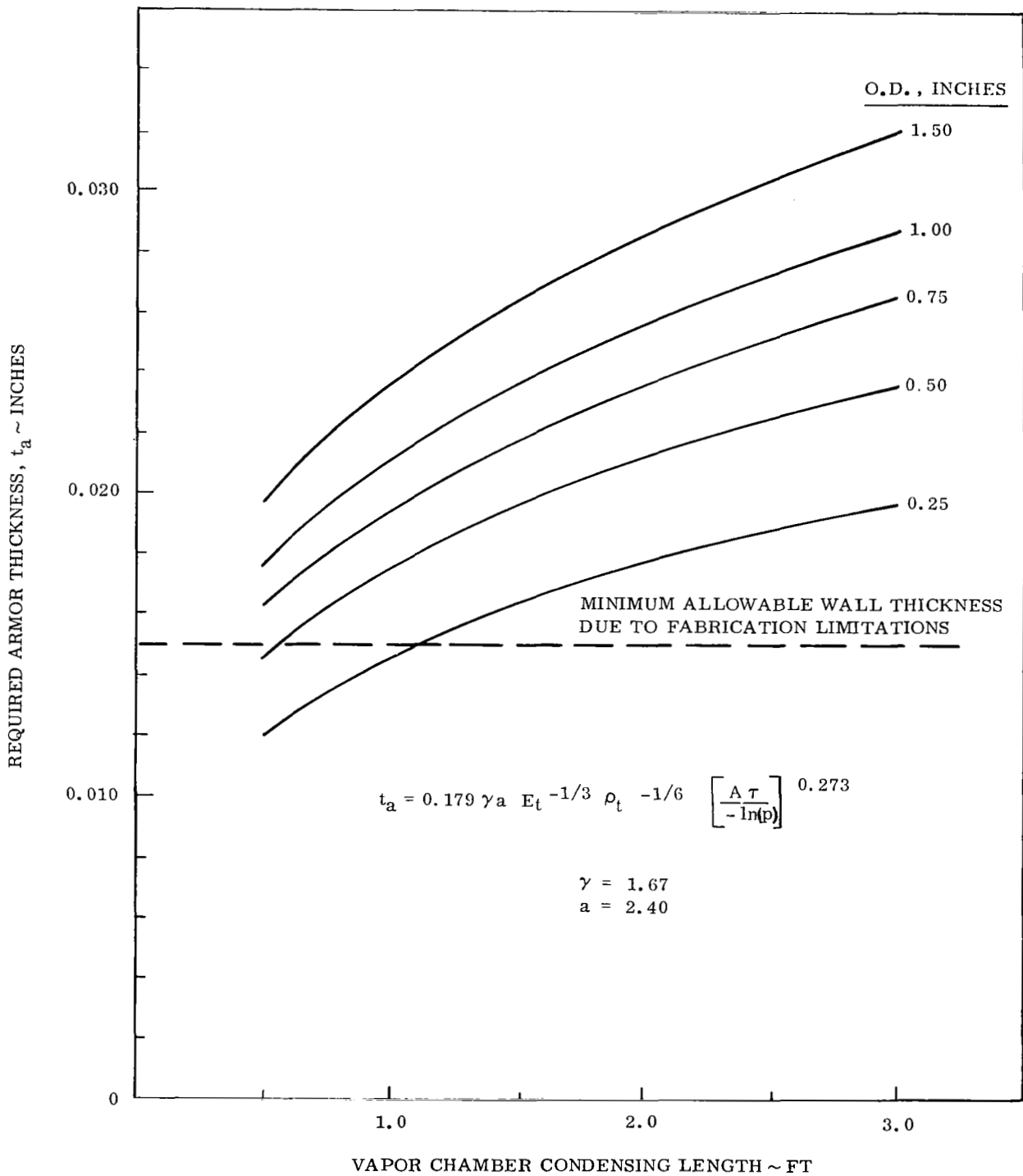


Figure 5-6. Required Armor Thickness Versus Vapor Chamber Condensing Length at Various Chamber Diameters

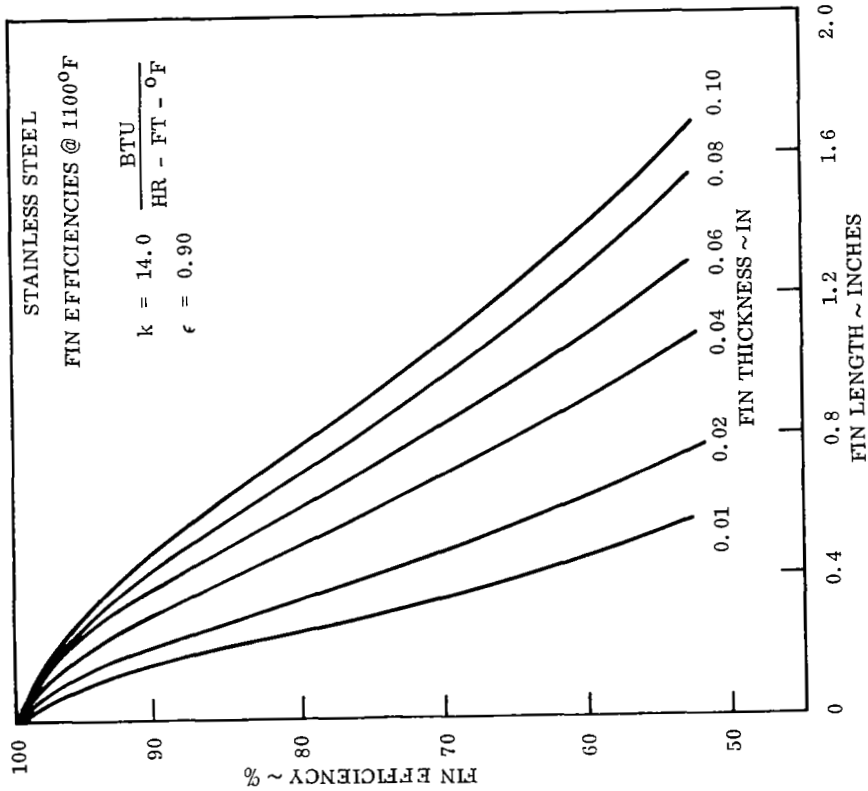


Figure 5-7. Fin Efficiency Versus Fin Length for Various Thickness Stainless Steel

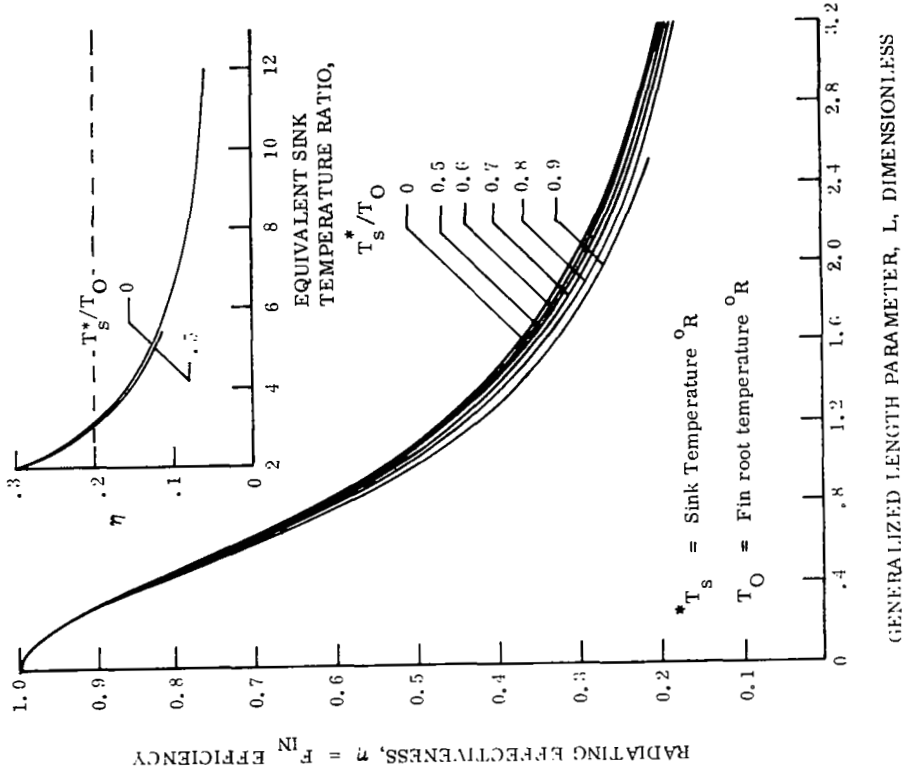


Figure 5-8. Variation of Radiating Effectiveness with Fin Plate Length (Reference 10)

where:

l_f = fin length

σ = Stephan - Boltzmann constant

ϵ_1 = emissivity of fin, side 1

ϵ_2 = emissivity of fin, side 2

F_1 = view factor of fin to sink, side 1

F_2 = view factor of fin to sink, side 2 (zero in this case)

T = fin root temperature

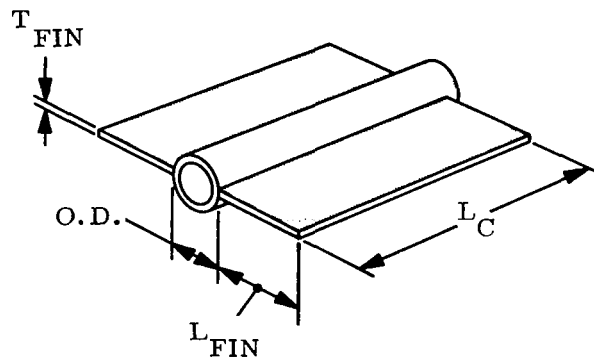
k = fin conductivity

t_f = fin thickness

With these inputs, the HPIPE program performed an incremental pressure drop calculation to see if Equation 5-8 was satisfied. Using an iterative technique, the wick thickness was changed until a pressure balance was obtained. Weight calculations, in terms of the chamber weight per kilowatt of heat rejected, were performed for each case (Geometries 1, 2 and 4), using potassium as the working fluid.

5.1.2.1 Geometry 1 Analysis

The parameters evaluated are shown below;



Figures 5-9, 5-10 and 5-11 are results of weight calculations performed for Geometry 1. The following statement can be made regarding Geometry 1.

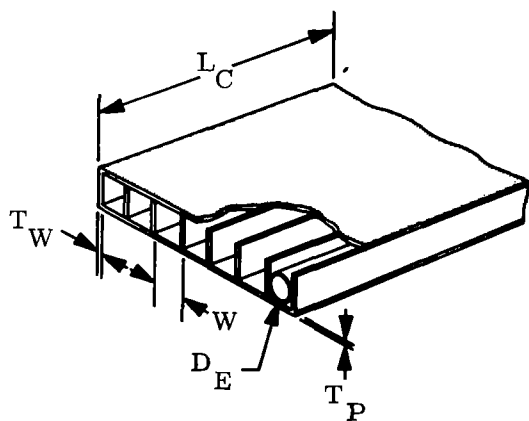
1. A fin thickness of 0.010 inches gave the lightest weight
2. In almost all cases, the presence of fins was advantageous
3. Increasing the condenser length increased the specific weight of the vapor chamber fins since the wick thickness must be increased.
4. It was always advantageous to maintain the flow diameter at the minimum allowable.

At the longer condensing lengths real cases could only be obtained for the larger diameter chambers. This is directly related to an inability of the pressure balance to be satisfied within the diameter provided. The longer chamber length, having a higher heat rejection capability, requires a larger vapor flow path and liquid return passage.

Selected cases for Geometry 1 were also run with sodium and cesium (see Figures 5-12 and 5-13). The vapor chambers utilizing sodium showed a substantial specific weight advantage over potassium while cesium was shown to be a very poor fluid for this application. The lower specific weight of the sodium chambers can be attributed to its high latent heat of vaporization and surface tension. Cesium has a much lower latent heat of vaporization and surface tension than either potassium or sodium.

5.1.2.2 Geometry 2 Analysis

The parameters evaluated for Geometry 2 are shown below.



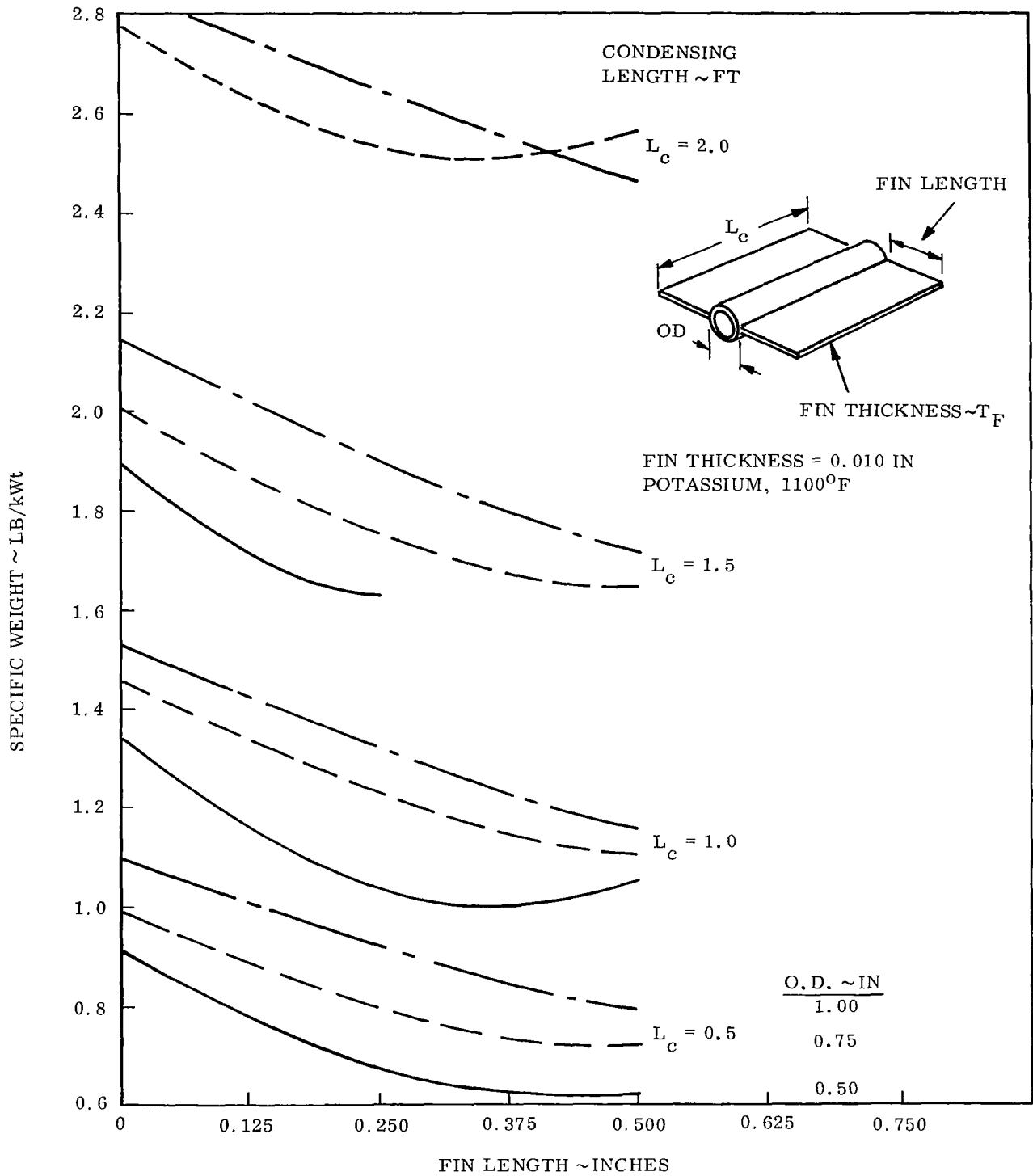


Figure 5-9. Geometry 1 Specific Weight Versus Fin Length ($T_F = 0.010$ in.)

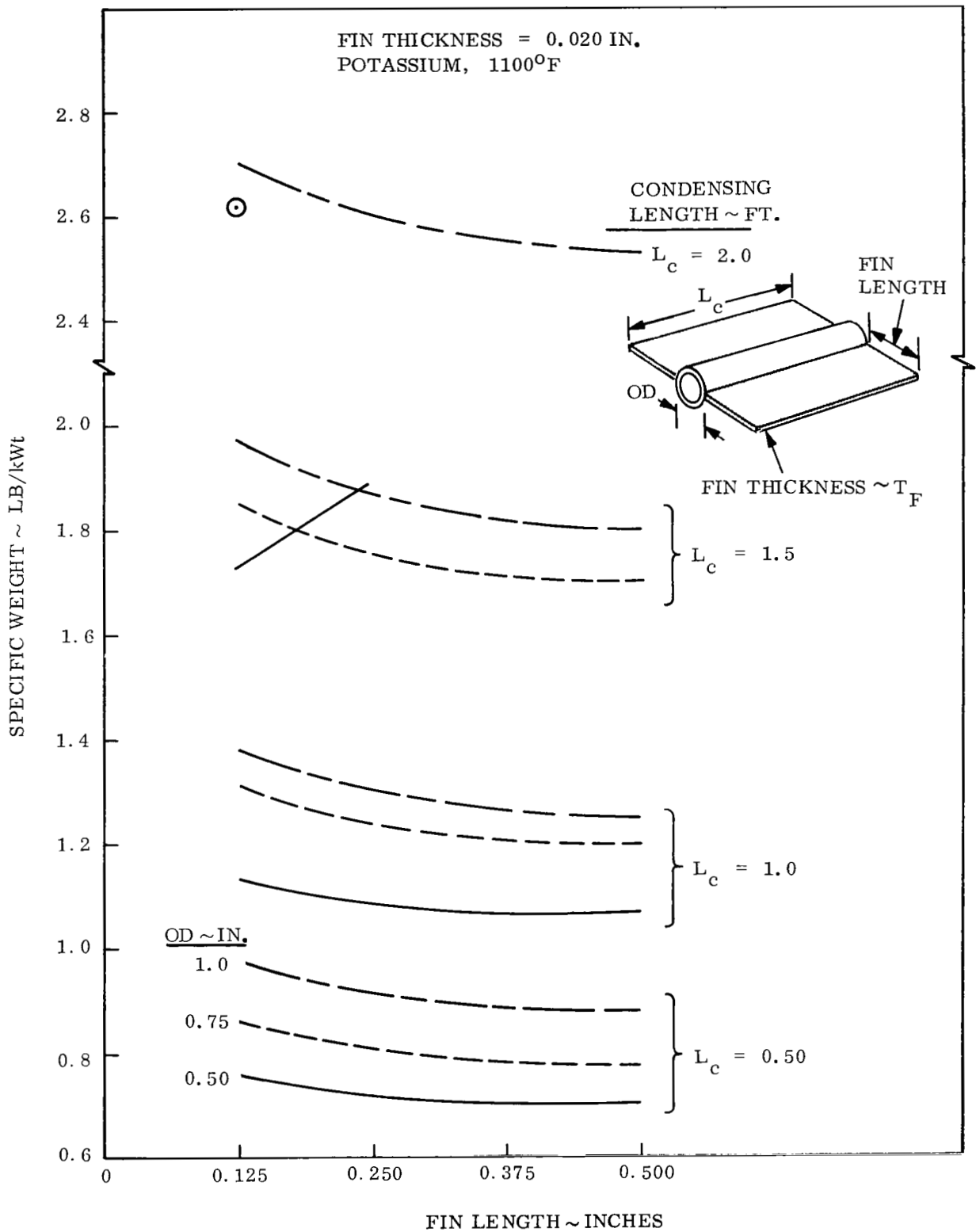


Figure 5-10. Geometry 1 Specific Weight Versus Fin Length ($T_F = 0.020$ in.)

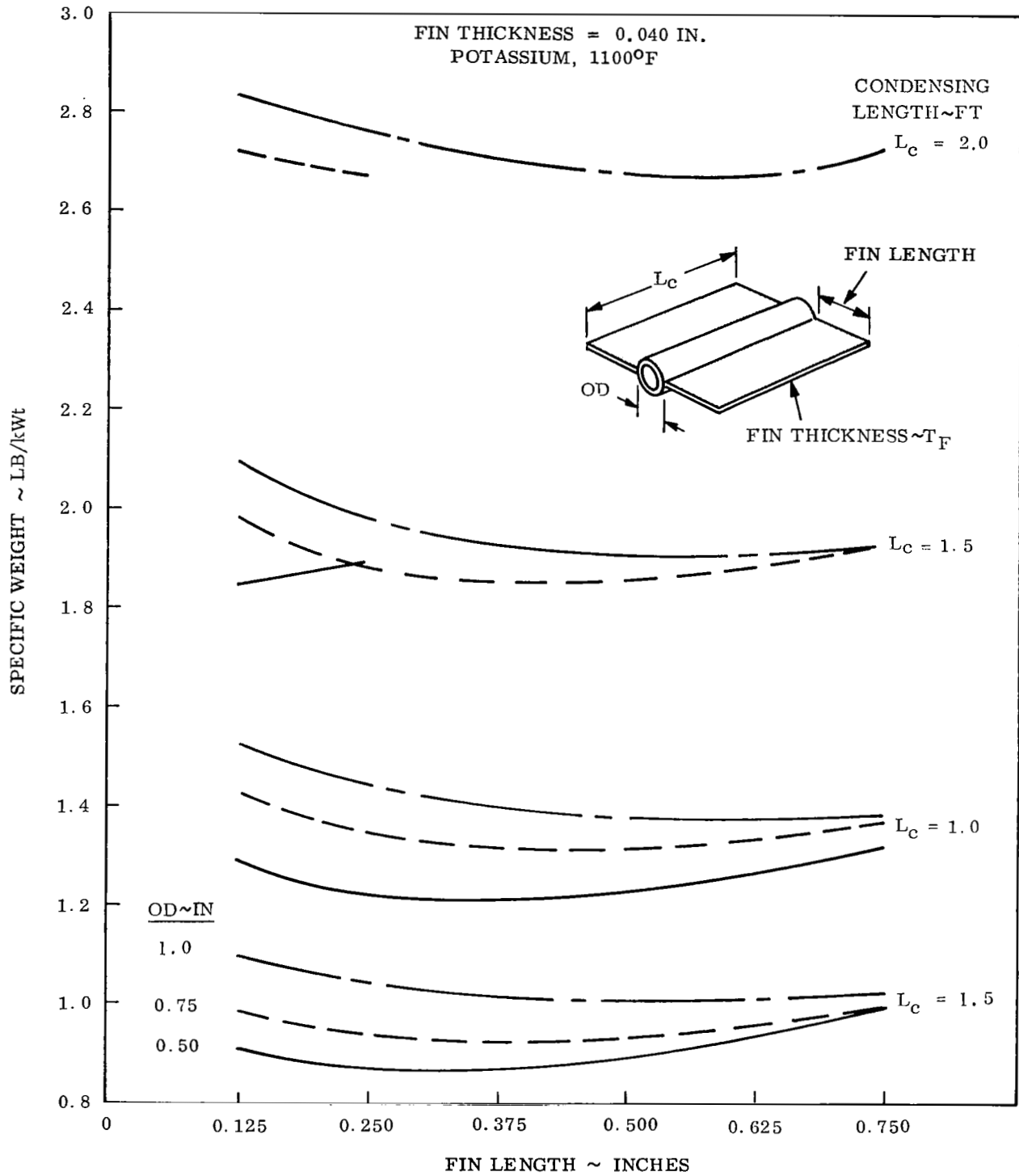


Figure 5-11. Geometry 1 Specific Weight Versus Fin Length ($T_F = 0.040$ in.)

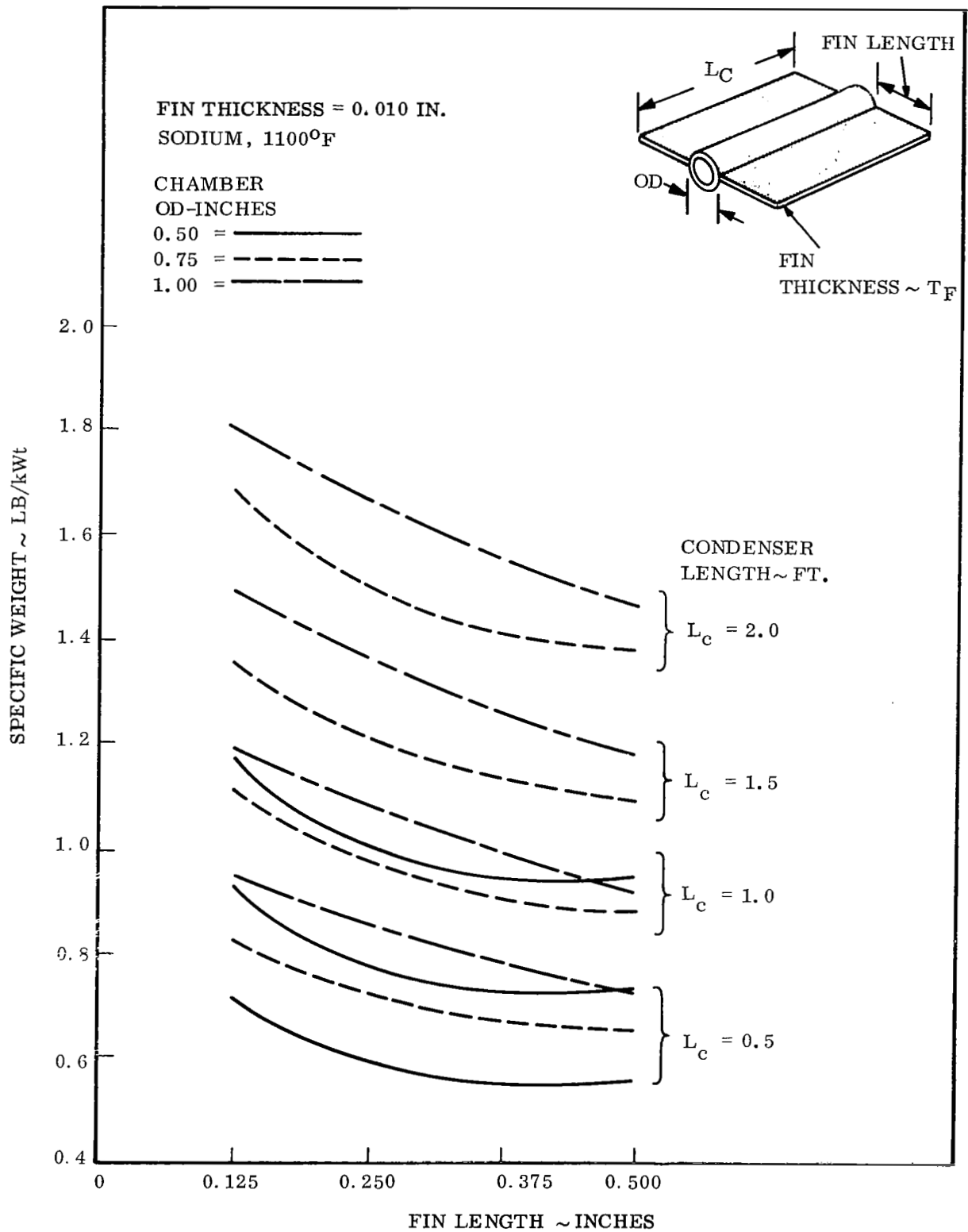


Figure 5-12. Geometry 1 Specific Weight Versus Fin Length (Sodium)

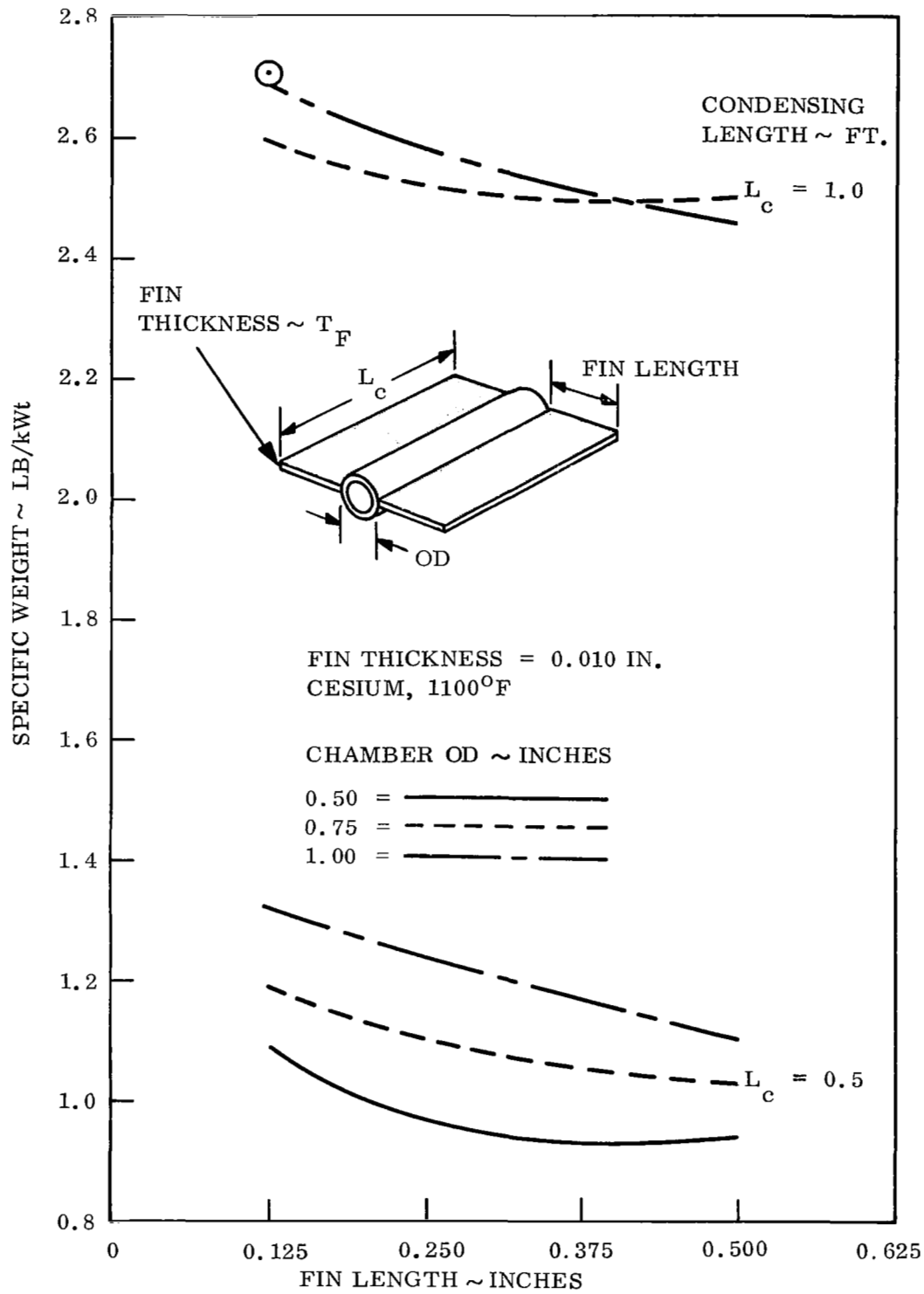


Figure 5-13. Geometry 1 Specific Weight Versus Fin Length (Cesium)

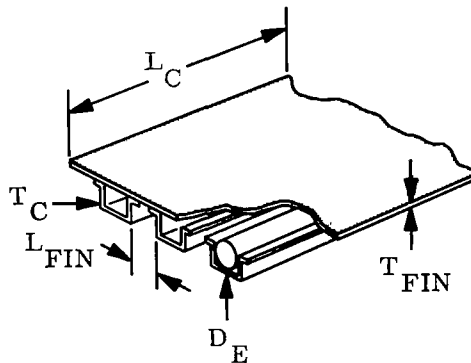
The results are shown in Figures 5-14 for potassium; the following characteristics can be observed:

1. In general, wide but short channels are advantageous (the relationship between channel height, width and hydraulic diameter are shown in Figure 5-15).
2. As in Geometry 1, the smaller the hydraulic diameter for a particular condensing length, the lighter the vapor chamber (unless the pressure balance could not be satisfied).
3. The required increase in wick thickness raises the specific weight as the chambers become longer.

Geometry 2 was also run using sodium as the working fluid. These results, which are lower in specific weight than the potassium cases, are presented in Figure 5-16.

5.1.2.3 Geometry 4 Analysis

The parameters evaluated for Geometry 4 are shown below.



The results of Geometry 4 (Figures 5-17 through 5-19) were similar to those of Geometry 1; small diameters, 0.50 inch conducting fins and short condensing lengths were found to be desirable. Although the specific weights of Geometry 4 are higher than either Geometry 1 or 2, it was expected that Geometry 4 would have certain fabrication and structural advantages. No sodium evaluation runs were performed for Geometry 4.

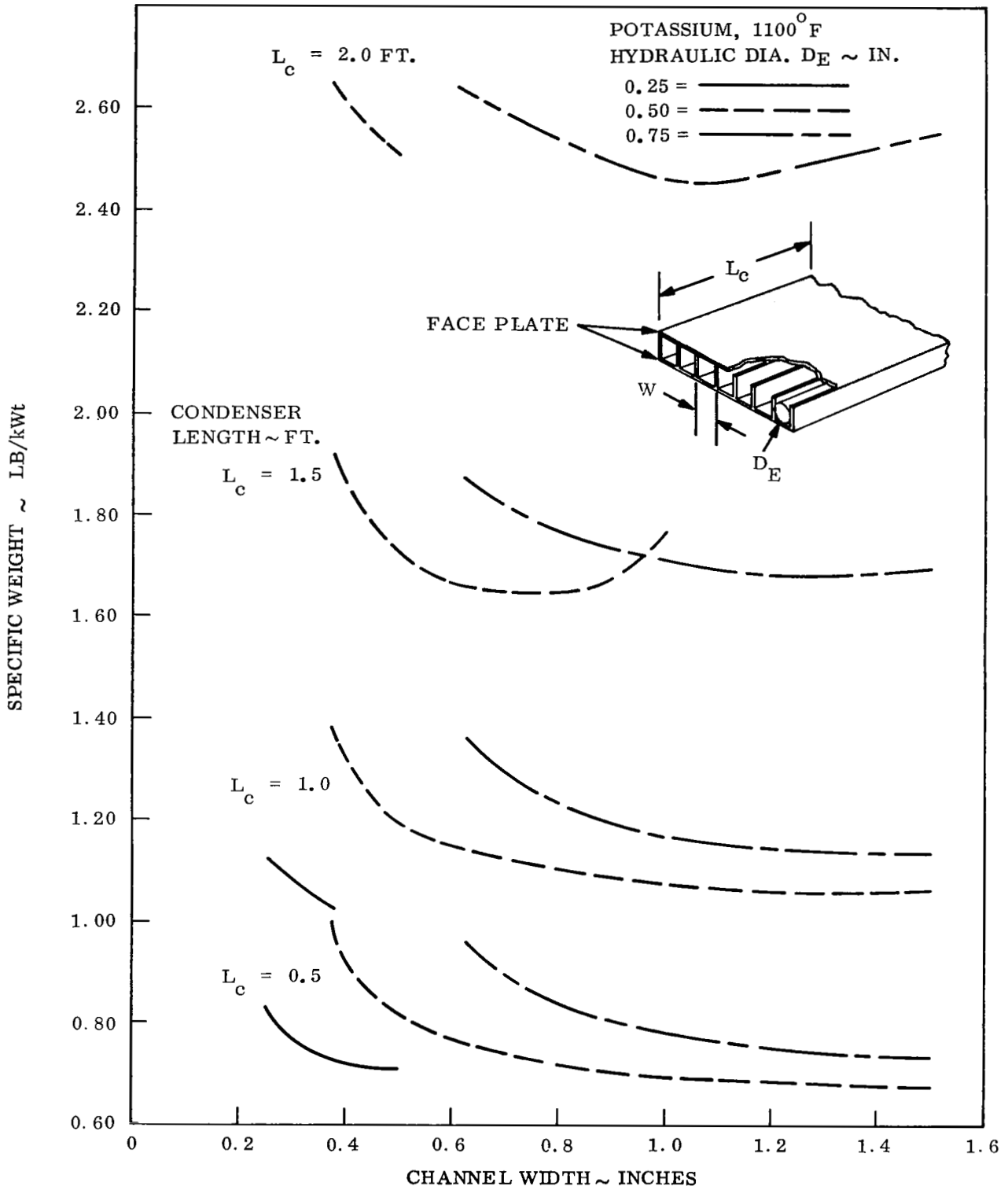


Figure 5-14. Geometry 2 Specific Weight Versus Channel Width (Potassium)

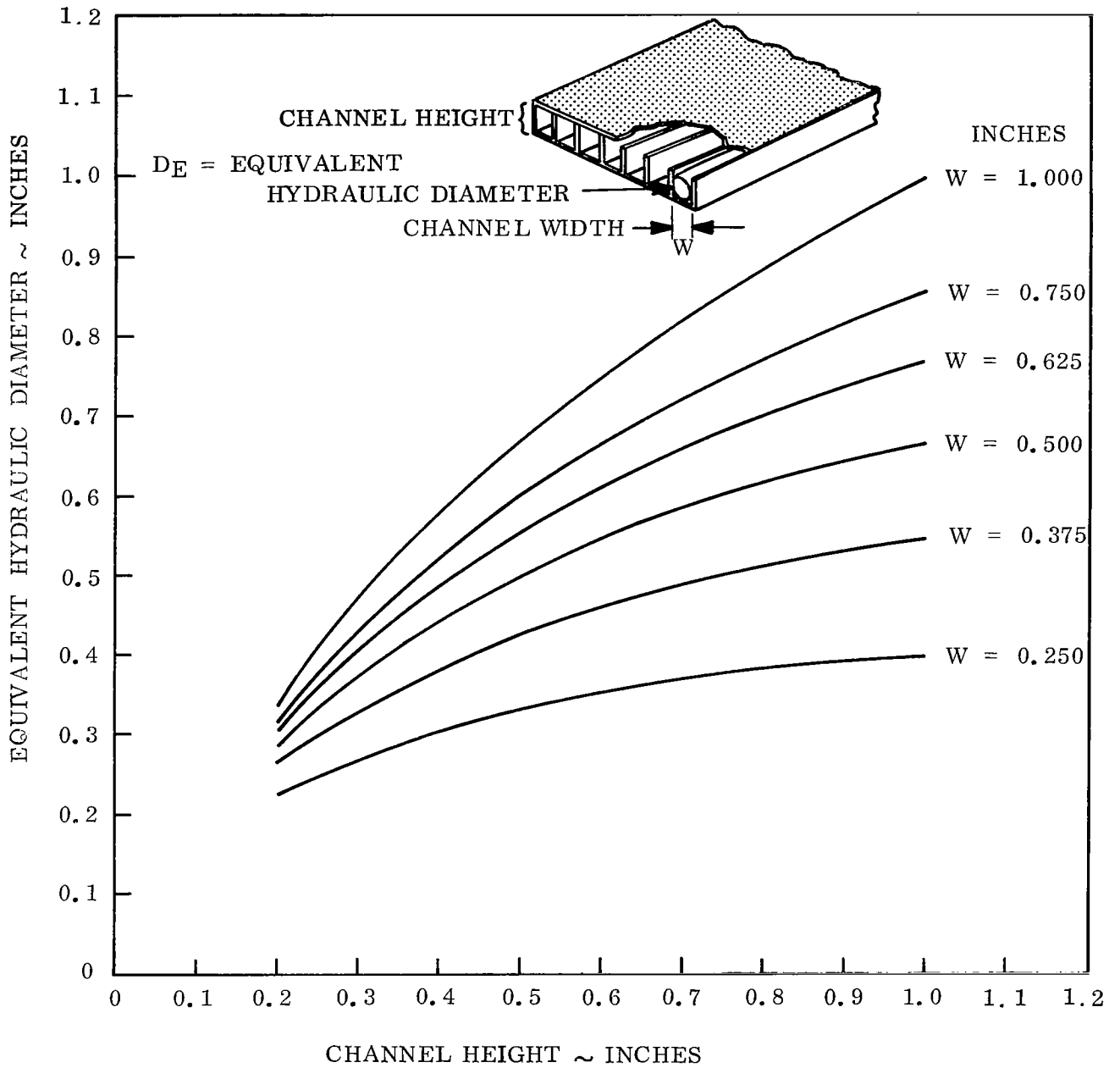


Figure 5-15. Geometrical Relationships Used for Geometry 2

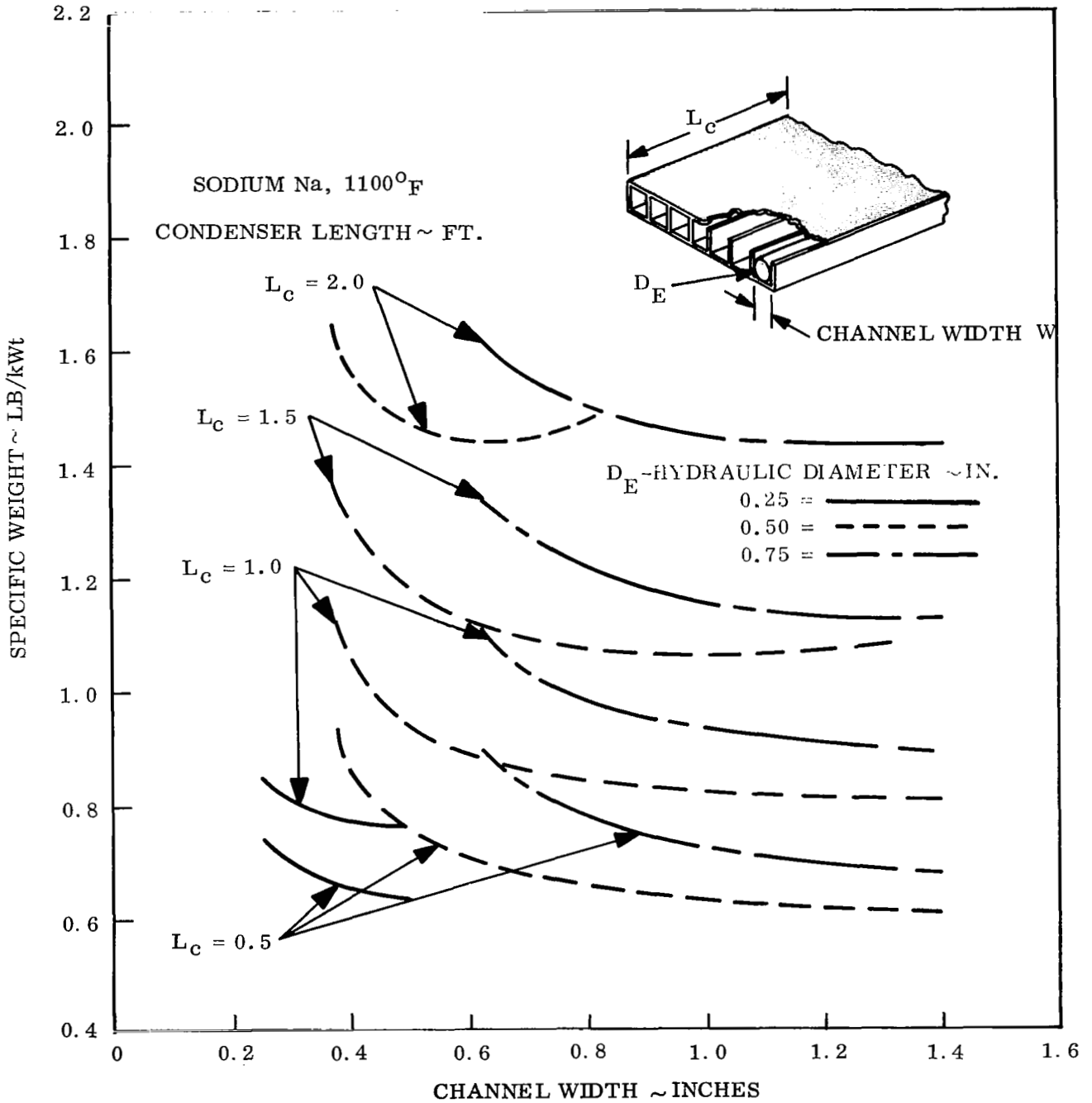


Figure 5-16. Geometry 2 Specific Weight Versus Channel Width (Sodium)

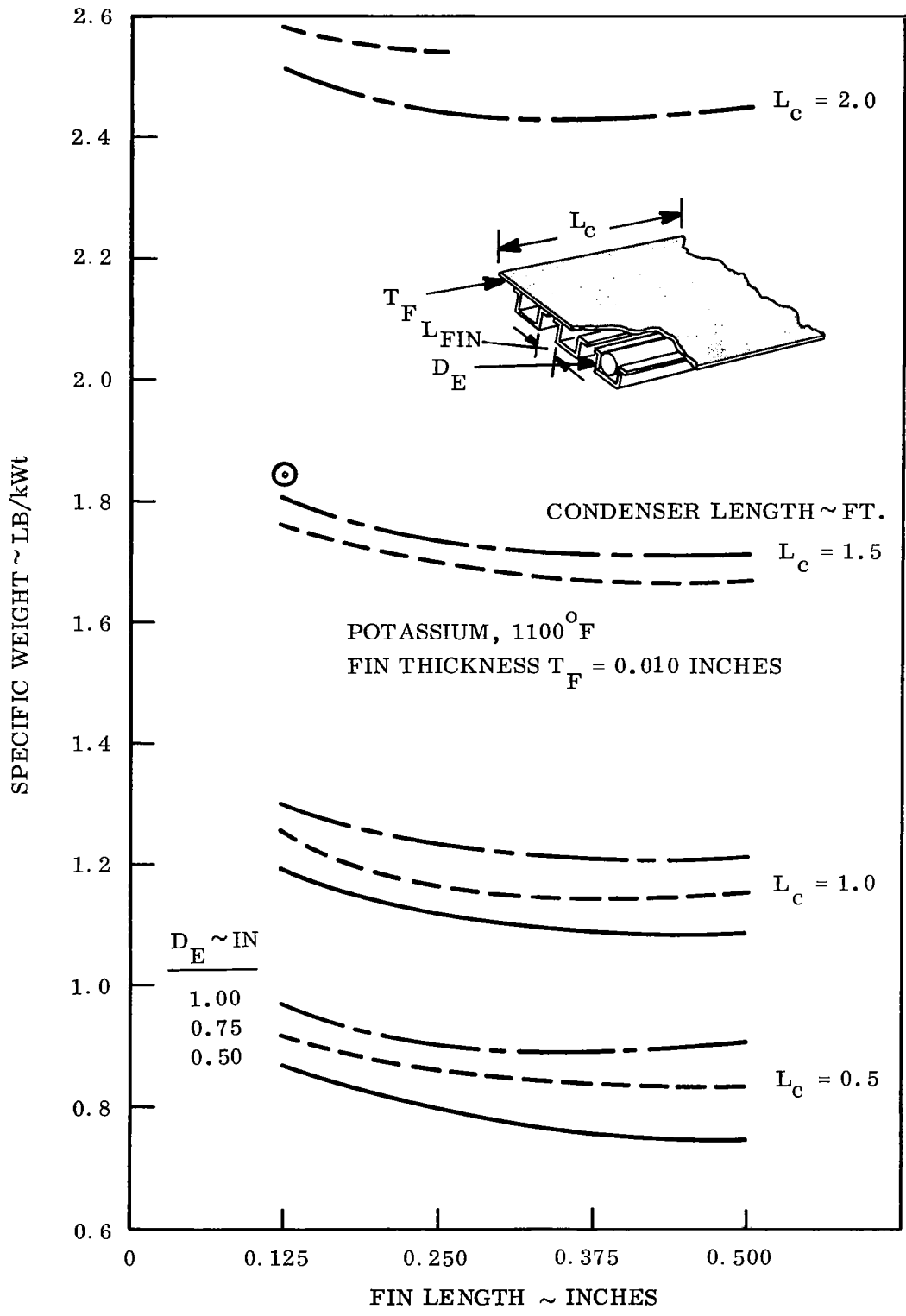


Figure 5-17. Geometry 4 Specific Weight Versus Fin Length ($T_F = 0.010$ in.)

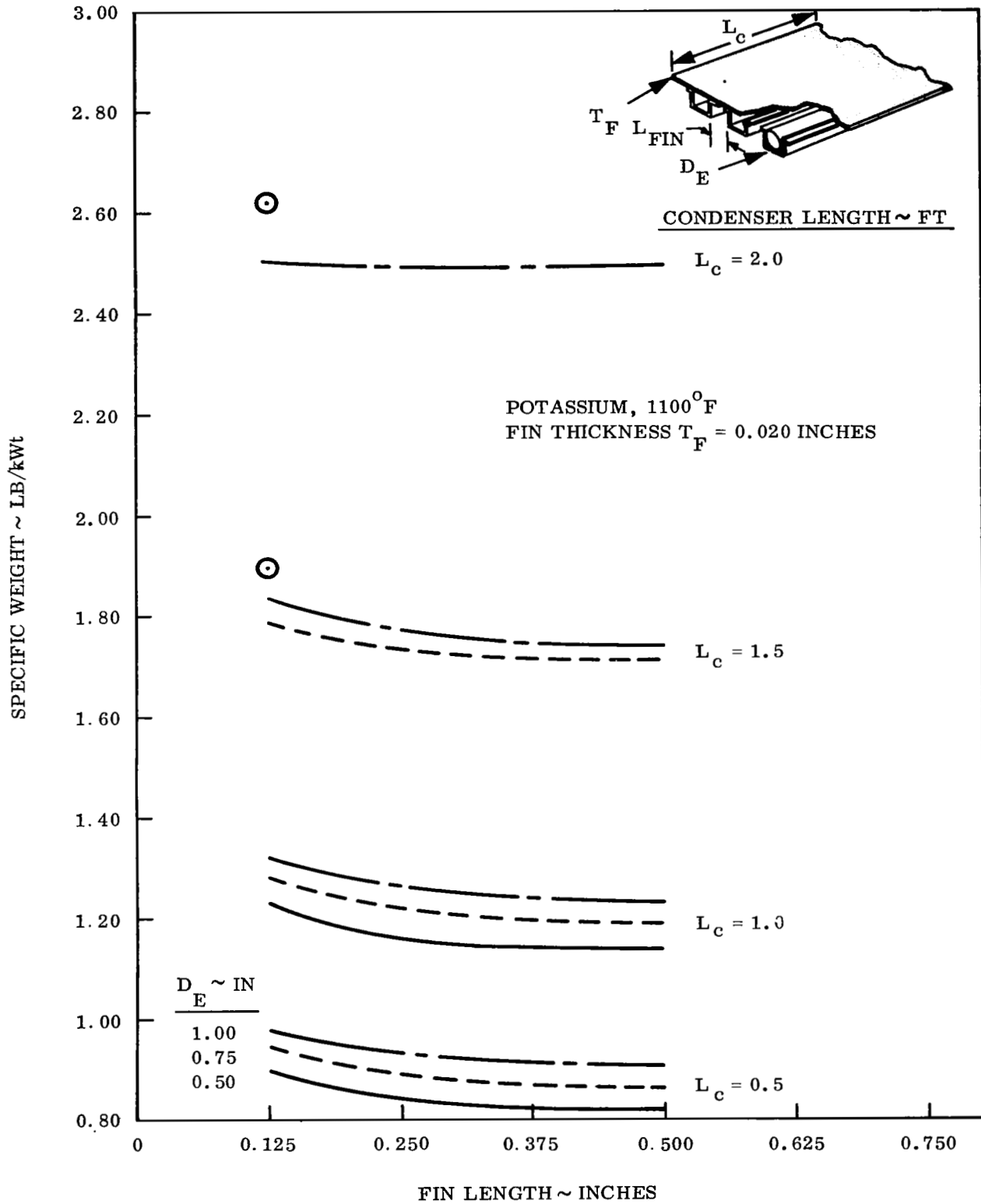


Figure 5-18. Geometry 4 Specific Weight Versus Fin Length ($T_F = 0.020$ in.)

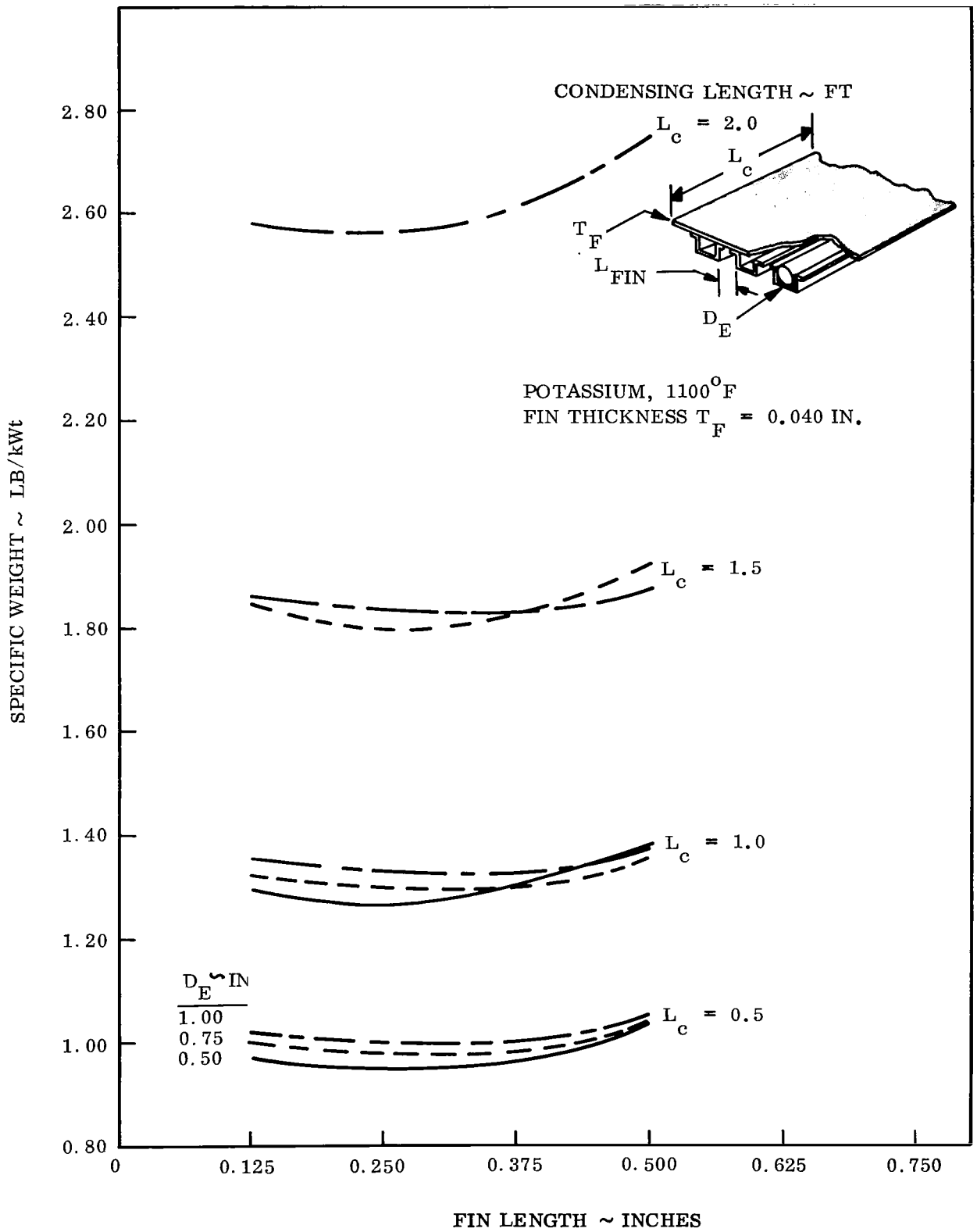


Figure 5-19. Geometry 4 Specific Weight Versus Fin Length ($T_F = 0.040$ in.)

5.1.2.4 Geometry 3 Analysis

The configuration of Geometry 3 represents a significant departure from current heat pipe experience. Consequently, the physical phenomena occurring within this hexagonal array of vapor chambers could not be modeled in the existing HPIPE computer code. Figure 5-20 shows a schematic of a vapor chamber fin/primary fluid duct arrangement. If the energy transfer processes are examined it can be shown that Hexagon A will receive energy from Hexagons E and F and will transfer energy to Hexagons B and C and also from its radiating surface to the environment. If the width of the hexagons is small, very little energy transfer will occur in the axial direction. In essence, Hexagons G, A and D would be operating at very similar temperatures and a negligible amount of energy would be transferred from side 5_G to 5_A and 2_A to 2_D . Condensation of fluid would occur on sides 3_E and 4_F while evaporation would take place on 3_A and 4_A . A portion of the evaporated fluid vapor would flow to sides 1_A and 6_A where it could condense. The remainder would have already condensed on the radiating surface. The latent heat of vaporization, released in the condensation process, evaporates liquid off sides 6_B and 1_C of Hexagons B and C, respectively. In this manner, heat can be transferred along the fin and also to the environment. The fluid within Hexagon A is returned from sides 6_A , 1_A and the radiating surface by an internal wick which covers the interior. No mass transfer is possible between chambers.

The obvious disadvantage of this arrangement is the fact that the presence of stainless steel walls and several evaporating and condensing surfaces in the direction of heat transfer incurs a relatively large temperature drop along the fin. In the three previous designs, the vapor chamber fin can be considered to be isothermal at any axial location. From the standpoint of the radiator providing support for the powerplant during launch, the hexagonal configuration is superior.

The performance of the hexagonal vapor chamber fin was evaluated primarily by the STEADY heat transfer code. In this model, the vapor space was assumed to be of infinite thermal conductivity. All walls running perpendicular to the primary fluid (in a direction along the fin) were assumed to have an infinite resistance. The condition corresponds to zero axial

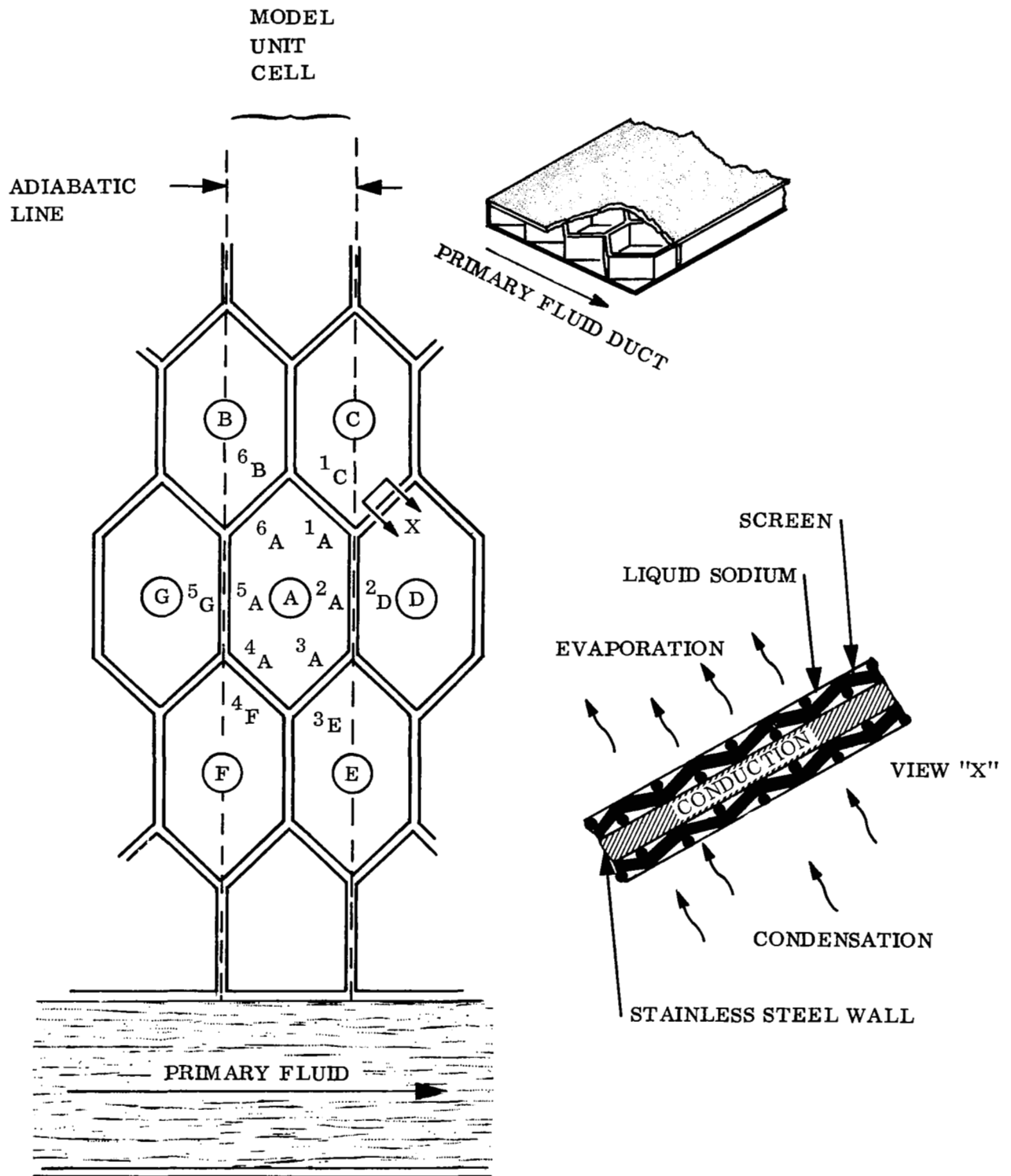
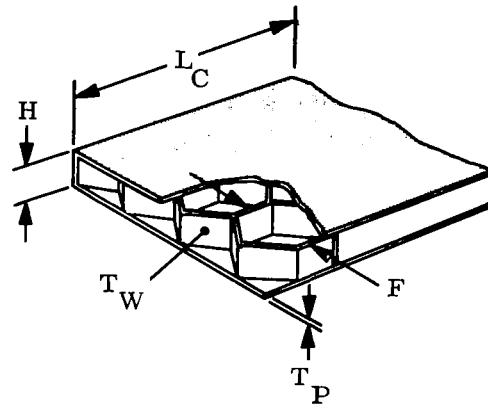


Figure 5-20. Hexagonal Geometry Computer Code Model

energy transfer. All other walls were assumed to consist of three resistances in series: a 0.009-inch layer of fluid (condensing surface), a sheet of stainless steel which formed the hexagon wall and a 0.009-inch layer of fluid which formed the evaporative wall. No vapor/liquid interface resistances were included and all heat transfer was assumed to be by conduction. A liquid layer of 0.009 inches was chosen since this corresponded to the thickness of a single layer of 100 x 100 mesh sintered screen. In all cases, sodium was considered to be the working fluid. Parameters evaluated are shown below.



The temperature distribution along the hexagonal vapor chamber fin is not continuous, but rather, stepwise. For convenience, the results from the STEADY computer program have been plotted in Figures 5-21 through 5-23 as a continuous function. From these illustrations, the following facts are evident:

1. The larger cell sizes incur fewer temperature drops, thereby maintaining a nearly isothermal fin
2. The smaller cell sizes which produce the best structure induce large temperature drops along the fin
3. Varying the wall thickness of the hexagonal core has only a moderate effect on performance.

The heat transfer results of the STEADY computer code were combined with weight calculations for the hexagonal geometry to obtain the specific weight as a function of condensing length, facing thickness, core thickness and cell size.

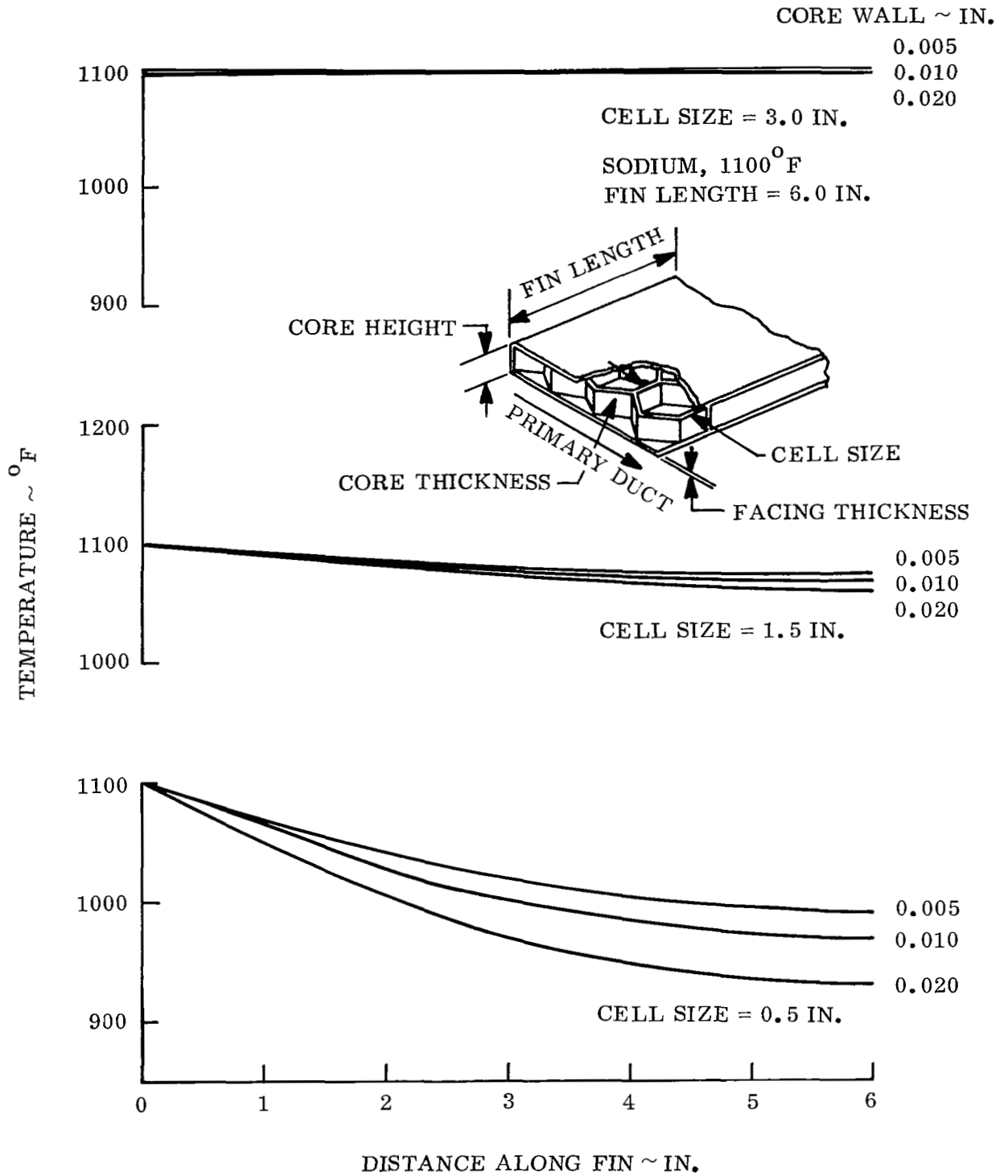


Figure 5-21. Geometry 3 Hexagonal Fin Temperature Profiles (Fin Length = 6 in.)

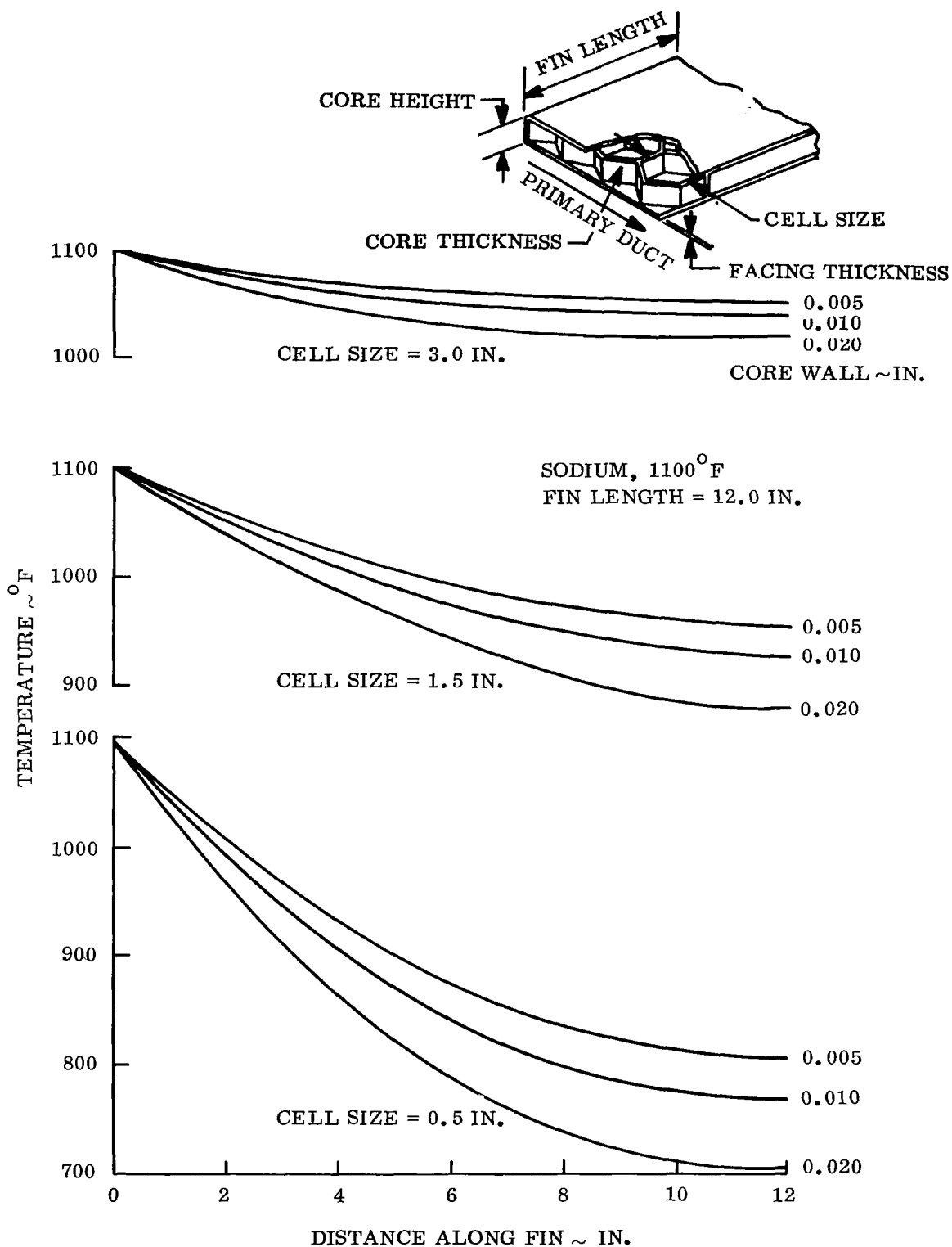


Figure 5-22. Geometry 3 Hexagonal Fin Temperature Profiles (Fin Length = 12 in.)

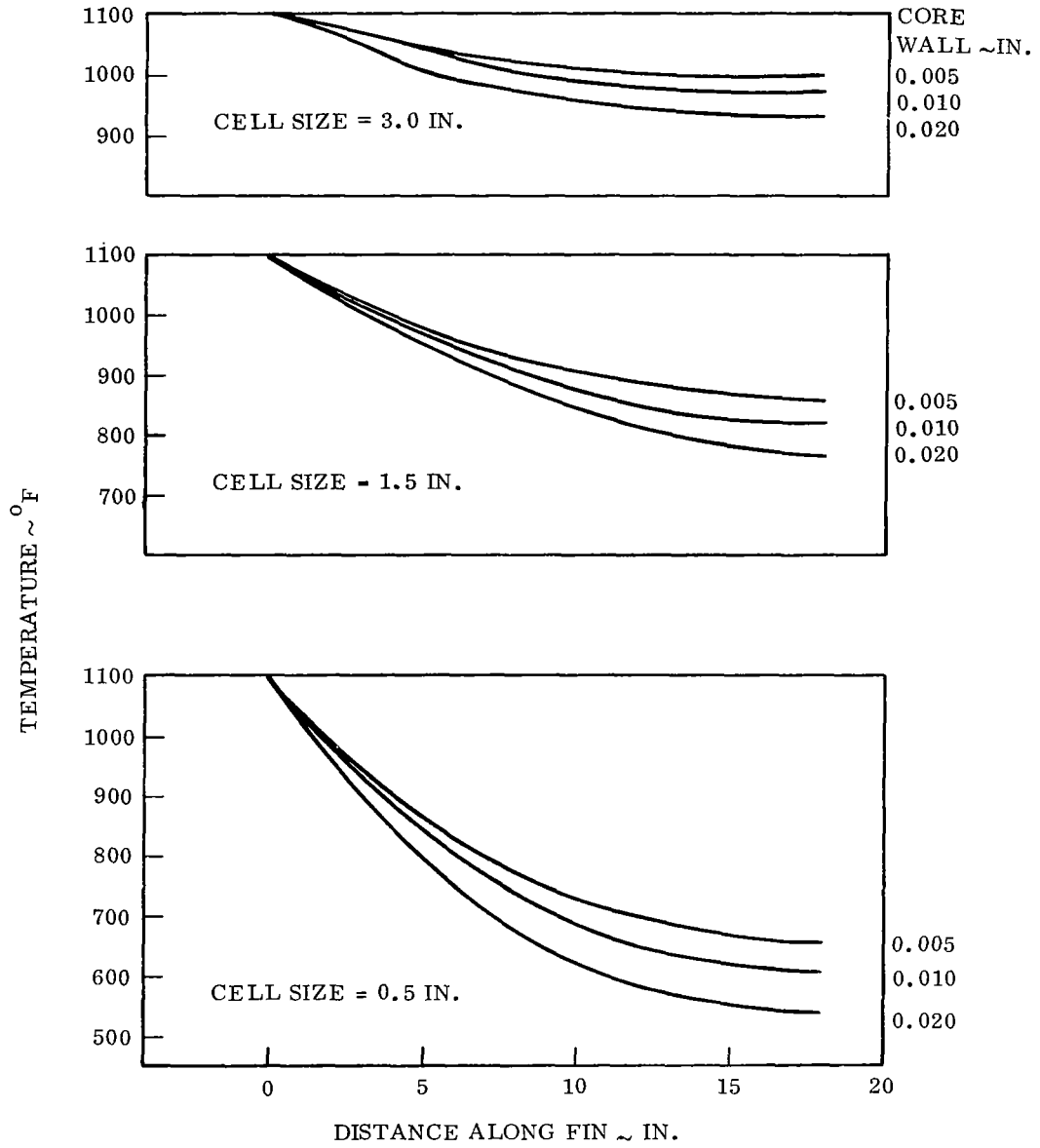
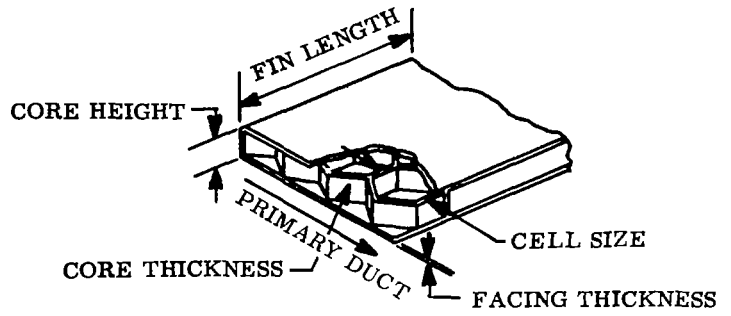


Figure 5-23. Geometry 3 Hexagonal Fin Temperature Profiles (Fin Length = 18 in.)

Figures 5-24, 5-25 and 5-26 show the specific weight versus the cell size for core heights of 0.250, 0.500 and 0.750 inches, respectively; for these cases, the core thickness was kept equal to the facing thickness. Obviously, from a thermal standpoint the lightest cases will consist of large cell sizes and thin faces and walls.

By factoring the structural considerations of this design into the problem, a more concise and meaningful presentation of the results is possible. Initially, the radiator will be subjected to atmospheric pressure while on the launch pad. For large cell sizes and thin facings, the radiator can become seriously deformed. In order to limit deformation during this period, the cell facing was allowed to deflect a distance equal to one-half of its thickness. This criteria is considered to be the limit of the elastic region. The following minimum facing thicknesses were stipulated:

<u>Cell Size (in.)</u>	<u>Facing Thickness (in.)</u>
0.500	0.005
1.000	0.010
1.500	0.020

By imposing these constraints on the results of Figures 5-24, 5-25 and 5-26, a locus of minimum weight radiators can be defined for each condensing length. This procedure is indicated on the respective figures.

Since thin core material is desirable from a heat transfer standpoint and relatively thick facing material is required from structural considerations, additional cases were generated in which the facing thickness was varied with a constant core thickness of 0.005 inches. These cases are shown in Figures 5-27 through 5-30. For each cell size, core height and vapor chamber length, it is now possible to select the minimum weight case. These results are shown in Figure 5-31. At vapor chamber lengths of 0.50 and 1.00 foot, the 0.250 inch core height is lighter. However, the 0.500-inch core height becomes more advantageous as the chamber is lengthened due to the need for more heat transfer area. Optimum cell sizes fell in the range between 0.75 and 1.00 inch. The data for the 2.0-foot vapor chamber length curves were extrapolated.

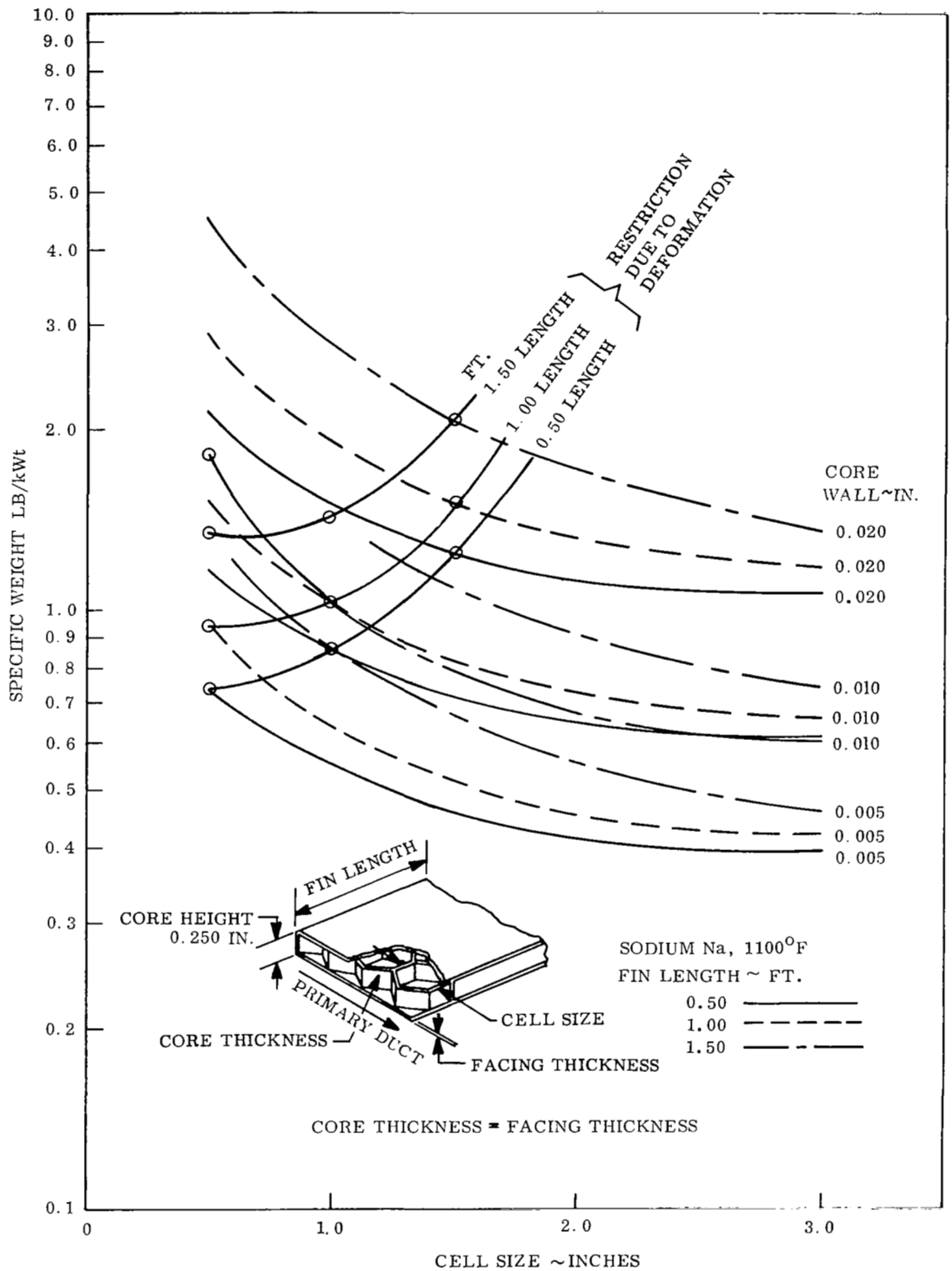


Figure 5-24. Geometry 3 Effect on Specific Weight with Core Height of 0.250 Inches

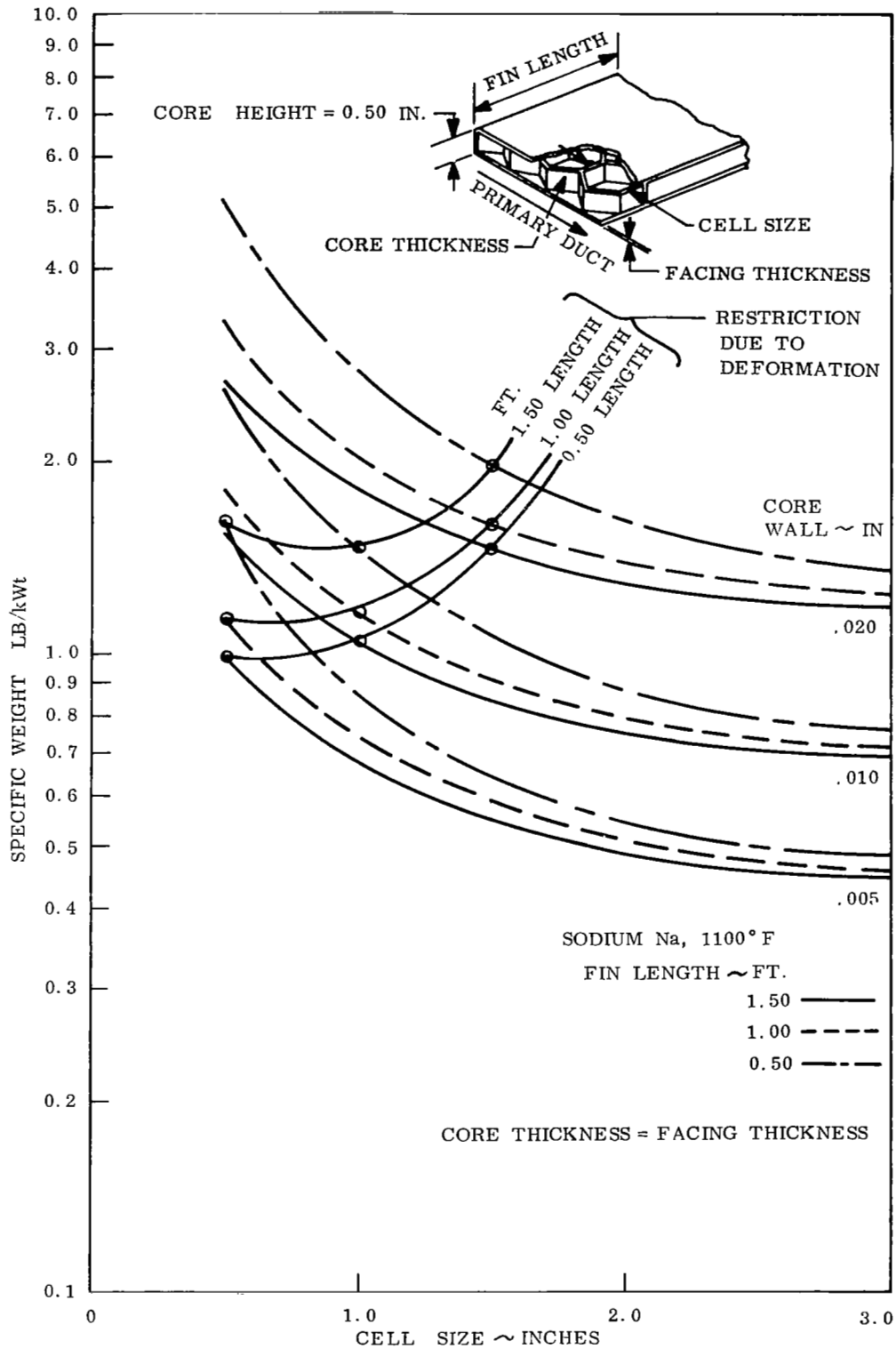


Figure 5-25. Geometry 3 Effect on Specific Weight with Core Height of 0.50 Inches

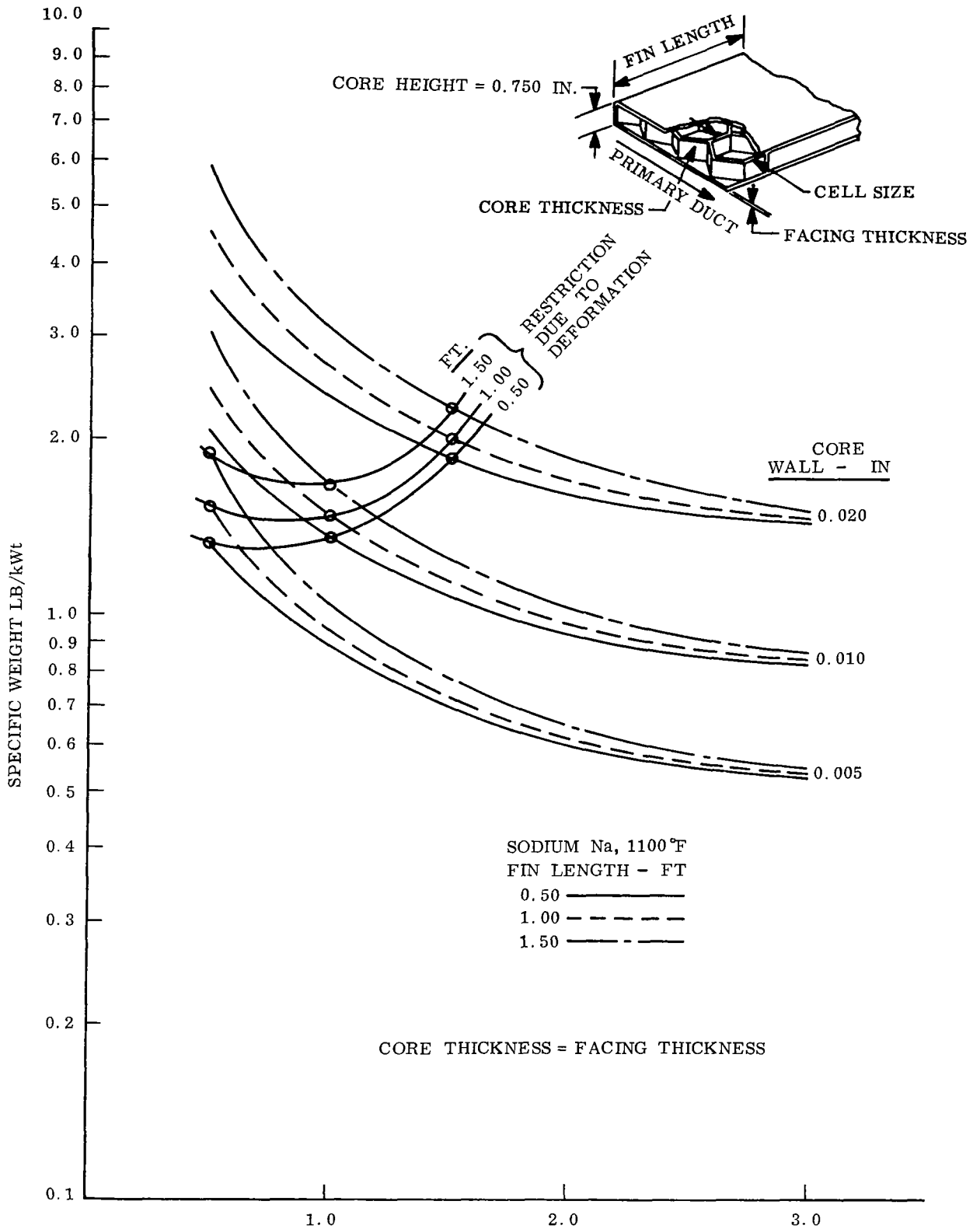


Figure 5-26. Geometry 3 Effect on Specific Weight with Core Height of 0.750 Inches

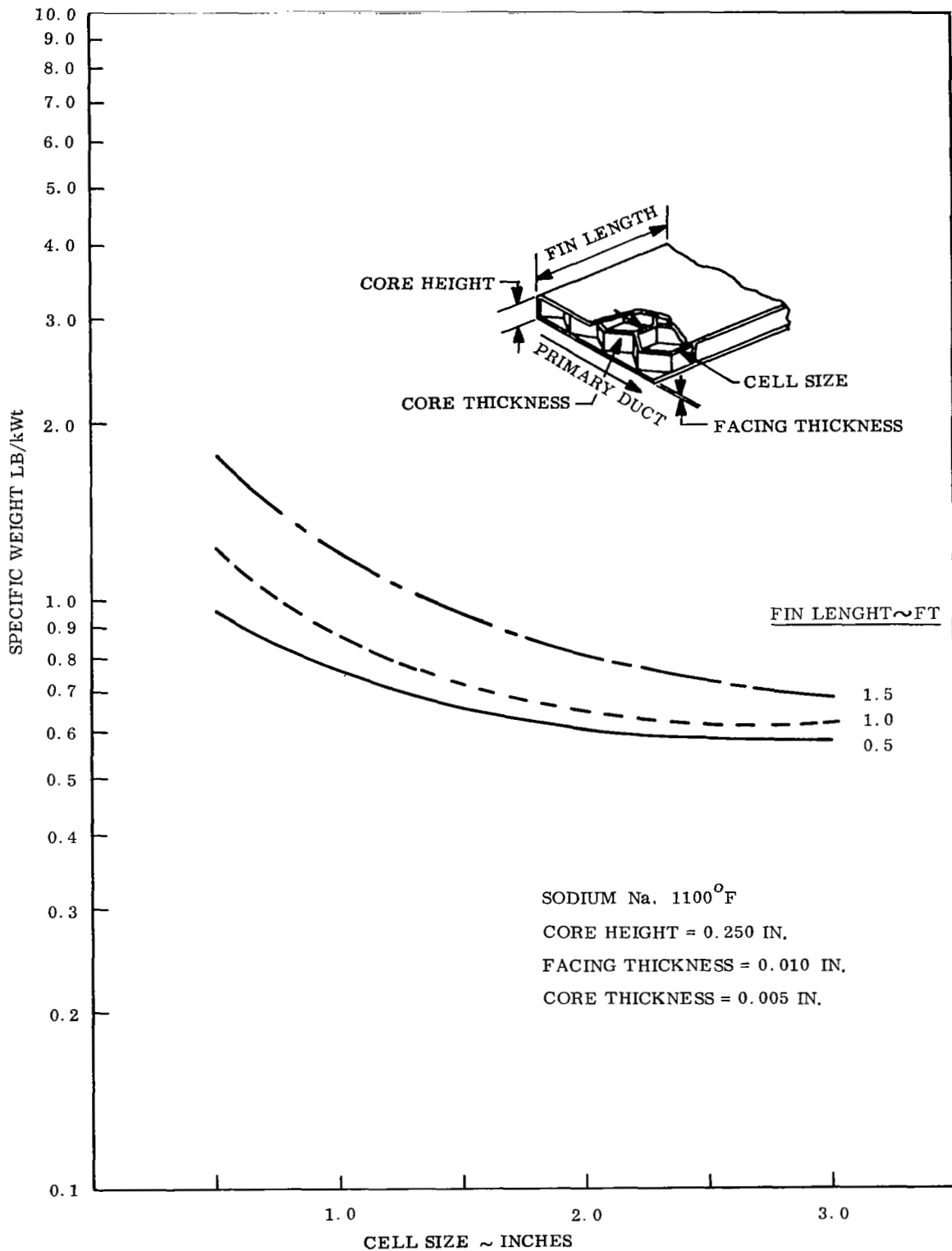


Figure 5-27. Geometry 3 Effect on Specific Weight with Facing Thickness of 0.010 Inches

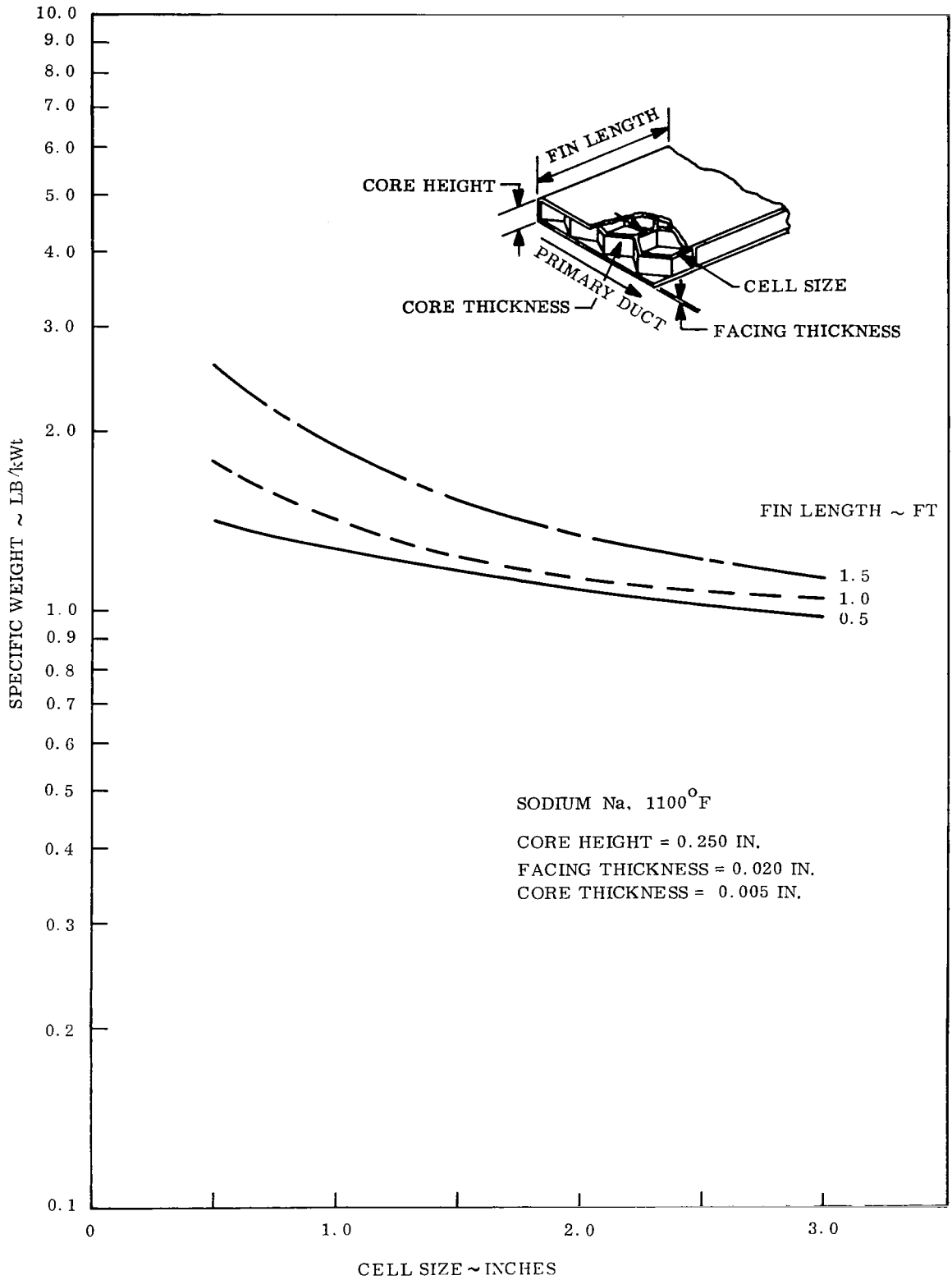


Figure 5-28. Geometry 3 Effect on Specific Weight with Facing Thickness of 0.020 Inches

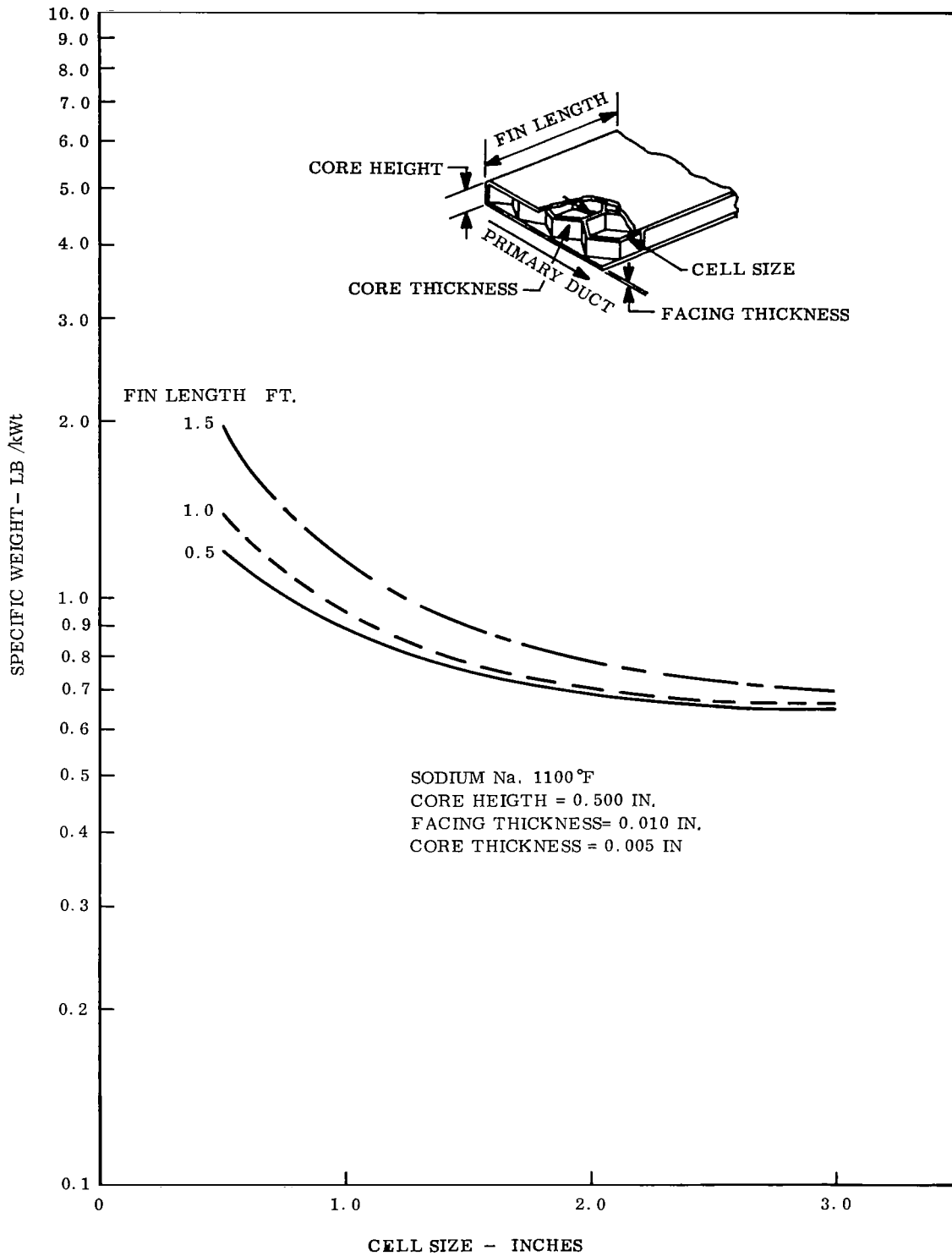


Figure 5-29. Geometry 3 Effect on Specific Weight with Facing Thickness of 0.010 Inches and Core Height of 0.5 Inches

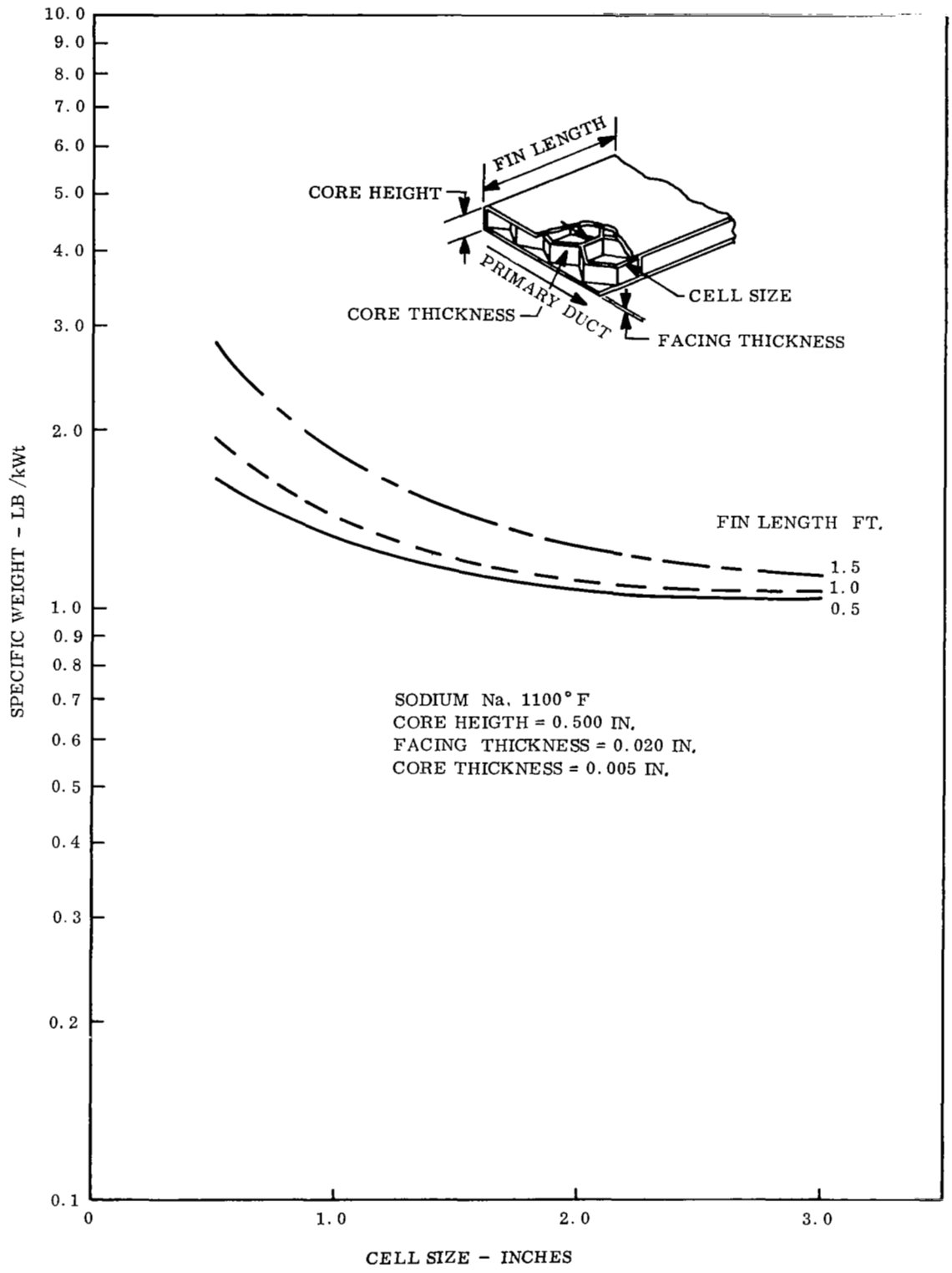


Figure 5-30. Geometry 3 Effect on Specific Weight with Facing Thickness of 0.020 Inches and Core Height of 0.5 Inches

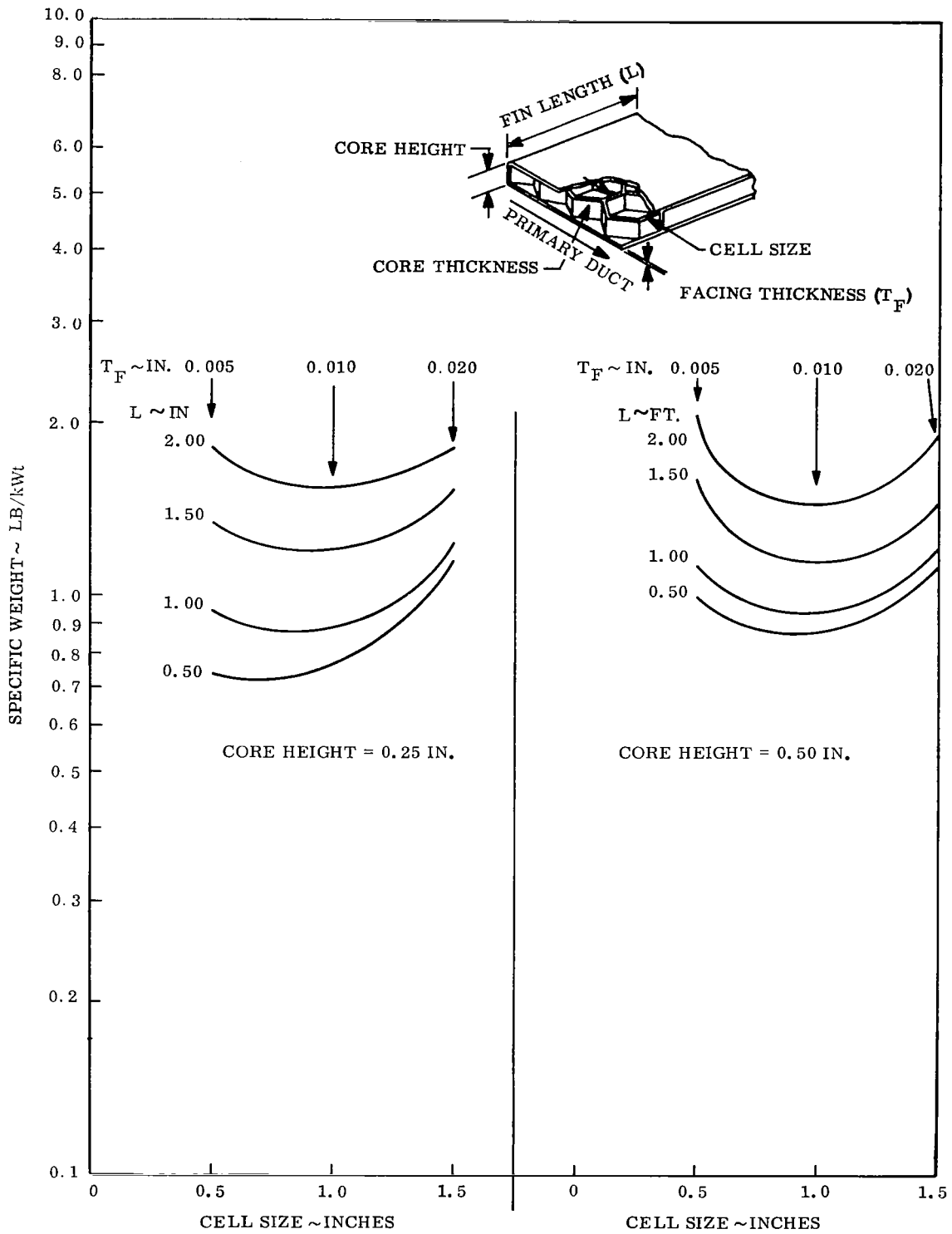


Figure 5-31. Geometry 3 Minimum Weight Hexagonal Fins for Core Height of 0.25 and 0.50 Inches

On a preliminary basis the hexagonal configuration does not demonstrate an advantage over the other geometries. This is a direct result of the temperature drop imposed in going from one cell to the next. Other approaches were examined which tried to take advantage of the honeycomb structure, yet did not involve a temperature drop in going from cell to cell. For example, by drilling small holes in the core, fluid could be transported from one cell to the next. This concept presented two problems: a pressure drop (and attendant temperature drop) would be incurred during passage through the holes, and secondly, the return fluid wicking would be extremely difficult to design and fabricate. The relationship between the vapor temperature drop and required flow area is shown in Figure 5-32 for a specific case.

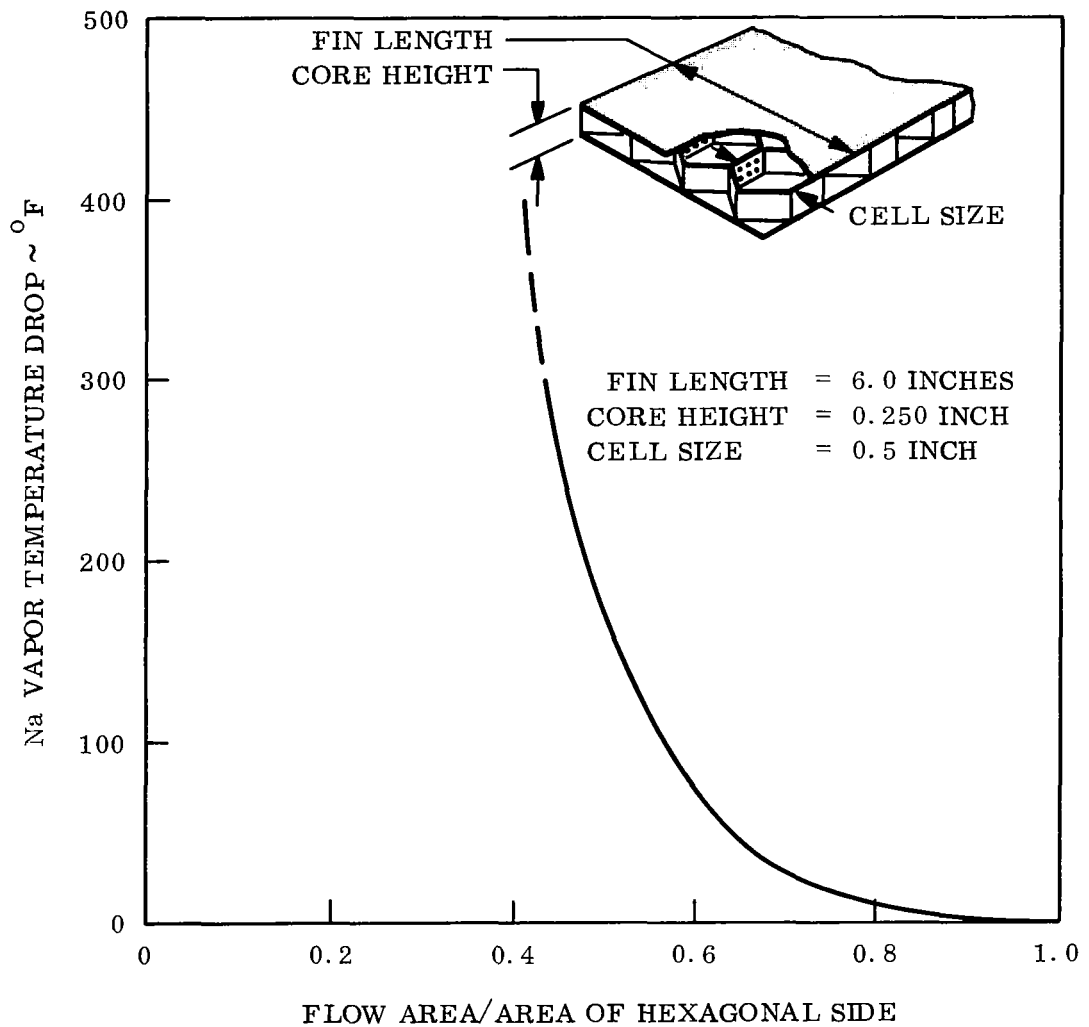


Figure 5-32. Axial Vapor Temperature Drop for Hexagonal Configuration with Holes

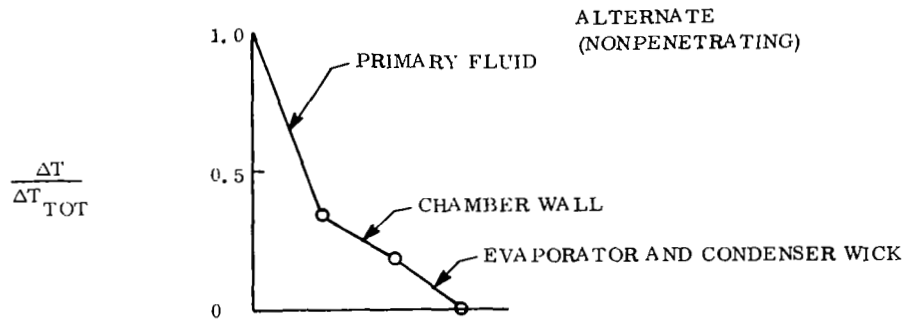
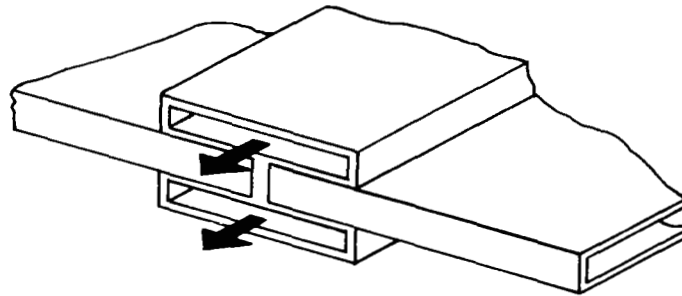
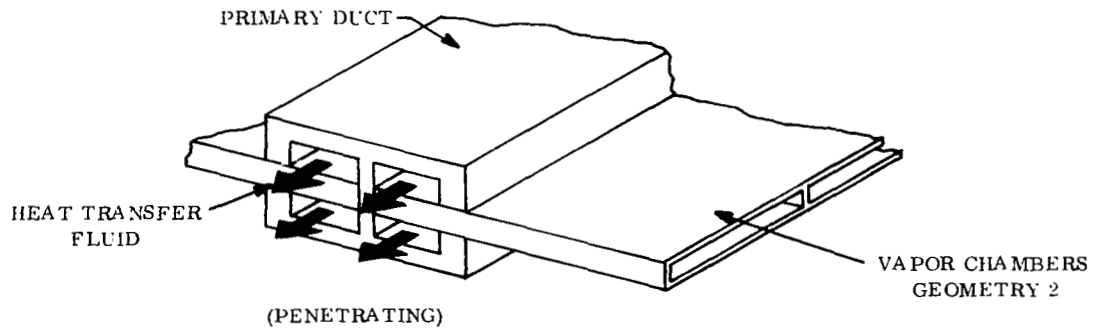
5.2 VAPOR CHAMBER FIN INTEGRATION EVALUATION

The next portion of the analysis examined the integration of vapor chamber geometries with the primary duct and effect of the primary fluid ducts on the overall radiator design. Two basic nonfinned duct configurations were considered. One concept which allows heat to be transferred to both sides of the heat pipe evaporator section, is shown in Figure 5-33 as integrated with Geometries 1 and 2. This concept should result in a higher effective radiating temperature and a smaller radiator area. The second concept, Figure 5-34 is a self-contained fluid duct which can transfer heat from only one of its surfaces. Unlike the first concept, the primary fluid is not in direct contact with the vapor chambers. However, this arrangement provides the primary fluid ducts with meteoroid "bumper" protection and is considerably easier to fabricate.

In order to draw a comparison between each radiator vapor chamber condenser geometry from an integration and total radiator standpoint, a computer code was written which would calculate: required primary duct size, primary duct armor thickness, total radiator area, radiator duct weight and fluid pump work. These results were then combined with data previously obtained from the vapor chamber condenser/fin analysis. In this fashion, a total radiator weight was calculated as a function of condenser length.

Figure 5-35 illustrates the logic utilized in calculating the weight of the fluid ducts and system pump work weight penalty. Although the logic is identical, two sets of equations were utilized within the code so as to reflect both primary duct concepts. Since the required length of the primary fluid ducts and the required armor thickness are interdependent, an iteration loop was necessary to effect a solution. The final output from the code was the primary fluid duct system weight as a function of duct width and vapor chamber fin condensing length.

One important aspect of the primary duct design is the flow velocity. This parameter strongly influences the primary duct pressure drop, coolant film temperature drop and vulnerable area. Consequently, preliminary cases were run in order to estimate the optimum primary fluid flow velocity. Using vapor chamber fin Geometry 2, in conjunction



ΔT 'S ASSOCIATED WITH PENETRATED DUCT CONCEPT

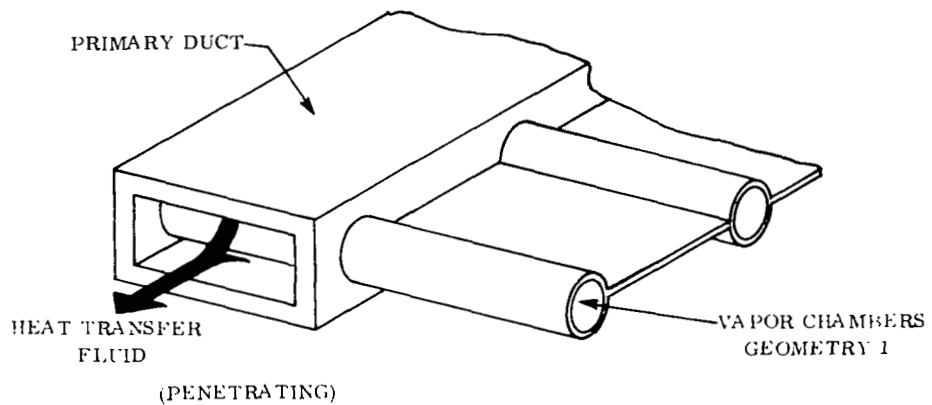
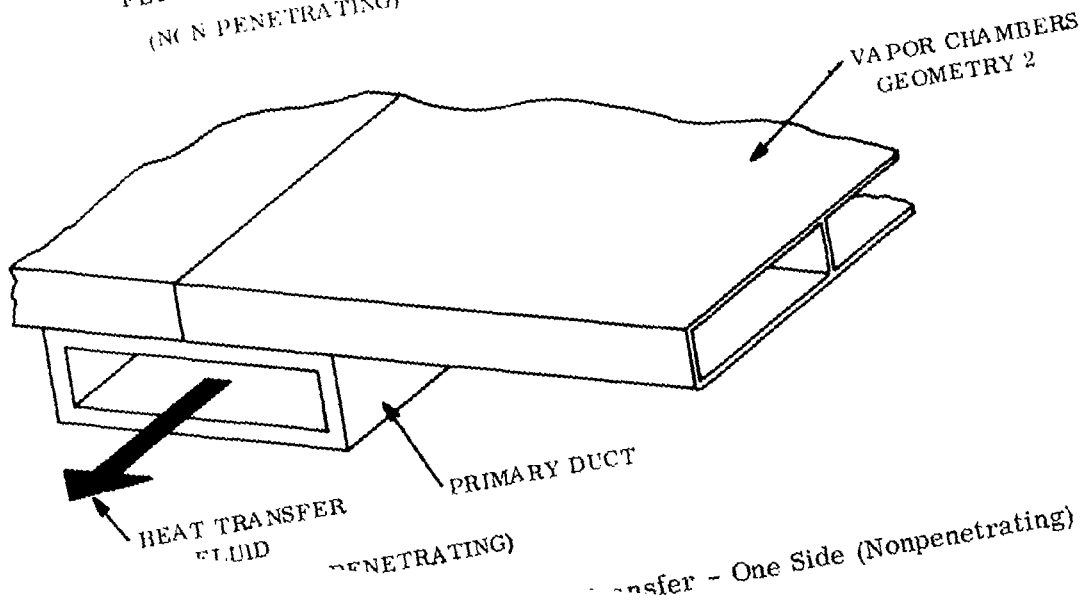
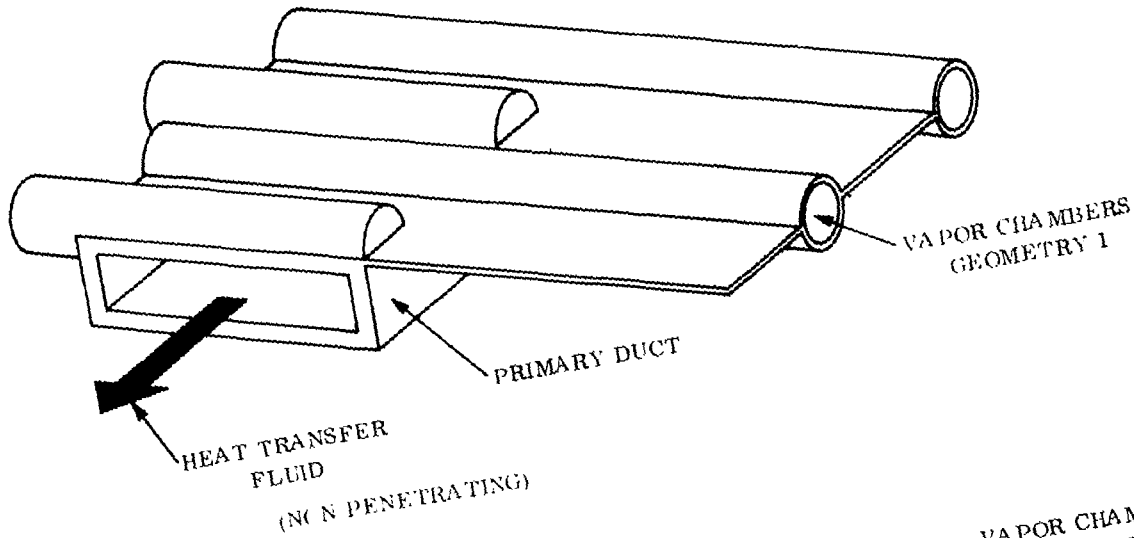
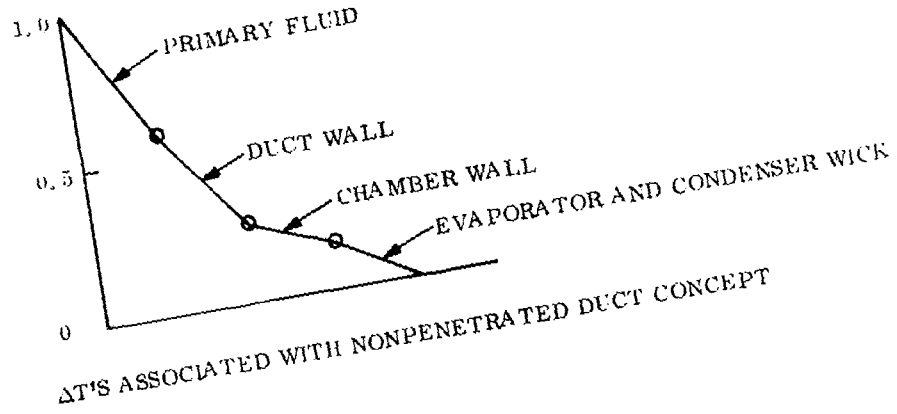


Figure 5-33. Primary Duct Concepts Heat Transfer - Both Sides (Penetrating and Nonpenetrating)

$$\frac{\Delta T}{\Delta T_{TOT}}$$



Transfer - One Side (Nonpenetrating)

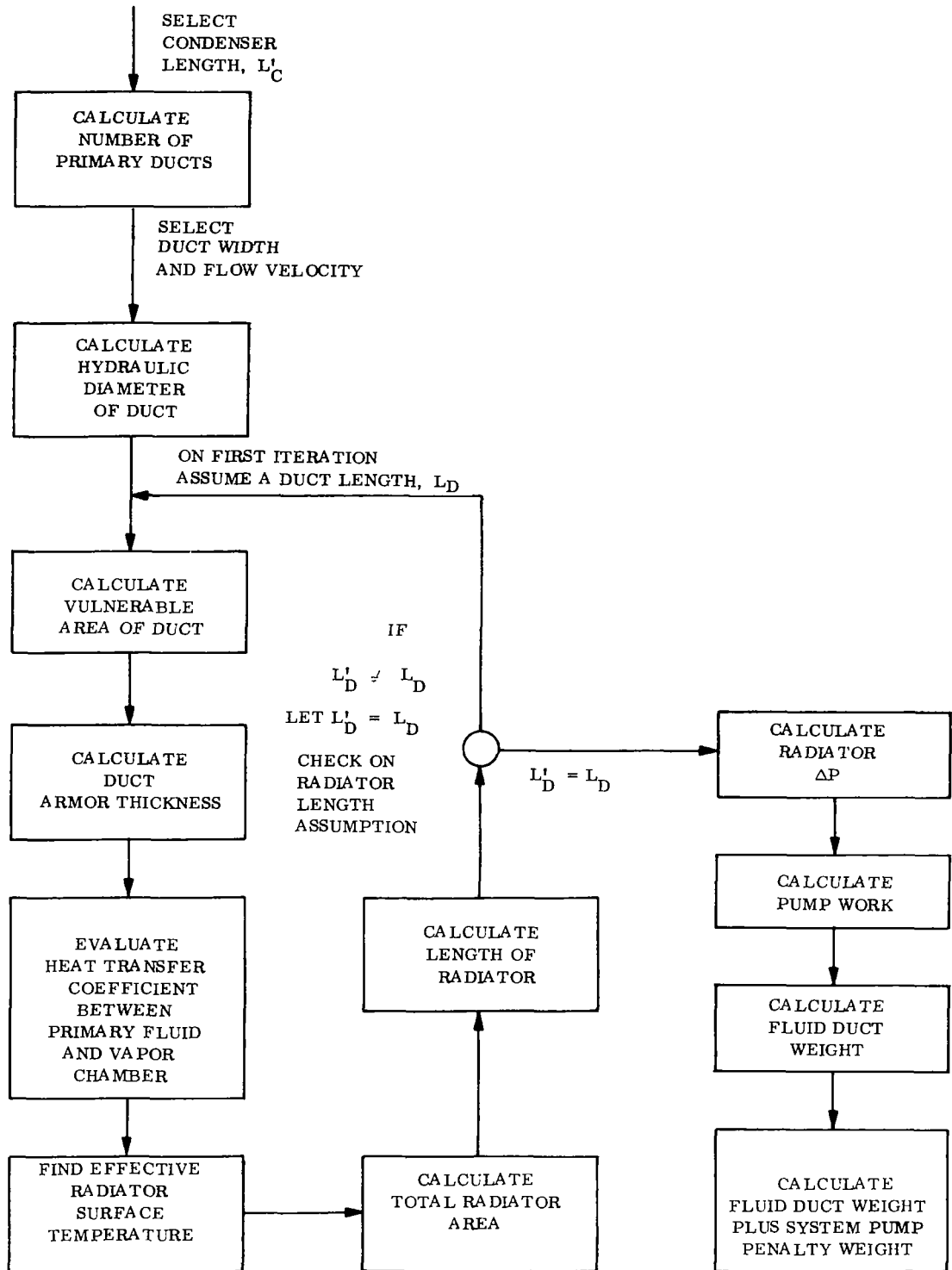


Figure 5-35. Flow Chart for Computer Program to Evaluate Primary Fluid Duct System Weight Penalty

with the nonpenetrated primary duct concept, the primary duct weight as a function of condensing length and flow velocity was determined. Figure 5-36 summarizes these results. For reasonable duct widths the optimum flow velocity was approximately 10 feet per second. This value was used for the remainder of the investigation.

The evaluation of the radiator optimum weight excluding structural considerations for each geometry was performed by combining the results of Section 5.1 (vapor chamber fin matrix weight) with the data from the primary fluid duct computer program. The manner in which this was done is described below.

The trade-offs involved in the analysis for all concepts can be understood by examining vapor chamber fin Geometry 1, with the offset nonpenetrating primary fluid duct. Figure 5-37 shows that as vapor chamber fin length decreases, the primary fluid duct weight increases. This is elementary since more primary fluid ducts are required. For each vapor chamber fin length, an optimum primary duct width exists. At a small duct width, a substantial ΔT is imposed between the bulk primary fluid and the vapor chamber fin condenser. This produces a lower effective radiator temperature, larger radiator area and longer, more heavily armored, primary ducts. As the duct width is increased, smaller radiator areas are possible. At some point, depending on the vapor chamber fin length, further extension of the duct width no longer drops the ΔT sufficiently to warrant the increase in duct vulnerable area. The corresponding radiator area for these cases is provided in Table 5-2.

Using the results obtained for the weight of the vapor chamber fin condenser sections (Section 5.1) and the output of Figure 5-37, a total nonstructural radiator weight can be obtained as shown in Figure 5-38. From Figure 5-38, a locus of points can be drawn through each condensing length minimum. Clearly, the total radiator weight decreases with decreasing condensing length. In order to determine the exact value for the minimum weight condensing length, the results are replotted in Figure 5-39. For the case examined, the optimum length occurred at 5.40 inches. In some instances, additional computer runs were performed to calculate the primary duct weight for particular condensing lengths. Below a six-inch condensing length, the primary fluid duct weight increases dramatically.

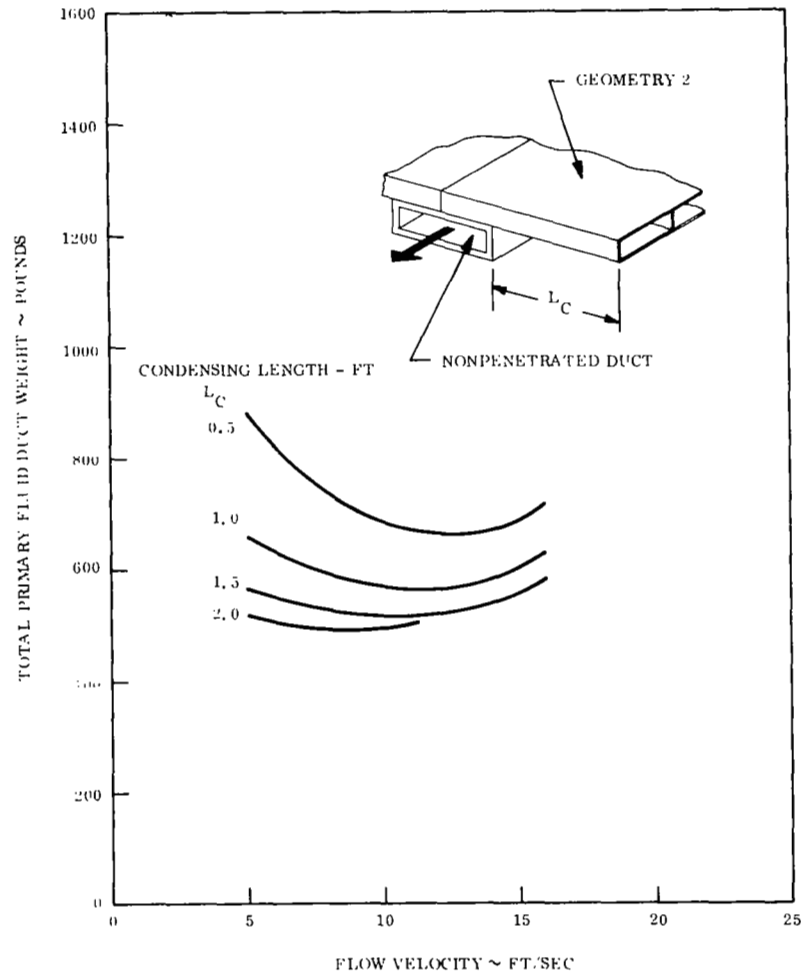


Figure 5-36. Effect of Flow Velocity and Variable Condensing Length on Primary Duct Weight

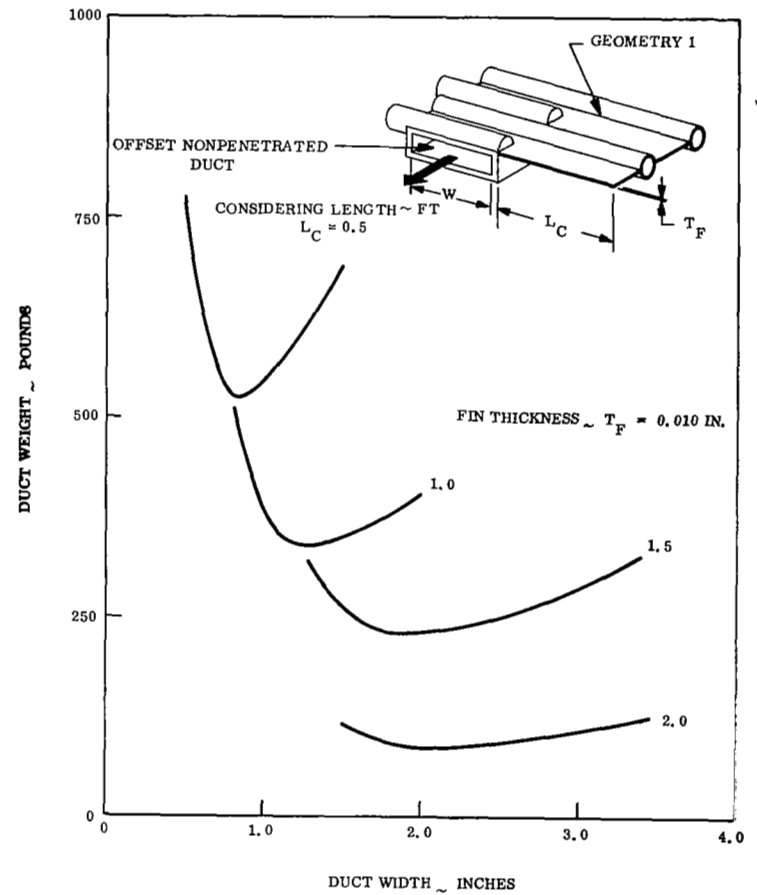


Figure 5-37. Variation of Primary Fluid Duct Weight as a Function of Duct Width and Vapor Chamber Length

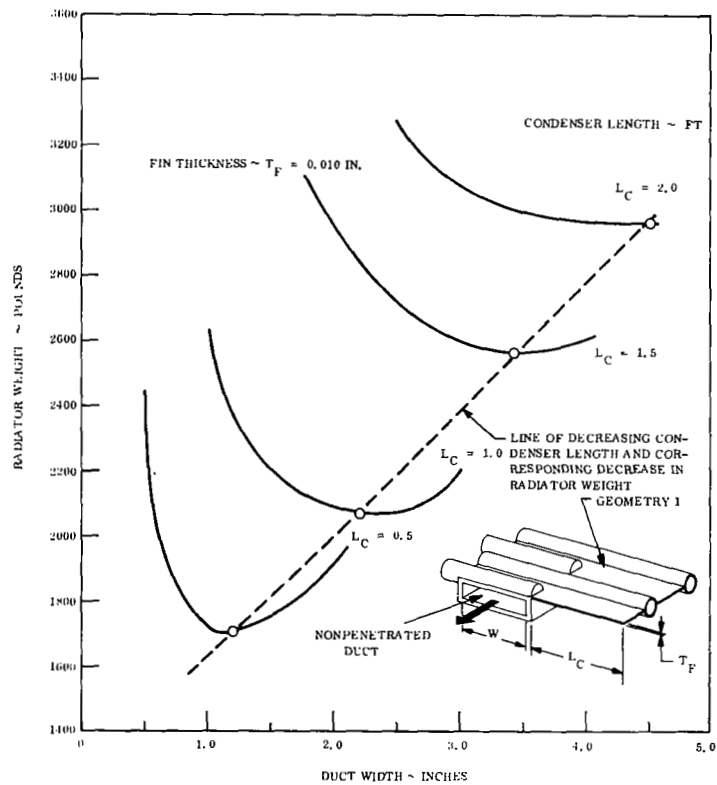


Figure 5-38. Radiator Weight as a Function of Vapor Chamber Fin Length and Primary Duct Width

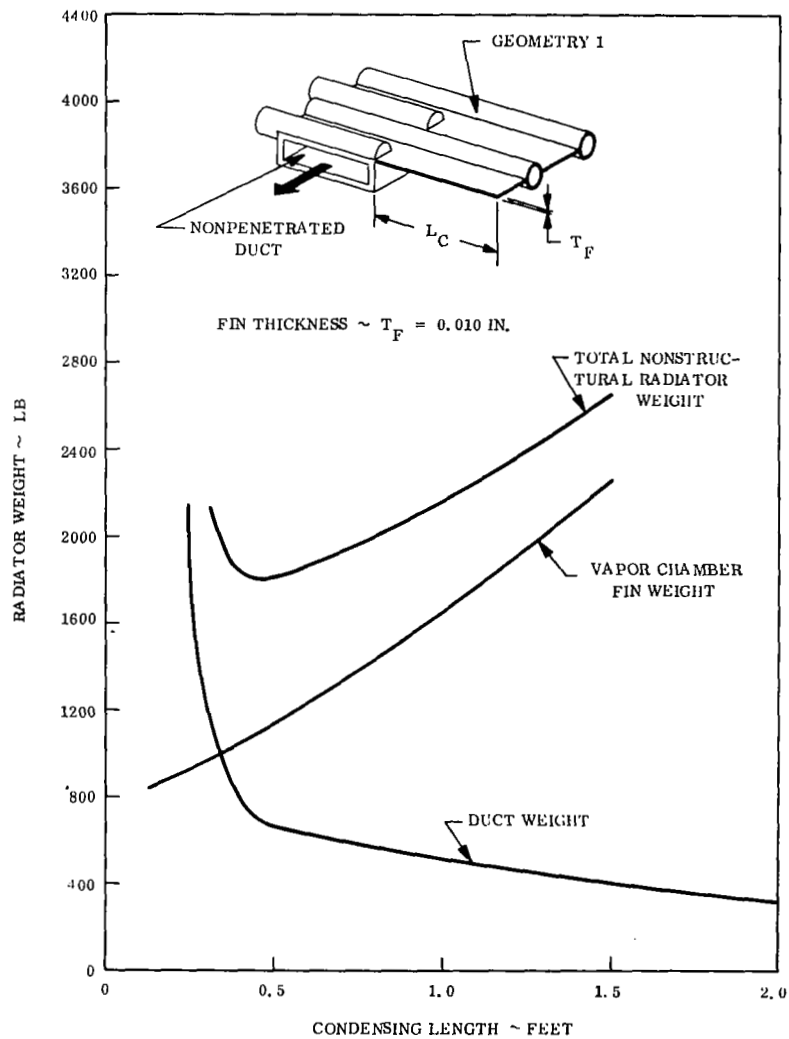


Figure 5-39. Variation of Radiator Weight with Condensing Length (Geometry 1)

Table 5-2 . Influence on Radiator Area for Various Duct Widths and Vapor Chamber Condensing Lengths

Vapor Chamber Length, L_c (Ft)	Duct Width W_D (in.)	Required Radiator Area, A (Ft ²)
0.5	0.50	1505
	1.00	1065
	1.50	965
	2.00	920
1.0	1.0	1545
	1.5	1270
	2.0	1160
	2.5	1090
	3.0	1040
1.5	1.5	1515
	2.0	1260
	2.5	1135
	3.0	1065
	3.5	1030
	4.0	1010
2.0	2.0	1290
	2.5	1145
	3.0	1070
	3.5	1030
	4.0	1015
	4.5	1005

A summary of the optimum radiator weights is shown in Table 5-3 for each configuration. The radiator weights for either type of primary fluid duct did not vary dramatically; however, the offset duct geometry generally incurred a 20-to-30 percent penalty. One outstanding result is the number of chambers required in the hexagonal vapor chamber concept. The weights presented do not include structural weight; this analysis is presented in the following section.

Table 5-3 . Optimum Radiator Weights Using Potassim* Vapor Chambers
(No Additional Structural Members)

Vapor Chamber Fin Geometry (Fin Thick. ~ in.)	Primary Duct Geometry	Optimum Condensing Length, in.	Optimum Nonstructural Radiator Weight, lbs.
1 (0.010 Fins)	Nonpenetrated Offset Duct	5.85	1800
1 (0.020 Fins)	Nonpenetrated Offset Duct	7.96	1950
2	Nonpenetrated Offset Duct	6.30	1520
3	Nonpenetrated Offset Duct	9.42	2850
4 (0.010 Fins)	Nonpenetrated Offset Duct	7.50	1980
4 (0.020 Fins)	Nonpenetrated Offset Duct	7.20	2075
1 (0.010 Fins)	Penetrated Central Duct	6.00	1510
1 (0.020 Fins)	Penetrated Central Duct	7.50	1700
2	Penetrated Central Duct	7.05	1670
3	Penetrated Central Duct	6.73	2500
4 (0.010 Fins)	Penetrated Central Duct	6.75	1710
4 (0.020 Fins)	Penetrated Central Duct	7.20	1725

*The hexagonal configuration (Geometry 3) utilized sodium

5.3 VAPOR CHAMBER FIN CONCEPT/RADIATOR STRUCTURAL EVALUATION

5.3.1 GENERAL

A realistic comparison between the candidate vapor chamber concepts must include an estimate of the overall weight, including additional structural members required to support the launch loads.

Figure 5-40 shows the four radiator panel concepts analyzed. Since the panels did not have sufficient strength, structure, in the form of rings and longerons, was added as required to support the launch load.

5.3.2 LOADS

For an unshrouded design, the flight loads consist of aerodynamic loads as well as acceleration or g loads. The most severe axial load distribution and shear and moment distributions, due to aerodynamic loading during a two stage Saturn V launch, are shown

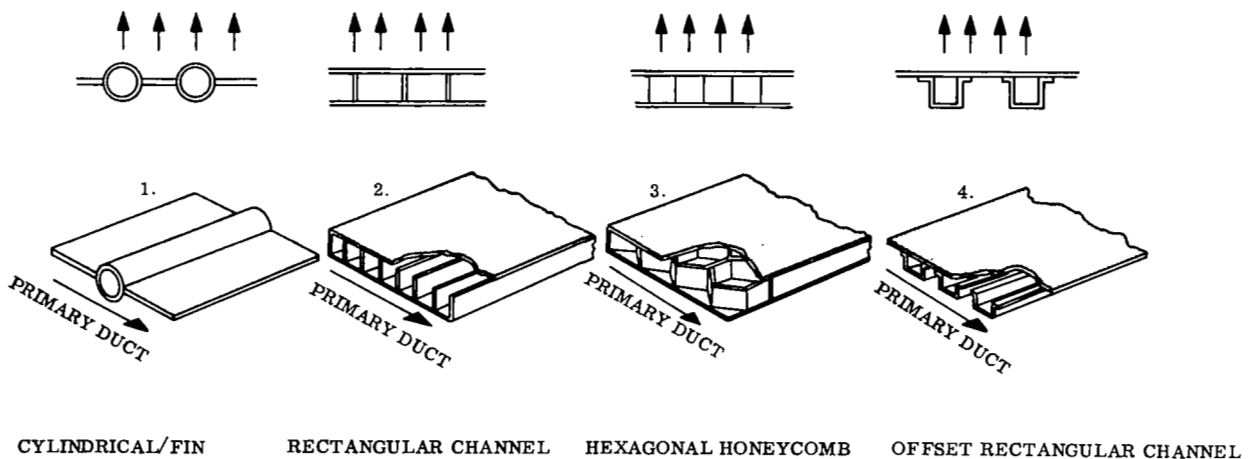


Figure 5-40. Vapor Chamber Fin Concepts

in Figure 5-41. This load condition occurs at maximum $q\alpha$, where, q , is the dynamic pressure and, α , is the vehicle angle of attack. The most severe axial load distribution and shear and moment distribution, due to acceleration, are shown in Figure 5-42. The load distribution due to aerodynamic and acceleration loads have been superimposed to obtain the design loads for the radiator/structure design.

For preliminary analyses purposes, the axial load and bending moment can be expressed in terms of an equivalent axial load by the equation

$$P_{eq} = P_{axial} + \frac{4M}{D} \quad (5-17)$$

where

P_{eq} = equivalent axial load

P_{axial} = axial load

M = bending moment

D = diameter

The equivalent axial load for a load bearing radiator, at the maximum $q\alpha$ condition for a two-stage Saturn V is shown in Figure 5-43.

5.3.3 ASSUMPTIONS

1. The radiator and support structure material is AISI 316 stainless steel.
2. The equipment forward of the radiator weighs 15,000 pounds.
3. The conical radiator can be approximated by a cylinder having a diameter equal to the average diameter of the radiator and a length equal to the slant height of the radiator and the relationship between the equivalent axial loads of the conical and cylindrical configurations can be expressed

$$P_{c_{eq}} = P_{cy_{eq}} \cos^2 \alpha \quad (5-18)$$

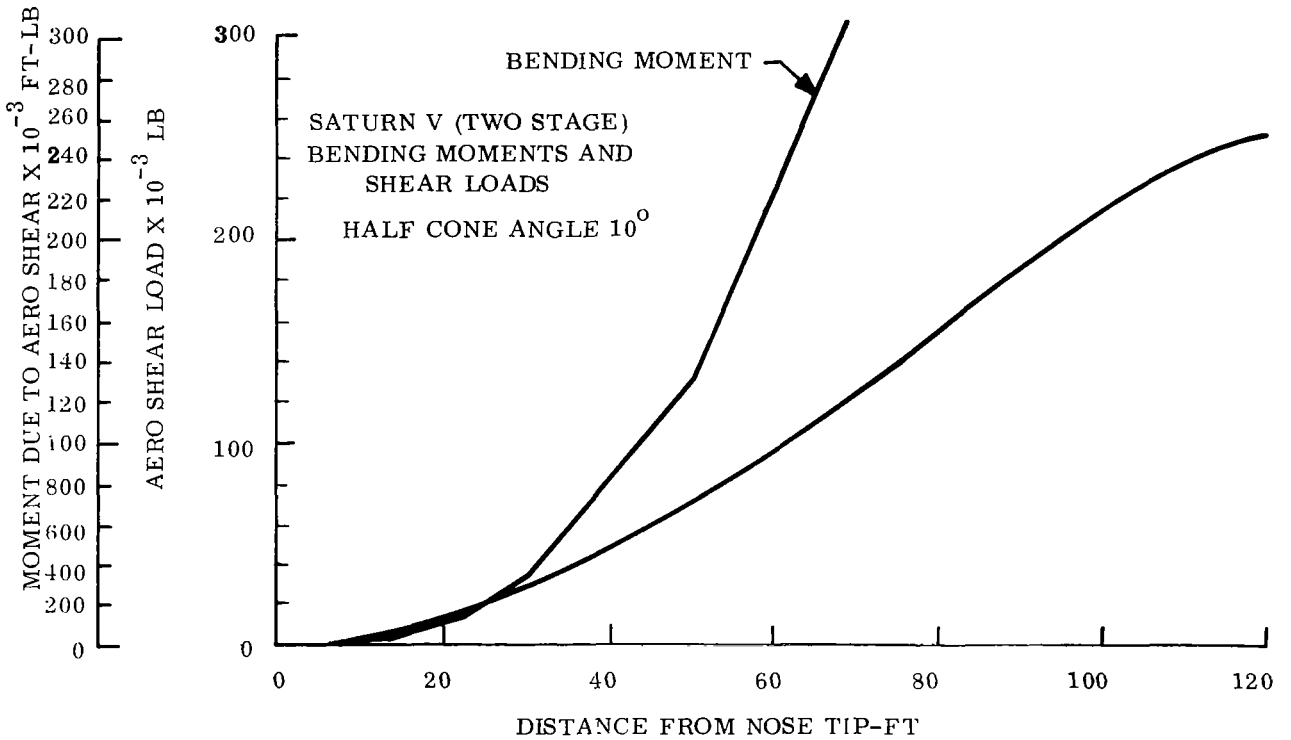
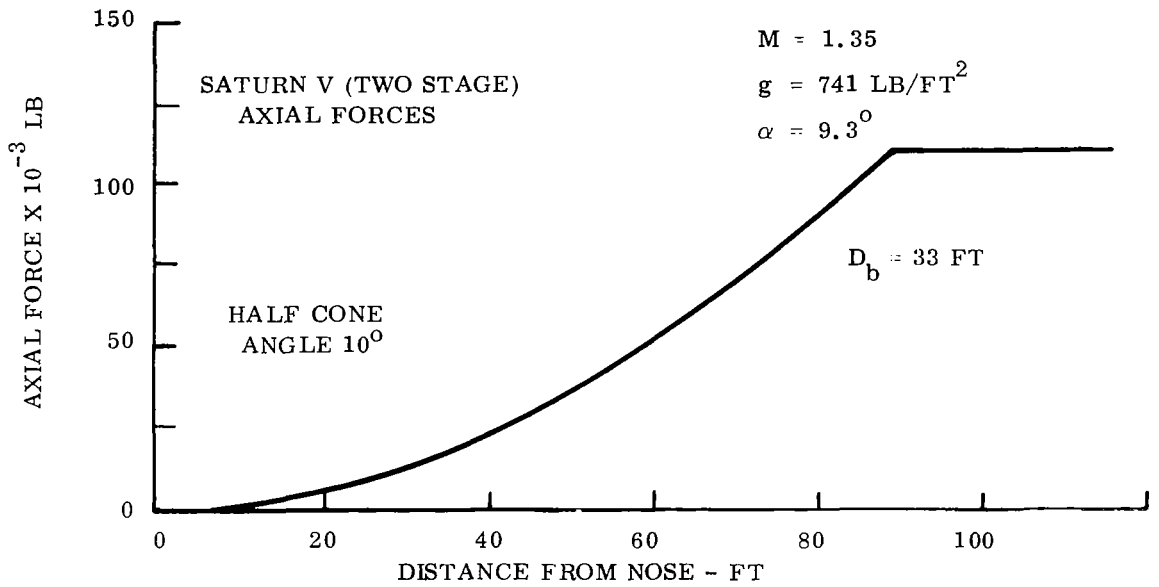


Figure 5-41. Aerodynamic Loads Imposed by Two Stage Saturn V

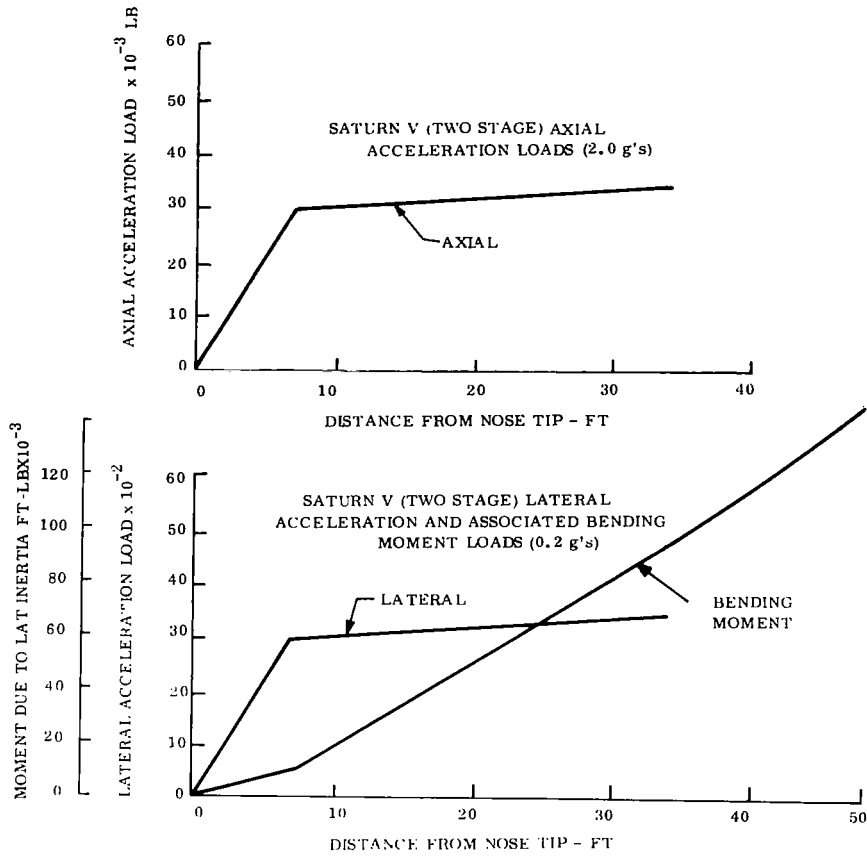


Figure 5-42. Acceleration Loads Imposed by Two Stage Saturn V

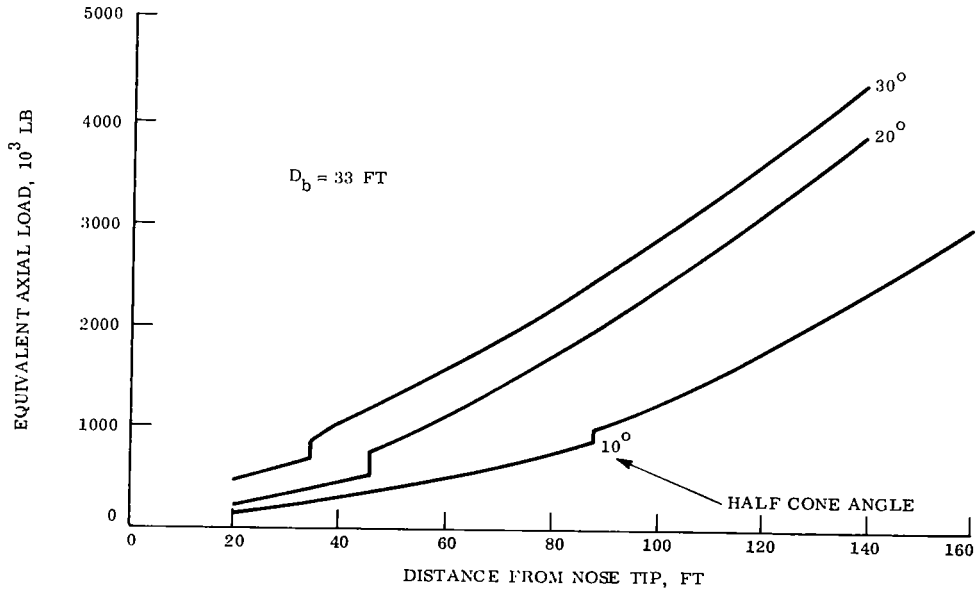


Figure 5-43. Equivalent Axial Load-Saturn V Launch Vehicle (Two Stage)

where

- $P_{c_{eq}}$ = equivalent axial load in cone
- $P_{cy_{eq}}$ = equivalent axial load on cylinder
- α = half-cone angle

5.3.4 ANALYSIS

The load carrying capability of reinforced shell type structures, such as the radiator assembly, is generally limited by structural instability. Three types of instability were examined for each radiator concept: (1) panel instability, (2) general instability and (3) local instability.

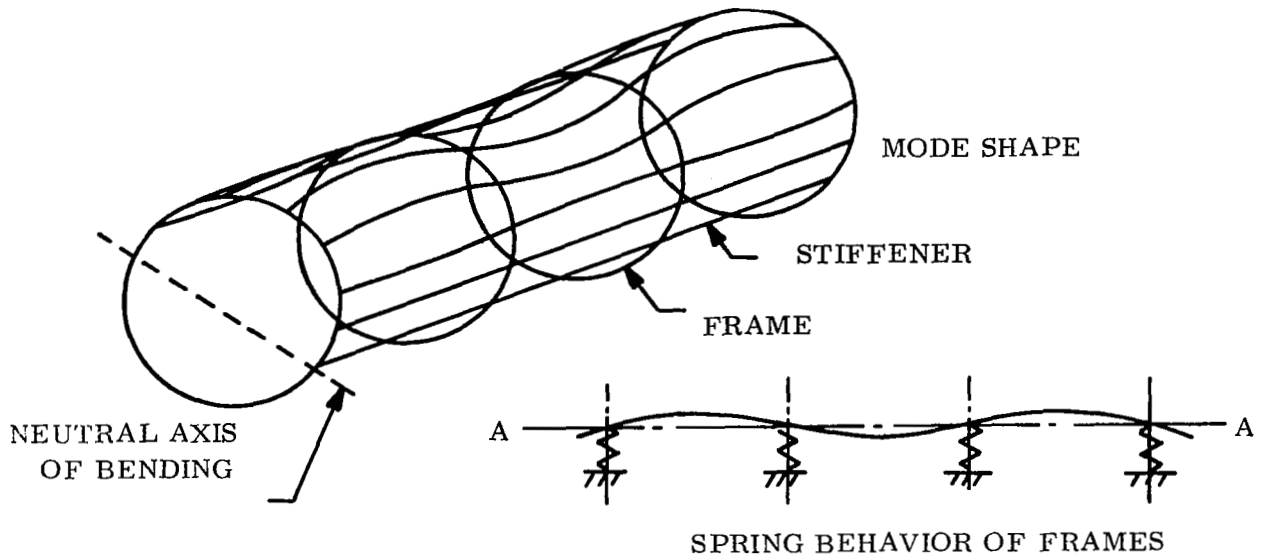
Panel instability, Figure 5-41 a, is characterized by buckling of the skin and longitudinal stiffeners between rings, which remain round. For the VCF radiator designs, the primary ducts act as longitudinal stiffeners. These are supplemented by additional longitudinal members as required. The relationship between the properties of the longitudinal stiffeners and the longitudinal load capability can be expressed

$$L_{cr} = \sqrt{\frac{\pi^2 E}{f_c}} \rho \quad (5-19)$$

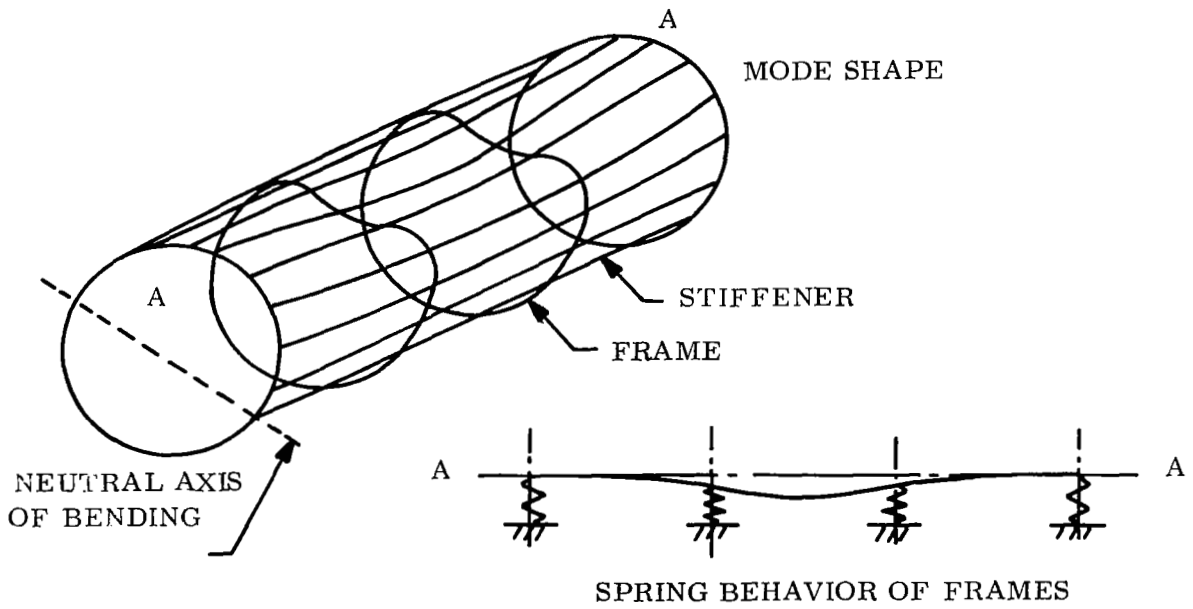
where

- L_{cr} = critical length between rings or frames
- E = modulus of elasticity of stiffener
- f_c = applied compressive stress
- ρ = radius of gyration

Therefore, knowing the equivalent axial load, P_{eq} , the applied compressive stress can be determined from the expression



A. PANEL INSTABILITY



B. GENERAL INSTABILITY

Figure 5-44. Mode Shapes for Panel and General Instability of Stiffened Cylinders in Bending

$$f_c = \frac{P_{eq}}{A_L + A_{Peff}} \quad (5-20)$$

where

A_L = area of longitudinal stiffeners

A_{Peff} = effective cross sectional area of radiator panels

Then apply Equation (5-19), the required ring or frame spacing, L_{cr} can be determined.

General instability, Figure 5-44b, is characterized by the out-of-round deflection of one or more frames or rings. This type of instability occurs when the rings or frames are not sufficiently stiff and therefore permit buckling of the longitudinal stiffeners to extend over several frames. The required stiffness of the rings or frames to prevent general instability is given by the expression

$$\bar{I}_f = C_f \frac{MD^2 d}{EL} \quad (5-21)$$

where

\bar{I}_f = required moment of inertia of frame

C_f = 6.25×10^{-5} (Reference 11)

M = applied bending moment

D = diameter of rings

d = L_{cr} - frame spacing

E = modulus of elasticity

L = total length of radiator

The third mode of failure considered is the local failure of the individual radiator panels by (1) sheet buckling such that nodes occur only at the attachment to rings and stiffeners or (2) by a number of discrete failures within each panel. The former can be evaluated from the expression:

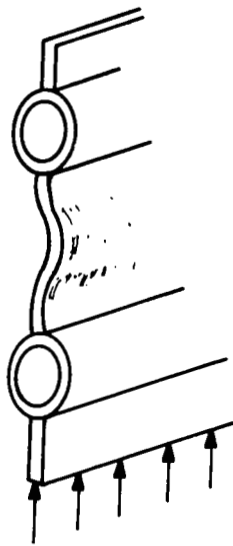
$$F_{c_{cr}} = \frac{K_c \pi^2 E}{12 (1 - \nu^2)} \left(\frac{t}{b} \right)^2 \quad (5-22)$$

where

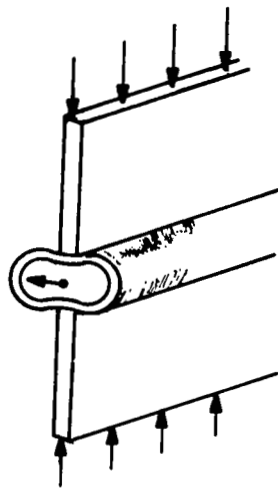
- $F_{c_{cr}}$ = critical compressive stress on panel
- K_c = coefficient given by Reference
- E = modulus of elasticity
- ν = Poisson's ratio
- t = effective thickness of radiator panel
- b = width of panel

The latter form of local failure is a function of the panel concept being investigated as illustrated in Figure 5-45.

The potential modes of local failure for Geometry 1 are tube failure or fin failure as illustrated in Figure 5-45a. The load capability for the tubes is given in Figure 5-46 as a function of wall thickness and tube diameter. The load capability for the fins is given in Figure 5-47 as a function of fin height and thickness. Since the tubes and fins carry equal loads, the optimum structural design exists when the allowable loads, P_o , as defined by both Figures 5-46 and 5-47 are equal. Therefore, for a given longitudinal load distribution, the appropriate tube and fin dimensions can be selected from Figures 5-46 and 5-47. Figure 5-47 is applicable also to Geometries 2 and 4.

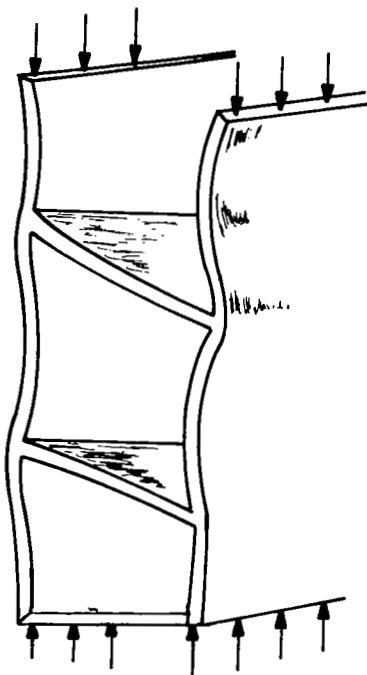


FIN BUCKLING

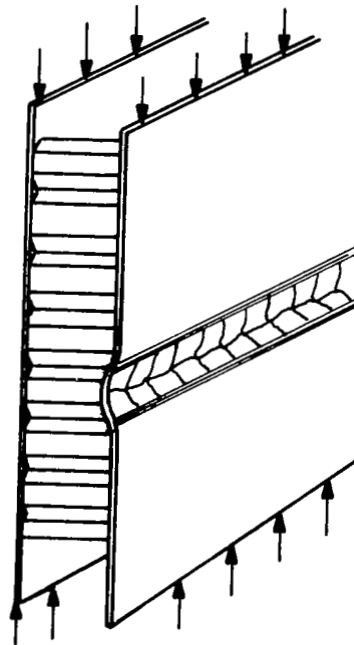


TUBE CRUSHING

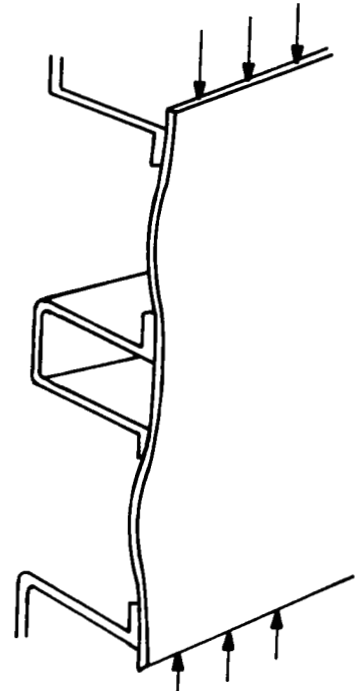
A. LOCAL FAILURE MODES FOR GEOMETRY 1



B. GEOMETRY 2
FIN BUCKLING



C. GEOMETRY 3
INTERCELL BUCKLING



D. GEOMETRY 4
FIN BUCKLING

Figure 5-45. Local Failure Modes

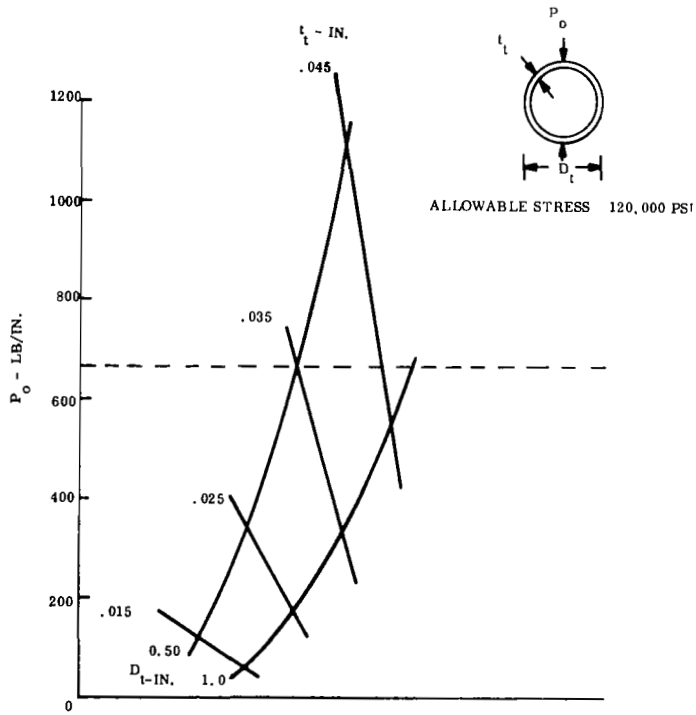


Figure 5-46. Allowable Load on Tubes

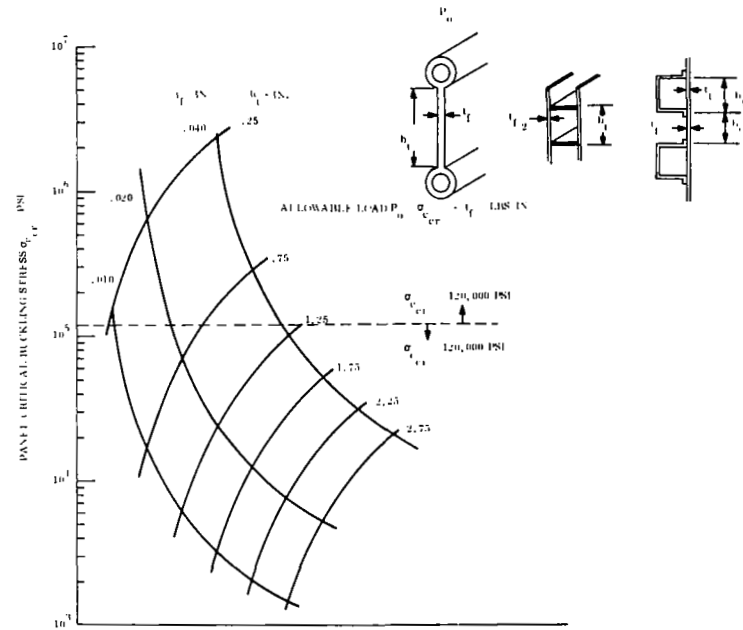


Figure 5-47. Fin Critical Buckling Stress vs. Panel Thickness Length and Size

Local failure of Geometry 3 can occur due to intercell buckling as illustrated in Figure 5-45c. This type of failure is characterized by buckling of the face sheets within the confines of individual cells. The critical stress for stainless steel face sheets is shown in Figure 5-48 as a function of cell size and face sheet thickness. The corresponding critical equivalent axial load, P_{eq} , acting on a cylindrical section of radiator is shown in Figure 5-49 as a function of the radiator diameter, the cell size and the face sheet thickness. Typical dimensions defined by thermal requirements are $S = 1.5$ inches and $t_f = 0.015$ inches. From Figure 5-48, it can be seen that the critical face sheet stress is approximately 30,000 psi compared to a yield stress of 120,000 psi or 25 percent of the maximum obtainable utilization. Figure 5-50 presents the density in pounds per square foot of radiator area as a function of the dimensions of the honeycomb panels. The core density and face sheet density is separated to permit freedom in trading off the geometric parameters. The use of Figures 5-48, 5-49 and 5-50 permit rapid preliminary evaluation of the effects of cell geometry and face sheet thickness on load carrying capability and weight.

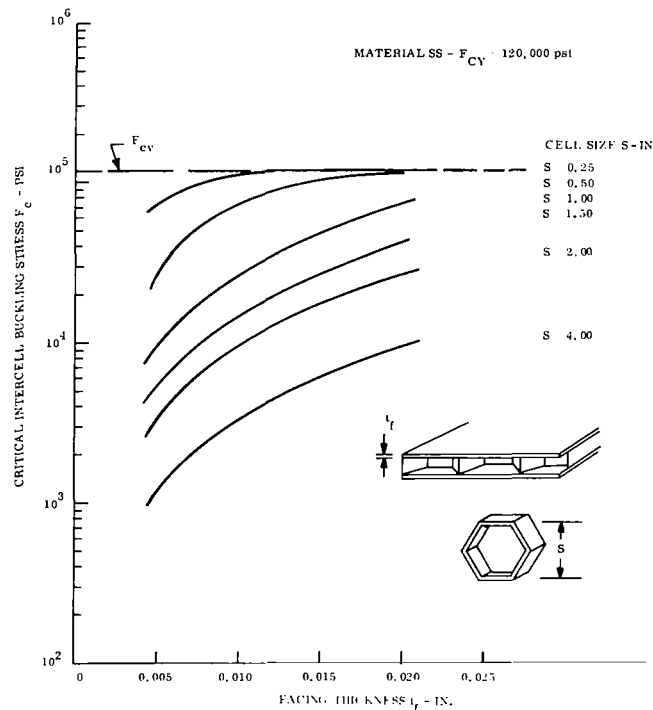


Figure 5-48. Intercell Buckling Stress vs Facing Thickness and Cell Size

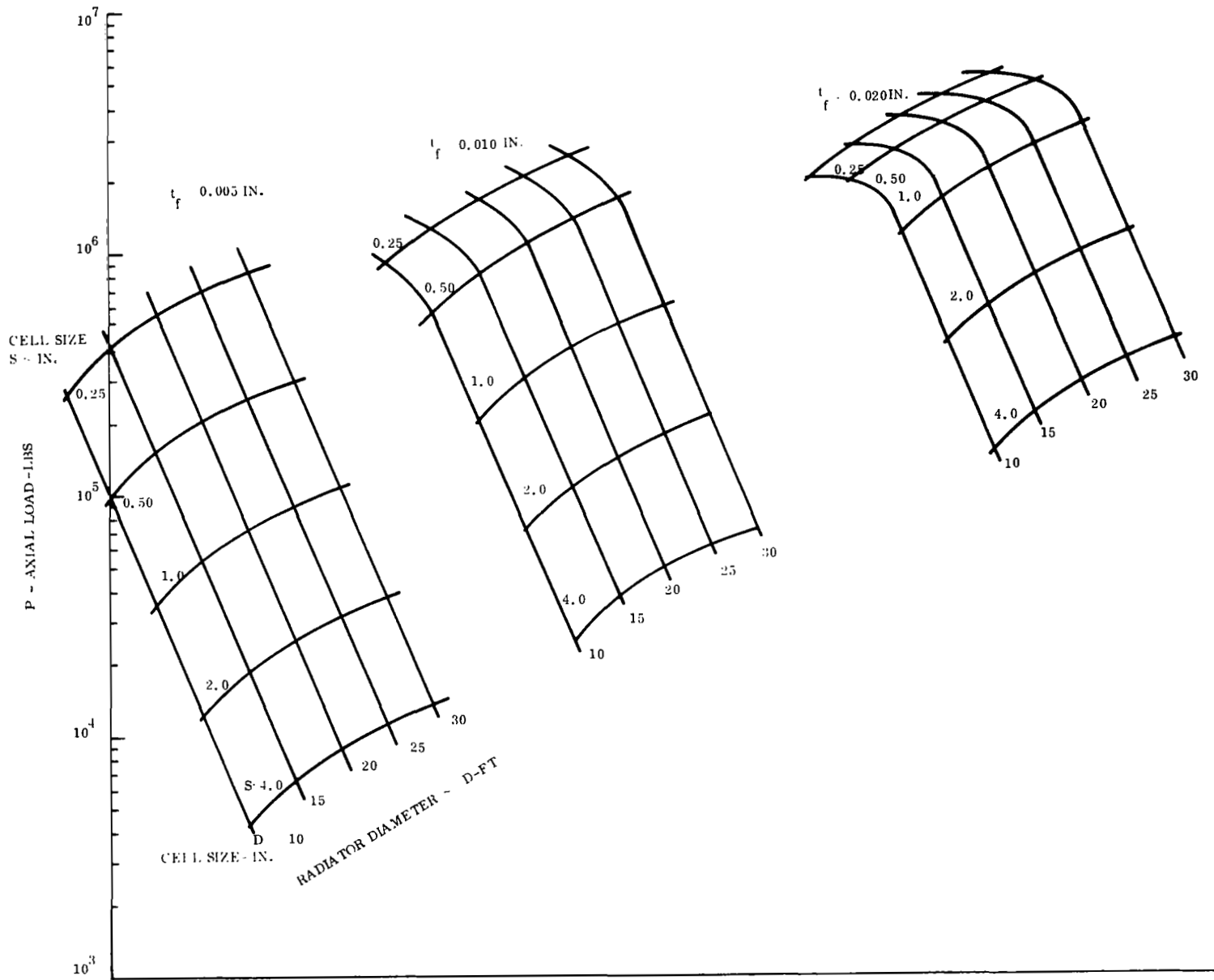


Figure 5-49. Equivalent Load to Cause Intercell Buckling

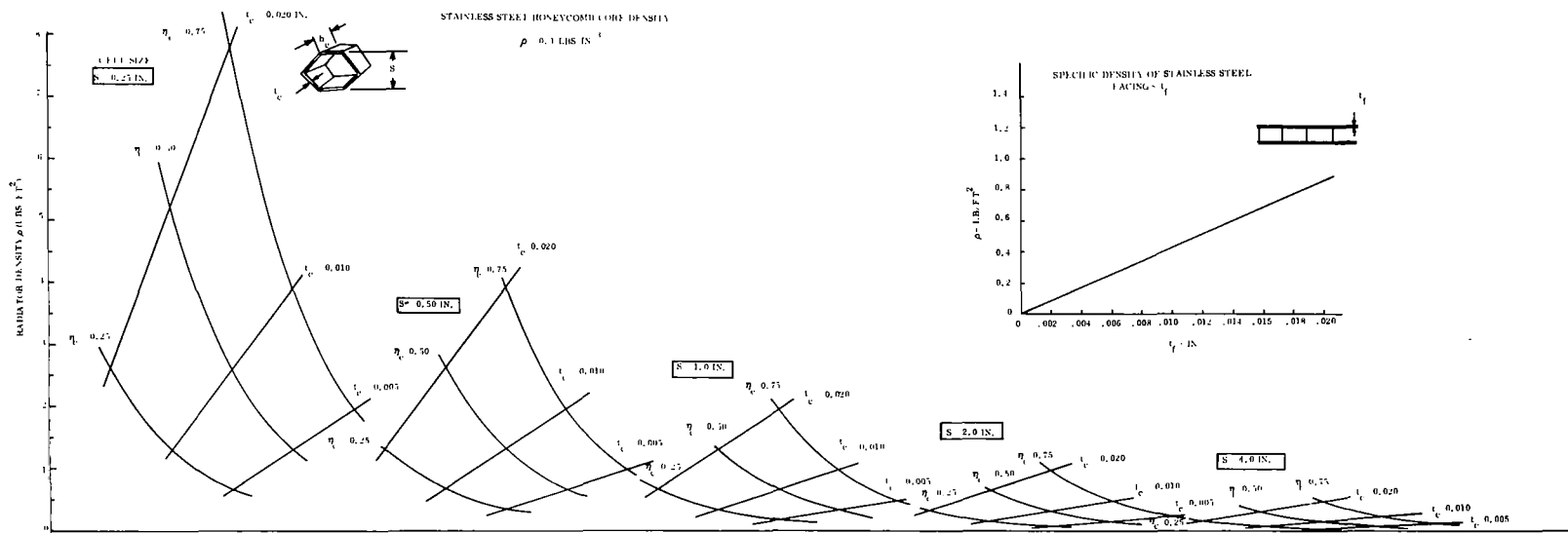


Figure 5-50. Stainless Steel Honeycomb Core Density

The load carrying capability of the individual radiator panels, having Geometries 2, 3 and 4, is adversely affected by the pressure differential existing across the face sheets during launch. This pressure differential, which exists due to the near vacuum within the chambers in the cold condition, deforms the face sheets as shown in Figure 5-51a. The loading condition of the section of face sheet covering an individual cell is shown in Figure 5-51b, where q is the differential pressure acting across the face sheet and P is the longitudinal compressive load derivable from Equation (5-17).

If the stress produced in the face sheet by the load P is denoted by f_c and if the critical buckling stress is denoted by f_{cr} , a safety factor of one for the condition $q = 0$ requires that $R_c = f_c / f_{cr} = 1$. If it is required that the sum of the applied compressive stresses must not exceed f_{cr} for the condition $q = 0$, then for a safety factor of one, $R_c + R_b = 1$, where $R_b = f_b / f_{cr}$ and f_b is the compressive stress due to the bending resulting from q . Then, for any finite value of R_b , R_c is reduced to $R_c = 1 - R_b$. The resulting relationships between R_c , R_b , t and l are shown in Figure 5-52. For example, if a reduction in load carrying capability of 60 percent is permitted due to the pressure differential, then $R_c = 0.40$ and $R_b \leq 0.60$. From Figure 5-52b, the minimum permissible face thickness, t , for a cell length, l , of 0.50 inches is approximately 0.027 inches. The significance of these curves is to illustrate the severity of the reduction in load carrying capability resulting from the pressure differential across the cell face sheets. Since the equivalent axial load, P , is fixed, additional structure is required to account for the reduction in axial load capability.

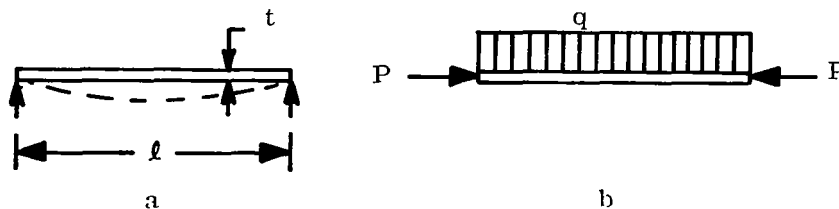


Figure 5-51. Face Sheet Loading

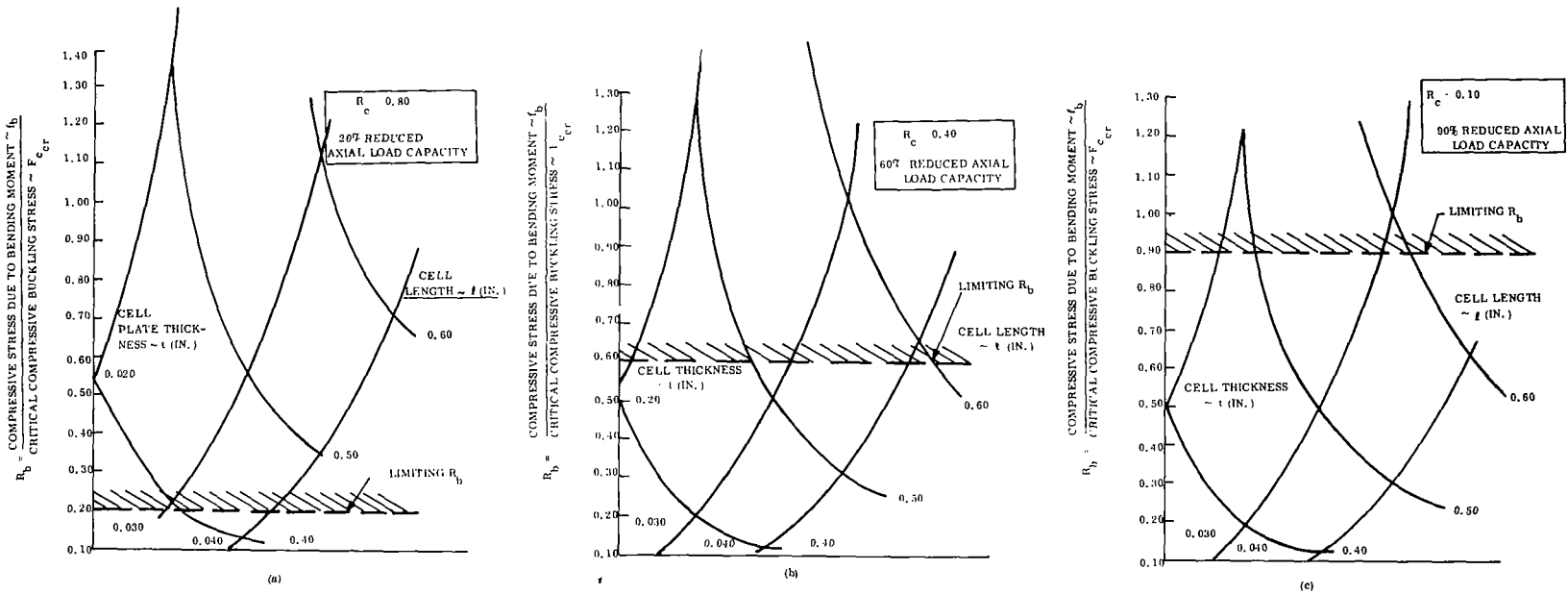


Figure 5-52. Stress Relationships of Radiator Panel Face Sheets

5.3.5 SUMMARY OF RESULTS

The results of the analyses described are summarized in terms of weight in Table 5-4 .

5.4 FABRICATION EVALUATION

5.4.1 GENERAL

A load bearing vapor chamber radiator consists of the following major elements:

1. Structural stiffening rings
2. Splice/attachment plates
3. Mounting/interface structure
4. Vapor chamber fins
5. Primary fluid ducts
6. Primary fluid headers and feed lines.

The structural and attachment members and fluid headers were not considered in this phase of the comparative evaluation since these techniques are not significantly dependent on vapor chamber geometry. Rather, a review was made of the fabrication and assembly of individual and groups of vapor chambers in conjunction with the primary fluid duct. Results were incorporated with the thermal, structural and weight evaluations performed to assist in the selection of the most desirable vapor chamber geometry for the radiator.

Ultimately the fabrication techniques required comprise a significant part of the overall cost and feasibility of the radiator. It is, therefore, considered important to select and test a vapor chamber geometry that is representative of concepts that would be employed.

Key criteria considered in the fabrication evaluation include:

Table 5-4. Summary of Radiator Structural Weights

Configuration/Geometry	Area (Ft ²)	No. of Chambers	Rings Required	Ring Weight (lbs)	Required Sheet Thickness (in.)	Sheet Weight (lbs)	Additional Structural (lbs)
(Open Ducts)							
1 10 mil fin	855	11,500	6	303	0.019	363	666
2 15 mil plates	630	9,200	4	195	0.018	166	361
1 20 mil fin	800	8,500	6	283	----	---	283
4 10 mil fins	885	8,900	6	314	0.019	375	689
4 20 mil fins	860	6,550	6	305	----	---	305
3 0.5 in. cells (0.0075 in.)	950	281,000	6	324	0.0095	155	479
(Closed Ducts)							
2 15 mil plates	750	11,100	4	232	0.018	197	429
1 10 mil fin	1000	12,800	10	560	0.018	382	942
1 20 mil fin	950	9,050	10	532	----	---	532
4 10 mil fins	990	8,950	8	436	0.023	470	906
4 20 mil fins	950	7,700	8	418	----	---	418
3 0.5 in. cells (0.0075 in.)	1370	405,000	8	464	0.011	362	826

1. Use of Stainless Steel (316 or equivalent).
2. Requirements for the fabrication and assembly of several thousand heat pipes, within reasonable time and cost constraints. Minimize complex structures.
3. Repetitive reliability in fabrication and assembly processes consistent with life-time and thermal requirements.
4. Incorporation of wicks in each heat pipe required.
5. Cleanliness of fabrication, charging of liquid metals and individual sealing of each pipe must be achieved.
6. Material joining techniques must be consistent with known and established procedures, near state-of-art fabrication technology assumed.
7. Vapor chambers must be compatible with primary fluid ducts.

5.4.2 FABRICATION TECHNIQUES

The geometrics lend themselves to one or more manufacturing processes largely dependent on the design characteristics of the vapor chamber. Manufacturing processes considered most appropriate are listed in Figure 5-53.

5.4.2.1 Sheet Metal Rolled and Welded

Pipe and tubular vapor chambers can be made by either butt welding or piercing, the latter being a seamless process. Heated strips of stainless steel which have edges beveled slightly are used so that they will meet accurately when formed in a circular shape. As the strip is pulled through the welding bell, the circular shape is formed and the edges are welded together. A final operation can pass the pipe through shaping and finishing rolls to give correct size (circular or elliptical).

5.4.2.2 Special Welding (Electron Beam and TIG)

Electron Beam or Tungsten Inert Gas (TIG) welding techniques afford a method of obtaining coalescence of materials within controlled environments. In the TIG technique, shielding of the weld joint is obtained from an inert gas such as helium or argon. Tungsten electrodes are usually used because of their high melting point and virtually nonconsumable nature.

GEOMETRY FABRICATION CANDIDATE	1	2	3	4
SHEET METAL/ROLLED/ WELDED	✓	✓	✓	✓
SPECIAL WELDING ELECTRON BEAM - TIG)		✓	✓	
BRAZING		✓	✓	✓
EXTRUSION	✓	✓		✓
DIFFUSION BONDING	✓	✓	✓	✓

Figure 5-53. Fabrication Processes for Vapor Chamber Geometries

Manual open welding can be accomplished with the use of inert gas jets. Horizontal and vertical welding chambers are available which provide an ultrahigh purity helium atmosphere and capable of handling hardware of several feet in diameter or length. Electron beam welding is performed in a specially designed vacuum chamber with remote welding capability. Essentially no foreign material is interjected into the weld to provide an extremely high purity noncontaminated weld joint. Since electron beam welding must be done under a vacuum, part size is more restrictive than that of TIG welding. Electron beam and TIG welds are considered well suited for heat pipe fabrication due to their relatively clean weld capability.

5.4.2.3 Brazing

Brazing affords a relatively low cost method of joining, particularly if several similar surfaces can be joined in a single application. Brazing involves the use of a nonferrous filler material applied between two closely fitting surfaces. The filler material, melted at a lower temperature (above 800⁰F) than the base material, is generally distributed by

capillary action. For a satisfactorily brazed joint, it is essential that the liquidous (melting) temperature of the filler material is reached and metal wet, or alloy, with the metal surfaces on which it is applied. The brazing temperature must be above the operating temperature of the part. Some of the advantages attributed to brazing are as follows:

1. The completed joint requires little or no finishing
2. The relatively low temperature at which the joint is made minimizes distortion
3. There is no flash or weld spatter
4. Brazing techniques do not require as much skill as the technique for electron beam and TIG welding
5. The process can be easily mechanized
6. The process is economical.

Disadvantages which must be considered when selecting joining methods are:

1. If the joint is to be exposed to corrosive media, the filler metal used must have the required corrosion resistance
2. All of the brazing alloys lose strength at elevated temperatures requiring careful selection and application of the brazing alloy.

Brazing is especially suited for relatively large surface area joints where good heat transfer is required or where configurations permit the joining of many surfaces in a single operation.

5.4.2.4 Extrusion

Many of the heat pipe configurations lend themselves to extrusion techniques, particularly shapes approaching circular or elliptical tubes. The principles of extrusion, similar to the act of squirting toothpaste from a tube, has long been utilized for a variety of materials and shapes. The extrusion of stainless steel must be done at elevated temperatures ($\sim 2400^{\circ}\text{F}$). Several limitations applicable to the extrusion of heat pipes are worthy of note.

Extrusion of nonuniform surfaces and thicknesses can cause part warpage especially where considerable lengths are involved. Extrusions of small diameter (< 3/8 inch) stainless steel tubes with wall thicknesses of 50 mils or less is difficult because of the inability to maintain close tolerances.

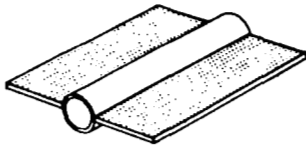
5.4.2.5 Diffusion Bonding

Diffusion bonding is one of the more recent and effective methods of attachment. The principle of the bonding mechanism is the use of a prescribed pressure and metal to metal contact at the proper temperature-time relationship to achieve a metallurgical bond. The actual bond of the materials is caused by the migration of atoms across the interface at sufficiently high temperatures to reduce the time required, and grain growth without recrystallization. Temperatures associated with stainless steel bonds are approximately 2000^oF. Interstitial materials such as nickel are sometimes added to increase diffusion and uniformity of the surface. Methods of applying pressure to the surfaces and size limitations of autoclave or similar type furnaces are constraints which must be considered before design or selection of a fabrication technique can be made. Due to the requirements for rather unique fixtures and facilities, the diffusion bonding technique is considered a relatively costly process but provides a very suitable method for the bonding of certain parts.

5.4.2.6 Vapor Chamber Geometry Fabrication Evaluation Results

A degree of fabrication difficulty comparison was made of each concept which was subsequently used in the overall evaluation which included thermal, integration, structural and fabrication considerations. Results of the fabrication evaluation for each of the four general concepts are contained in Figures 5-54 through 5-57. Geometry 2 was judged to be more difficult than Geometry 1 due to end closures and wall joining techniques. Brazes required may give somewhat lower reliability than welds.

Of the four basic geometries considered, the number of individual vapor chambers required for the complete radiator were calculated to range from less than 7000 for Geometry 4 to over 400,000 for Geometry 3.

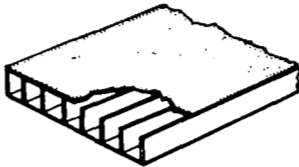


CANDIDATES: SHEET METAL/ROLLED/WELD
EXTRUSION
DIFFUSION BONDING

RATING

SHEET METAL/ ROLLED/WELD	<ul style="list-style-type: none"> WELDING OF 0.015 INCH MATERIAL NOT AS RELIABLE AS DESIRED WHERE COMPLETE TUBE SEALING IS MANDATORY. END CAP FABRICATION CONSIDERED RELATIVELY EASY 		3
EXTRUSION	<ul style="list-style-type: none"> EXTRUSION OF TUBE AND LIP IS A LIKELY CANDIDATE BUT OVERALL SURFACE TOLERANCES ARE DIFFICULT TO MAINTAIN. FIN WELDED TO LIP PROVIDES GOOD SEAL. END CAP FABRICATION CONSIDERED RELATIVELY EASY 		1
DIFFUSION BONDING	<ul style="list-style-type: none"> DIFFUSION BONDING PROVIDES CAPABILITY OF FORMING CHAMBER/FIN IN ONE PIECE PROVIDES GOOD SEAL COSTS ARE HIGH (FABRICATION DIFFICULT) END CAP SEALING MORE DIFFICULT 		2

Figure 5-54. Geometry 1 Fabrication Techniques



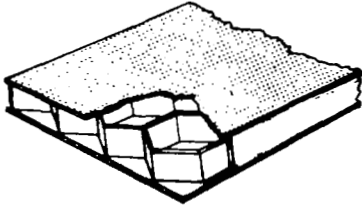
CANDIDATES: SHEET METAL/BRAZING
SHEET METAL/WELDING
DIFFUSION BONDING
EXTRUSION

RATING

SHEET METAL/ BRAZING	<ul style="list-style-type: none"> SUITABLE METHOD IF FLANGES ARE PROVIDED OR CORRUGATED CONCEPT IS EMPLOYED END CAP WELD IS DIFFICULT CONFIGURATION WITHOUT FLANGE IS CONSIDERED DIFFICULT 		1
SHEET METAL/ WELDING	<ul style="list-style-type: none"> WELDING CONSIDERED MORE DIFFICULT THAN BRAZING DUE TO PROJECT REQUIREMENTS AND SMALL SURFACES, BUT MAY PROVIDE BETTER SEALING END CAP WELD IS DIFFICULT CONFIGURATION WITHOUT FLANGE IS DIFFICULT 	<p>SAME AS ABOVE BUT WELDS</p>	1
DIFFUSION BONDING	<ul style="list-style-type: none"> USE OF BOXES AND SHEETS CONSIDERED FEASIBLE MAINTENANCE OF METAL THICKNESS/WEIGHT MAY BE MORE DIFFICULT END CAP CONSIDERED DIFFICULT 		2
EXTRUSION	<ul style="list-style-type: none"> CONSIDERED DIFFICULT AND NOT PRACTICAL WITH PRESENT TECHNOLOGY 		3

Figure 5-55. Geometry 2 Fabrication Techniques

CANDIDATES: SHEET METAL/BRAZING/ELECTRON
BEAM WELD DIFFUSION BONDING



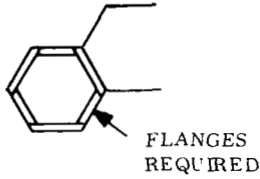
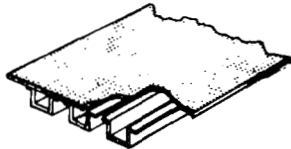
<p>SHEET METAL BRAZING ELECTRON BEAM WELD</p>	<p>INDIVIDUAL HONEYCOMBS ELECTRON BEAM WELDED BRAZING OR WELDING OF COMB TO SHEETS REQUIRE FLANGES OR TABS TO PROVIDE SEALING, CONSIDERED VERY DIFFICULT WICKING, CHARGING AND SEALING VERY DIFFICULT</p>	 <p>FLANGES REQUIRED</p>	<p>1</p>
<p>DIFFUSION BONDING</p>	<p>SIMILAR TECHNIQUES VERY DIFFICULT FABRICATION HIGH COST WICKING. CHARGING AND SEALING VERY DIFFICULT</p>		<p>2</p>

Figure 5-56. Geometry 3 Fabrication Techniques



CANDIDATES: SHEET METAL BRAZING
SHEET METAL WELDING
EXTRUSION
DIFFUSION BONDING

RATING


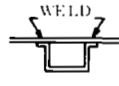


<p>SHEET METAL BRAZING</p>	<ul style="list-style-type: none"> • SUITABLE METHOD WITH FLANGES AFFORDING A SINGLE BRAZE • END CAPS AND WICKING MORE DIFFICULT THAN CONFIGURATION 1 • WICK CAN BE SPOT WELDED 		<p>1</p>
<p>SHEET METAL WELDING</p>	<ul style="list-style-type: none"> • SUITABLE METHOD CONSIDERED TO BE ESSENTIALLY EQUAL TO BRAZING • END CAPS AND WICKING MORE DIFFICULT THAN CONFIGURATION 1 		<p>1</p>
<p>EXTRUSION</p>	<ul style="list-style-type: none"> • EXTRUSION CONSIDERED FEASIBLE BUT TOLERANCE AND STRAIGHTNESS PROBLEMS ARE EXPECTED • END CAPS DIFFICULT (WELD) 		<p>2</p>
<p>DIFFUSION BONDING</p>	<ul style="list-style-type: none"> • CONSIDERED FEASIBLE BUT COSTS MAY BE PROHIBITIVE • OFF WEIGHT OPTIMUM • END CAPS DIFFICULT (WELD) 		<p>2</p>

Figure 5-57. Geometry 4 Fabrication Techniques

5.5 VAPOR CHAMBER FIN DESIGN CONCLUSIONS

From the analysis presented, Geometry 2 using a closed nonpenetrated duct was selected as the optimum VCF configuration. This decision was based on a combination of factors including thermal performances, radiator weight, integration with primary duct, structural weight and ease of fabrication. Figure 5-58 summarizes the evaluation results.

Total radiator weights for each radiator concept are provided in Table 5-5. In general, the open penetrated primary fluid duct provided a lighter weight system than the completely enclosed nonpenetrated configuration. However, the overall radiator weights of Geometries 1, 2 and 4 did not vary that greatly. The 0.010 inch thick fin cases for Geometries 1 and 4 required excessive structural members which lessened their attractiveness. The honeycomb configuration was considerably heavier, largely as a result of its lower effective radiating temperature. The large number of individual chambers in this design is another deterrent to its selection.

Sodium was chosen as the working fluid because of its superior performance over the entire radiator temperature range. The results of the fluid analysis, obtained with the HPIPE computer code, for Geometry 1 are provided in Figure 5-59. Cesium was the poorest fluid by a wide margin; in fact, with a 0.5 inch pipe diameter, the only operating region possible was in the vicinity of 1100^oF. At higher temperatures the surface tension of cesium was inadequate to provide the capillary pumping, while at temperatures below 1100^oF a lower vapor density, coupled with the low surface tension made it impossible to satisfy the pressure balance. Although potassium exhibited satisfactory performance, the higher conductivity, latent heat of vaporization and surface tension of sodium results in lower weights for these cases.

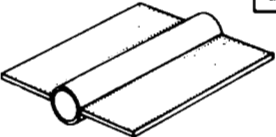
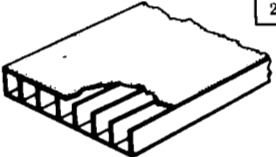
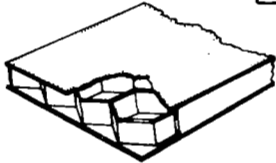

GEOMETRY	THERMAL	INTEGRATION	STRUCTURAL	FABRICATION	RECOMMENDED
	<p>1</p> <p>HIGH RATIO OF FLOW AREA TO HEAT PIPE CIRCUMFERENCE MINIMUM WEIGHT</p>	<p>3</p> <p>MORE DIFFICULT THAN GEOMETRY ② AND ③ BUT AN ACCEPTED RADIATOR GEOMETRY</p>	<p>3</p> <p>LOW LOAD AREA AND SMALLER PRIMARY DUCT RADIUS OF GYRATIONS CAUSE LOCAL AND PANEL INSTABILITIES</p>	<p>1</p> <p>CONSIDERED ON A PAR WITH ④ IF EXTRUSION IS USED</p>	
	<p>2</p> <p>HIGH EFFECTIVE RADIATOR TEMPERATURE GOOD EVAPORATOR INTERFACE MINIMUM RADIATOR AREA</p>	<p>1</p> <p>PROVIDES TWO FLAT SURFACES FOR GOOD ATTACHMENT WITH PRIMARY DUCT AND SPLICE PLATES</p>	<p>1</p> <p>THERMALLY DEFINED GEOMETRY MORE CLOSELY MEETS LOCAL AND PANEL STABILITY REQUIREMENTS MINIMUM STRUCTURAL WEIGHT.</p>	<p>2</p> <p>SOMEWHAT MORE DIFFICULT THAN ① OR ④ BUT USE OF FLANGES PERMITS GOOD BRAZE OR WELD.</p>	✓
	<p>3</p> <p>GOOD EVAPORATOR INTERFACE POOR HEAT TRANSFER</p>	<p>3</p> <p>PROVIDES TWO FLAT SURFACES FOR GOOD ATTACHMENT TO PRIMARY DUCT AND SPLICE PLATES, HOWEVER PRESENTS POOR EVAPORATOR SURFACE AREA</p>	<p>1</p> <p>GOOD STRUCTURE BUT INCREASED RADIATOR AREA REQUIREMENTS NECESSITATE LARGER BAYS .∴. THUS INCREASE PANEL INSTABILITY</p>	<p>3</p> <p>CONSIDERED VERY DIFFICULT IN THE CHARGING AND SEALING OF CHAMBERS</p>	
	<p>4</p> <p>GOOD METEOROID RESISTANCE AREA COMPARABLE TO ① HIGHER WEIGHT</p>	<p>2</p> <p>ONE FLAT SURFACE. RATHER DIFFICULT PENETRATED DUCT ARRANGEMENT</p>	<p>3</p> <p>LOW LOAD AREA AND SMALL PRIMARY DUCT RADIUS OF GYRATION CAUSE LOCAL AND PANEL INSTABILITIES</p>	<p>2</p> <p>CONSIDERED TO BE SIMPLE TO FABRICATE BY WELDING OR BRAZING</p>	

Figure 5-58. Vapor Chamber Geometry Evaluation Summary

Table 5-5. Summary of Radiator Weights

Geometry	Thermal Evaluation			Structural Evaluation					Total Weight (LB)
	Area ² (ft ²)	No. of Chambers	Radiator Weight (LB)	Rings Required	Ring Weight (LB)	Required Sheet Thickness (IN)	Sheet Weight (LB)	Structural Weight (LB)	
(Nonpenetrated Ducts)									
2 15 mil plates	750	11, 100	1520	4	232	0. 018	197	429	1949
1 20 mil fins	950	9050	1950	10	532	---	---	532	2482
4 20 mil fins	950	7700	2075	8	418	---	---	418	2493
1 10 mil fins	1000	12, 800	1800	10	560	0. 018	382	942	2742
4 10 mil fins	990	8950	1980	8	436	0. 023	470	906	2886
3 0. 5 inch cell (. 0075 inch)	1370	405, 000	2850	8	464	0. 011	362	826	3676
(Penetrated Ducts)									
1 20 mil fins	800	8500	1700	6	283	---	---	283	1983
2 15 mil plates	630	9200	1670	4	195	0. 018	166	361	2031
4 20 mil fins	860	6550	1850	6	305	---	---	305	2155
1 10 mil fins	855	11, 500	1510	6	303	0. 019	363	666	2176
4 10 mil fins	885	8900	1710	6	314	0. 019	375	689	2399
3 0. 5 inch cell (. 0075 inch)	950	281, 000	2500	6	324	0. 0095	155	479	2979

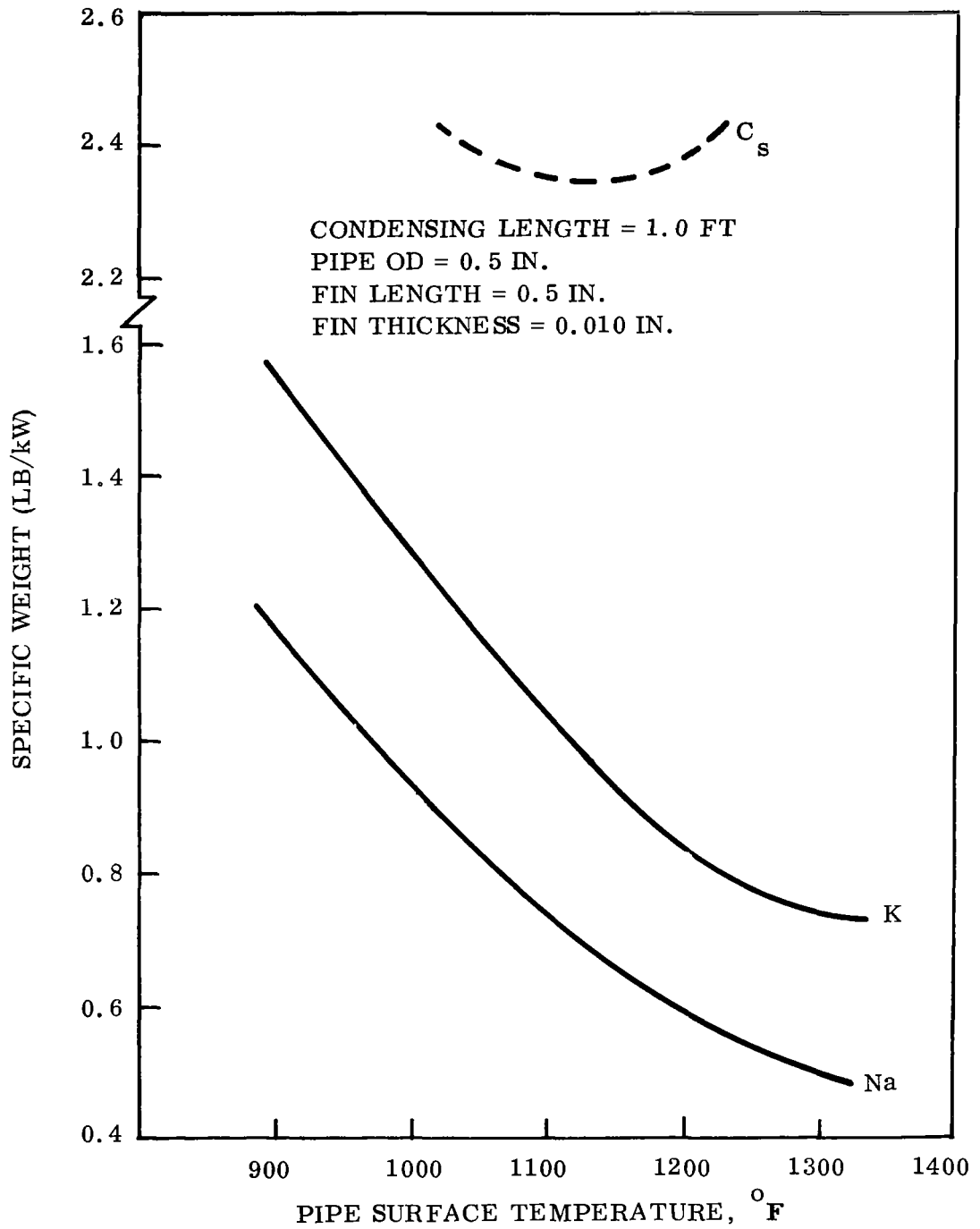


Figure 5-59. Fluid Comparison Finned Cylinder Geometry 1

SECTION 6
VAPOR CHAMBER (HEAT PIPE) TEST PROGRAM

6.1 TEST OBJECTIVES AND REQUIREMENTS

The objective of the vapor chamber test was to obtain accurate performance data on the selected concept (geometry 2) in order to substantiate the analytical predictions obtained from the HPIPE computer code and to provide data for the preliminary design of the vapor chamber fin radiator. The primary areas of concern were:

1. The magnitude of the evaporative and condensing temperature drops as a function of the vapor chamber heat rejection rate
2. The determination of the axial vapor temperature drop as a function of the heat rejection rate
3. The pumping capability of the sodium within the wick.

Limiting evaporative heat flux limits were also to be measured. Test requirements associated with these objectives are listed in Table 6-1.

Table 6-1. General Test Requirements

Data	Obtain sound engineering performance and design data to be substantiated by an error analysis.
Temperature Range	Test program vapor chamber operating temperature ranges 900 ^o to 1300 ^o F.
Test Accuracy	Measurement of evaporating and condensing ΔT to $\pm 1^{\circ}$ F. Measurement of heat fluxes within ± 10 percent.
Test Increments	Operating temperatures, 900 ^o -1000 ^o -1100 ^o -1200 ^o -1300 ^o F. Heat flux levels, 5000-10,000-20,000-30,000-40,000-80,000 Btu/Hr-Ft ² .
Test Orientation	Normal operation - horizontal Pumping test 0 ^o to 30 ^o \pm 1 ^o Tilt

6.2 TEST APPROACH

The major consideration in the design of the test was the precise measurement of temperatures and heat fluxes. Consequently, the entire test design reflected these goals. A detailed test plan was prepared and is included as reference material in the appendix.

6.2.1 VAPOR CHAMBER ORIENTATION

Of primary importance as the orientation of the vapor chamber fin with respect to the heat input and heat rejection environment. Utilizing the selected geometry and primary duct arrangement on a spacecraft, the heat input section of the vapor chamber fin is on the side opposing the heat rejection surface; this is illustrated in Figure 6-1. In a zero g environment there are no forces perpendicular to the return flow path to aid in the refluxing of the sodium. However, location of the evaporator and condenser surfaces on opposite sides in an earth test introduces a gravitational force which could aid in returning the liquid to the evaporator. Although the gravitational force is small in comparison to the capillary forces available, it was decided to place the heat input and output sections on the same surface of the pipe as shown in Figure 6-2. This configuration removes the effect of gravity on the test results and presents a physical situation more typical of heat pipe applications.

6.2.2 TEST VAPOR CHAMBER DESIGN AND FABRICATION

The prime vapor chamber (heat pipe) design specifications were obtained from results of the vapor chamber analysis described in Section 5.1. Emphasis was placed on attaining a configuration which closely corresponds with projected space radiator design. A design sketch of the heat pipe is shown in Figure 6-3.

A composite wick design was utilized in order to maintain operation at high evaporative heat flux levels. The interior of the heat input surface was covered with five layers of fine screen which results in a large capillary pumping capability. Specifications of the evaporator wick were five layers of 200 by 200 304 stainless steel mesh with a 0.0022 inch wire diameter. The layers were spot welded to the vapor chamber to form a tight, uniform matrix.

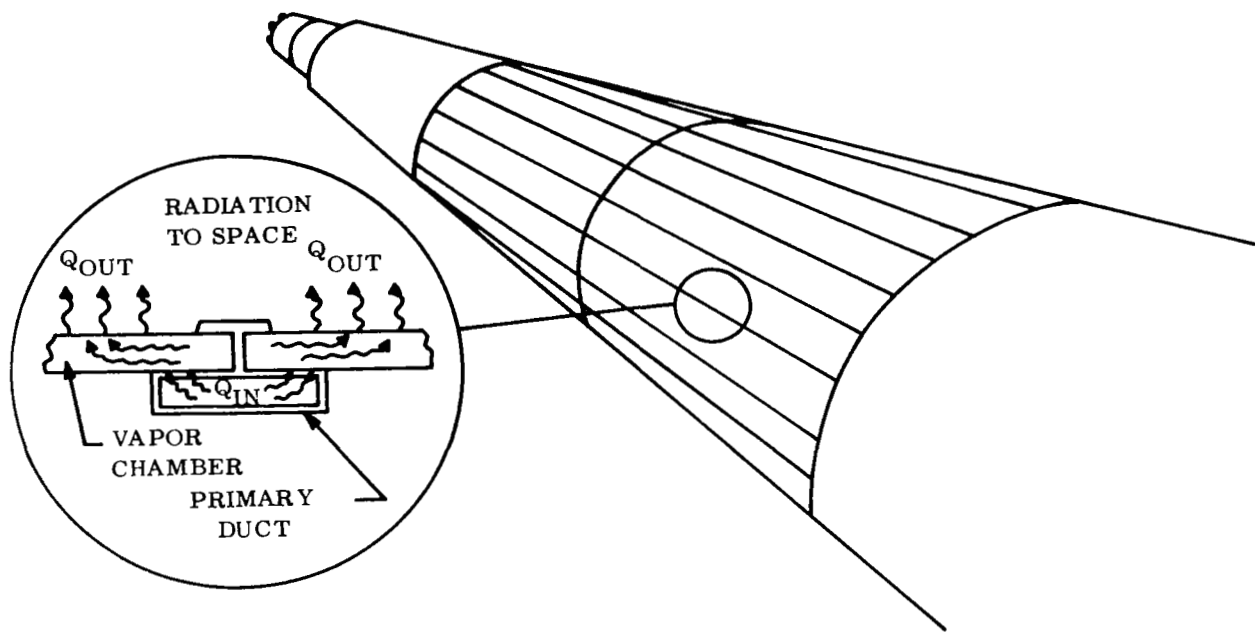


Figure 6-1. Vapor Chamber Thermal Orientation on Spacecraft

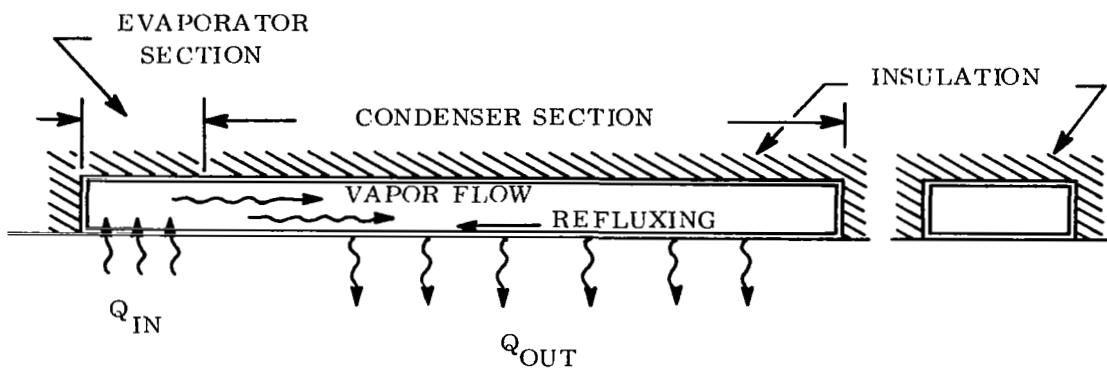


Figure 6-2. Vapor Chamber Test Orientation

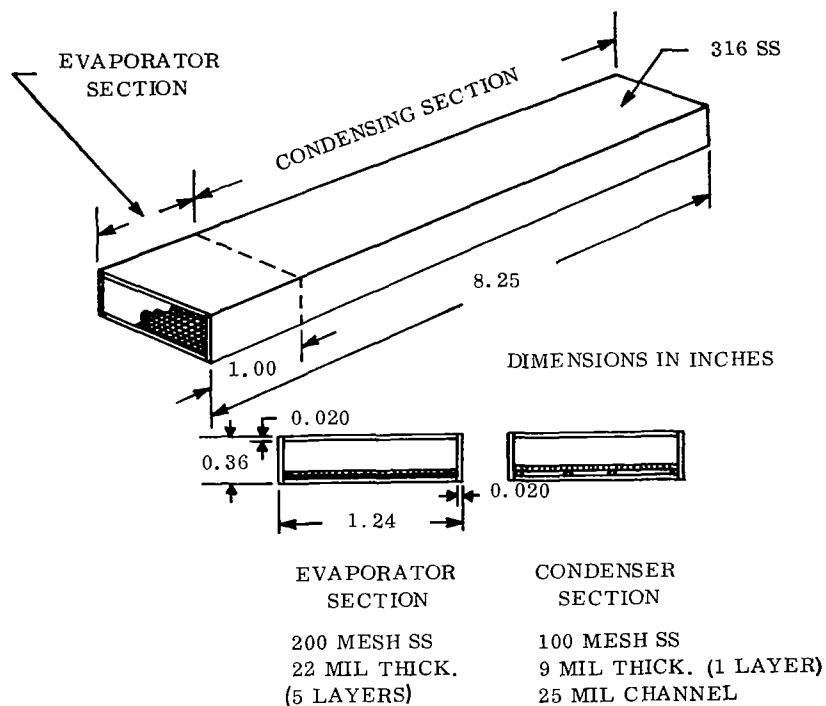


Figure 6-3. Vapor Chamber (Heat Pipe) Design

The condenser fluid return annulus was formed by four 0.025 inch diameter 308 SS wires which were placed axially along the VCF. A single layer of 100 by 100 mesh 304 stainless steel screen, having a 0.0045 inch wire diameter, was stretched across the wires in order to complete the return fluid passage.

Heat pipe enclosures were fabricated from 316 stainless steel. The disassembled heat pipe is shown in Figure 6-4. A closeup view of the evaporator and condensing wick interface area is shown in Figure 6-5.

The calculated void volume below the wick surface was determined to be 3.73 cc. A check of the liquid volume of the wick and annulus was made by dropping distilled water on the wick surface. Good wetting behavior was observed in both the condenser and evaporator wick. The volume required to fill the wick was determined to be approximately 4 cc. The liquid sodium fluid inventory of the prime heat pipe was 7.95 cc. Sodium was filled under a vacuum

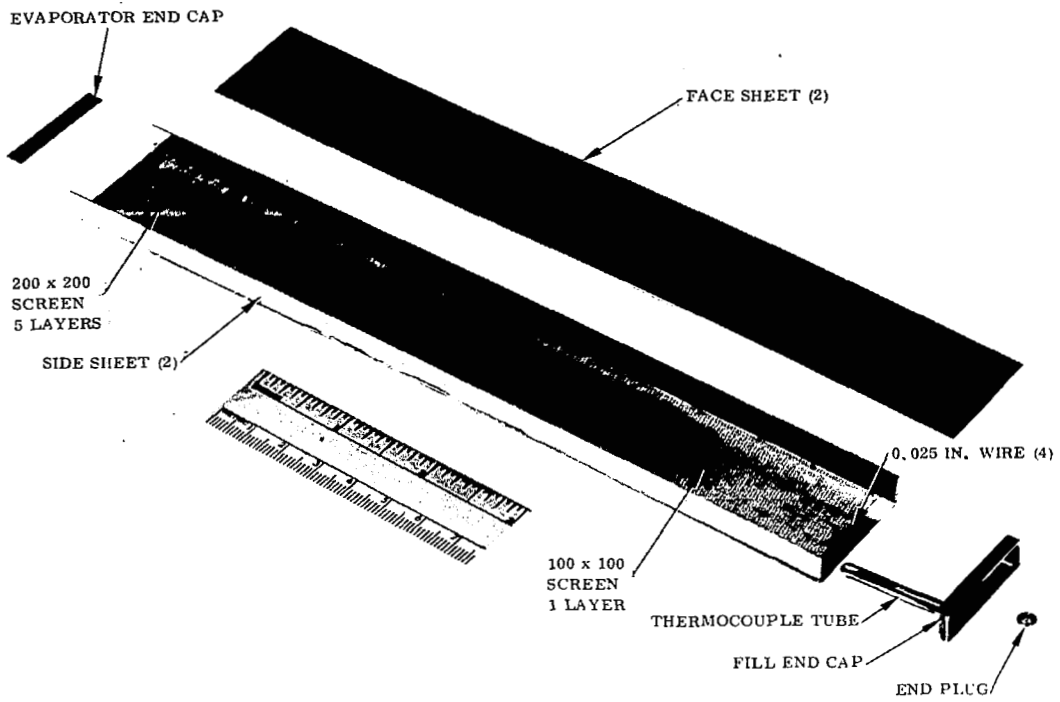


Figure 6-4. Disassembled Vapor Chamber (Heat Pipe)

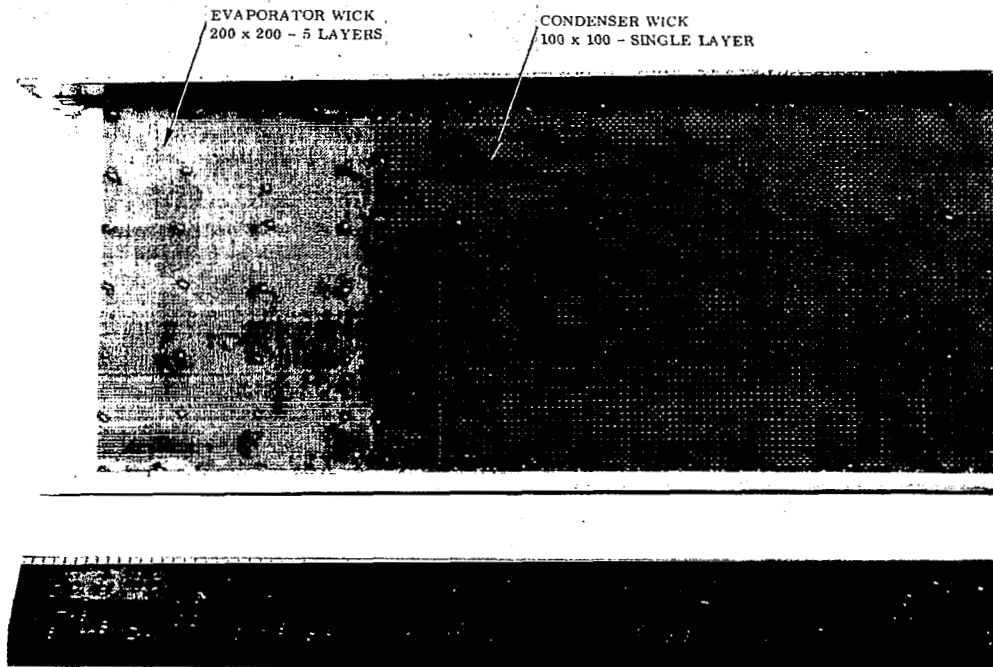


Figure 6-5. Closeup View of Vapor Chamber Wick

of 10^{-5} torr or less and the end plug was inserted and electron beam welded to the end cap in the same facility.

The completed heat pipe assembly is shown in Figure 6-6. The pipe was coated with a high emissivity iron titanate coating prior to test.

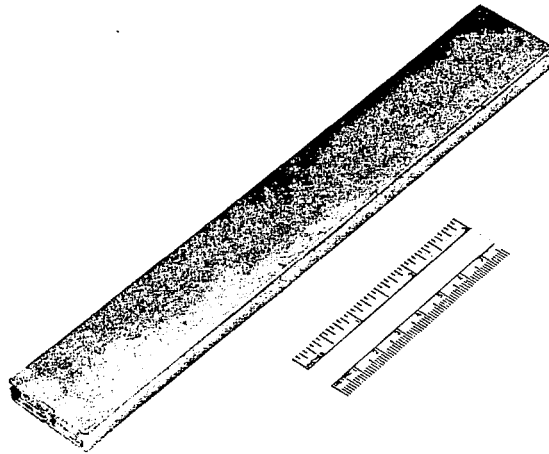


Figure 6-6. Assembled Vapor Chamber

6.2.3 HEATER AND CALORIMETER DESIGN AND FABRICATION

Consideration was given to having all four sides of the vapor chamber evaporator receive and accept heat. This alternative required a more complicated test fixture and excessive heat input capability and may not conform as closely to operational configurations. Consequently, heat input from a single side was selected.

The results of Section 5.1 indicated that heat input fluxes on the order of 75,000 Btu/Hr-ft² are required for an optimized vapor chamber fin radiator. This high power density limited the choice of a heat source to only a few possibilities, namely:

1. An active alkali metal fluid loop
2. Silicone carbide "glow bar"
3. Induction heating
4. Electron bombardment heating.

An alkali metal loop was not immediately available and appeared to offer unwarranted complexity. The induction heater and silicon glow bar did not lend themselves to accurate measurement of the energy they transferred to the vapor chamber. From these four alternatives the electron bombardment heater was selected as the most compatible approach.

The uniside bombardment heater designed, fabricated and used in the test is shown in Figure 6-7. The heater was designed to be positioned 0.25 inch below the vapor chamber. The tungsten wire can be strung with variable spacing depending on the concentration of energy desired over the heat input surface.

It was hoped that the energy transmitted to the vapor chamber by the electron bombardment heater could be measured by means of a watt meter attached to the vapor chamber. A method was devised described in the test plan in the appendix to evaluate the radiation heat transfer contribution of the EB heater to the vapor chamber.

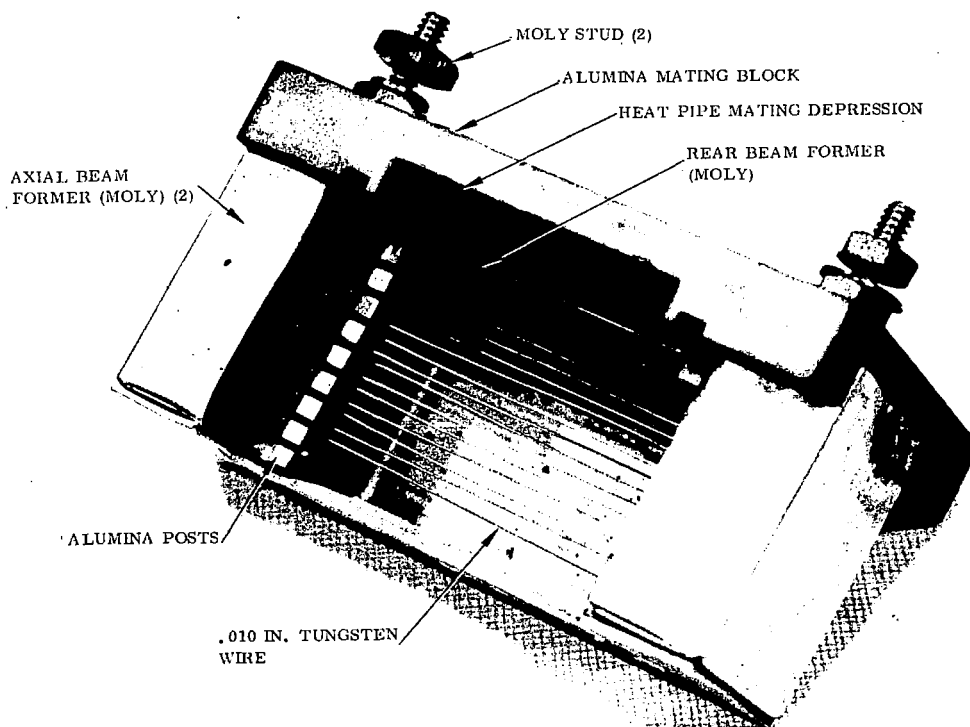


Figure 6-7. Uniside Electron Bombardment Heater

If no heat losses are present, the heat input to the vapor chamber should be equal to the heat rejected. The amount of energy rejected was measured by a specially designed water calorimeter shown in Figure 6-8. Therefore, the energy transferred by the vapor chamber could be measured in two ways. Another check on the heat balance exists by virtue of the Stephan-Boltzman relation:

$$\left(\frac{Q}{A}\right)_c = \epsilon \sigma T^4 \quad (6-1)$$

where

$$\left(\frac{Q}{A}\right)_c = \text{condenser heat flux}$$

ϵ = emissivity of vapor chamber surface

σ = Stephan-Boltzman constant
 (1.713 x 10⁻⁹ Btu-Ft⁻² - R⁻⁴)

T = absolute temperature of the vapor chamber surface.

Therefore, three possibilities of measuring heat flux were available with the test design.

6.2.4 TEST UNIT INSULATION

Heat losses were reduced to a minimum by use of molybdenum multifoil insulation in conjunction with a pressed silica fiber insulation. (Conductivities of this insulation are listed in Table 6-2.) Multifoil insulation possesses extremely low thermal conductivities, thereby making possible a compact yet effective barrier to heat transfer. The use of the silica fiber insulation provided a rigid fixture for the test assembly and also aided in reducing heat losses. A photograph of the major test block hardware is shown in Figure 6-9. A view of the vapor chamber with multifoil in place and mounted on the test block is shown in Figure 6-10.

Table 6-2. Typical High Temperature Insulations

Manufacturer	Type	Characteristics	K Watts/Cm ^o K		Environment
			100 ^o C	700 ^o C	
Linde	Nickel Foil, Refrasil	96 layers/in.	8×10^{-5}	1×10^{-4}	V
Linde	Nickel Foil, Astroquartz Cloth	120 layers/in.	1×10^{-4}	9×10^{-4}	V
Linde	Copper Foil, Refrasil Quartz Fiber Paper	83 layers/in.	4×10^{-5}	6×10^{-4}	V
TECO	Tungsten Foil Thorium Oxide	-	10^{-6}	3×10^{-4}	V
TECO	Tantalum Foil Thorium Oxide	-	10^{-6}	2×10^{-4}	V
TECO	Molybdenum Foil Thorium Oxide	-	10^{-6}	1.6×10^{-4}	V
Johns Manville	Dynaquartz (Silica fiber)	10.0 lb/ft ³	6×10^{-4}	1×10^{-3}	A
Eagle Picher	Supertemp Block	17.0 lb/ft ³	5×10^{-4}	1.5×10^{-3}	A
Johns Manville	MIN-K2000	25.0 lb/ft ³	1.5×10^{-4}	3.2×10^{-4}	A

Key

V = vacuum

A = air

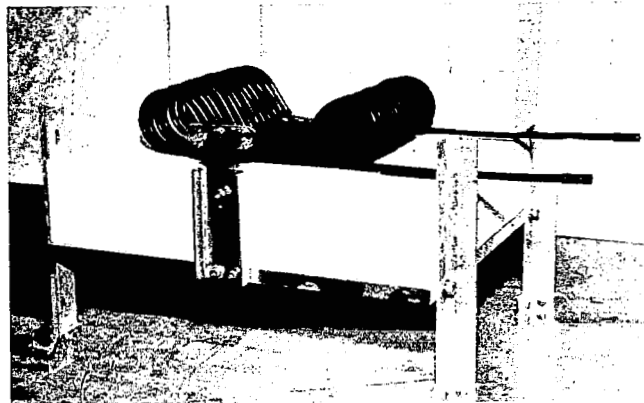
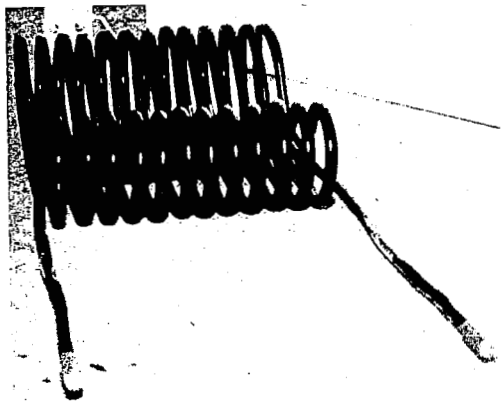


Figure 6-8. Calorimeter

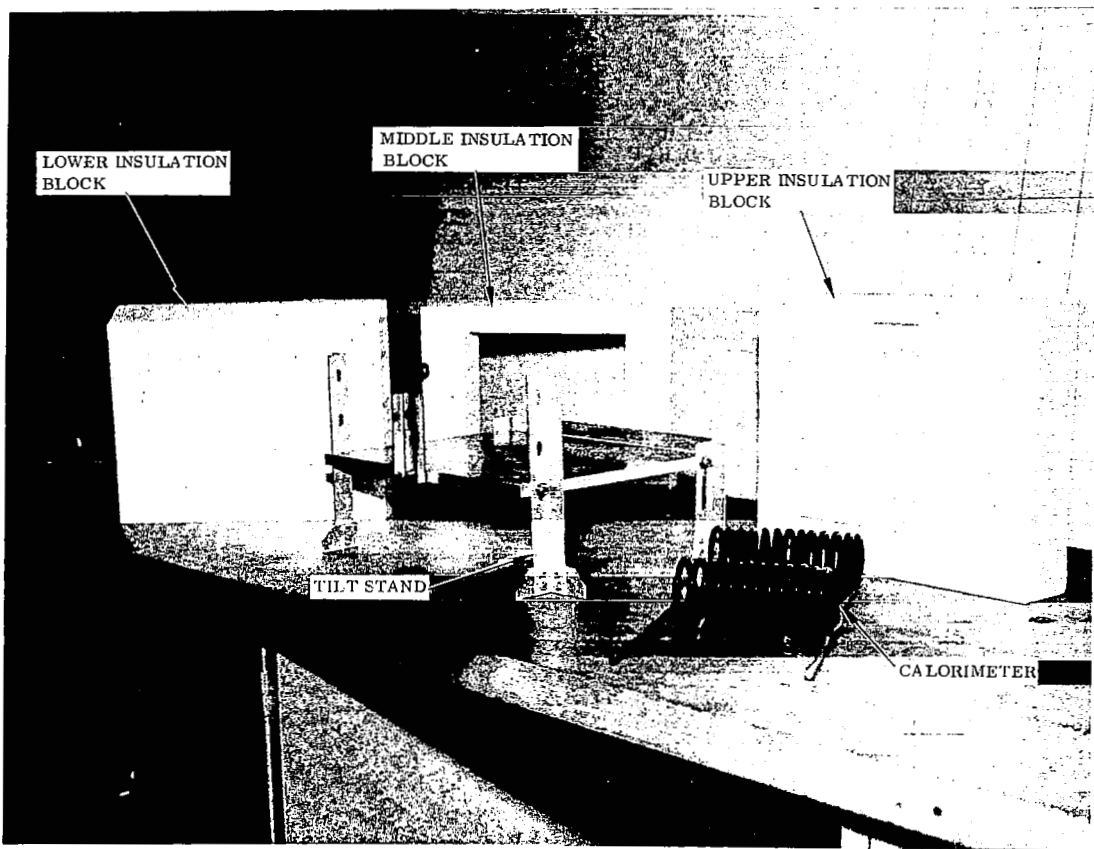


Figure 6-9. Unassembled Test Block Hardware



Figure 6-10. Multifoil Insulation Around Vapor Chamber

6.2.5 TILT ADJUSTMENT

Since one aspect of the test involved tilting the vapor chamber, the entire assembly was mounted on an aluminum table. The table was designed to be adjusted such that the vapor chamber could be situated at any angle between 0 and 30 degrees with the horizontal. In order to avoid realignment of the heater with respect to the evaporator section, the heater base was fastened to the table such that the heater and vapor chamber were titled in unison. Figure 6-11 shows the test block and heater base mounted on the aluminum tilt stand.

6.2.6 TEST UNIT SETUP

The fixture configured to perform the vapor chamber (heat pipe) test is shown schematically in Figure 6-12. An actual photograph of the test setup in operation is shown in Figure 6-13.

The vapor chamber was mounted within the specially designed and insulated test block which in turn was inserted in a stainless steel bell jar vacuum system. Calorimeter, power and grounding connections were brought through sealed umbilicals at the bottom of the chamber.

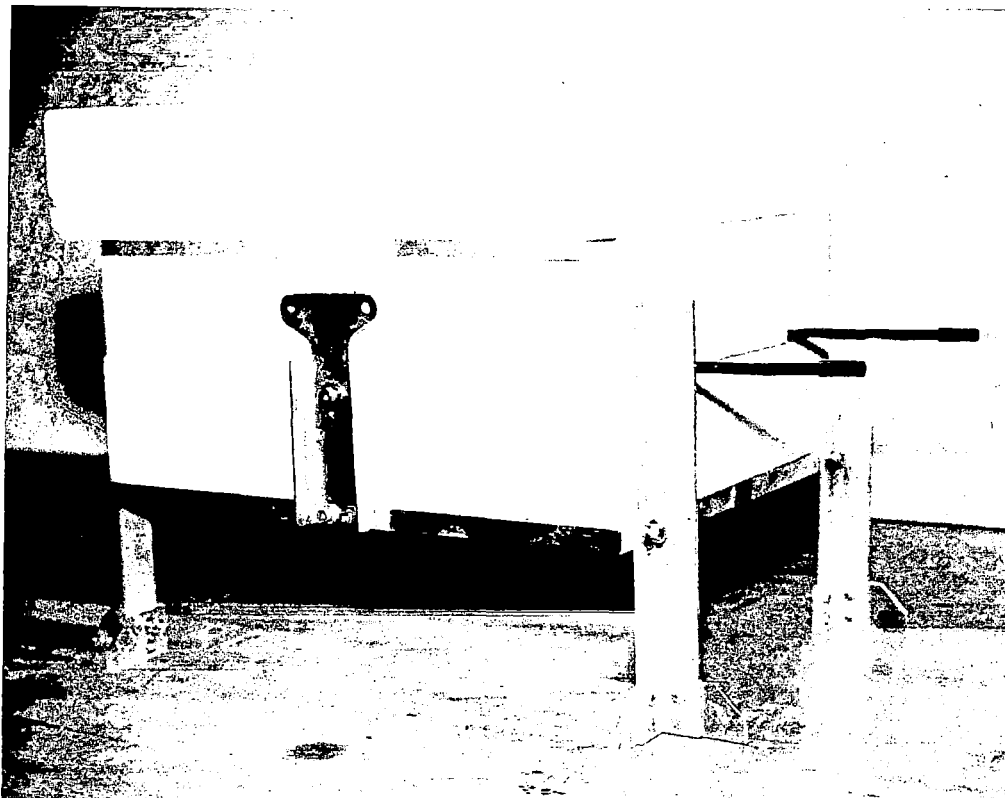


Figure 6-11. Assembled Insulation Test Block on Tilt Stand

Thermocouple leads were fed through sealed umbilicals at the center of the jar. Calorimeter water was provided by a ten-foot stand pipe which provided a constant pressure head. Flow was measured by a precision turbine flow meter feed into a frequency to dc converter and then to a digital readout. This device was capable of metering a water flow rate of 0.02 to 0.2 gpm within ± 0.2 percent of true flow.

A 2000 volts dc power supply coupled with an isolation transformer and variac control was used to supply ac and dc to the heater.

Thermocouple readouts were made with a Howell direct readout, and an Esterline 24 point strip chart recorder. Precision primary test data was obtained by use of an L&N K5 potentiometer.

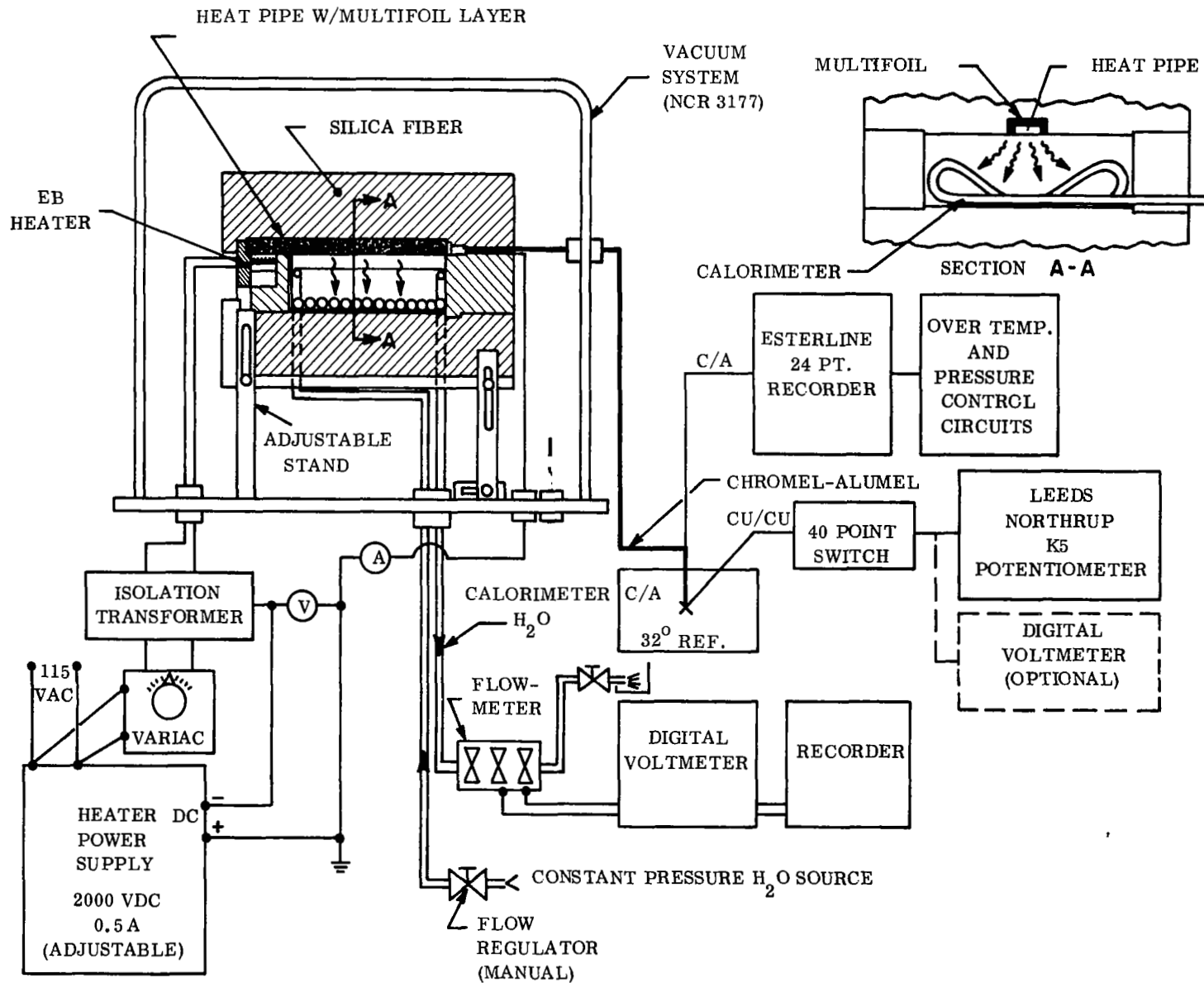


Figure 6-12. System Block Diagram Vapor Chamber (Heat Pipe) Test

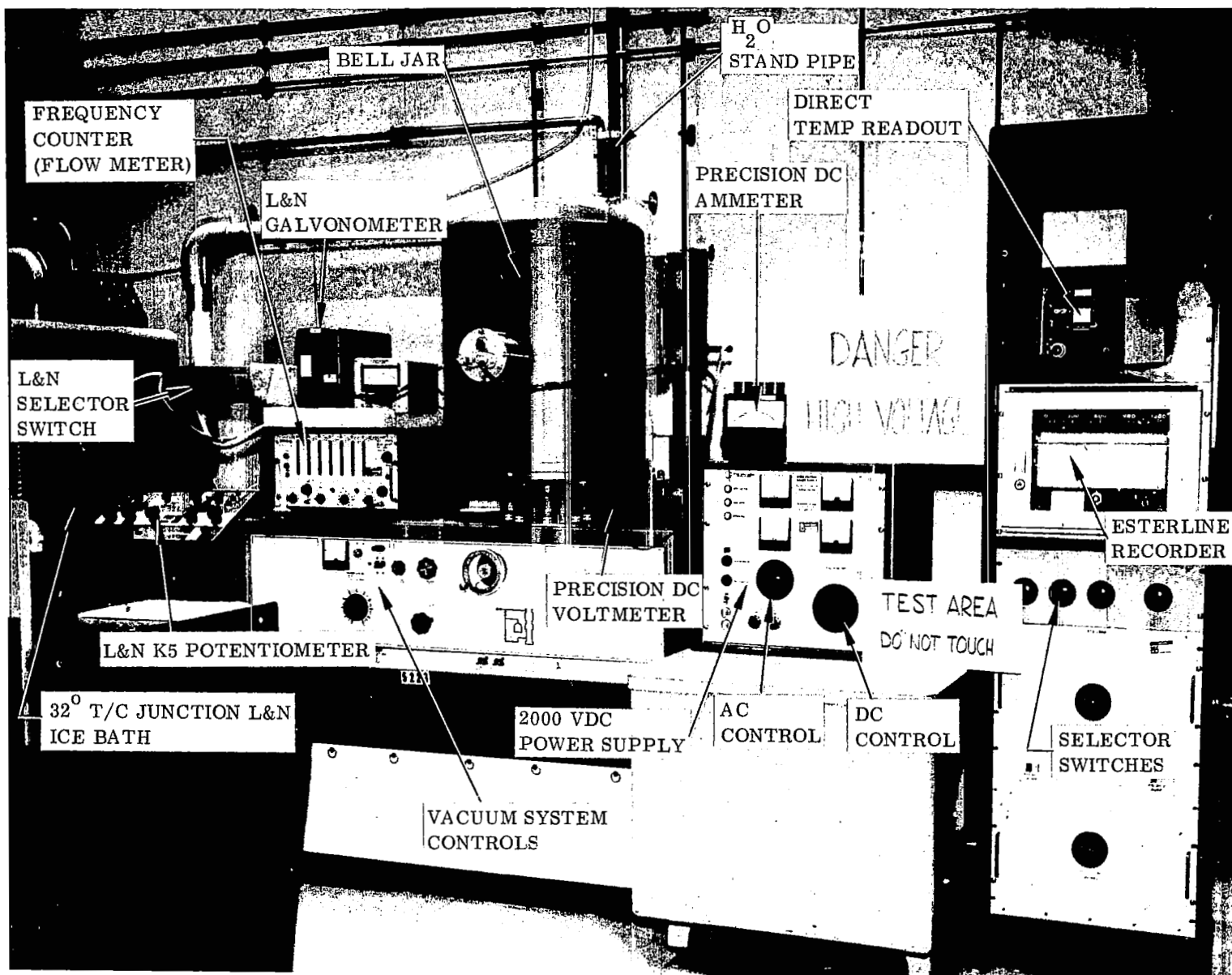


Figure 6-13. Vapor Chamber Test Setup

6.3 VAPOR CHAMBER INSTRUMENTATION

6.3.1 GENERAL

Forty chromel-alumel thermocouples were calibrated and used to instrument the heat pipe. Thermocouples were calibrated against an L&N platinum standard thermocouple at fifty degree intervals between 900^o and 1300^o F in a special L&N calibration furnace. The calibration setup is shown in Figure 6-14.

A turbine flow transducer was placed in the output line of the calorimeter. Flow rates were measured in gpm within ± 0.2 percent.

All heater voltage and current readings were made on meters calibrated within one percent accuracy.

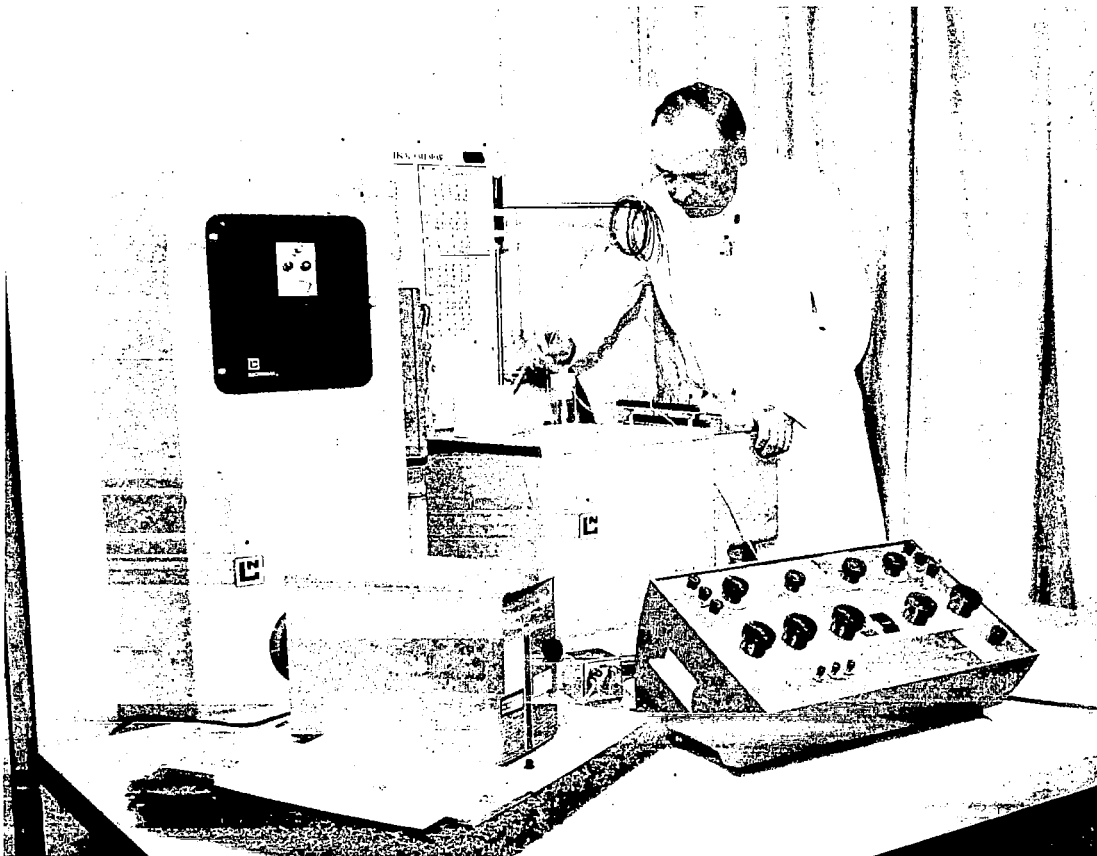


Figure 6-14. Thermocouple Calibration

All thermocouples were connected to a 32^oF reference junction and to an L&N K5 potentiometer for primary data recording. Key thermocouples were also connected to a 24-point recorder which in turn operated an over-temperature safety control.

6.3.2 THERMOCOUPLES LOCATION

Thermocouple placement was made as identified in Figure 6-15. On the top insulated surface, Thermocouples 2 through 7 could be expected to read temperatures very near the vapor temperature at that axial location. This is due to the minimal calculated heat loss through multifoil insulation. Therefore, Thermocouples 2 and 3 represent the vapor temperature in the evaporator, Thermocouples 5, 6, and 7 are condenser vapor temperatures, and Thermocouple 4 should indicate the vapor temperature in the adiabatic section separating the evaporator and the condenser.

Due to the electron bombardment at the evaporator surface, this area was left devoid of thermocouples. It was anticipated that Thermocouple 1 would provide temperatures sufficiently close to the evaporator surface temperature. The overall evaporator ΔT could be measured as the difference between Thermocouples 1 and 2 or 1 and 3 (Figure 6-16)

Four thermocouples, 8 through 11, were attached to the heat rejection surface. The end of the condenser was designed with a well which protruded into the vapor space; Thermocouple 12 was placed into this well. The difference between the readings of Thermocouples 11 and 12 afforded a means of measuring the overall condensing ΔT . Furthermore, it was expected that the readings of Thermocouples 7 and 12 could act as a check on each other.

6.3.3 THERMOCOUPLE ATTACHMENT

Two methods of thermocouple attachment were considered: spot welding the thermocouple directly to the vapor chamber surface; and secondly, a sheathed type thermocouple, strapped to the surface, as shown in Figure 6-17. Experience had shown the sheathed thermocouple to provide more accurate and consistent data.

In order to demonstrate the greater accuracy of sheathed thermocouple, a test was performed in air and vacuum. Five thermocouples were placed on a stainless steel block; two thermo-

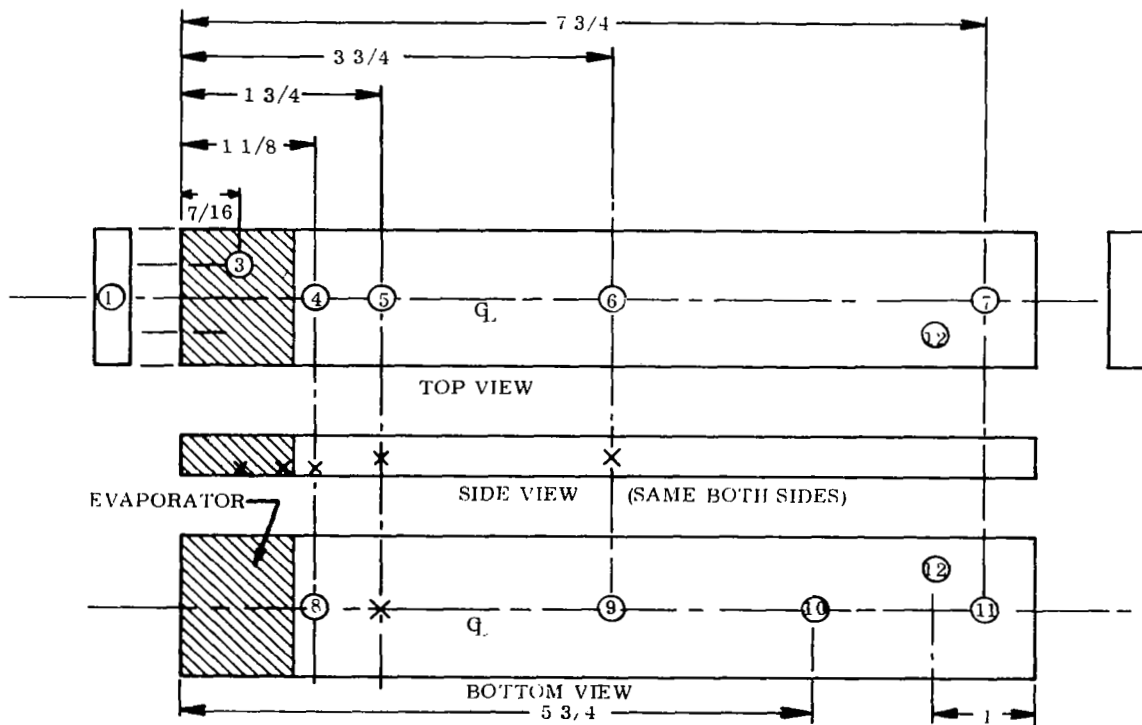
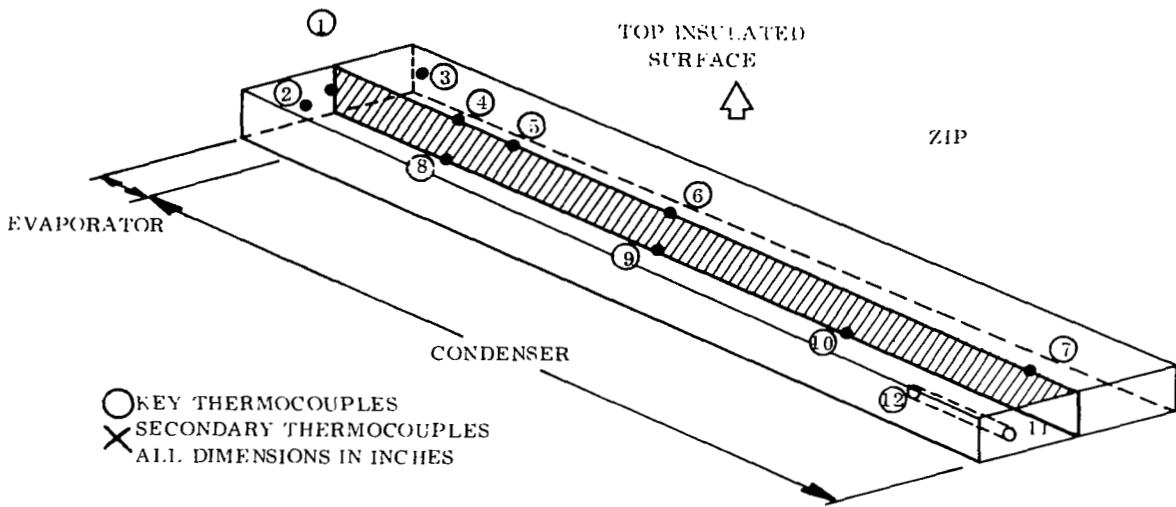


Figure 6-15. Thermocouple Locations

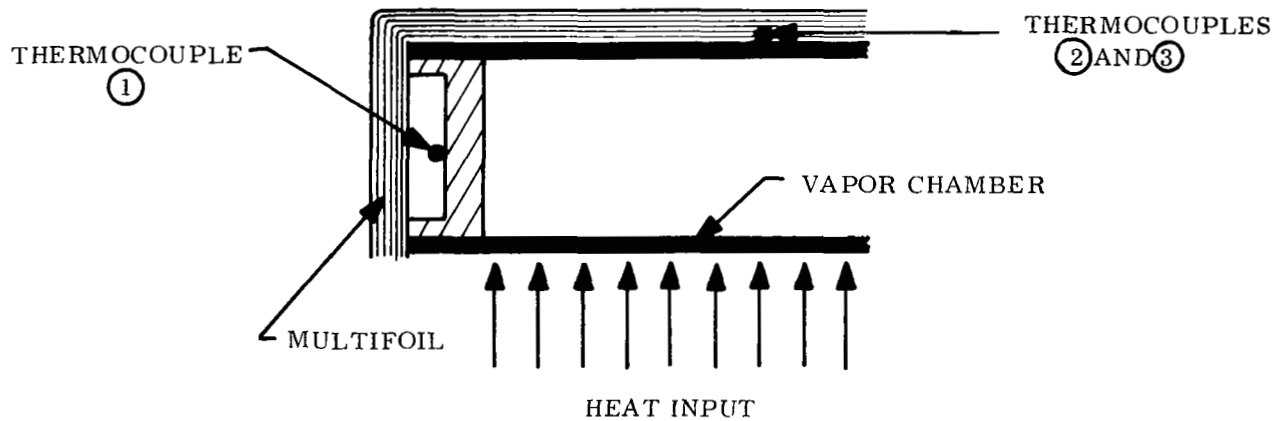


Figure 6-16. Arrangement of Thermocouple 1 and Heat Input Surface (To Scale)

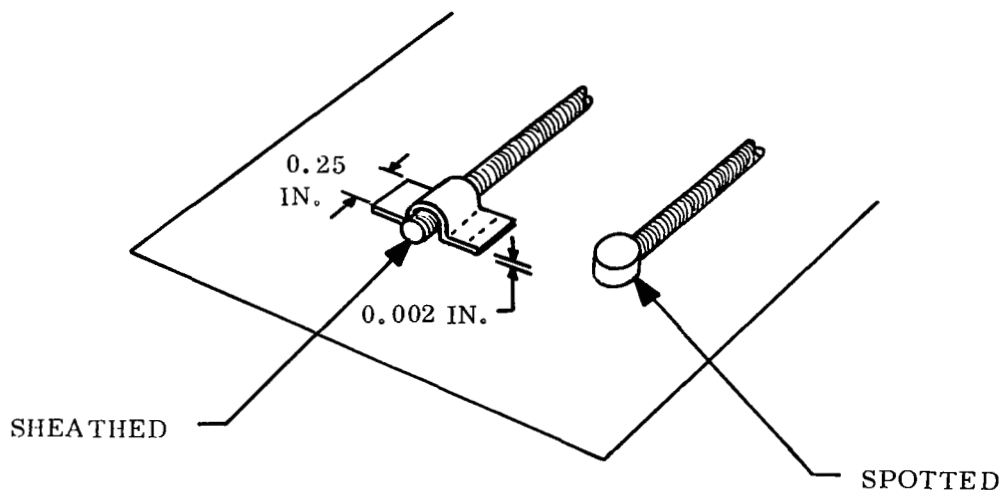


Figure 6-17. Thermocouple Attachment

couples were spot welded to the surface and three were strapped. This arrangement is shown in Figure 6-18. A heater block was attached to the underside of the block and the data presented in Table 6-3 was recorded. In every instance the sheathed thermocouples gave slightly higher readings, indicating a superior method of attachment.

6.4 VAPOR CHAMBER TEST ASSEMBLY EVALUATION

Two major objectives of the test were the measurement of heat fluxes to within an accuracy of ± 10 percent and temperature drops of $\pm 1^{\circ}\text{F}$. An error analysis performed on the test assembly is described below.

6.4.1 HEAT FLUX MEASUREMENT

Two measurements are required in the evaporator heat flux determination: the evaluation of the heat input area, and the heat transfer rate. It is estimated that the width of the evaporator section can be measured during fabrication to within a tolerance of ± 0.005 inches or a possible error of 0.4 percent. The length of the evaporator is determined primarily by the heater

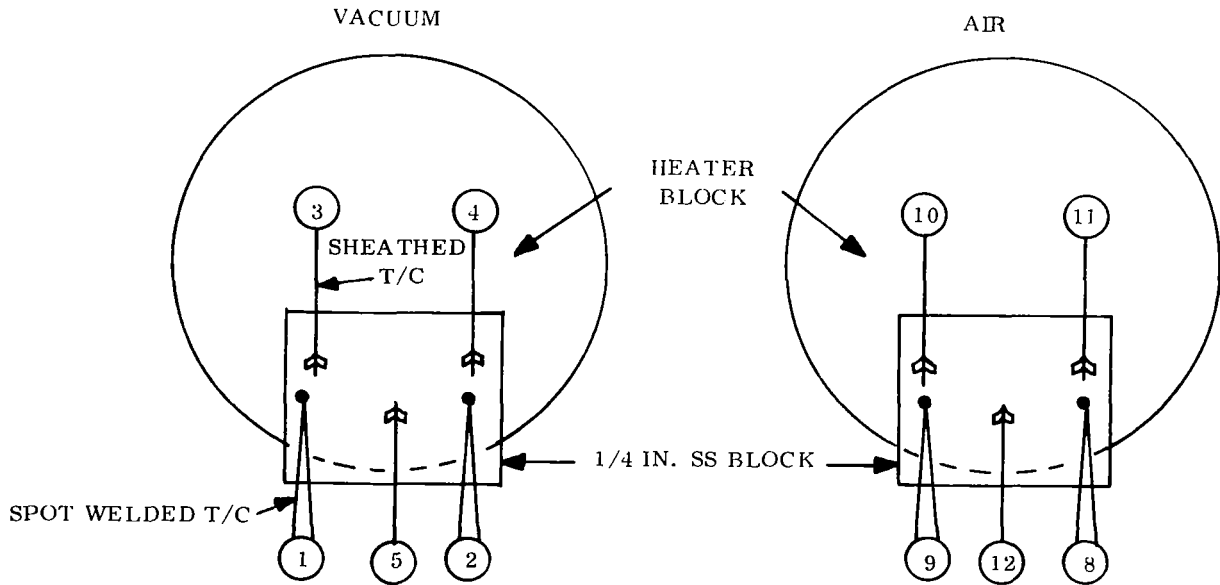


Figure 6-18. Thermocouple Test Configuration

Table 6-3. Thermocouple Test Data (Vacuum and Air)
 (Sheathed TC's 3, 4, 5, 10, 11, 12 Spot Welded TC's 1, 2, 8, 9)

T/C No.	Test Readings °F									
	Vacuum Test Data									
	1.4×10^{-5} Torr			5×10^{-5} Torr		1.3×10^{-5} Torr		4×10^{-6} Torr		
1	516	528	532	648	658	761	762	763	762	
2	513	526	530	644	654	756	758	758	758	
3	518	530	534	651	660	762	764	764	764	
4	518	531	534	651	660	763	764	765	765	
5	518	530	534	651	660	766	768	765	765	
	Air Test Data									
8	570	578	596	606	642	561	564			
9	570	578	595	605	640	561	562			
10	568	578	596	606	640	561	562			
11	576	584	603	612	648	567	568			
12	572	578	600	608	642	562	562			

length and the electron path. The use of molybdenum shields prevents the electron beam from dispersing. This enables the length of the evaporator to be gauged to within ± 0.015 inch or a possible error of ± 1.5 percent. Therefore, the error involved in determining the evaporator area is ± 1.9 percent.

6.4.1.1 Heat Flux Measurement Via Calorimeter

One method of measuring the heat input rate is provided for by the calorimeter in the heat rejection section. Three principal error sources in the calorimetry measurements are:

1. Heat losses through insulation and thermocouples
2. Cooling water flow rate measurement
3. Cooling water ΔT measurement.

Several digital computer code runs were made to calculate the heat losses through the insulation for two different geometries. Figure 6-19 shows the temperature distribution in the insulation for a vapor temperature of 1300°F with 0.060 inch of multifoil and 1.9 inches of Dyna-Quartz. The power loss amounted to 5.9 watts. Reduction of the Dyna-Quartz thickness to 1.5 inches increased the losses to only 6.1 watts as shown in Figure 6-20. At a vapor temperature of 900°F , the heat loss rate is 1.4 watts with the 1.5 inch thick Dyna-Quartz. Since the 1.9 inch slab of Dyna-Quartz did not offer a substantial reduction in the heat loss rate, the 1.5 inch thick slab was deemed sufficient.

The errors involved in estimating this heat loss are due to inaccuracies in the physical properties of the insulating materials and approximations in the modeling of a three dimensional problem using two dimensions. For the test of interest, the value of the thermal conductivity is by far the most critical item. The thermal conductivity of the multifoil insulation is extremely sensitive to temperature, varying by a factor of thirty over the operating temperature range predicted by the STEADY runs. Therefore, the thermal conductivity of high temperature multifoil insulation is dependent upon the temperature gradient across the multifoil which is peculiar to each experimental situation. The thermal conductivity of the

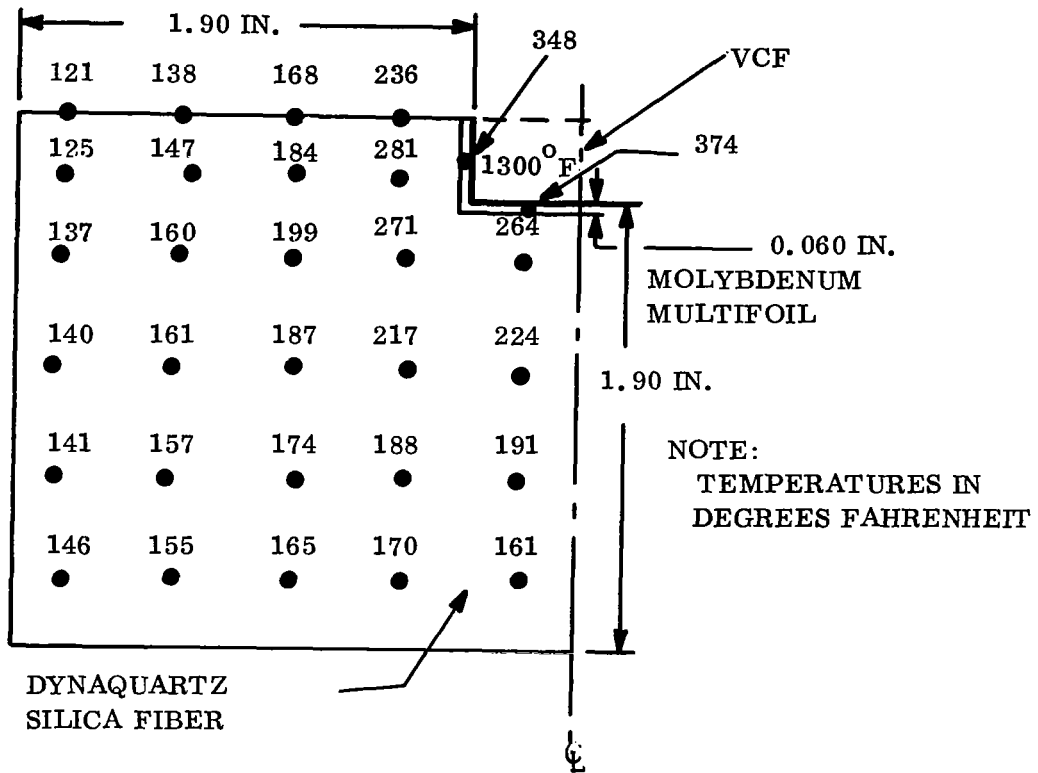


Figure 6-19. Insulation Block (1.90 in.) Temperature Distribution

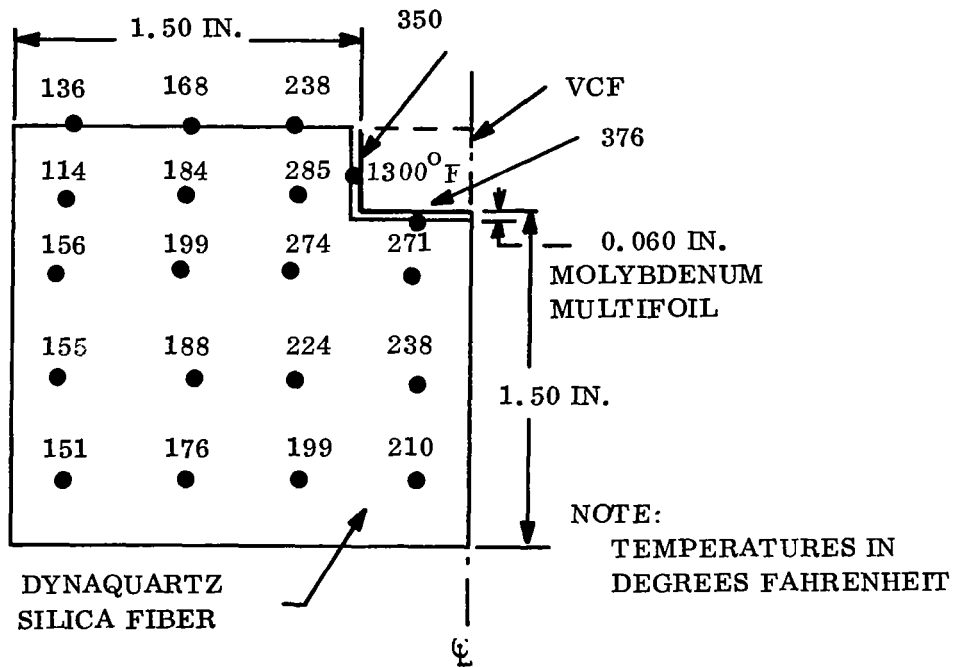


Figure 6-20. Insulation Block (1.50 in.) Temperature Distribution

Dyna-Quartz is dependent upon its temperature and density. According to Johns-Manville, the density can be controlled to within ± 10 percent which corresponds to an error of less than ± 3 percent in the thermal conductivity. The variation of the thermal conductivity for this material with temperature is well documented and is considered to be known to within the accuracy permitted by the density.

In light of the uncertainties involved in the thermal conductivities, the computer runs were run with the values corresponding to the highest temperature in the system. Therefore, the heat loss quantities obtained by the computer runs are conservative and represent a maximum heat leak. The extreme at the other end of the spectrum would be a heat leak approaching zero. Therefore, the maximum percentage error involved in the insulation heat loss calculation is:

1300^oF

$$\frac{\text{MAX. HEAT LOSS (WATTS)}}{\text{HEAT REJECTED (WATTS)}} \times 100 = \frac{6.1}{261} \times 100 = 2.3\% \quad (6-2)$$

900^oF

$$\frac{1.4}{93.6} = 1.5\%$$

The heat loss through the thermocouples was also estimated in a conservative manner; the difficulty in performing an exact calculation is due to the tolerances associated with the sheath, wire and insulation thickness. The heat loss through the 25 thermocouples was estimated to be no greater than 2.7 watts at 1300^oF and 0.9 watt at 900^oF. Using the logic applied to the insulation heat losses, the maximum percentage error is approximately 1 percent at both 900^oF and 1300^oF.

A turbine flow meter was used to measure the water flow rate. Over a calibrated range the flow meter is rated to produce an error of ± 0.2 percent. The digital voltmeter used in conjunction with the flow meter can be calibrated to within ± 0.5 percent of the absolute accuracy.

The determination of the water ΔT introduces another possible source of error. The water ΔT was measured by two in-line thermocouples, at the inlet to and outlet from the vacuum chamber. By once again employing the calibration technique, an accurate evaluation of the ΔT is possible. With the heat pipe inoperative, the water ΔT is essentially equal to zero if the water temperature is close to that of the room; thermocouples were referenced to one another at this condition. The accuracy of the calibration is ensured since the temperature of the water during the test did not change appreciably. The remaining error is limited to that of the potentiometer reading $\pm 0.15^\circ\text{F}$.

6.4.1.2 Heat Flux Measurement by Measuring Heat Input

The second proposed method of determining the evaporative heat flux is by measurement of the heat input. Energy is transferred to the evaporator by electromagnetic radiation and electron bombardment. Prior to test, the radiation contribution was estimated to be less than eight percent of the total energy transfer. An estimate of the actual radiative energy contribution was to be made using the calorimeter. In light of the previous analysis for the calorimeter, the radiation contribution can be determined to within ± 6 percent or to within 0.48 percent of the total heat transfer.

The heating attributed to electron bombardment can be measured using a watt meter, consisting of a volt and ammeter. The error introduced by these devices is 1.0 percent each. No other sizable errors are envisioned using this procedure. Unfortunately, the radiative contribution from the electron bombardment heater comprised over 60 percent of the energy transfer. Therefore, this method of measuring the heat input to the vapor chamber could not be employed as a check on the calorimetry.

6.4.1.3 Heat Flux Measurement Conclusions

Measurement of heat flux by determining the heat input was not employed. However, as discussed in Section 6.2, the Stephan-Boltzmann relationship was used to calculate the heat being rejected from the vapor chamber. This method agreed well with the calorimetry data.

A summary of the errors involved in the calorimetry heat flux measurement is given in Table 6-4.

Table 6-4. Summary of Heat Flux Measurement Errors

Calorimetry Procedure	Error Factors	
	Test at 900 ^o F	Test at 1300 ^o F
Area Measurement	1.019	1.019
Insulation Heat Loss	1.015	1.023
Thermocouple Heat Loss	1.010	1.010
Flow Rate - Meter	1.002	1.002
DVM	1.005	1.005
Water ΔT	1.0075	1.0025
Maximum Percentage Error	5.9%	6.3%

6.4.2 TEMPERATURE DROP (ΔT) MEASUREMENT

Measurement of the evaporative and condensing ΔT 's are required to $\pm 1^{\circ}$ F. The procedure and measurements made to minimize ΔT error include the strategic placement and attachment of thermocouples, the reduction or elimination of thermocouple switches and junction points, the use of a carefully controlled ice bath and the calibration and subsequent readout of thermocouples by precision instruments. Although the presence of a switching device can introduce a small error, this was negated by calibration of the switch within the system.

Thermocouple placement is shown in Figure 6-15. Thermocouples in the evaporator section had to be placed on the surface of the VCF under cover by the multifoil insulation and not in view of the EB heater radiation. The most accurate reading obtainable of the vapor temperature was provided by a thermocouple in a well near the end of the condenser. Calibration against a platinum standard over the measurement range and subsequent calibration and vapor chamber test readout by a L&N K5 potentiometer gave assurance of obtaining accurate ΔT measurements.

6.5 TEST DESCRIPTION AND RESULTS

The vapor chamber fin test was divided into four phases: (1) calibration of the electron bombardment heater energy transfer; (2) heat flux and ΔT measurements; (3) tilt test; and (4) limiting evaporative heat flux determination. The primary objective of the test was to obtain accurate design data for a sodium VCF.

The following observations were made from the tests:

1. The rectangular VCF, using sodium, performed satisfactorily in the 825^oF to 1600^oF temperature range.
2. Tilting the vapor chamber through 10 degrees (evaporator raised) did not alter its performance.
3. A high evaporative heat flux condition (1.4×10^5 BTU/Hr-Ft²) was attained without evidence of burnout. Testing at higher heat fluxes was precluded by temperature limitations.
4. A condensing ΔT substantially larger than that predicted was observed. This ΔT was time dependent and decreased as a substantial amount of test hours were accumulated on the VCF.

6.5.1 CALIBRATION TEST (PHASE 1)

The purpose of the calibration test was to determine the quantity of radiative energy transferred to the VCF from the EB heater as a function of VCF temperature. Since the EB energy transfer can be measured by a watt meter, the sum of the electrical and radiative measurements can be utilized to provide the total energy transfer. This information was necessary for the second phase of the test.

Using the procedure outlined in the test plan (Appendix B), it was expected that the radiative heat transfer could be measured to within ± 15.0 percent. However, it was anticipated that the total radiative heat transfer would comprise less than eight percent of the total heat transferred. The electron bombardment energy contribution was expected to be measured to within ± 2.0 percent. Using the procedure outlined in the test plan, the data shown in Table 6-5 was obtained. The heating contribution due to radiation was significantly higher than that

anticipated. This was explained by an apparent overdesign of the heater. As a result, the overall error involved in measuring the heat input by this method would have increased to a greater degree than permitted by the test ground rules. Therefore, this method of measurement was not pursued; the calorimetry data and the Stephan-Boltzmann relationship were relied upon for this heat input evaluation as described in Section 6.4.

Table 6-5. Radiative Heat Transfer Test Data

Evaporator Temperature (°F)	Radiative Energy Transfer (watts)	Total Heat Rejected (watts)	Percentage of Energy Transferred by Radiation (%)
893 °F	68.9	77.0	89.5
1065 °F	94.9	123.0	77.2
1158 °F	101.0	156.0	64.7
1249 °F	108.0	187.0	57.8

6.5.2 HEAT FLUX AND ΔT MEASUREMENTS (PHASE 2)

6.5.2.1 Evaporative Heat Flux Versus ΔT

The second phase of the testing obtained temperature and calorimetry data between 800 °F and 1300 °F. The instrumentation as discussed in Section 6.3 was devised such that accurate readings of the input surface (Thermocouple 1), condenser surface temperature (Thermocouples 8, 9, 10 and 11) could be obtained. Figure 6-15 illustrates the location of these thermocouples. Although no thermocouple could be placed directly on the heat input section due to the EB heater, Thermocouple 1 provided an accurate substitute. The arrangement of Thermocouple 1 and the evaporator surface is shown in Figure 6-16. The proximity of Thermocouple 1 to the evaporator, the relatively good thermal path between the two, and the presence of the multifoil insulation ensured a minimal ΔT between the evaporator surface and Thermocouple 1. From analytical calculations which were later substantiated by test results, Thermocouple 1 was estimated to reflect the evaporator surface temperature to within 1 °F.

Seven runs were made in this phase of the test; the results are shown in Figure 6-21. The vapor chamber exhibited definite heat pipe action when the evaporator temperature surpassed 825°F. Typical startup data obtained from the strip recorder is shown in Figure 6-22.

Due to the low vapor density of sodium at this temperature level, a large vapor velocity must exist at the evaporator/condenser interface in this temperature regime. This causes an axial vapor pressure drop which results in a sizable temperature drop. The sensitivity between pressure and temperature for saturated sodium vapor is shown in Figure 6-23.

Since a thermocouple was not placed in the vapor at the evaporator section, it was not possible to measure either the evaporative or the axial vapor ΔT directly. In order to estimate each of these temperature drops, the sum of the two (Thermocouple 1 minus Thermocouple 12) was plotted as a function of evaporator heat flux and evaporator surface temperature as illustrated in Figures 6-24 and 6-25, respectively. The shape of these curves reflects the fact that at low power levels (and temperatures) a very large vapor ΔT exists. As the temperature of the vapor increases, the vapor density rises exponentially, thus reducing the vapor velocity and pressure drop. Eventually, the evaporator temperature drop dominates, resulting in a bowl shaped curve. The temperature drop contributed by the evaporator wick can be estimated by the Fourier conduction equation:

$$\Delta T_{EW} = \left(\frac{q}{A} \right)_{EW} \left(\frac{\Delta X}{k} \right)_{EW} \quad (6-3)$$

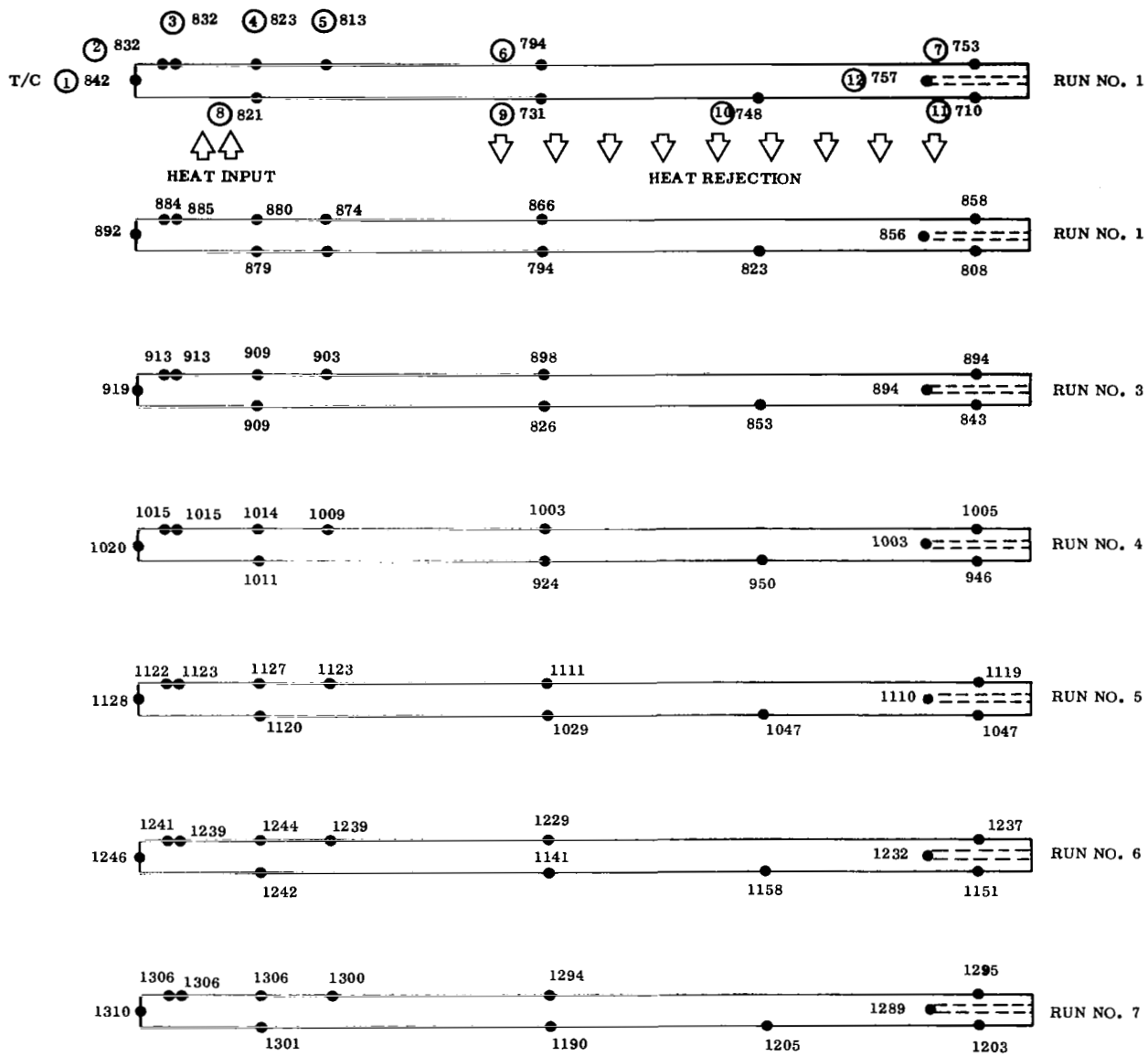
where

$\frac{q}{A}$ = evaporative heat flux

ΔX = wick thickness

ΔT_{EW} = temperature drop across evaporator wick

k = effective wick thermal conductivity



TEST RESULTS °F

TEST RUN	NOMINAL TEMP °F	TC NO. 1	TC NO. 2	TC NO. 3	TC NO. 4	TC NO. 5	TC NO. 6	TC NO. 7	TC NO. 8	TC NO. 9	TC NO. 10	TC NO. 11	TC NO. 12	COND. ΔT 12-11
1	800	842	832	832	823	813	794	753	821	731	748	710	747	47
2	850	892	884	885	880	874	866	858	879	794	823	808	856	48
3	900	919	913	913	909	903	898	894	909	826	853	843	894	51
4	1000	1020	1015	1015	1014	1009	1003	1005	1011	924	950	946	1003	57
5	1100	1128	1122	1123	1127	1123	1111	1119	1120	1029	1047	1047	1110	63
6	1200	1246	1241	1239	1244	1239	1229	1237	1242	1141	1158	1151	1232	81
7	1300	1310	1306	1306	1306	1300	1294	1295	1301	1190	1205	1203	1289	86

Figure 6-21. Temperature Data for Heat Flux vs. ΔT Tests

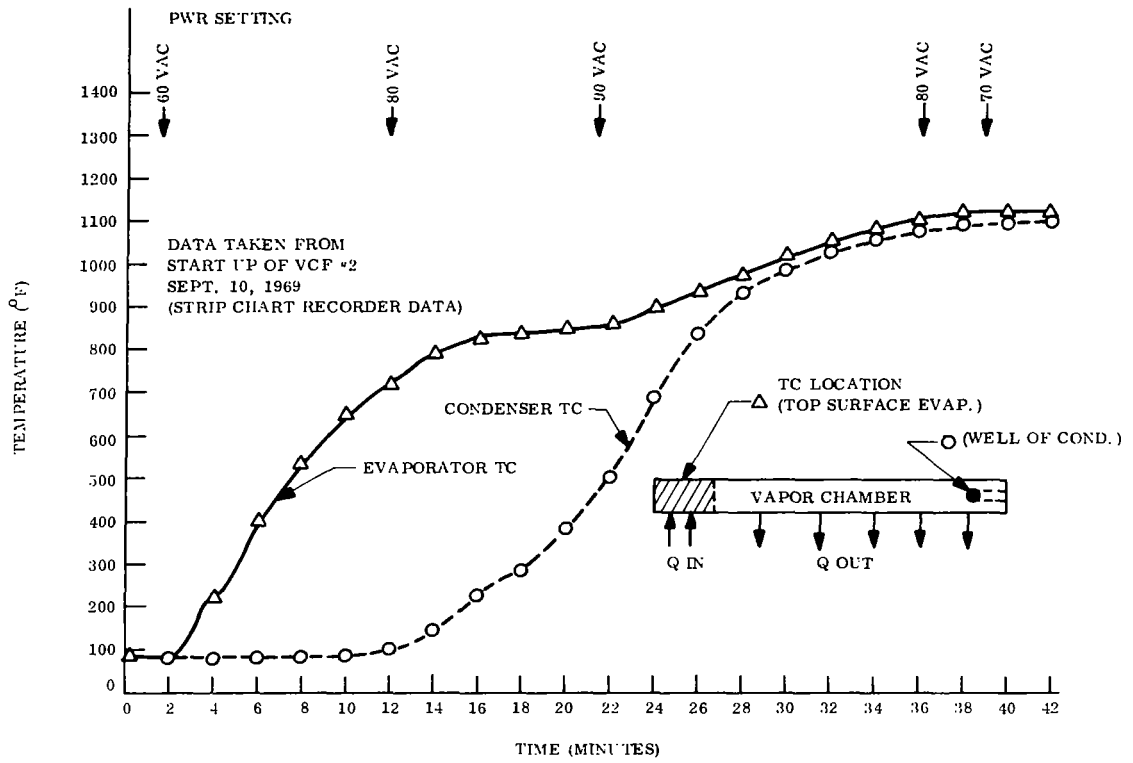


Figure 6-22. Startup Data from VCF No. 2

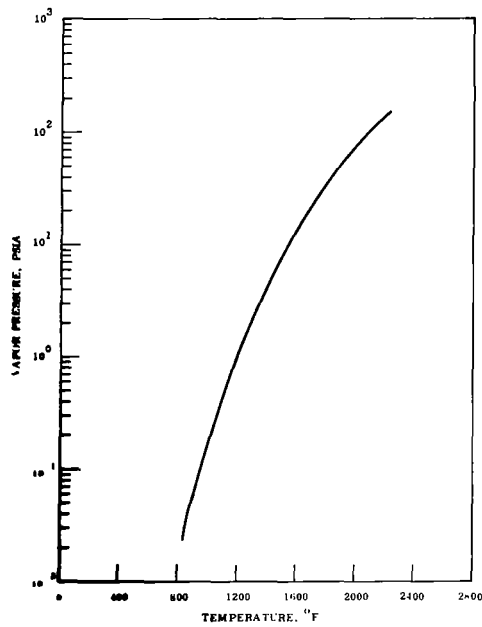


Figure 6-23. Vapor Pressure of Sodium

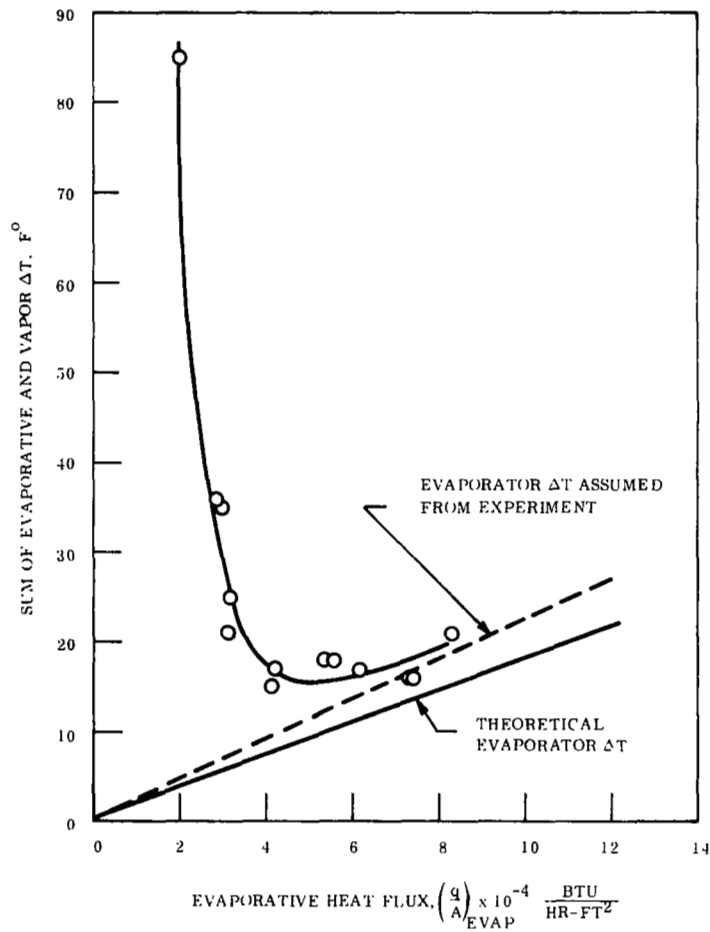


Figure 6-24. Evaporative and Vapor Temperature Drop as a Function of Evaporative Heat Flux

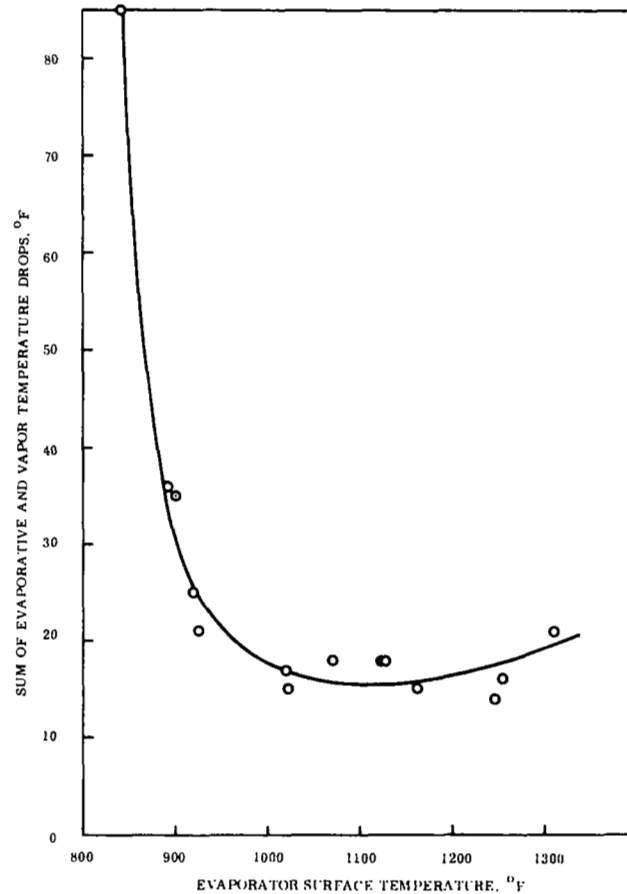


Figure 6-25. Sum of Evaporative and Vapor Temperature Drop as a Function of Evaporative Temperature

The thickness of the evaporator wick is 0.022 inch; five layers of 200 x 200 mesh with a 0.0022 inch wire diameter. An effective wick thermal conductivity was calculated using the following expression:

$$k_{\text{wick}} = p k_{\text{Na}} + (1 - p) k_{\text{ss}} \quad (6-4)$$

where

p = porosity of the wick

k = thermal conductivity

The predicted evaporative temperature drop is also shown in Figure 6-24.

The experimental vapor temperature drop was obtained by subtracting the assumed evaporative temperature drop from the upper curve of Figure 6-24. This result is shown in Figure 6-26 where the vapor temperature drop is defined as the difference between the vapor temperature drop is defined as the difference between the vapor temperature in the evaporator space and the temperature recorded by Thermocouple 12. Also shown are the results from the General Electric HPIPE computer program. This computer code utilizes the equation for the vapor pressure gradient as presented by Cotter (Reference 12) for cylindrical geometry. The discrepancy between the two curves is the rectangular geometry of the test chamber.

Figure 6-27 illustrates the dependence between the vapor temperature drop and the maximum vapor velocity.

6.5.2.2 Condenser Temperature Drop

The outstanding observation of the initial vapor chamber testing was the large condensing temperature drop as measured by the difference between Thermocouples 11 and 12. These results are provided in Figure 6-28. Prior to test, the total condensing ΔT was predicted to approximate the lower curve in Figure 6-28. This expectation was based on the following heat transfer resistances:

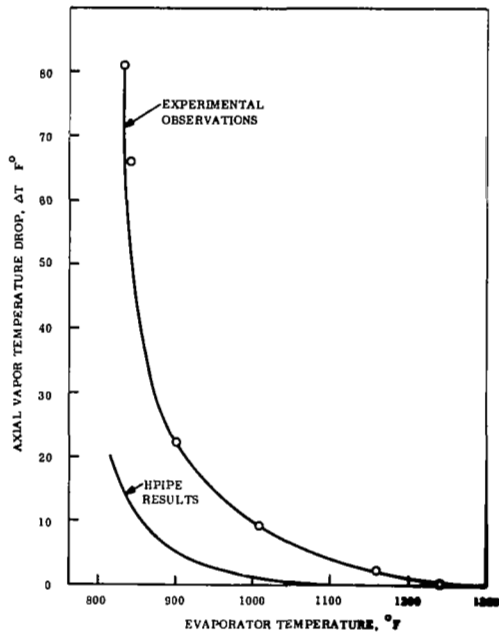


Figure 6-26. Axial Vapor Temperature Drop as a Function of Evaporator Temperature

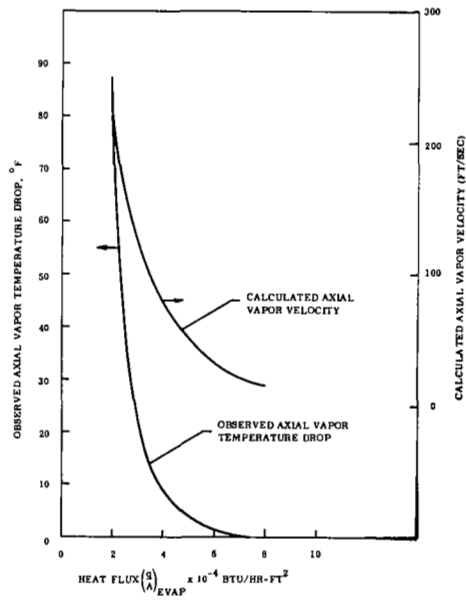


Figure 6-27. Maximum Axial Vapor Velocity and Vapor Temperature Drop with Respect to Evaporator Heat Flux

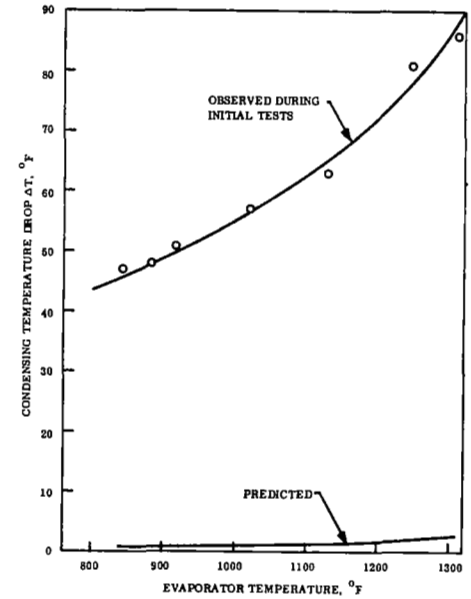


Figure 6-28. Condenser Temperature Drop vs. Evaporator Temperature

1. A ΔT across the vapor/liquid interface due to non-ideal condensing of the sodium.
2. A conductive temperature drop across the sodium filled, stainless steel wick.
3. A layer of sodium which fills the fluid return annulus.
4. Stainless steel vapor chamber wall.

Each of these four resistances can be evaluated in a straightforward manner by the Fourier equation, except the interfacial resistance. An expression for the condensing heat transfer coefficient across the vapor/liquid interface is provided by Sawochka (Reference 13)

$$h_v = \sigma_c \lambda \left[\frac{M}{2 \pi RT} \right]^{1/2} \left[\frac{dP}{dT} - \frac{P}{T} \right] \quad (6-5)$$

where

σ_c = fraction of molecules which strike the condensing surface which actually condense

λ = latent heat of vaporization

M = molecular weight of the gas

R = universal gas constant

P = vapor pressure

T = temperature of vapor

Each of the above parameters is known for sodium except σ_c which is a measure of the efficiency of the condensing process. Tests performed by Sawochka, inferred a value of σ_c equal to 0.2 for potassium. This departure of σ_c from 1.0 is attributed to the presence of dimer and trimer as well as the monomer specie of potassium. According to Ewing (Reference 14), the sodium has a higher concentration of monomer than does potassium, and on this basis, it is expected that the value of σ_c for sodium would be at least 0.2. Assuming a σ_c of 0.2, values of h_v were predicted from Sawochka's relationship. If the interfacial resistance was responsible for the large condensing ΔT , it is reasonable to expect the calculated and experimental values for h_v to be of the same order of magnitude.

Using the following relationships, values of h_v for sodium were obtained from experiments in the following manner:

$$\text{Overall Coefficient } U = \frac{Q}{A_{\text{COND}} \Delta T_{\text{COND}}} \quad (6-6)$$

and

$$U = \frac{1}{\frac{\Delta X_{\text{ss}}}{k_{\text{ss}}} + \frac{\Delta X_{\text{Na}}}{k_{\text{Na}}} + \frac{\Delta X_{\text{W}}}{k_{\text{W}}} + \frac{1}{h_v}} \quad (6-7)$$

where

ΔX = thickness

k = thermal conductivity

h_v = heat transfer coefficient across vapor/liquid interface

Solving for h_v , the values shown in Figure 6-29 were obtained; also presented are the values calculated from equation (6-1).

The large discrepancy between the experimental and calculated values for h_v suggest that some other phenomenon is responsible for the large condensing ΔT . This assumption was substantiated in later tests.

6.5.3 TILTING TEST (PHASE 3)

The next phase of the test involved operating the vapor chamber with the condenser section tilted 10 degrees down from the horizontal. The results of this series of tests produced data nearly identical to that observed in the horizontal position. Temperature data for these runs are presented in Figure 6-30. The almost identical temperature patterns produced in the tilted and horizontal positions indicate that the vapor chamber had excellent pumping capability and could successfully operate in a zero g condition.

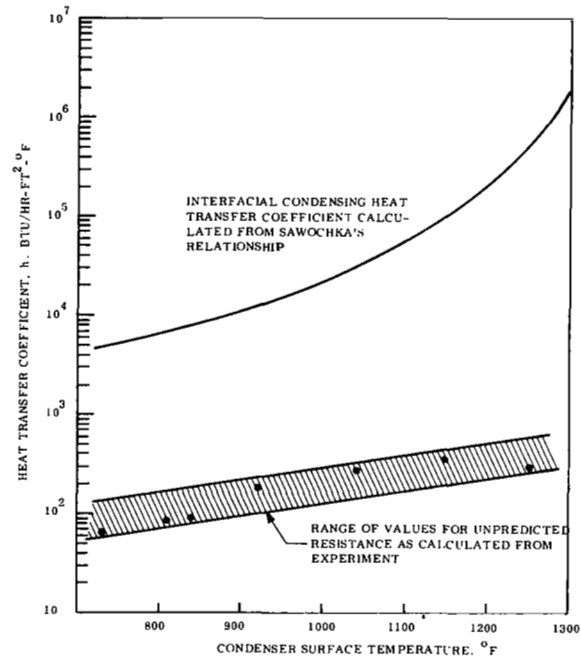


Figure 6-29. Comparison of Calculated Interfacial Resistance with Observed Thermal Resistance

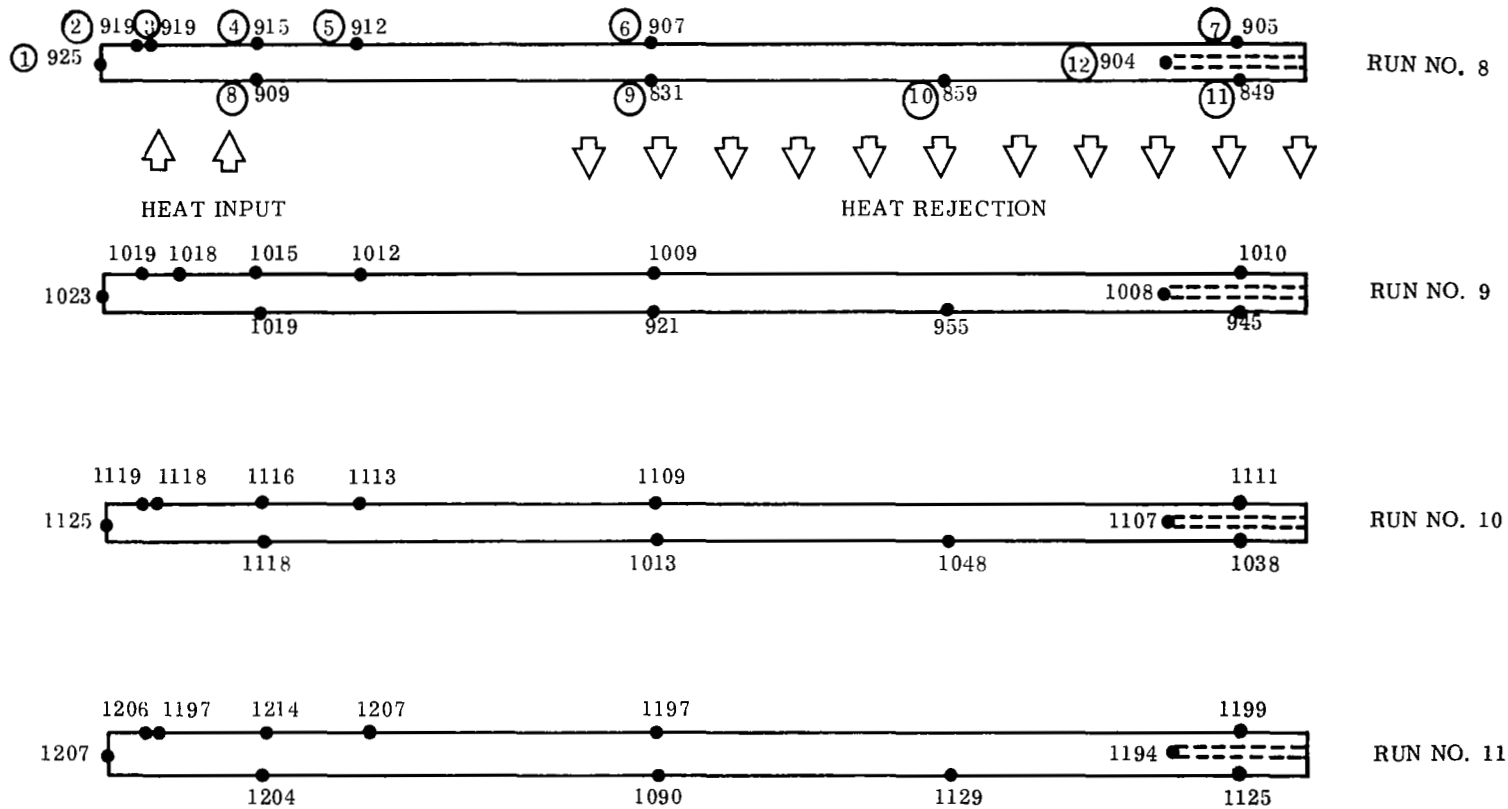
6.5.4 LIMITING HEAT FLUX TEST (PHASE 4)

An attempt to ascertain the limiting evaporative heat flux was terminated after reaching an evaporator temperature of 1600°F without sign of abnormal operation. This corresponds to an evaporator heat flux of $146,000 \text{ Btu}/\text{Hr}-\text{Ft}^2$.

Further increases in temperature were precluded by the distinct possibility of chamber rupture. Upon removal from the test rig, the heat pipe showed a marked deformation of the two horizontal surfaces (Figure 6-31). This was caused by the increased sodium vapor pressure as well as a lower chamber wall strength. Results from the limiting heat flux test are shown in Figure 6-32.

6.5.5 ADDITIONAL INVESTIGATIONS OF THE CONDENSING TEMPERATURE DROP

The large condensing temperature drop exhibited by the first VCF (Number 1) prompted the testing of a second chamber. Consequently, Chamber Number 2, which had been fabricated at the same time as VCF 1, was placed on test; the design of these chambers was identical.



TILT TEST RESULTS °F

TEST RUN	NOMINAL TEMP °F	TC NO. ①	TC NO. ②	TC NO. ③	TC NO. ④	TC NO. ⑤	TC NO. ⑥	TC NO. ⑦	TC NO. ⑧	TC NO. ⑨	TC NO. ⑩	TC NO. ⑪	TC NO. ⑫	COND. ΔT ⑫ ⑪
8	900	925	919	919	915	912	907	905	909	831	859	849	904	55
9	1000	1023	1019	1018	1015	1012	1009	1010	1019	921	955	945	1008	63
10	1100	1125	1119	1118	1116	1113	1109	1111	1118	1013	1048	1038	1107	69
11	1200	1207	1206	1197	1214	1207	1197	1199	1204	1090	1129	1125	1194	69

Figure 6-30. Temperature Data for Tilt Test (10 degrees)

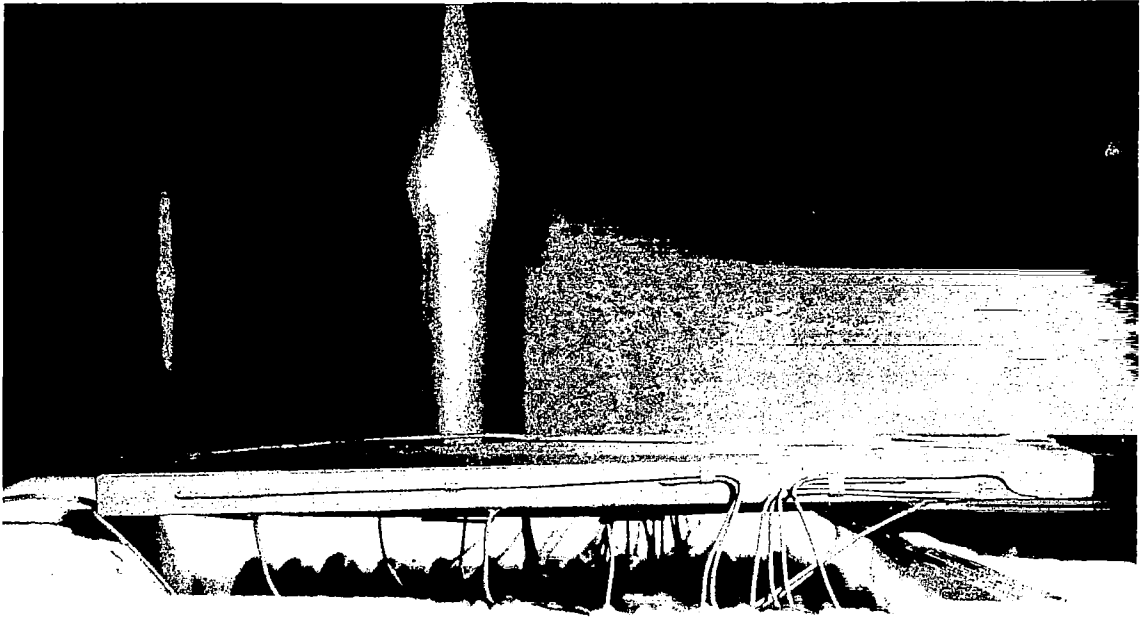


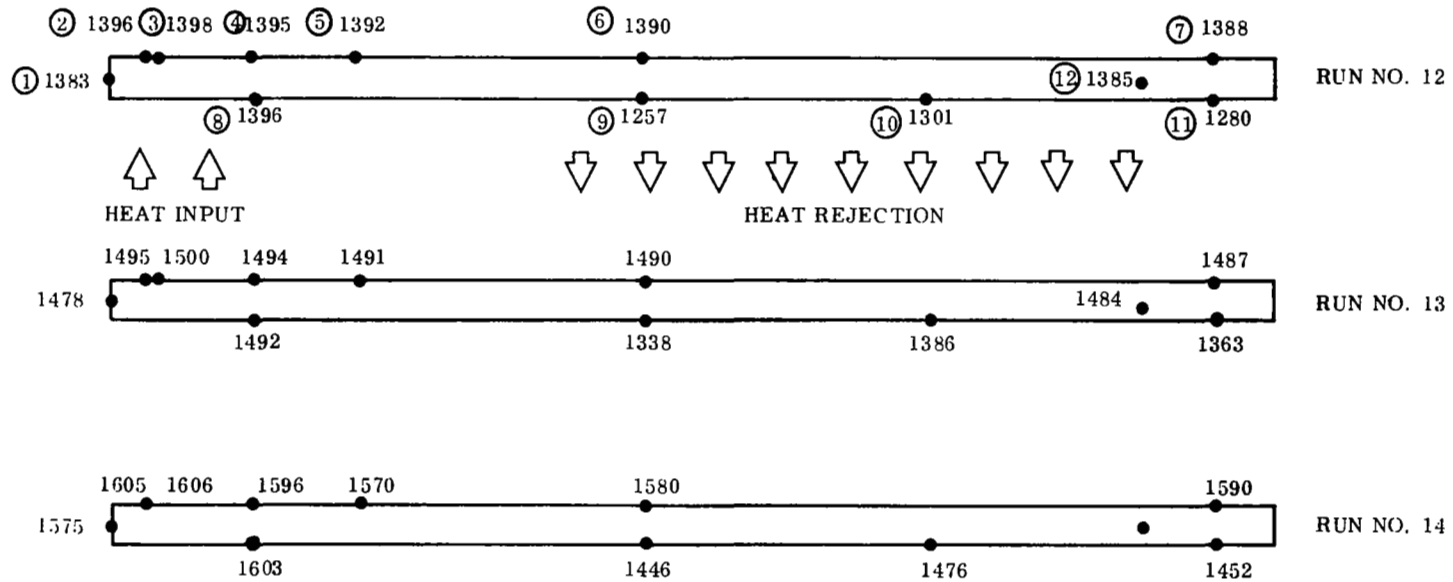
Figure 6-31. Deformation of Heat Pipe After Limiting Heat Flux Test

Initial results obtained from the testing of VCF 2 were comparable to those of VCF 1. Subsequently, testing of VCF 2 was halted while tests of other wick configurations proceeded yielding inconclusive results. VCF 2 was again placed on test ten weeks later. These tests were conducted in the same test facility and utilized instrumentation previously used. In this series of investigations, the observed condensing drops were markedly lower; Figure 6-33 summarizes these observations.

In neither series of tests did the condensing temperature drop approach predicted figures. However, using even the worst data obtained, the VCF is 80 percent efficient. A seven inch length of stainless steel, 0.040 inch thick, has a fin efficiency of approximately ten percent at 1100°F .

6.5.6 DISCUSSION OF TEST RESULTS

The data provided by Figure 6-24 indicate that the evaporative temperature drop matched the predicted values closely. This result becomes clear upon examination of data in the higher



LIMITING HEAT FLUX TEST RESULTS °F

TEST RUN	NOMINAL TEMP °F	TC NO. (1)	TC NO. (2)	TC NO. (3)	TC NO. (4)	TC NO. (5)	TC NO. (6)	TC NO. (7)	TC NO. (8)	TC NO. (9)	TC NO. (10)	TC NO. (11)	TC NO. (12)	COND. ΔT (12) - (11)
12	1400	1383	1396	1398	1395	1392	1390	1388	1396	1257	1301	1280	1385	105
13	1500	1478	1495	1500	1494	1491	1490	1487	1492	1338	1386	1363	1484	121
14	1600	1575	1605	1606	1596	1570	1580	1590	1603	1446	1476	1452	1598	146

Figure 6-32. Temperature Data for Limiting Heat Flux Test

NOMINAL TEMP.	900°F	1000°F	1100°F	1200°F	1300°F
VCF 2 TEST 1 CONDENSING ΔT (°F)	N.A.	TC (7) 963 TC (12) 974 TC (11) 936 ΔT_c 38	1059 1070 1025 ΔT_c 45	1162 1172 1122 ΔT_c 50	1266 1276 1222 ΔT_c 54
VCF 2 TEST 2 CONDENSING ΔT (°F)	TC (7) 830 TC (12) 832 TC (11) 823 ΔT_c 9	N.A.	1069 1077 1063 ΔT_c 14	N.A.	1258 1270 1252 ΔT_c 18
THEORETICAL CONDENSING ΔT (°F)	ΔT_c 0.8		ΔT_c 1.6		ΔT_c 2.5

DECEMBER
3, 1969

FEBRUARY
16, 1970

TEMPERATURES IN °F

Figure 6-33. Condenser Test Results of VCF No 2

heat flux regions where the vapor frictional pressure drop must approach zero. Observed axial vapor temperature drops were within reasonable bounds of the expected values. Due to the exponential dependence of saturation vapor pressure with respect to temperature, the large disparity between calculated and observed data in the lower temperature regime is to be expected.

The condensing temperature drop, which is defined as the difference between the vapor and condenser surface temperatures, was more than an order of magnitude larger than that predicted. Evaluation of the thermal barrier strongly suggests that a gaseous resistance must be present between the bulk vapor and condenser surface over a substantial portion of the condensing area. The logical conclusion is that the annulus beneath the condenser screen (see Figure 6-3) was incompletely filled with sodium. This statement is supported by two additional facts. First, the condensing surface temperature distributions are relatively uneven; see Figure 6-21. Secondly, the thermal resistance offered by a layer of sodium vapor 0.020 inch thick is greater than that observed ($h \sim 7$). Therefore, the value of the unexplained observed thermal resistance is intermediate between that of a 0.020 inch layer of sodium vapor and a 0.020 inch layer of sodium liquid.

The reason for the improved performance of the vapor chamber when subjected to further testing cannot be explained with any certainty. However, it appears probable that some conditioning process between the sodium and stainless steel screen occurred which enabled the sodium to distribute more evenly and completely beneath the screen.

SECTION 7 RADIATOR DESIGN, ANALYSIS AND FABRICATION

7.1 GENERAL DISCUSSION

The development of a vapor chamber fin radiator was proposed as a method of obtaining a lighter, smaller and more reliable heat rejection system than the more conventional conduction fin radiator. However, the added cost of developing the vapor chamber fin radiator can only be justified if its characteristics are significantly superior to more conventional systems. The prime objectives of this radiator design study are to identify a promising Rankine cycle vapor chamber radiator and compare this radiator to the alternative conduction fin radiator. This study formulates conceptual designs which offer the best potential performance for both the stainless steel vapor chamber and stainless steel clad copper conduction fin radiators.

The basic ground rules imposed on both radiators are identified in Table 3-1 of Section 3.

7.2 CONDUCTION FIN RADIATOR

7.2.1 CONDUCTION FIN RADIATOR ANALYSIS

7.2.1.1 General

The configuration of the conduction fin radiator used in this study was dictated primarily by the requirements specified in Section 3. The offset fin/tube geometry as shown in Figure 7-1 was employed. The tube and armor material was 316 stainless steel; the fin material, a composite of stainless steel and copper. The high thermal conductivity of copper enables high fin efficiencies to be obtained with reasonable fin thicknesses, while the stainless steel in the fin provides the necessary structural rigidity. Copper is used as the interior material since the exterior iron titanate emissive coating adheres more readily to stainless steel.

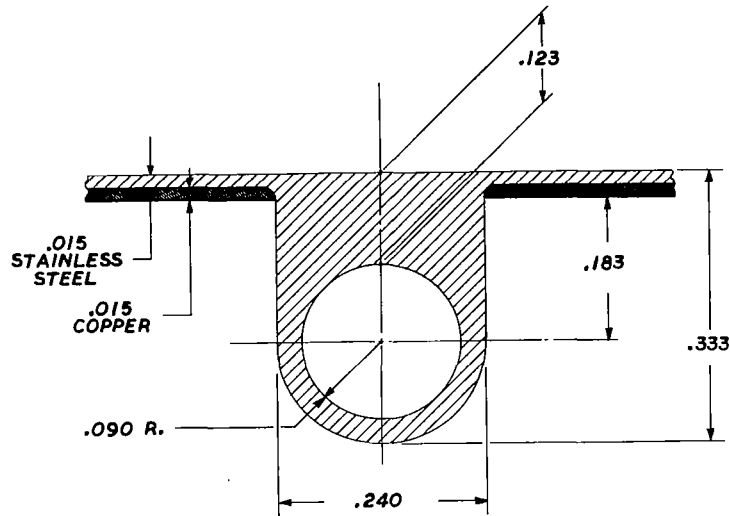


Figure 7-1. Offset Fin Tube Geometry

7.2.1.2 Thermostructural Analysis

A thermostructural systems analysis was performed to establish an operational thermal distribution that would minimize structural discontinuities.

The trade-offs of this analysis are summarized in Figure 7-2. Thermal distributions resulting from either horizontal or vertical orientation of the Nak headers/feedlines are shown. Figure 7-2a illustrates the thermal distributions resulting from placing the input headers (1200°F) at either the midsection or extremities of the radiator with the return headers (980°F) at the extremities or midsection, respectively. The resulting thermal distribution of this configuration is illustrated by lines ① and ②. Line ③ shows the thermal distribution obtained by placing the input headers at the top and midsection and placing the return headers at the midsection and bottom of the radiator. This latter distribution is least desirable since a 220°F temperature discontinuity is imposed at the radiator midsection; a more complex load bearing, mating ring would be required with this approach. Figure 7-2b illustrates the vertical placement of the fluid headers. This design is less structurally efficient since the radiator tubes are not used in providing axial stiffening to the structure. Relatively large circumferential stresses and increased fabrication complexity are other disadvantages. The horizontal header distribution ① offers minimum thermostructural discontinuity loads and lower radiator interface temperatures, thus making the radiator sections more thermally

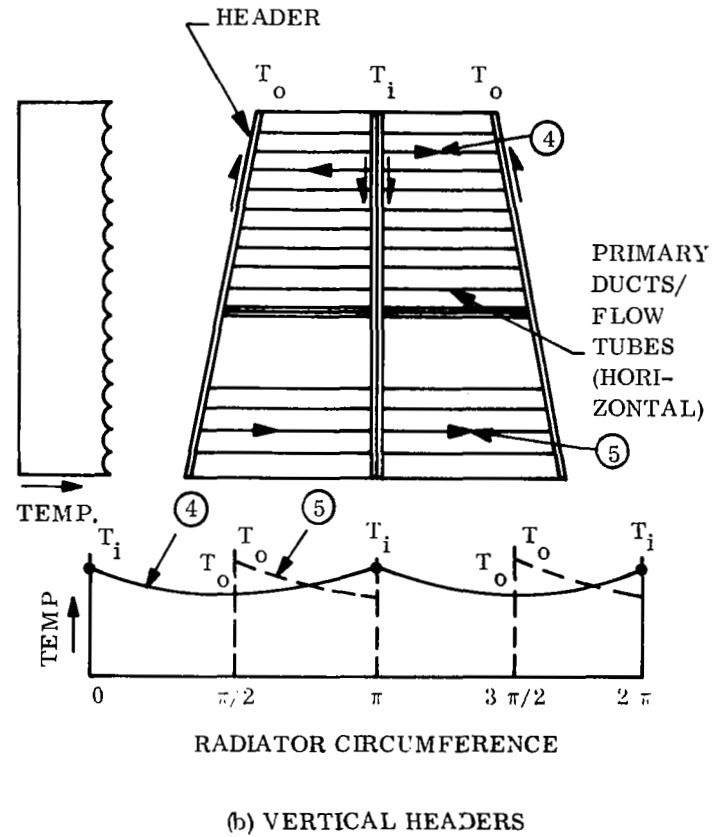
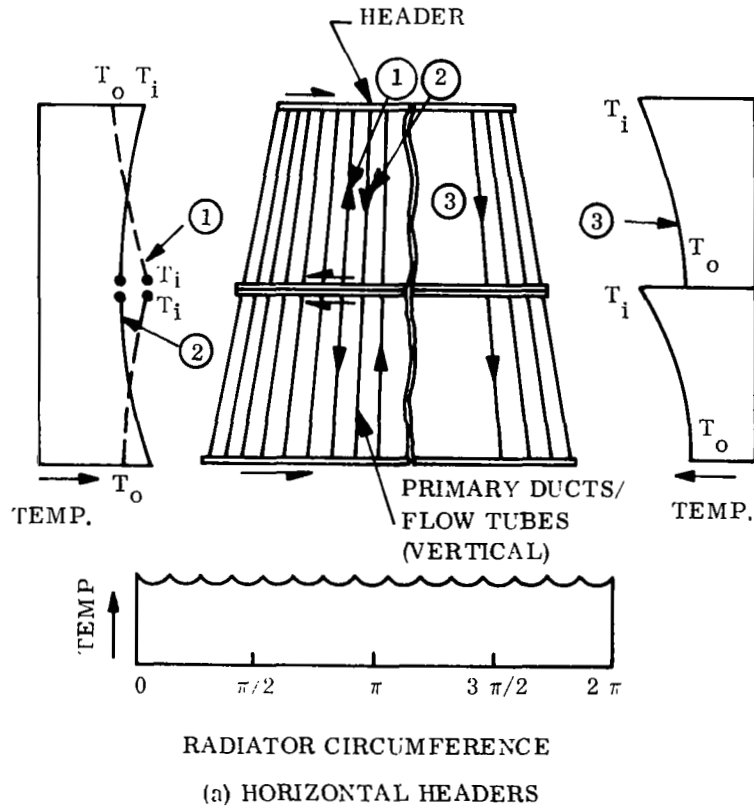


Figure 7-2. Header/Flow Tube Orientation

compatible with adjacent radiator/structural panels. The configuration represented by distribution ① was chosen for the subsequent design and structural analysis.

The subsequent fluid loop configuration for the conduction fin radiator is illustrated in Figure 7-3. Four independent loops are shown, each feeds two panels. The feed lines carry fluid to the panel inlet headers which in turn distribute the fluid to the individual tubes. At the end of the flow tubes, the outlet headers carry the fluid to the return lines and finally back to the heat exchanger.

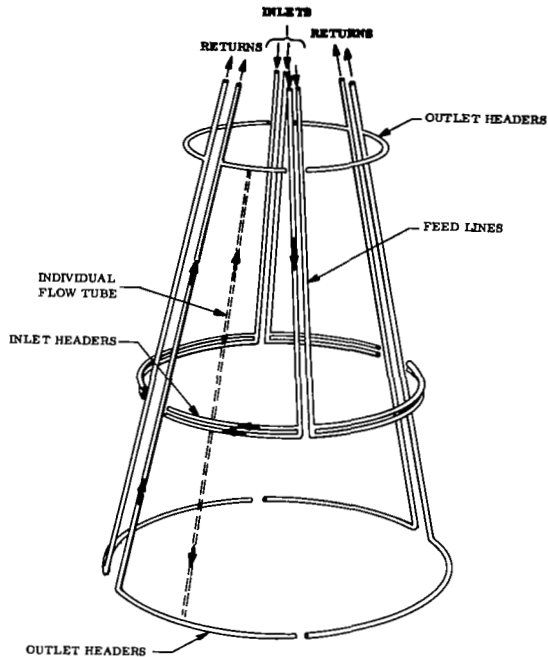


Figure 7-3. Fluid Loop Configuration

7.2.1.3 Thermal/Design Optimization

The thermal design analysis of the conduction fin radiator was performed with the Spartan III computer optimization code.

This computer code considers the thermal, hydraulic and meteoroid protection aspects of radiator design. The code has the ability to optimize up to twenty parameters simultaneously in order to achieve a minimum weight. The weight optimization criterion used is defined by the following relationship:

$$\text{System Weight} = (Wt_R, \text{ lbs}) + (PW, \text{ kWh}) \left(PP, \frac{\text{lbs}}{\text{kWh}} \right) \quad (7-1)$$

where

Wt_R = radiator weight (vapor chambers, primary ducts, feed lines, headers, and associated fluid)

PW = required primary fluid hydraulic pump work

PP = additional powerplant weight penalty due to parasitic power pumping requirements.

The value of PP used in the study was calculated in the following manner:

$$PP = \frac{PSW \frac{\text{lb}}{\text{kWe}} (100)}{\eta_P \frac{\text{kWh}}{\text{kWe}}} \quad (7-2)$$

where

PSW = powerplant specific weight, 50 lb/kwe

η_P = pump efficiency, 20 percent

For the radiator cases of interest, four variables were optimized:

1. Inside tube diameter
2. Tube spacing
3. Fin thickness
4. Feed line diameter

Initially an effort was made to determine the ideal percentage of copper and stainless steel in the fin. The results are shown in Figure 7-4 for two sets of meteoroid survival probability conditions. In all cases it was assumed that 1 of 4 loops failed during the mission. At the lower meteoroid protection requirement, 0.99 at 20,000 hours, the optimum composition was 50 percent copper and 50 percent stainless steel. At a 0.999 probability and a mission time of five years, 60 percent stainless steel 40 percent copper gave the minimum weight. The higher percentage of stainless steel at the more stringent survival probability is advantageous because its physical properties afford greater meteoroid bumper protection to the tubes.

Using these results, weight versus area characteristics were generated with the Spartan III code for the 0.999 (5-year lifetime) and 0.99 (20,000 hour lifetime) survival probabilities. Figure 7-5 illustrates the significant weight penalty associated with the higher survival probability and longer lifetime.

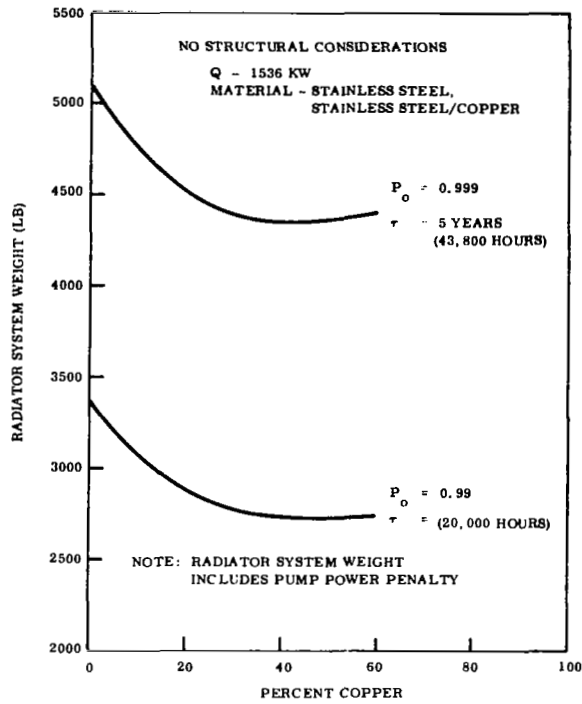


Figure 7-4. Conduction Fin Radiator System Weight vs Percent Copper in Fins

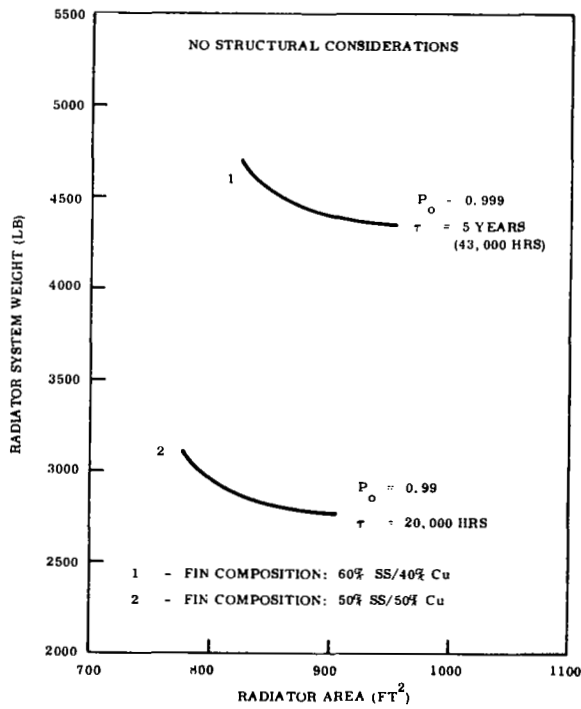


Figure 7-5. Conduction Fin Radiator System Weight vs Heat Rejection Area

The weight advantage of using a composite fin was also investigated with the aid of the Spartan III code. Figures 7-6 and 7-7 show the relationship between weight and area for 100 percent stainless steel conduction fin radiators at both the 0.99 and 0.999 survival probability conditions. As the meteoroid survival probability increases, the incentive for fabricating a stainless steel/copper fin diminishes.

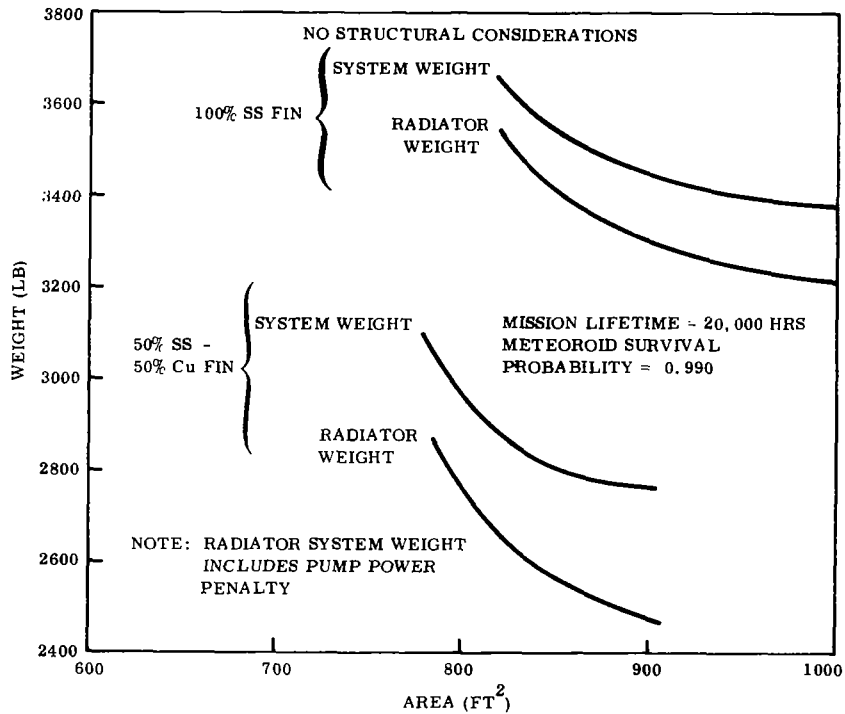


Figure 7-6. Conduction Fin Radiator Weight/Area Relationship ($P_o = 0.990$)

As discussed in Section 5.1.1, recent test data indicates a higher cratering coefficient, γ , for stainless steel than the value reported in Reference 6. Since the sensitivity of the conduction fin radiator weight with respect to meteoroid damage probability is particularly important in a comparison with the VCF radiator, the effect of the new γ on radiator weight was examined. Figure 7-8 shows the conduction fin radiator weights for a value of γ equal to 2.62; the value used in preceding results was 1.67. A fin composition of 70 percent stainless steel/30 percent copper was estimated to be optimum for this condition. Comparison of Figure 7-8 with Figure 7-5 indicates a large increase in the conduction fin radiator weight as a result of the higher meteoroid armor requirements.

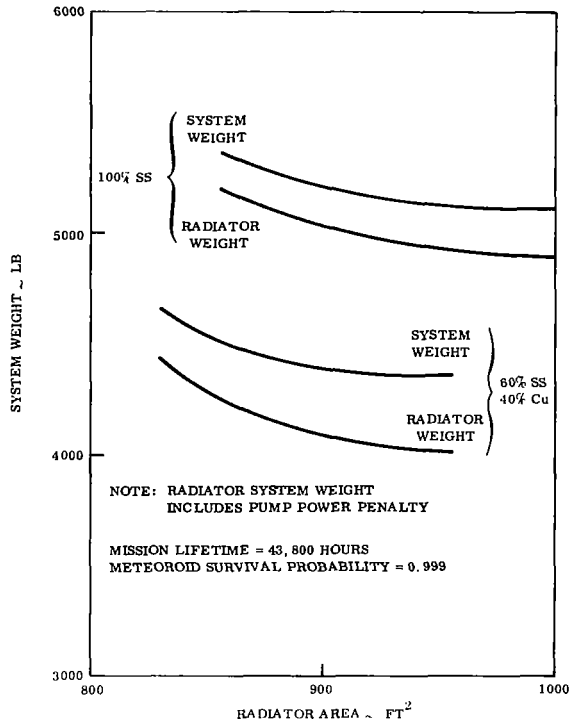


Figure 7-7. Conduction Fin Radiator Weight/Area Relationship ($P_0 = 0.999$)

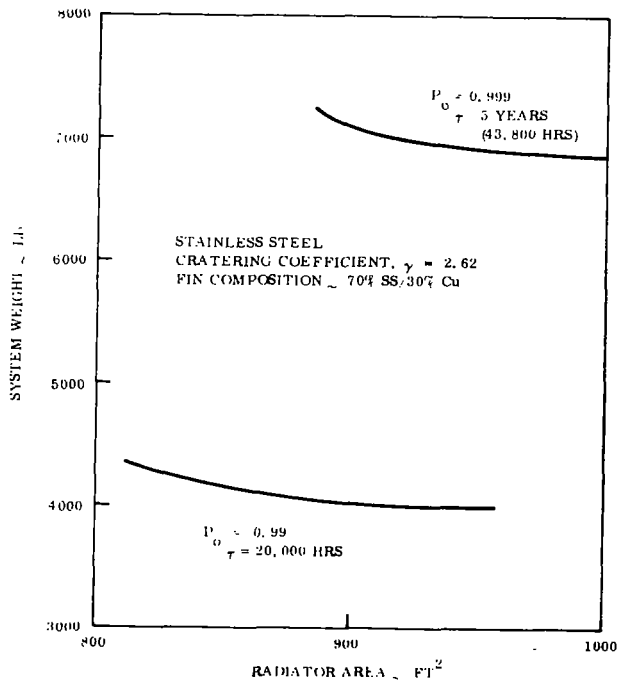


Figure 7-8. Radiator System Weight vs Heat Rejection Area ($\gamma = 2.62$)

7.2.1.4 Structural Analysis

The weight optimizations shown in the preceding figures include fluid, feedline, header and radiator panel weight. In addition, various types of structural support members and interface rings may be required. An analysis was made of the additional structural requirements for the condition fin radiator subjected to the same loading and launch conditions as the VCF radiator discussed in Sections 3 and 5.3.

The three structural failure modes (local instability, panel instability and general instability) considered for the VCF were analyzed for the conduction fin radiator employing the Conical Radiator Analysis of Stability Stress (CRASS) computer code. This code analyzes each bay of an offset fin/tube conduction fin radiator at three locations - namely the top, center, and bottom for each of the three failure modes. The code treats a conical bay as an equivalent cylinder where the buckling stress for local instability is given by:

$$F_{P_{cr}} = \frac{K_c \pi^2 E}{12 (1-\nu^2)} \left(\frac{t_f}{b} \right)^2 \quad (7-3)$$

For a conduction fin radiator, the thickness, t_f , is that of the fin and the width, b , is the distance between tubes. The buckling coefficient K_c is conservatively taken as 4.0 representing a long panel with edges simply supported and no curvature.

For panel instability, the stiffening element, which is the armored tube with effective fin, is analyzed as an Euler column:

$$F_{t_{cr}} = C \pi^2 E \left(\frac{\rho}{l} \right)^2 \quad (7-4)$$

where

- $F_{t_{cr}}$ = critical buckling stress of the stiffening tube in panel instability.
- C = "fixity factor" (structural support coefficient)
- ρ = Radius of gyration
- l = stiffener length

When local instability is prevented, the fin can be assumed to be fully effective, that is, its entire cross sectional area can be lumped with the stiffener. Simple support of the ends is assumed, corresponding to a coefficient C of 1. If it is found that the panel instability stress is below the ultimate design stress, the CRASS code will determine the size and spacing of additional stiffening rings required to bring the radiator up to strength. Sizing of these intermediate rings makes use of the Shanley criteria (Reference 15). For general instability, the method of Becker and Gerard (Reference 11) was used. This theory uses a relation in the form:

$$F_{g_{cr}} = \frac{K_c \pi^2 EI_s}{t_s L^2} \quad (7-5)$$

where

- $F_{g_{cr}}$ = critical buckling stress for general instability
- K_c = buckling coefficient
- I_s = distributed moment of inertia of the stiffeners
- t_s = distributed thickness of the stiffeners
- L = length of the radiator section

The buckling coefficient K_c is a complex function of stiffener and frame properties, fin thickness, radiator radius and length.

A structural analysis was performed on the conduction fin radiator designed for a 0.990 meteoroid survival probability condition. This analysis assumed that the radiator formed the aerodynamic shroud and supported a 15,000 pound load throughout all phases of a two-stage Saturn V launch. The structural evaluation was performed for three points on the weight versus area curve of Figure 7-5. The structural assessment concluded that for the cases examined, cylindrical frames/stiffeners were required in order to provide sufficient lateral stiffness. Longitudinal splice plates, header and feed line clamps were also required.

7.2.1.5 Weight Analysis

Table 7-1 summarizes the total conduction fin radiator system weight including the weight attributed to the results of the thermal and structural evaluations for several selected concepts. Data is presented for the 0.990 and 0.999 meteoroid survival conditions for 100 percent stainless steel radiators as well as stainless steel/copper radiators. The total system weight is comprised of radiator panel weight, structural weight and a pumping power weight penalty. It is interesting to note that the minimum structural penalty accompanies the use of a composite fin material.

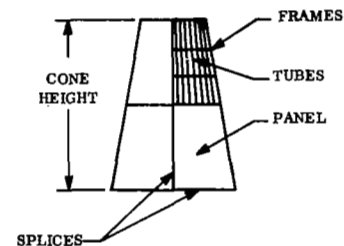
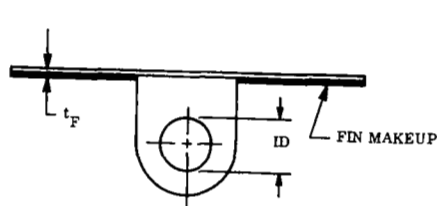
7.2.2 CONDUCTION FIN RADIATOR DESIGN

The design of the conduction fin radiator is based on the requirements as specified in Section 3 and on the results of the thermal, integration and structural analyses as well as fabrication considerations. The design is characterized by the conventional offset fin/tube geometry primarily dictated by the meteoroid protection requirements.

The horizontal header, and vertical flow tube arrangement selected is based on the results of the analysis in Section 7.2.1.2. Vertical orientation of the flow tubes enables them to be utilized as supporting structure and eliminates the need for fabricating curved tube sections.

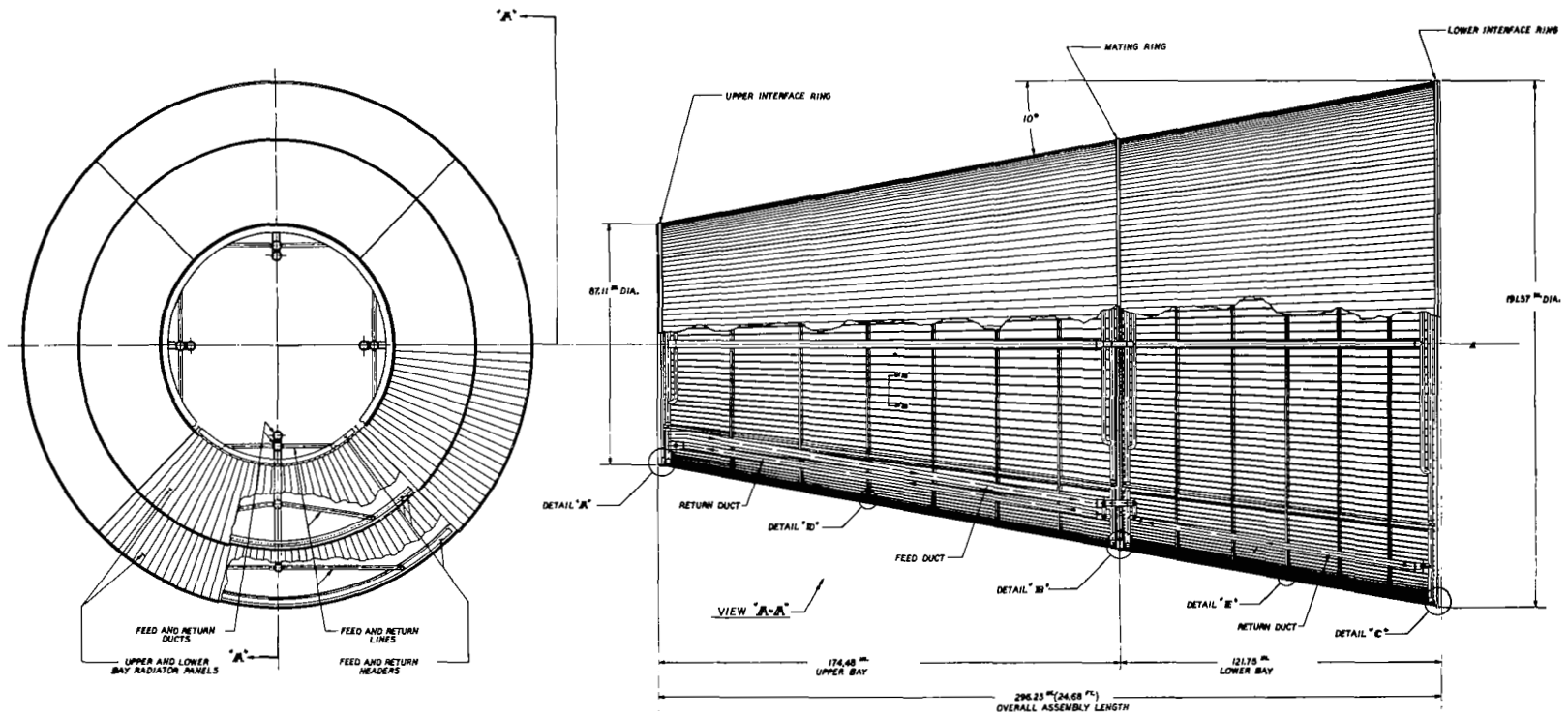
The detailed design of the conduction fin radiator is shown in Figures 7-9 and 7-10. Consideration was given to thermal/dimensional incompatibilities caused by the corresponding expansion and contraction of radiator and feed line sections operating at different temperatures. The use of either a feed line deflection spring or a bellows spring concept can be employed.

Table 7-1. Weight Evaluation Summary - Total Conduction Fin Radiator System



Selected Concepts	Fin Makeup	Fin Thickness t_F (in.)	Average No. of Tubes/ Panel	Tube ID (in.)	Feed Line ID (in.)	Cone Height (in.)	Radiator Area ² (ft ²)	*Radiator Weight (lb)	**System Weight (lb)	Frames (No.) (lb)	Clamps, Splices etc. (lb)	Struct. Weight (lb)	Total Radiator Weight (lb)
$P_o = 0.990$ $\tau = 20,000$ hours													
1	50% Cu 50% SS	0.030	53	0.18	2.12	293	906	2467	2761	21 296	83	379	3140
2	50% Cu 50% SS	0.033	64	0.18	2.09	277.5	841	2587	2821	18 254	81	335	3156
3	50% Cu 50% SS	0.039	73	0.18	2.13	267	801	2754	2952	17 240	80	320	3272
4	60% Cu 40% SS	0.030	51	0.18	2.14	291	897	2459	2760	Eliminated from further consideration in favor of Concept 1			
5	100% SS	0.036	87	0.18	2.25	315	1005	3210	3376	18 254	88	342	3718
6	100% SS	0.039	97	0.18	2.19	298	931	3259	3413	16 225	84	309	3722
7	100% SS	0.044	127	0.18	2.15	273	824	3513	3640	14 200	80	280	3820
$P_o = 0.999$ $\tau = 43,800$ hours													
1	40% Cu 60% SS	0.048	43	0.18	2.13	304	959	3975	4376	A detailed structural analysis was not performed for these cases. The weight of the structure was obtained by a manual calculation and estimates based on results of the 0.990 cases.			
2	50% Cu 50% SS	0.047	41	0.18	2.17	303	956	3979	4396				
3	100% SS	0.059	73	0.18	2.14	314	1000	4896	5110				

*Includes fluid inventory
 **Includes pump power penalty



NOTE: ALL DIMENSIONS IN INCHES
UNLESS OTHERWISE SPECIFIED

Figure 7-9. Conduction Fin Radiator Design Layout

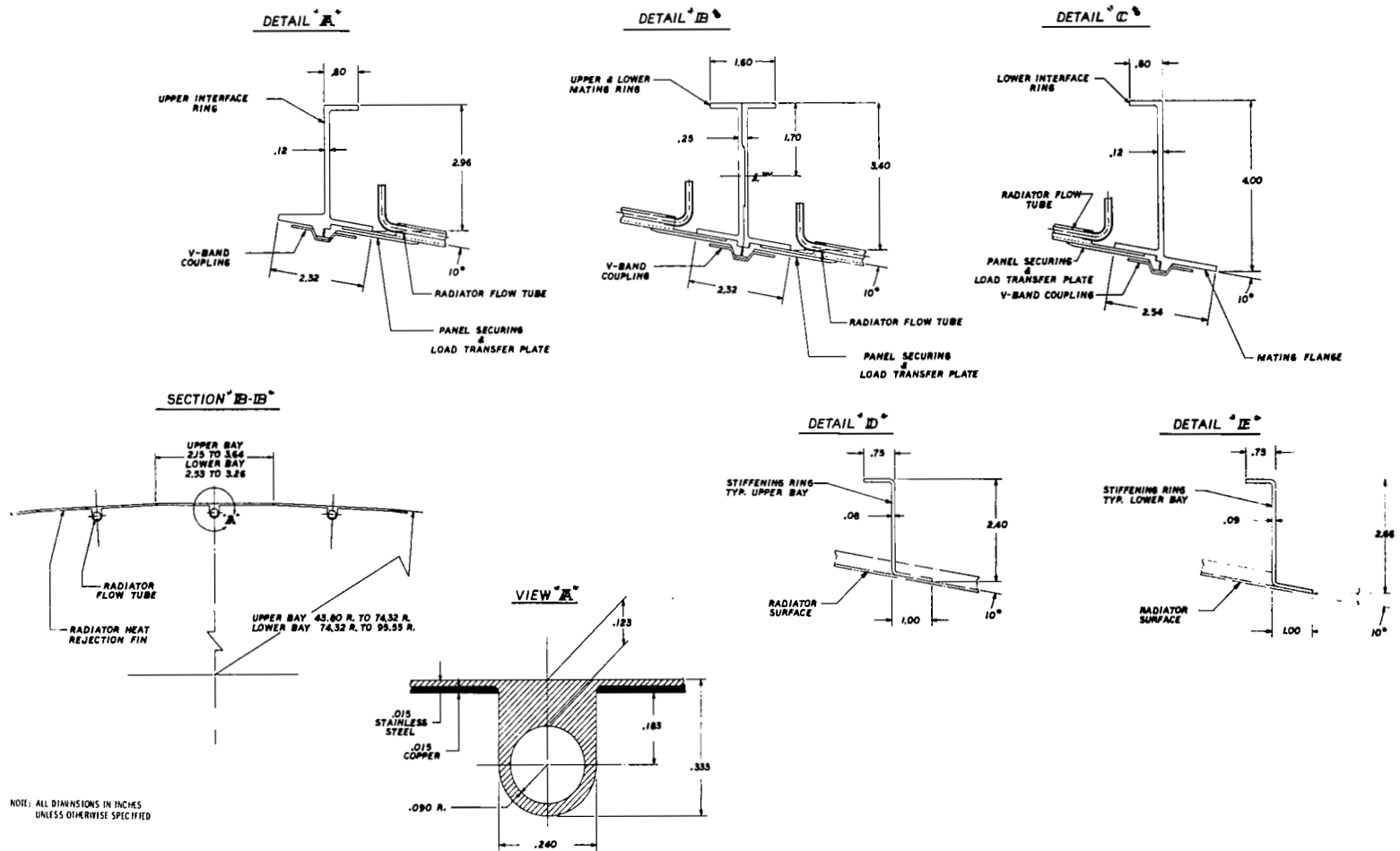


Figure 7-10. Conduction Fin Radiator Design Details

The design shown for the conduction fin radiator employs the use of a deflection spring where the feed line configuration, changed from a circular cross section to a rectangular section, allows for the required dimensional variations. Individual flow tubes are connected to the headers by pigtails designed to compensate for the dimensional changes of the headers and radiator. Fin composition consists of 316 stainless steel on the outer surface and a bonded layer of copper along the inner surface to increase the fin conductance. Plasma sprayed iron titanate high emissivity coating is applied to the outer surface.

The radiator design dictated by the thermal, integration and structural evaluations was supplemented by a conceptual evaluation of the techniques and relative ease of fabrication and assembly. The results of this evaluation are discussed below.

7.2.3 FABRICATION AND ASSEMBLY

7.2.3.1 General

Radiator design, dictated by the thermal, integration and structural evaluations, was supplemented by a conceptual evaluation of the techniques and relative ease of fabrication and assembly.

The vapor chamber fin and conduction fin radiator concepts each involve the fabrication and assembly of a 10 degree half angle cone structure over 20 feet in length with a 15 foot base diameter. Each concept employs an upper and a lower bay, each bay separated into four panel sections. Two panel sections are serviced by one of four independent loops which consist of fluid headers and feed lines. Both radiators require structural stiffeners. The close similarity ends at that point. The conduction fin radiator requires a relatively large number (over 280) primary fluid ducts equally spaced (approximately three inches). The heat transfer between fluid ducts is increased by the addition of a copper layer which is bonded to the stainless steel fin. The vapor chamber radiator consists of fewer primary ducts, spaced about 18 inches apart. The primary heat transfer mode to the radiator surfaces is by heat pipe action rather than fin conduction. Although the number of primary ducts is reduced by a factor of five, the fabrication requirement for large numbers of individual heat pipes

increases the manufacturing difficulty over the conduction fin design (e.g., reference design vapor chamber radiator consists of approximately 10,000 sodium filled heat pipes).

A preliminary fabrication analysis was performed on each radiator to identify potential fabrication techniques and obtain a comparative assessment of the degree of complexity, which can be used as a figure of merit in the comparative evaluation of the radiator concepts. The fabrication and assembly considerations and techniques required for the conduction fin radiator are described below. A similar evaluation of the vapor chamber fin radiator is contained in Section 7.3.

7.2.3.2 Conduction Fin Radiator Fabrication and Assembly

The conduction fin radiator layout and design details are shown in Figures 7-9 and 7-10. Fabrication techniques identified are considered preliminary. In some instances alternative design or fabrication techniques have been identified.

Step 1 - Flow Tube/Fin Assembly (Figure 7-11)

Each coolant duct fin consists of two elements: a machined or extruded stainless steel channel or tube, and a stainless steel/copper bonded fin. The stainless steel tube/fin can be fabricated by extrusion and/or machining. A half section of 0.030 inch wall tubing is then welded to the fin. An alternative to this procedure would consist of the braze of a 0.030 inch wall tube to the extruded or machined fin. A layer of copper is brazed to the stainless fin after the assembly of the fin or after the assembly of the panel in Step 2.

Step 2 - Panel Assembly and Test, Upper and Lower Bay (Figure 7-12)

An assembly jig is used to place and hold individual fins together for welding into a quarter panel. Stainless steel pigtails are inserted on inlet and outlet ends of each coolant duct, headers are positioned and all welds are made. Each quarter panel assembly is flushed clean and inspected for leaks.

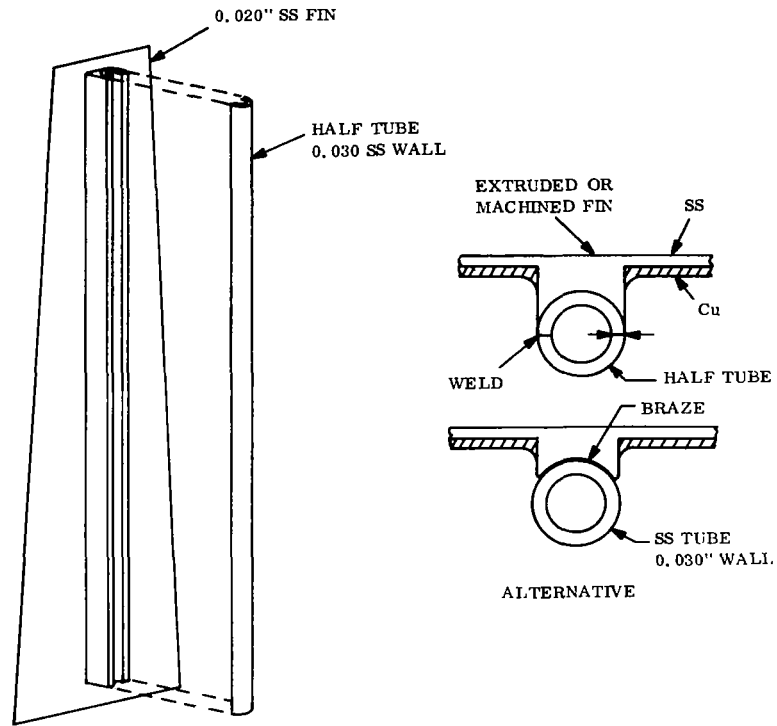


Figure 7-11. Flow Tube/Fin Assembly (Step 1)

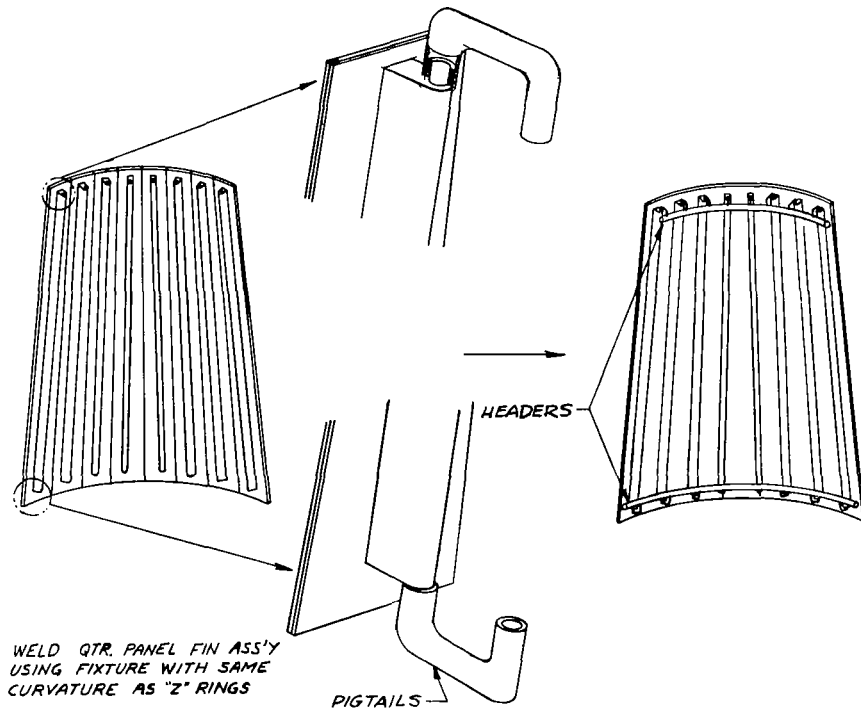


Figure 7-12. Conduction Fin Panel Assembly (Step 2)

Step 3 - Splice Plates and Z Rings (Figure 7-13)

Z rings are fabricated in quarter sections and notched to receive flow tubes and splice plates. An assembly fixture is used to mount, join and rivet together the interface and mating rings. Axial splice plates are then welded or riveted to the Z rings.

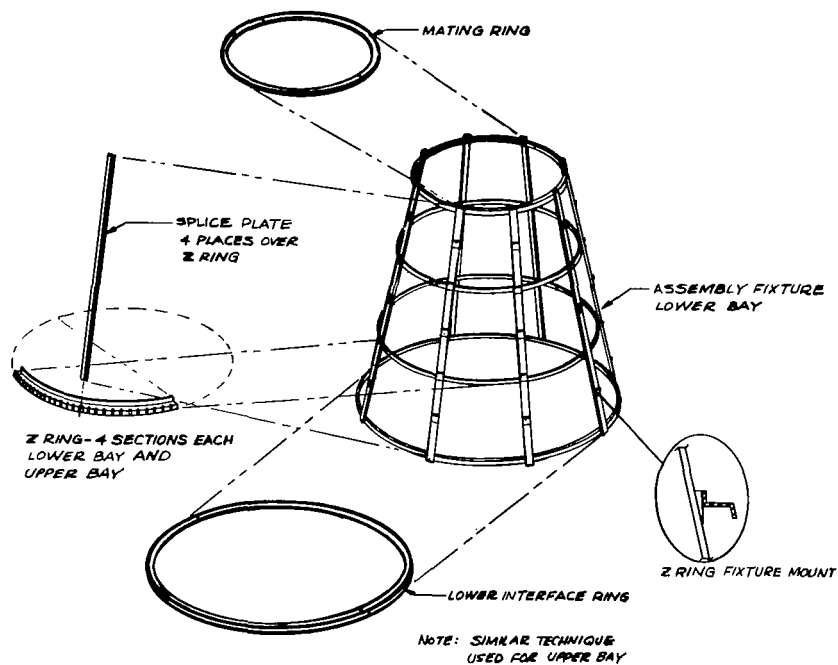


Figure 7-13. Assembly of Z Rings and Mating Rings on Fixture (Step 3)

Step 4 - Lower Radiator Bay Assembly (Figure 7-14)

Lower quarter panels (4) are positioned over the Z rings on the assembly fixture and riveted to the splice plates and Z rings. V-band couplings are installed on the interface rings.

Step 5 - Upper Radiator Bay Assembly (Figure 7-14)

A similar procedure to that described in the preceding steps is followed to assemble the upper bay. The preferred procedure involves the assembly of each bay individually, however, the upper assembly fixture could attach to the lower fixture and assembly of both bays could be accomplished in that configuration.

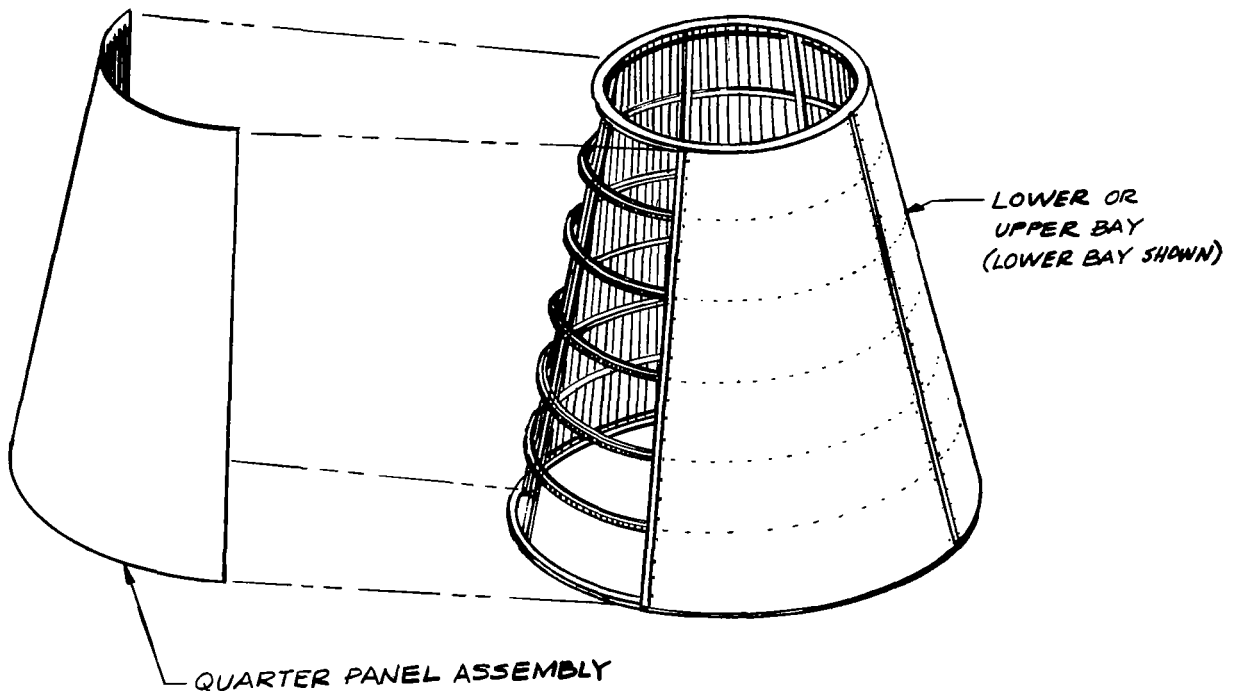


Figure 7-14. Radiator Bay Assembly (Steps 4 and 5)

Step 6 - Removal of Assembly Fixtures

The radiator bays can be supported by a crane to remove and release the partially collapsible lower and upper assembly fixtures.

Step 7 - Lower and Upper Bay Mating (Figure 7-15)

The upper bay is hoisted by crane (hook height at least 25 feet) and positioned over the lower bay for mating. Bolting of the center mating rings and V-band coupling will allow the separation of radiator bays with appropriate consideration for feed lines.

Step 8 - Feed and Return Line Installation

Stainless steel feed lines are installed within the radiator bays. All joints and piping connections are inspected for cleanliness and obstructions, and if required, purged prior to TIG welding. Leak and pressure checks of the entire coolant system are performed.

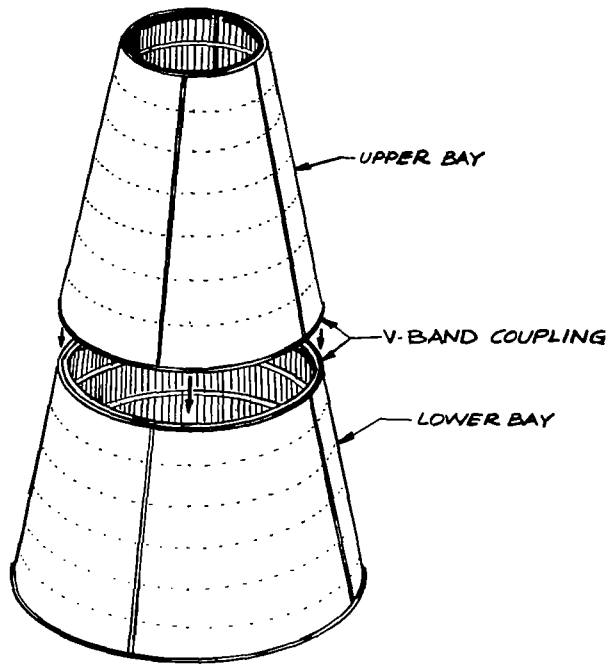


Figure 7-15. Mating of Upper and Lower Bays (Step 7)

Step 9 - Radiator Coating

The radiating surface of the radiator is thoroughly cleaned of foreign matter and given a fine grit blast prior to coating. A plasma spray of iron titanate is applied within a controlled environment. Alternative coating procedures involving individual quarter panels can be considered, however, care must be taken to maintain cleanliness and integrity of the coated radiator surface in subsequent assembly operations.

Assembly Procedure Alternatives

The size of the radiator permits the assembly of individual panel headers and pigtails within the assembled radiator. Individual panel and header tests, however, could not be made prior to installation of the panel on the radiator bay.

7.3 VAPOR CHAMBER FIN RADIATOR

7.3.1 VAPOR CHAMBER FIN RADIATOR ANALYSIS

On the basis of the analysis presented in Section 5 and the tests of Section 6, Geometry 2 (sandwiched rectangular channel) was selected as the concept to be input to the Spartan VI optimization code and integrated into a total radiator system. Sodium was selected as the vapor chamber fluid. The closed primary duct concept examined in Section 5.2 was employed. The overall radiator requirements for both the vapor chamber fin and conduction fin radiators were those specified in Section 3.

7.3.1.1 Thermostructural Analysis

The feedline header and primary duct configuration for the vapor chamber fin radiator used in the analysis and subsequent design is essentially the same as that proposed for the conduction fin radiator. Fluid flow, structural capability and thermal discontinuity considerations are important; however, length restrictions, fabrication and operational characteristics of heat pipes are added parameters in the analysis. The relatively short heat pipe/vapor chamber lengths dictated by the thermal analysis requires the spacing of primary fluid ducts approximately 18 inches apart. The vertical placement of these primary ducts around the circumference of the radiator, permits their use as longitudinal stiffeners and readily integrates with the separate radiator loop and panel concept. The representative header, primary duct and vapor chamber orientation selected is shown in Figure 7-16.

7.3.1.2 Thermal/Design Optimization

The analysis to optimize the radiator weight and design was performed by the Spartan VI computer code. A major portion of the input data was obtained from the results of the evaluation presented in Section 5. The Spartan VI analysis included the effects of the overall meteoroid environment, radiator thermal and hydraulic requirements, as well as vapor chamber operational characteristics. A series of optimized cases were generated, employing sodium as the vapor chamber fluid in conjunction with the closed primary duct concept. The optimized variables included primary duct width, number of ducts and duct height. Geometric values for the vapor chamber passage were obtained from the results presented

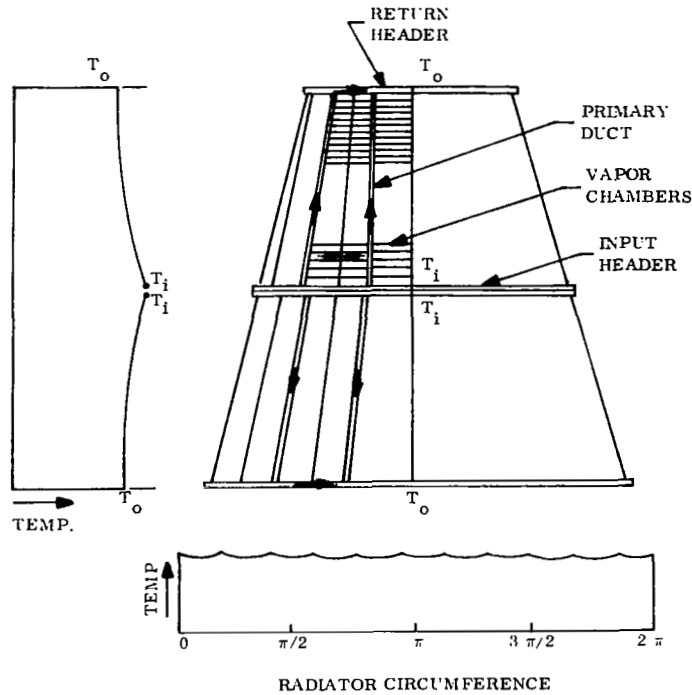


Figure 7-16. Header, Primary Duct, Vapor Chamber Orientation

in Section 5. Results of the weight optimization analysis are given in Figure 7-17 for overall survival probabilities of 0.990 and 0.999 where three of four radiator loops are assumed to survive. Typical characteristics of the optimum cases are shown in Table 7-2.

The inside duct height optimized at the minimum allowable value of 0.250 inch; it was assumed that further reduction of this parameter would involve fabrication problems. Vapor chamber condensing lengths optimized at values less than nine inches which agreed with results obtained in the earlier phases of the study. At the program outset, optimized VCF lengths of 12 to 20 inches were anticipated. Longer VCF lengths reduce the required number of primary fluid ducts and associated armor. However, the optimization procedure found the shorter VCF lengths to be desirable because of the minimal armor thickness required by the redundant primary fluid duct concept (3 of 4 survive).

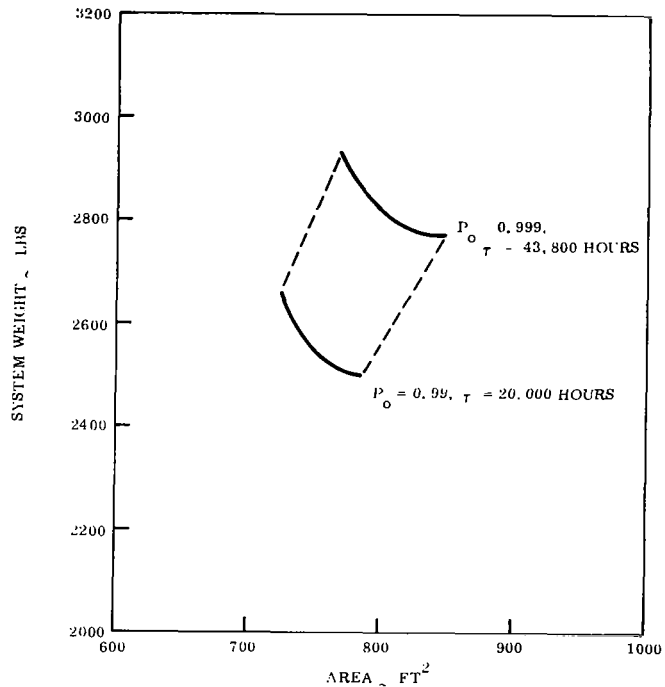


Figure 7-17. Vapor Chamber Fin Radiator Optimization Results

Table 7-2. Optimum Vapor Chamber Fin Radiator Characteristics

Characteristics	Survival Probability/Mission Time	
	0.99/20,000 hrs	0.999/43,800 hrs
Radiator Area, Ft ²	785	848
Radiator Matrix Weight, lb (including feed and return lines)	2464	2734
Number of Panels	8	8
Number of Primary Fluid Ducts per Panel	6	6
Inside Duct Height, inches	0.250	0.250
Inside Duct Width, inches	2.80	2.50
Duct Wall Thickness, inches	0.021	0.044
Number of Vapor Chambers	9120	9851
Vapor Chamber Condensing Length, inches	8.58	8.93
Vapor Chamber Width, inches	1.24	1.24
Vapor Chamber Wall Thickness, inches	0.020	0.020
Pump Work, kilowatts (hydraulic)	0.138	0.150

A more complete understanding of the important parameters affecting radiator weight and area was obtained by varying several of the key parameters. Examination of the optimized cases indicates a large temperature drop across the primary fluid boundary layer. For the reference design (0.99 meteoroid survival probability) the temperature drop from the bulk fluid to the inside wall was 42^oF. This temperature drop decreases the effective radiator temperature and raises the radiator area. With the present design this ΔT can be reduced by increasing the primary duct width or the total number of ducts; both of these perturbations cause an increase in vulnerable area. Therefore, the magnitude of the primary duct fluid film drop is a trade-off between total radiator area (or weight) and the primary duct armor weight requirements.

The primary fluid ΔT may also be reduced by the addition of extended surface areas within the duct. Often, advantages accrued from this type of design complexity are offset by the fabrication problems introduced. A study was performed, using Spartan VI, to show the trade-off between the radiator weight and gap size between the primary duct fins. Figure 7-18 shows the effect of introducing fins (0.010-inch thick) in the primary fluid duct on radiator weight and area for the optimized case at a 0.99 probability and a lifetime of 20,000 hours. Additional cases were run to obtain the locus of optimized radiators as a function of weight and area for two meteoroid survival probability conditions, these are illustrated in Figure 7-19. For these radiators a minimum gap size of 0.100 inch was allowed in order to lend an element of manufacturing credibility to the designs. However, the information presented in Figure 7-18 suggests that further gains from increasing the number of fins would be inconsequential.

7.3.1.3 Structural Analysis

The structural analysis of the reference design consisted of an extension of the approach which was used in the evaluation presented in Section 5.3. General, panel and local instabilities were considered. Local instabilities were prevented by maintaining the vapor chamber geometric values used in the previous analysis. In order to ensure against panel instability circumferential Z rings were added. Results of the evaluation indicated that a minimum of five Z rings spaced every 18 inches plus two interface rings were required for

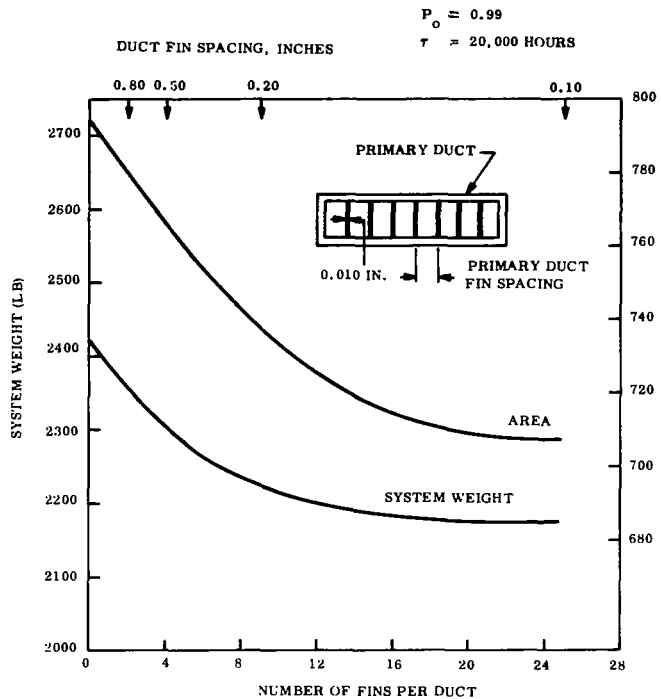


Figure 7-18. Effect of Extended Surfaces in Primary Fluid Duct on Vapor Chamber Fin Radiator Weight

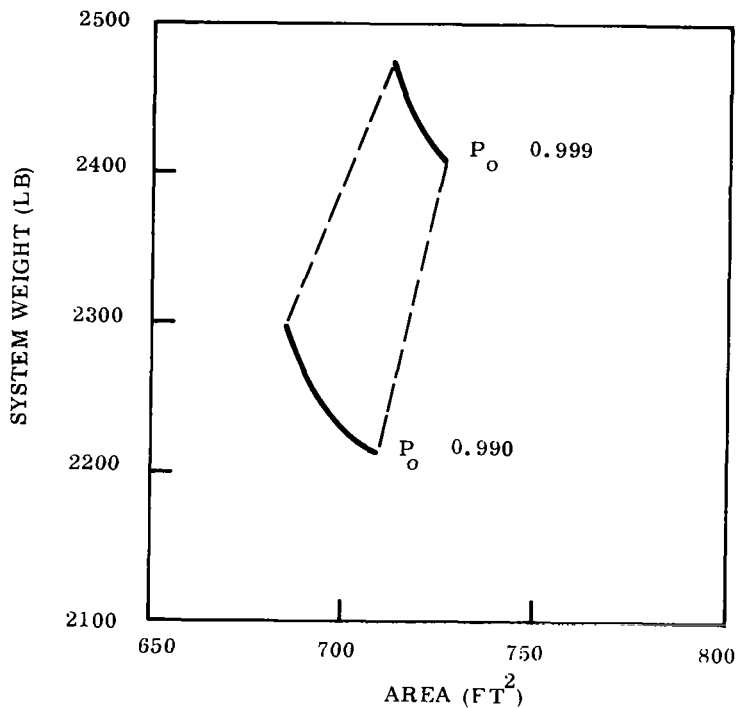


Figure 7-19. Vapor Chamber Fin Radiator Weight/Area with Optimum Number of Primary Duct Fins

the lower bay and six Z rings spaced every 22 inches plus two interface rings were required for the upper bay. General instability was prevented by increasing the cross-sectional area of the primary fluid ducts. Vapor chamber fin radiator weights, including structure, are given in Figure 7-20 as a function of area for the two levels of meteoroid survival probability. Also shown are curves for the design concept in which conduction fins are provided within the primary fluid ducts.

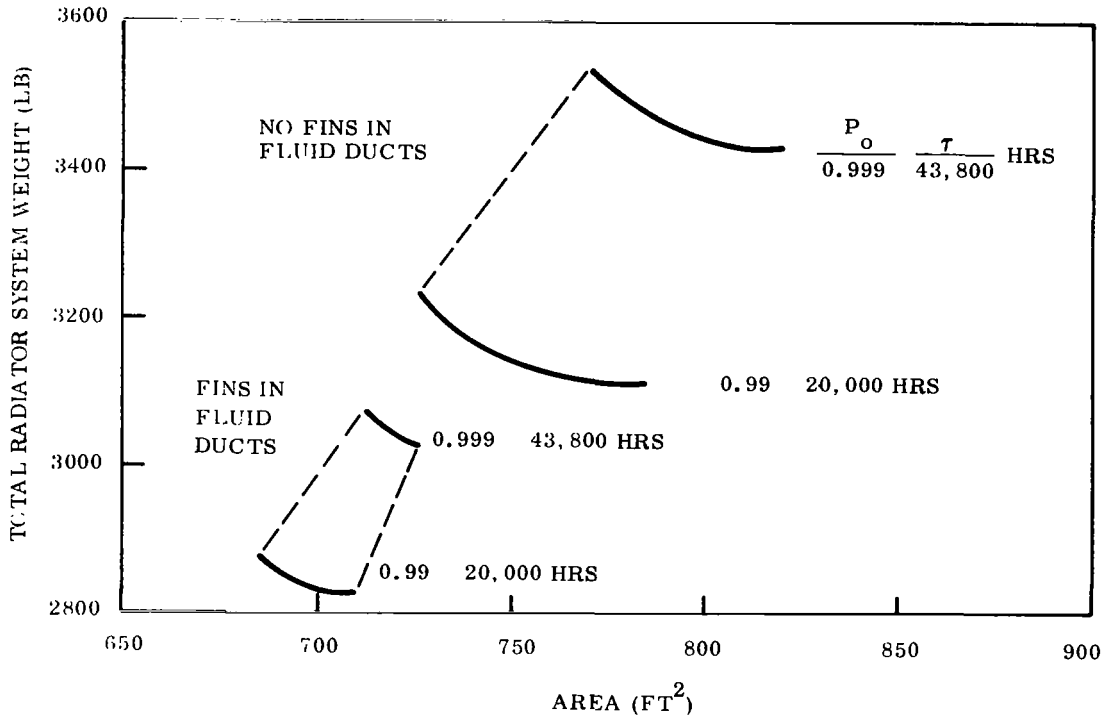


Figure 7-20. Vapor Chamber Fin Radiator Weights Including Structure

7.3.1.4 Weight Analysis

Characteristics of several radiator cases considered including the minimum weight designs are listed in Table 7-3. The total radiator weight is comprised of panel weight, structural weight fluid, headers and feed lines and a pumping power weight penalty. The pumping power weight penalty for the vapor chamber radiator is considerably less than the conduction fin radiator due to the shorter flow distances and larger flow areas.

Table 7-3. Evaluation Summary - Vapor Chamber Fin Radiator Characteristics

Selected Cases	Spartan VI Thermal Evaluation											Structural Evaluation			Total Radiator Weight (lb)	
	Fluid Ducts Per Panel	Inside Duct Height (in.)	Inside Duct Width (in.)	Duct Wall Thickness (in.)	Number of Vapor Chambers	Vapor Chamber Condenser Length (in.)	Vapor Chamber Width (in.)	Vapor Chamber Wall Thickness (in.)	Hydraulic Pump Work (kw)	Radiator Area (ft ²)	Radiator Weight *(lb)	Radiator System Weight **(lb)	Stiffener Frames (No.) (lb)	Clamps Splices etc. (lb)		Structural Weight (lb)
$P_o = 0.990$ $\tau = 20,000$ hours 1 Minimum Weight 2 3	6	0.25	2.80	0.021	9,120	8.58	1.24	0.020	0.138	785	2464	2498	15 210	405	615	3113
	7	0.25	3.55	0.036	10,141	6.76	1.24	0.020	0.131	748	2735	2768	No detailed structural evaluation was performed for these cases			
	6	0.25	2.00	0.020	8,239	8.98	1.24	0.020	0.206	709	2215	2266	No detailed structural evaluation was performed for these cases			
	(Finned Duct Employed - Gap = 0.100 in., Fin Thickness = 0.010 in.)															
$P_o = 0.999$ $\tau = 43,800$ hours 1 Minimum Weight 2 3	6	0.25	2.05	0.044	9,851	8.93	1.24	0.020	0.150	848	2734	2771	15 225	439	439	3435
	6	0.25	3.60	0.052	8,939	8.15	1.24	0.020	0.133	770	2904	2937	No detailed structural evaluation was performed for these cases			
	6	0.25	2.45	0.043	8,264	8.73	1.24	0.020	0.181	712	2474	2519	No detailed structural evaluation was performed for these cases			
	(Finned Duct Employed - Gap = 0.100 in., Fin Thickness = 0.010 in.)															

* Includes feed lines and fluid inventory

** Includes pump power penalty

7.3.2 VAPOR CHAMBER FIN RADIATOR DESIGN

Both the conduction fin and the vapor chamber fin radiators were limited to the requirements and envelope restrictions as specified in Section 3. The selected vertical orientations of the primary ducts necessitated the placement of the vapor chambers in the circumferential direction. The relative shortness of the individual vapor chambers as determined from the evaluation presented in Section 5.1 allowed the design and fabrication of straight vapor chamber fins. The chambers are laid over the primary ducts affording the ducts additional meteoroid protection and improving overall radiator fin efficiency.

The detailed design of the radiator is shown in Figures 7-21 and 7-22. Each panel has been subdivided into several segments to allow for easier fabrication and replacement of segments and panels. A reduction in the number of segments is possible with an associated reduction in total radiator weight due to the elimination of several joining splice plates.

Three significant temperature drops occur between the primary radiator fluid and the radiating surface:

1. Primary duct fluid to evaporator outer wall ΔT .
2. Evaporative ΔT .
3. Condensing ΔT .

The first ΔT is minimized by providing a relatively large heat transfer surface area from the bulk fluid to the working surface of the primary duct. The ΔT between the evaporator and primary duct mating surfaces is minimized by using a metallurgical bonding process. The second ΔT occurs across the evaporator necessitating an efficient design of the evaporative wick and the provision of adequate evaporative and primary duct contact area to permit an even temperature distribution. The condensing temperature drop is largely dependent upon the thickness of the condensing film. Efforts to reduce this temperature drop were directed toward identifying a condensing wick design which would limit the film thickness, but at the same time provide sufficient flow area and refluxing capability for heat flux requirements exceeding 80,000 BTU/hour-ft². The condensing wick identified in the design

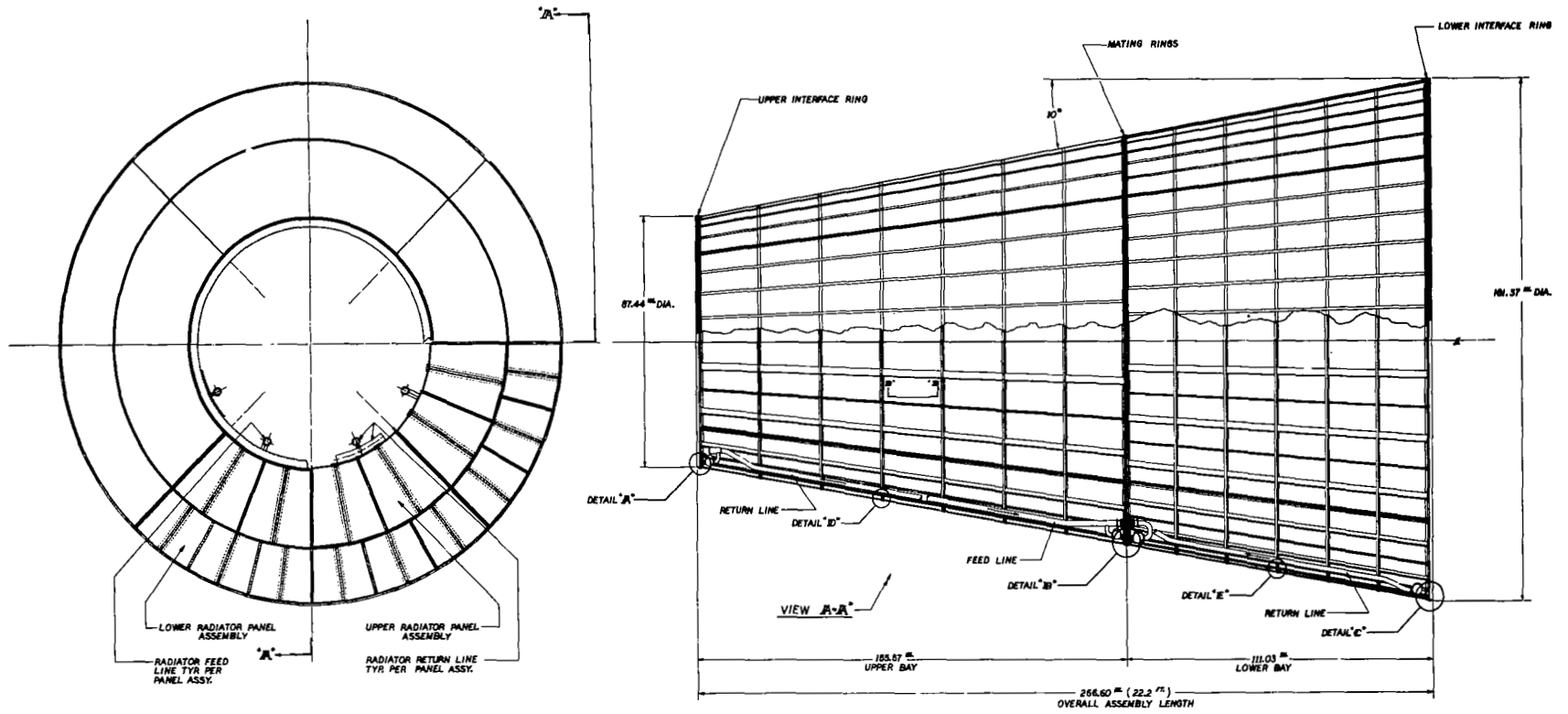


Figure 7-21. Vapor Chamber Radiator Design Layout

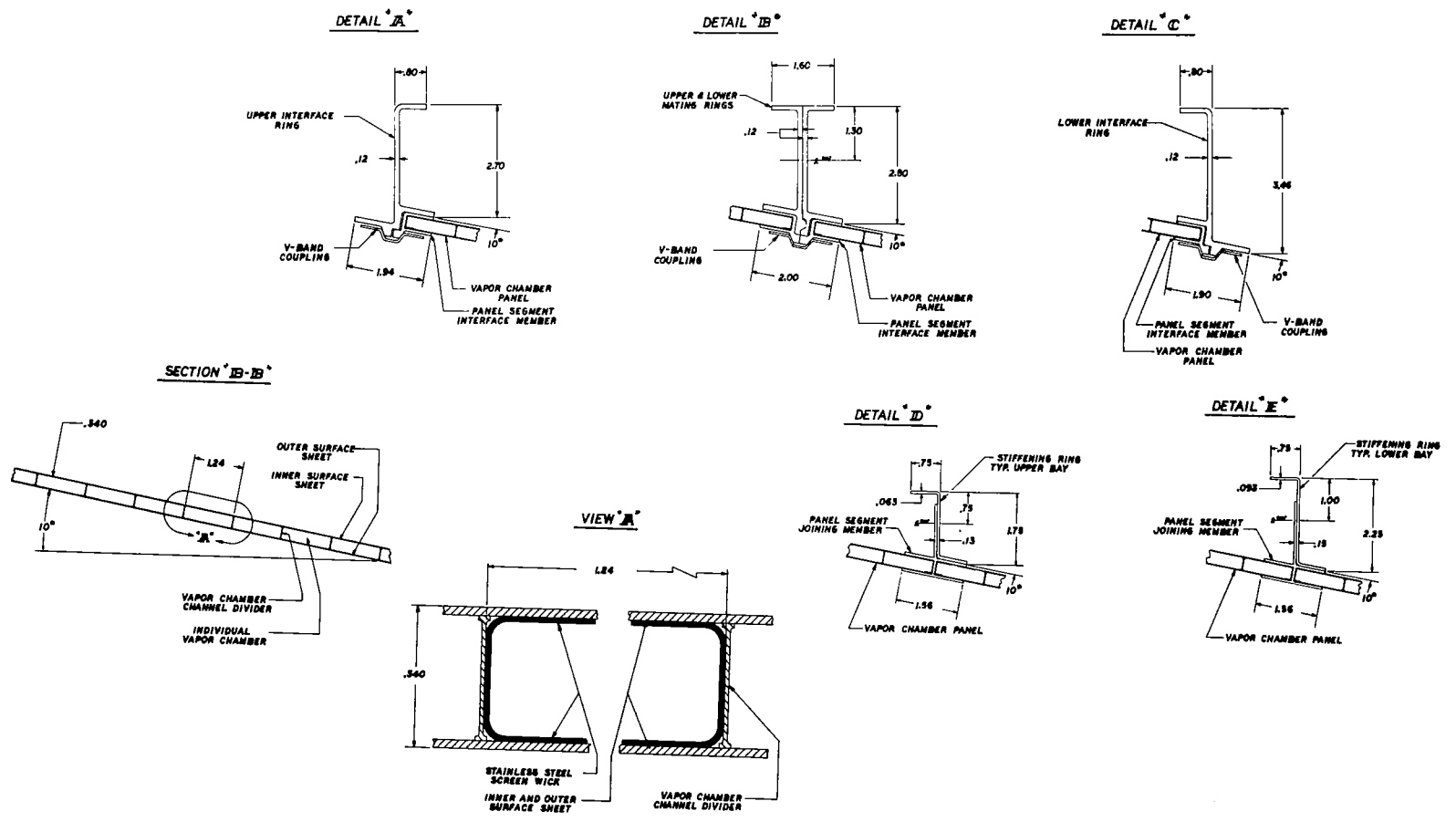


Figure 7-22. Vapor Chamber Radiator Design Details

consists of two layers of 150 mesh stainless steel screen wrapped around all sides of the chamber. Although an annulus wick of a single layer of 150 mesh screen supported off the chamber wall by 25 mil wire was tested during the test program, test results were inconclusive and therefore this configuration is not shown in the radiator design.

Concepts similar to those designed for the conduction fin radiator are provided for the elimination of thermal/dimensional incompatibilities. A bellows spring is shown for the dimensional control of the feed lines; however, a deflection spring concept similar to that shown with the conduction fin radiator could also be employed.

7.3.3 FABRICATION AND ASSEMBLY

The vapor chamber radiator layout and design details are shown in Figures 7-21 and 7-22. A concept and notable alternatives for the fabrication of the complete radiator are given in the steps below.

Step 1 - Primary Coolant Ducts (Figure 7-23)

The primary coolant duct is made of 316 stainless steel and carries the NaK liquid metal coolant at temperatures as high as 1200⁰F. The base, with its structural stiffener, and the cover plate are machined from bar stock and welded together. End plates and bushings on each end of the duct are welded in place. Cleaning and leak tests are made during and after assembly and inlet and outlets are temporarily capped.

Step 2 - Vapor Chamber Panel Subassembly (Figures 7-24, 7-25, and 7-26)

Two techniques appear most practical for the fabrication and assembly of the vapor chamber panels. Both techniques discussed provide the opportunity of welding a majority of the critical heat pipe seals, whereas other techniques evaluated consisted of a larger quantity of brazes. The sealing of each individual heat pipe (vapor chamber) is critical to the operation of the radiator and requires extremely careful inspection and controlled procedures.

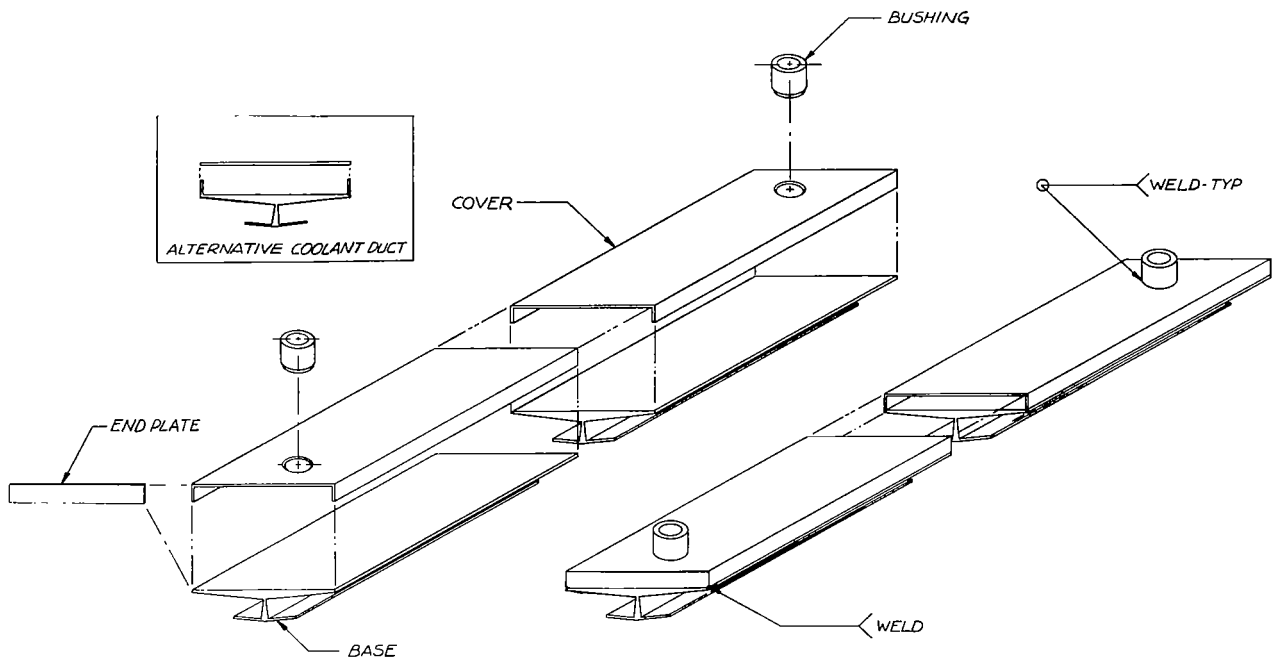


Figure 7-23. Primary Coolant Duct Fabrication and Assembly (Step 1)

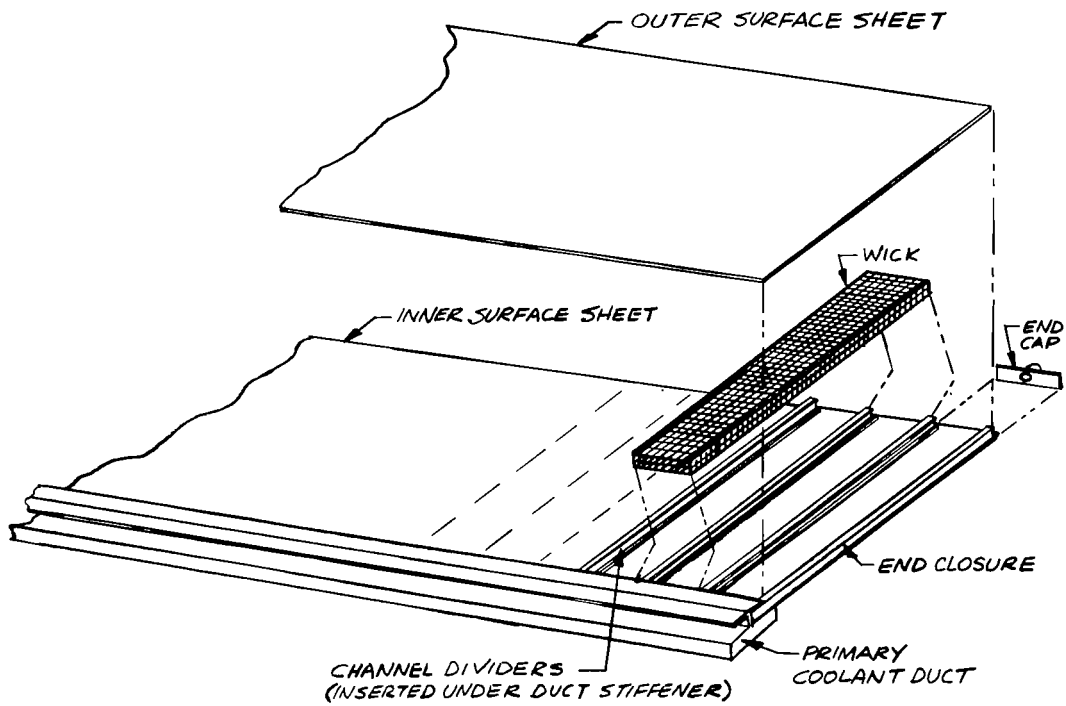
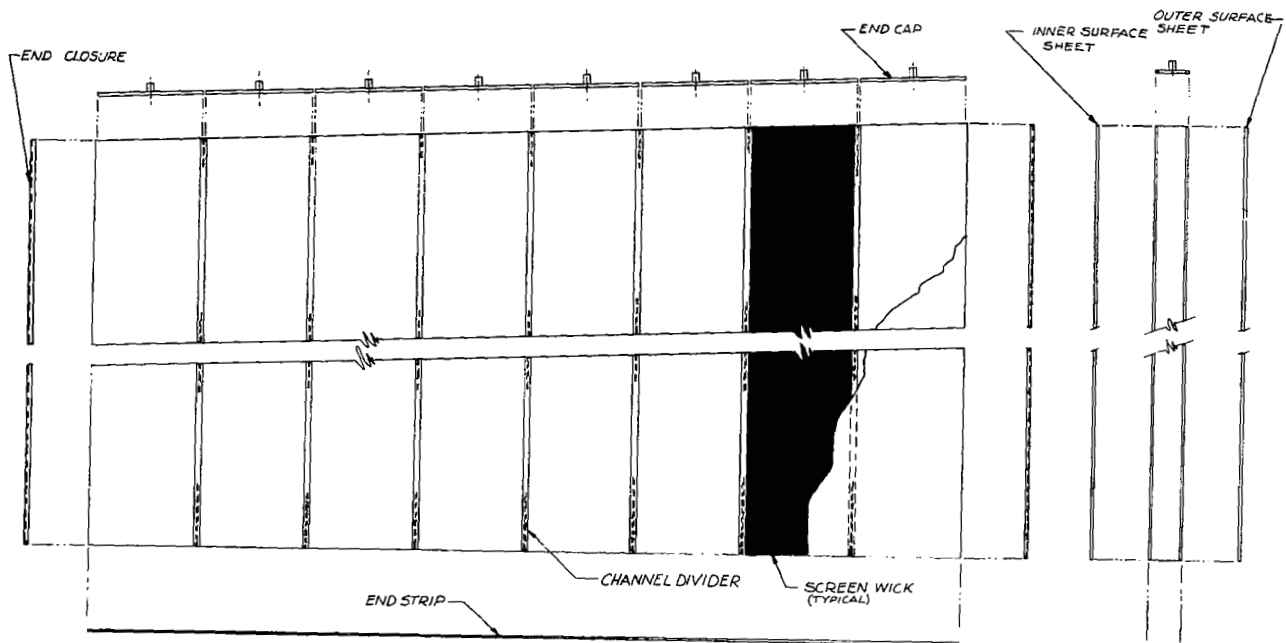


Figure 7-24. Vapor Chamber Panel Subassembly - Alternative 1 (Step 2)



*ASSY SEQUENCE OF
PANEL SEGMENT*

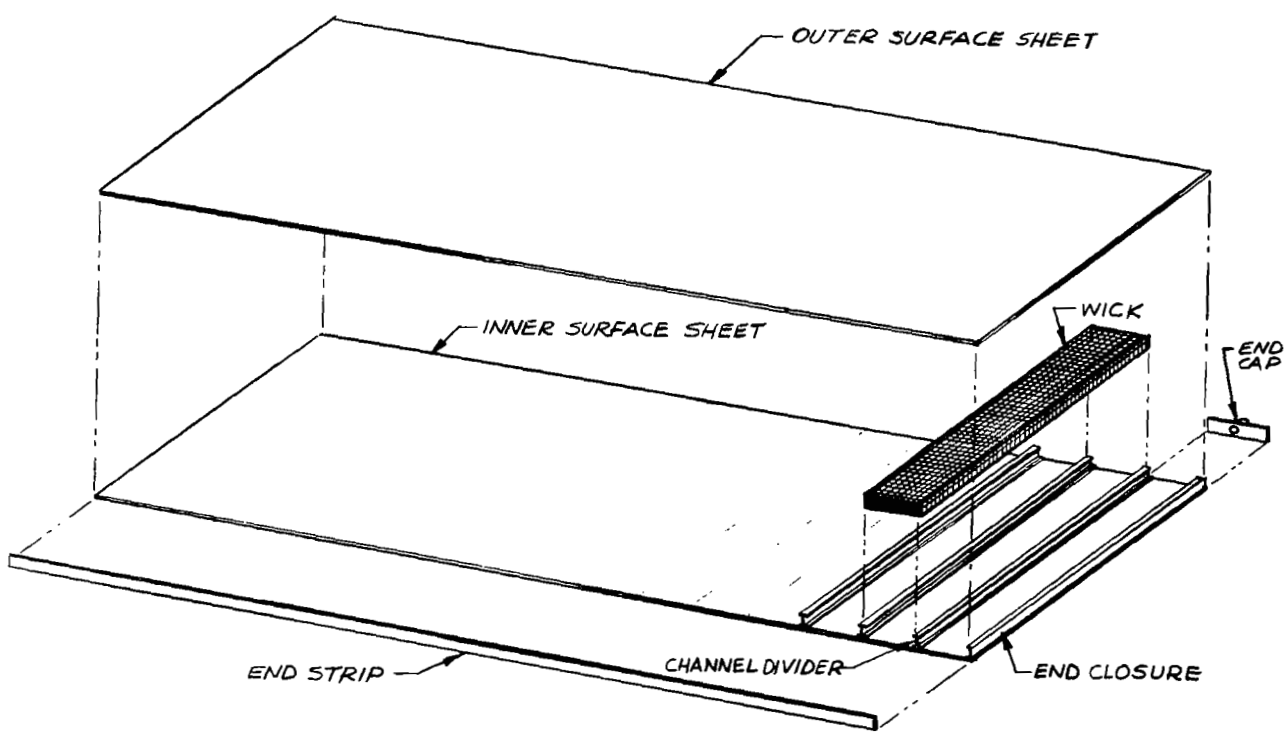


Figure 7-25. Vapor Chamber Panel Subassembly - Alternative 2 (Step 2)

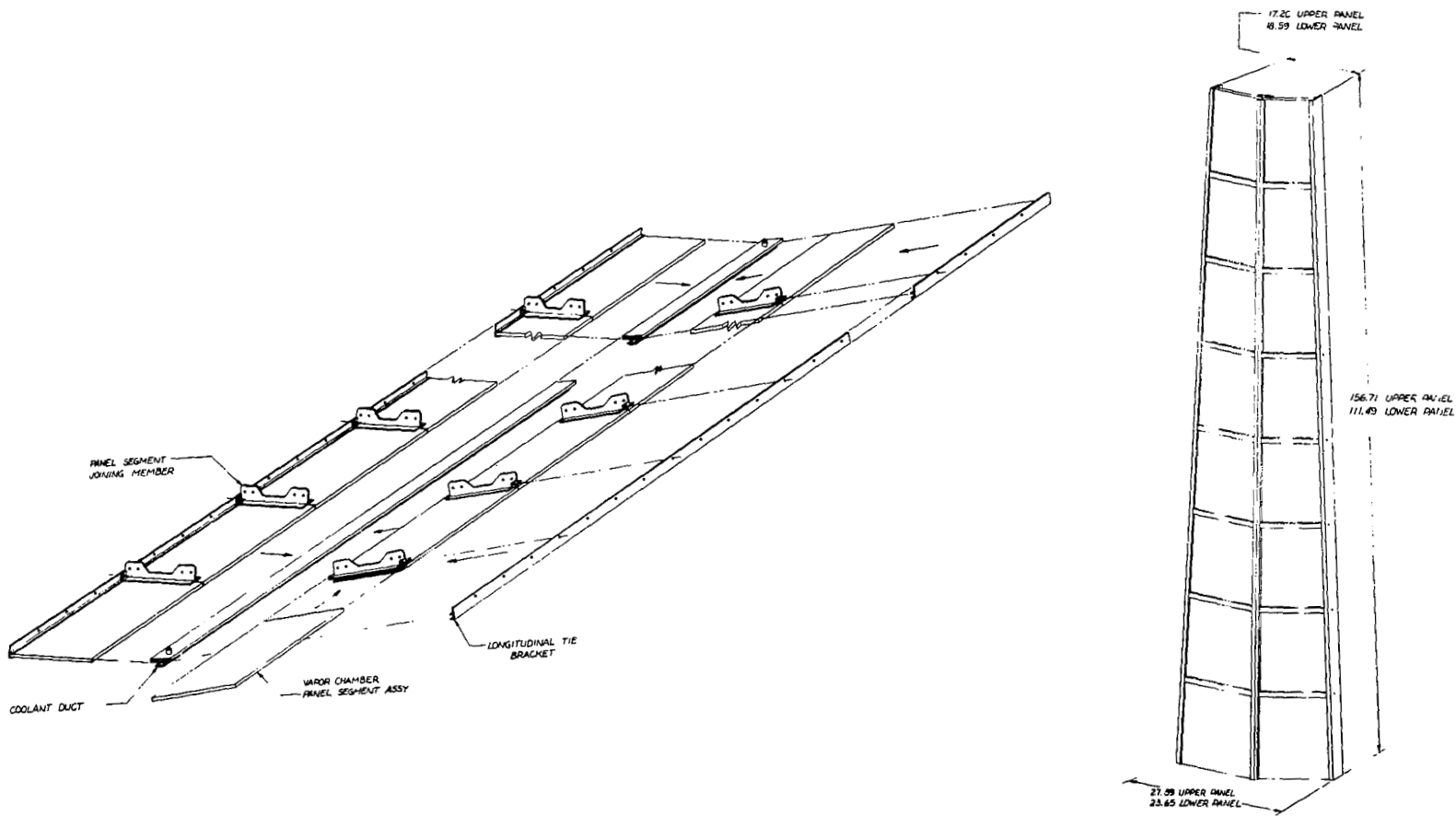


Figure 7-26. Vapor Chamber Panel Subassembly - Alternative 2 (Step 3)

1. Alternative 1 (Figure 7-24). The vapor chamber panel consists of two 20 mil sheets of 316 stainless steel separated by equally spaced 10 mil channel dividers which form the individual heat pipes. A wick consisting of two layers of 150 mesh stainless steel screen is wrapped around all sides of each chamber. A preformed wick is considered.
 - a. The fabrication sequence begins with the placement, spacing and welding of the channel dividers on the inner surface sheet. A fixture holding the channel dividers in position could be prepared, the inner surface sheet laid over them, and the individual dividers EB or TIG welded. If brazing were to be performed, a careful selection of brazing sequences and temperatures would be required.
 - b. Each panel, separated by a joining member, is subsequently inserted into the primary coolant duct. All interfaces with the duct are carefully welded with the exception of the thermal contact surface of the vapor chamber. (This surface is brazed after all the welds are made on all panels with a silver/copper alloy braze at a temperature of approximately 1570^oF.)
 - c. Preformed wicks cut to size are then laid in each channel and spotted to the inner surface sheet and the channel dividers. Special forming and positioning tools will be required to perform this task.
 - d. The outer surface sheet is now positioned over the assembly and welds are made along the primary coolant duct and each channel divider. The remaining spot welds are made in the upper surface of the wick. The braze of the assemblies to the primary duct can be made at this time.
 - e. Cleanliness and individual chamber integrity are vitally important. End caps are welded. A thorough cleaning, bake out and leak test must be performed prior to liquid metal charging.
 - f. Liquid metal charging and final EB welds and sealing are performed in a vacuum environment. (Consideration should be given to the performance of items (e) and (f) within the same environment to reduce the possibility of unwanted foreign material.
2. Alternative 2 (Figures 7-25 and 7-26). Alternative No. 2 is pictorially described in Figures 7-25 and 7-26. Although this alternative involves the use of an additional end plate next to the primary duct, it has the advantage of permitting a leak check of a vapor chamber panel subassembly prior to its installation in the primary duct. All surface sheets, end caps and channel dividers are welded and/or brazed, wicks spot welded and the entire panel cleaned and leak checked prior to the primary duct braze. Brazing of the subassembly to the primary coolant duct must be performed prior to liquid metal charging due to the temperatures involved. Final bake out, cleaning, charging and end cap sealing would again be performed within a vacuum environment.

Step 3 - Longitudinal Tie Brackets and Joining Members (Figure 7-26)

Longitudinal stiffeners and tie brackets are mounted along each edge of the assembly as shown in the figure (Alternative 2 described). Each bracket and joining member is TIG welded to the vapor chamber assemblies.

Step 4 - Panel Assembly and Test (Figure 7-27)

The individual subassembly panels are assembled into quarter panel assemblies by riveting together the longitudinal stiffeners. Inlet and outlet headers and pigtail piping are installed and welds made. Leak and flow tests of each quarter panel assembly can now be made prior to final assembly and installation of feedline connections.

Step 5 - Frame Assembly (Figure 7-28)

The lower bay structure support frame (interface rings, Z ring stiffeners and longerons) are assembled as a riveted frame. The upper bay frame is similarly assembled. Bolted assemblies are used where replacement capability is desired.

Step 6 - Lower and Upper Bay Assembly (Figure 7-28)

Final assembly of the radiator bays consist of riveting or bolting the individual panel assemblies (four per bay) to the frame. Bolted assemblies are used where replacement capability is desired.

Step 7 - Final Assembly (Figure 7-28)

Structural attachments are made between the two bays and at the interface rings with the addition of V-band couplings. Feedline piping and expansion manifolds are installed. All joints and connections are inspected for cleanliness and obstructions, purged and subsequently TIG welded. Leak and pressure checks of the entire coolant system are performed.

Step 8 - Radiator Coating

The radiating surface is thoroughly cleaned of foreign matter and given a fine grit blast prior to coating. A plasma spray of iron titanate is applied within a controlled environment.

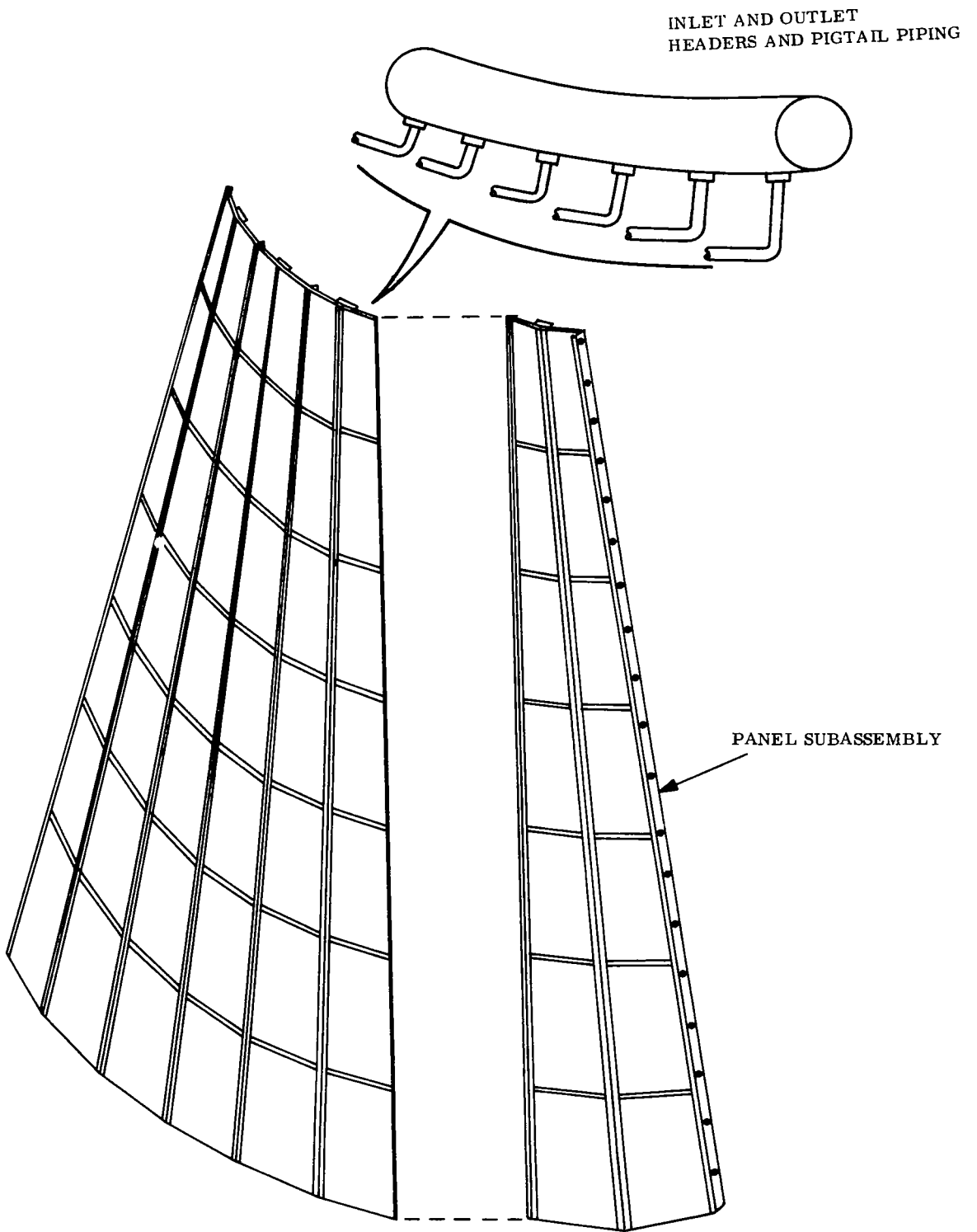


Figure 7-27. Panel Assembly (Step 4)

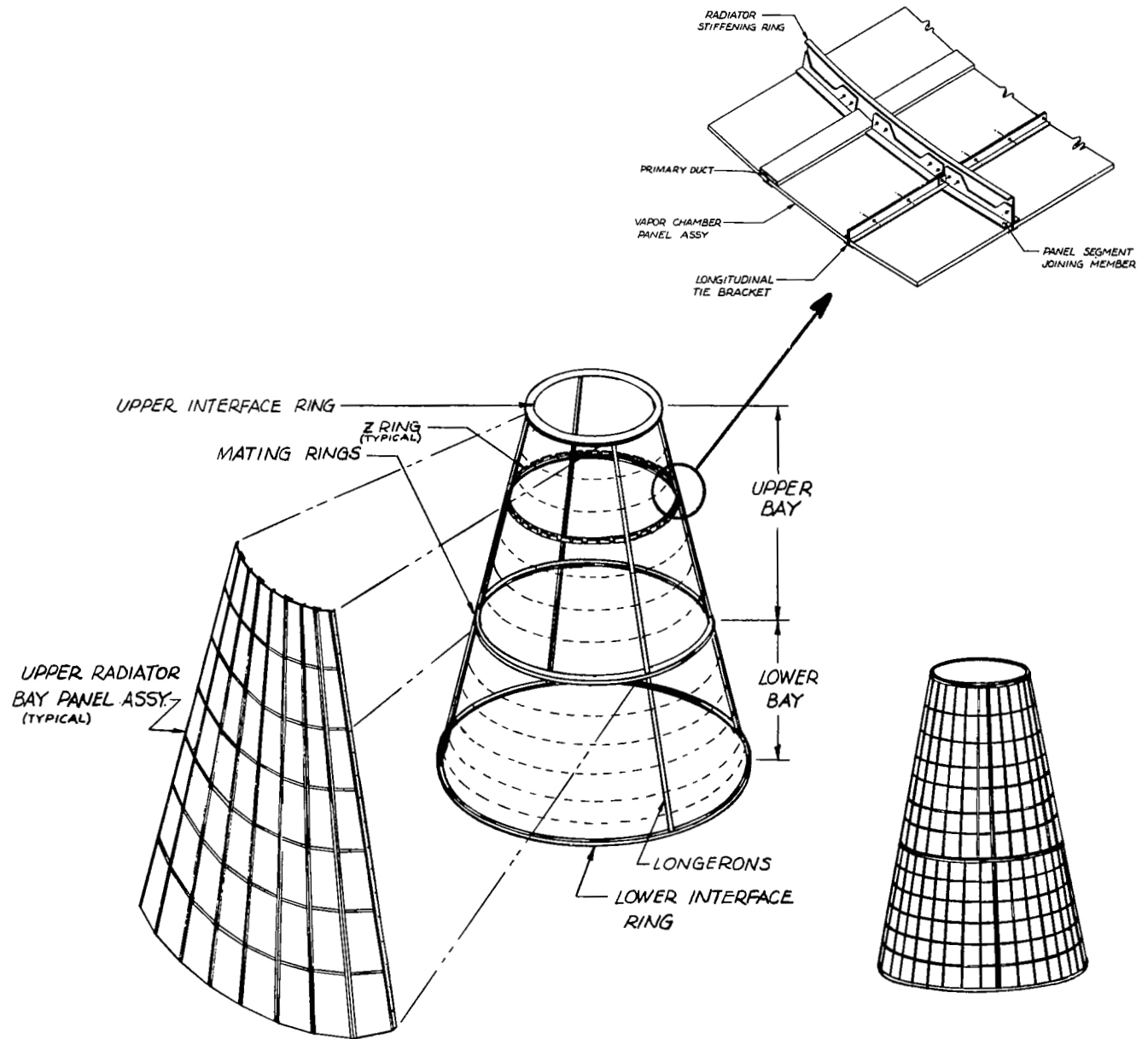


Figure 7-28. Final Assembly (Step 5 and 6)

Alternative coating procedures can be considered if coating facilities are size limited. Coating can be applied to quarter panels; however, care must be taken to maintain cleanliness of the radiator surface and integrity of the radiator coating.

7.4 STARTUP CONSIDERATIONS

7.4.1 GENERAL

The ultimate selection of a liquid metal radiator concept is affected by operational considerations such as the ability of the entire system to successfully startup, and possibly restart in space.

The design implications of startup constitute a minor effect upon system weight for most components of proposed nuclear space power systems. However, the unique function and configuration of liquid metal heat rejection systems may preclude a simple solution for this component. In fact, by its very nature, the radiator will be the coldest component within the power system loop, thereby making it susceptible to working fluid freezeup.

The solution of this specific startup problem is dependent on a particular mission plan and powerplant/radiator and launch vehicle configuration and characteristics.

No firm design and performance conclusions concerning the solution to the startup problem appears readily obtainable. The intent is to compare the inherent characteristics of the vapor chamber fin and conduction fin radiators so as to qualitatively evaluate their susceptibility to the startup problem. Eventually, with a particular set of mission and design requirements, a quantitative comparison of these two concepts can be made by translating the solutions into design concepts and additional system weight.

The weight and design concepts required of supporting systems to effect startup will depend on the following factors:

1. Type of fluids in system
2. Total fluid inventory
3. Fluid location and disbursement
4. System/Mission considerations.

Each of these factors are comparatively discussed in relation to the two radiator concepts.

7.4.2 TYPE OF FLUID IN SYSTEM

Both the conduction and vapor chamber fin radiators contain NaK (78 w %k) as the primary fluid which has a melting point of 12°F . This fluid will likely be liquid at and during launch with appropriate insulation from the upper S-II cryogenic tank. Actually during ascent, skin heating rates can considerably influence radiator temperatures where no external shroud is provided. Figure 7-29 shows the skin temperature of the nine degree half angle three-stage Saturn V launch adapter during ascent. Radiator skin temperatures are expected to be over 200°F during this period. Once earth orbit is achieved, the effective sink temperature for most orbital conditions will be above 12°F . This is shown in Figure 7-30. It can be concluded that under most earth orbital conditions the NaK-78 radiator would remain liquid and not present a major freezing problem. Strip heaters or an isotope heater can be applied in susceptible locations. Circulation of the working fluid can also be a means of preventing localized freezeup.

The startup of a radiator during an interplanetary mission where the effective sink temperature is lower than 12°F , will require freezeup preventative techniques.

The vapor chamber radiator also contains a heat pipe (vapor chamber) fluid which in the case of the reference design is sodium with a melting point of 208°F . The presence of frozen sodium in the vapor chamber cannot be cited as a definite disadvantage since heat pipes start operating from a frozen condition without any major time delay. The location within the heat pipe of the frozen sodium is important however, a discussion of this point is presented in subsequent paragraphs.

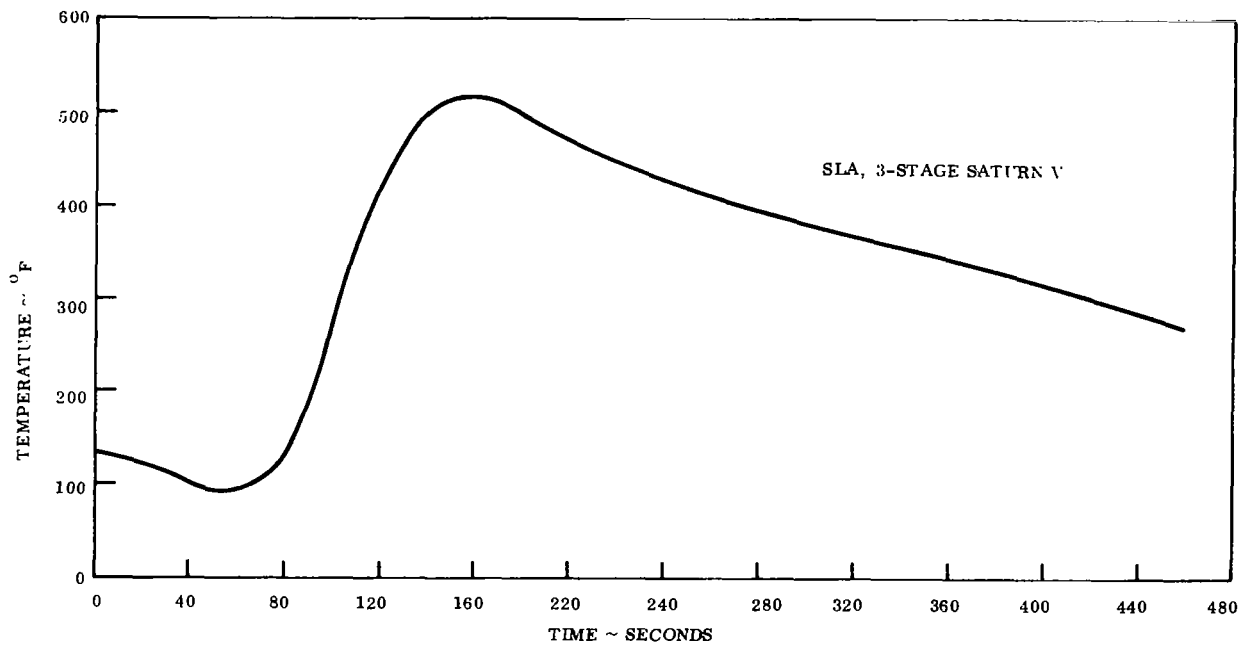


Figure 7-29. Ascent Temperature of Outer Skin

7.4.3 TOTAL FLUID INVENTORY

The total fluid inventory in the system will affect the startup requirements from a frozen condition since, as a minimum, the latent heat of fusion must be supplied to the system by some auxiliary source. The primary fluid inventory for each system at the 0.990 survival probability condition is summarized in Table 7-4.

Table 7-4. Comparison of VCF and Conduction Fin Fluid Inventory

Radiator	Fluid Inventory, lb			Total
	Headers	Feedlines	Tubes (Ducts)	
Conduction Fin	174	134	29	337
Vapor Chamber Fin	64	132	103	299

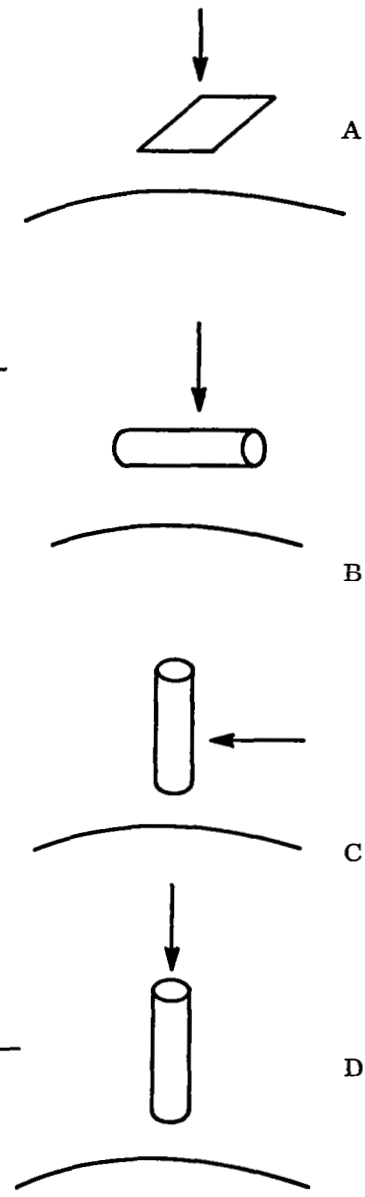
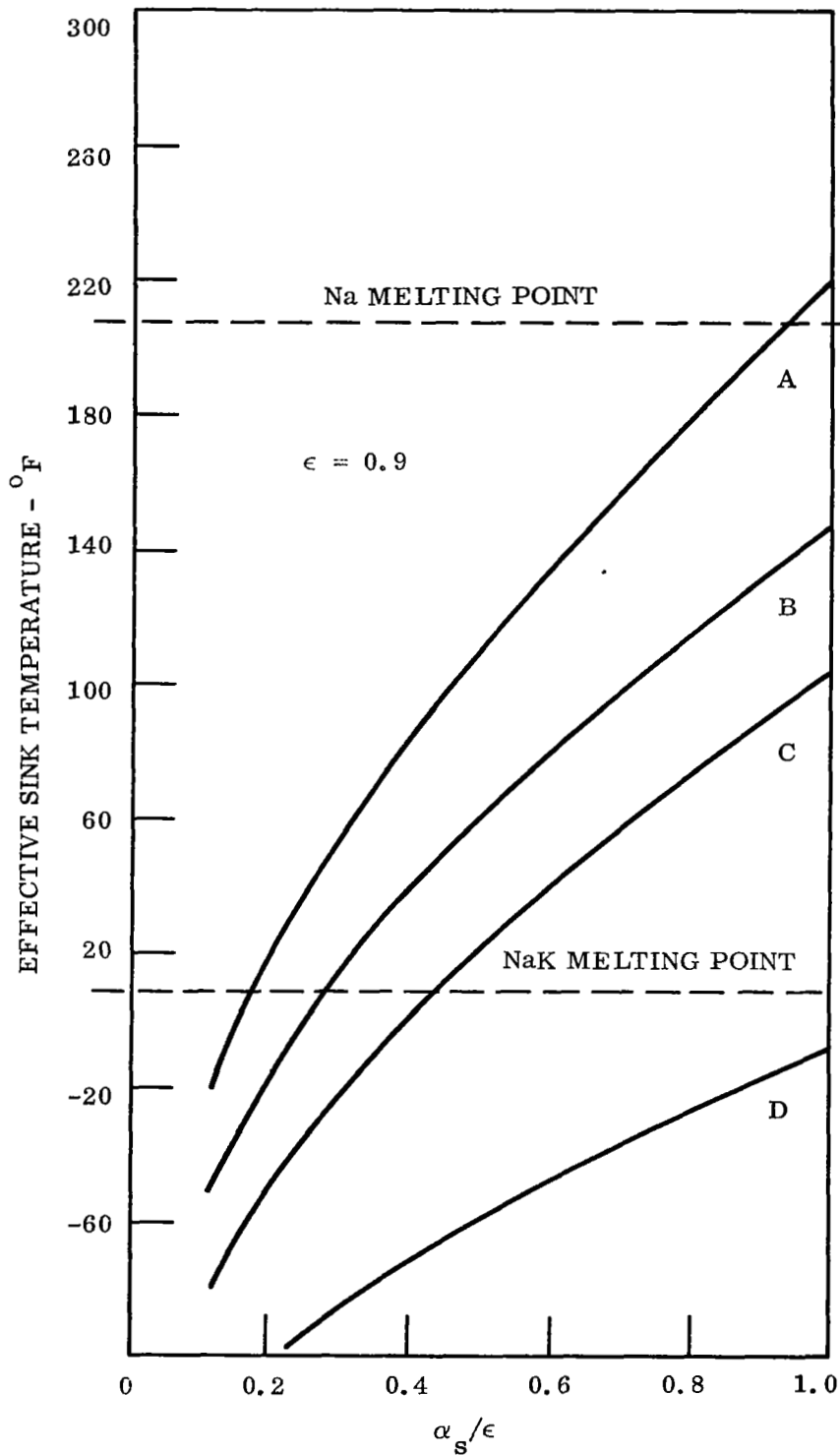


Figure 7-30. Effect of Radiator Surface Properties on Effective Sink Temperature for 100 nm Earth Orbit

The conduction fin radiator has a 10 percent greater fluid inventory primarily as a consequence of the comparatively large headers required for this concept. The headers act as a plenum so that the flow path through any tube provides the same pressure drop. In the conduction fin design the fluid tube spacing is less than 3.0 inches, making it necessary to run the header along the entire panel length. The large spacing of 18 to 20 inches between vapor chamber primary ducts enables a more compact header. On the basis of fluid inventory, a slight advantage can be accorded the VCF radiator.

7.4.4 FLUID LOCATION AND DISBURSEMENT

In conditions where temperatures below the freezing point of the fluid are encountered, the location of the fluid in the radiator can play an important part in determining the amount of energy required to keep it liquid. From this standpoint, the vapor chamber radiator has an advantage in that the concentration of primary fluid in relatively few ducts enables a simpler distribution system for the auxiliary power source. More importantly, the wide separation between fluid ducts means that the fluid ducts can be maintained at a temperature above the NaK freezing point while the effective radiator temperature is kept at a lower level. An example calculation supporting this statement indicates that the NaK in the vapor chamber radiator can be maintained at 50^oF with a total energy loss of 9.1 kW while 25 kW would be rejected by the conduction fin radiator.

Figure 7-31 pictures a vapor chamber fin radiator with one feed and return fluid loop kept liquid, as well as one primary fluid duct. When startup of the system is required, elevation of the fluid temperature to 500 to 600^oF could initiate vapor chamber action. This would result in the adjacent vapor chambers (those connected to the next primary duct and adjoining the condensing end) starting up, working in reverse, and melting the NaK in the adjacent primary ducts. An entire panel could be brought up to operating temperature much more quickly than is possible with a conduction fin radiator. This is due to the high conductivity of the vapor chambers.

The process described above is dependent upon the containment of sodium at the evaporative end of the vapor chamber. If a system is kept inoperative for a long period of time with one

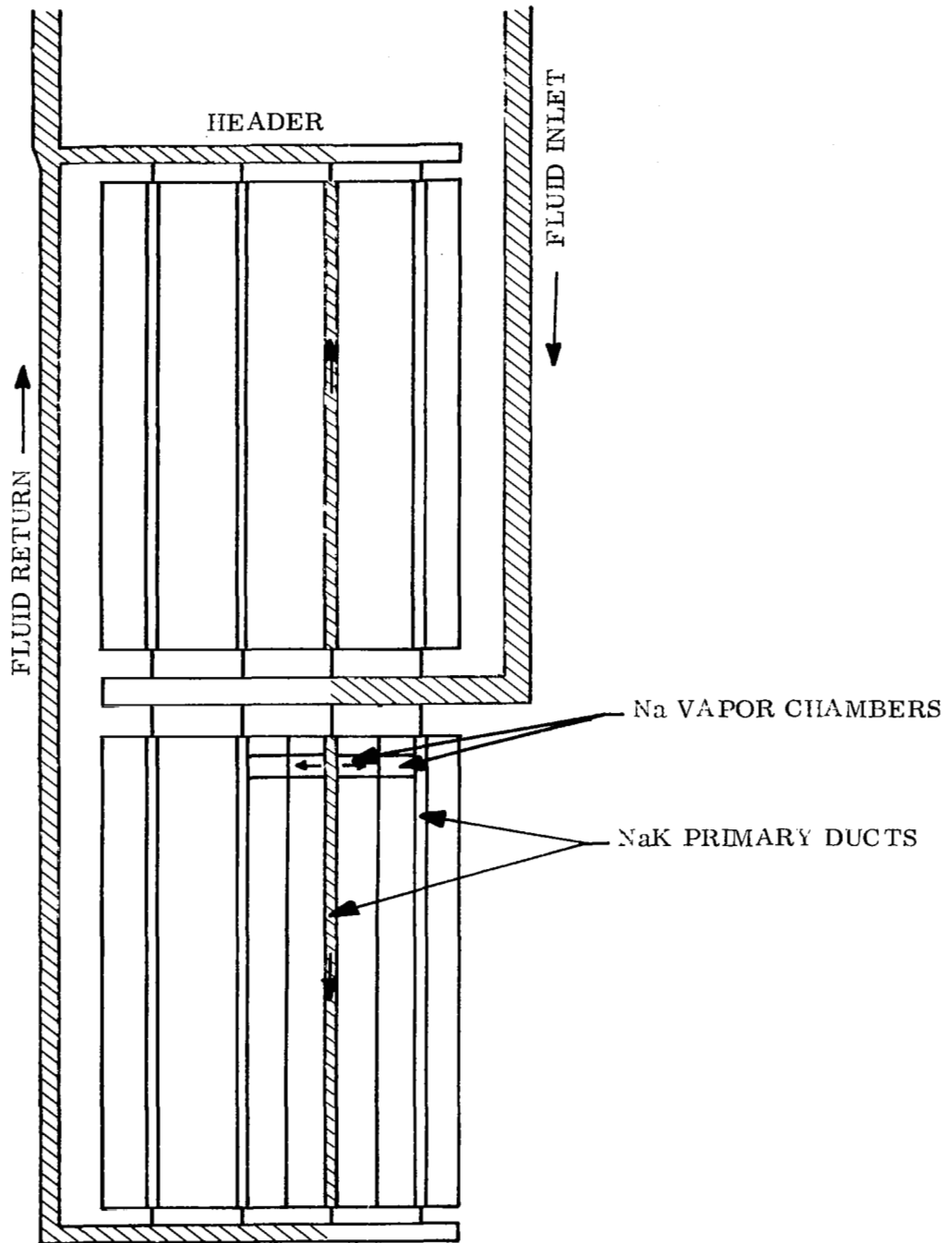


Figure 7-31. Vapor Chamber Fin Radiator in Standby Condition

loop in a fluid state, it is possible for sublimation of the sodium to occur with a resultant mass transfer of sodium to the condenser section. This process could continue until the evaporator section was devoid of sodium. The possibilities of sodium transfer to the condenser was also examined during launch ascent. Although it is accepted that sodium previously frozen could be liquified and redistributed within the vapor chambers due to gravitational and acceleration forces, the circumferential orientation of the chamber precludes the possibility of adjacent vapor chambers with dry evaporators. Contingencies of this nature must be examined more extensively for each particular set of startup conditions before firm decisions can be made.

7.4.5 SYSTEM/MISSION CONSIDERATIONS

The configuration of the radiator and interfacing vehicles and structures must be considered. One aspect of the startup problem, of concern to both designs, is the effect of thermal stresses on the radiator and interfacing structure. If a dry launch were used, hot fluid injected into the lines could create stresses which might buckle the radiator skin. At a minimum, the implications of this occurrence could be cracking and flaking of the emissive coating. Dimensional changes of several inches are possible along the length and circumference of a large radiator subjected to differential temperatures of 1200 to 1300⁰F. Startup procedures must reflect these considerations. A thorough analysis of each radiator would be required to determine which design is more susceptible to this kind of damage.

From the points considered, it appears that for most earth orbital missions either radiator concept can be designed to alleviate potential startup problems. The VCF radiator primary loop possesses several inherent characteristics which could minimize these problems; however, the significance of these advantages cannot be ascertained until a more specific definition of the system startup requirements and characteristics is available.

SECTION 8

RADIATOR COMPARISON AND CONCLUSIONS

8.1 GENERAL

The Rankine cycle vapor chamber and conduction fin radiator reference designs were based on the same ground rules and performance considerations. Therefore, each unit is capable of accomplishing the same function with the same reliability over the mission lifetime. The designs derived from the study were evaluated and compared to determine whether significant performance advantages could be obtained by use of the vapor chamber radiator.

The primary figures of merit used in this comparison are:

1. Performance (weight/area)
2. Fabrication feasibility
3. Required development effort
4. Operational

8.2 PERFORMANCE (WEIGHT/AREA)

A comparison between the reference VCF and conduction fin radiator designs on the basis of weight and area is shown in Figure 8-1. These results are based on the conditions specified in Section 3. The radiator weights in this figure include panel, feedline, pump penalty and structural weight.

At the lower meteoroid protection requirement ($P_o = 0.990$), both concepts are equivalent from a weight standpoint; however, the VCF has a 10 to 15 percent area advantage. The relative insensitivity of the VCF radiator weight to changes in meteoroid survival requirements is demonstrated by weight/area curves; whereas the conduction fin radiator increases in weight by 50 percent, the VCF radiator exhibits a weight increase of less than ten percent at a $P_o = 0.999$.

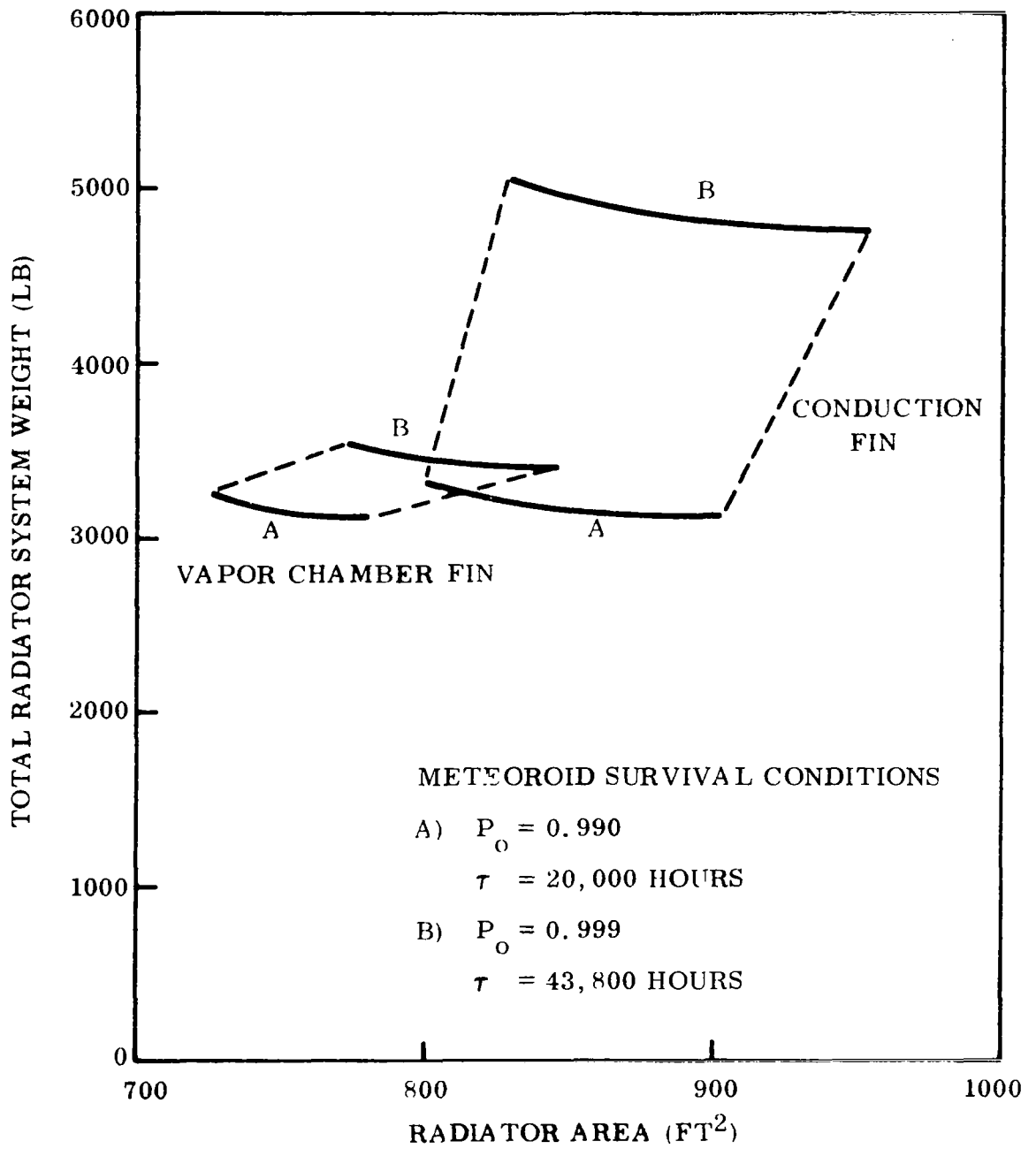


Figure 8-1. Total Radiator Weight versus Area for Vapor Chamber and Conduction Fin Radiators

This characteristic is a direct consequence of the smaller vulnerable area of the primary fluid ducts in the VCF radiator. The VCF design has obvious weight advantages as meteoroid protection requirements become more severe.

The area and weight of the vapor chamber radiator uses the condensing ΔT calculated by the HPIPE program. Experimental results were at least an order of magnitude larger than predicted by HPIPE. If the experimental results had been used to design the vapor chamber radiator, it would have been anywhere from approximately 4 to 20 percent larger and heavier, depending on the experimental results used.

The results of the evaluation incorporate a meteoroid cratering coefficient of stainless steel equal to 1.67. More recent estimates as discussed in Sections 5.1.1 and 7.2.1 suggest a value of 2.62 to be more accurate. The effect of this change is to significantly increase radiator weight. Continuing reassessments of the meteoroid hazard have the potential of significantly affecting the weight comparison presented.

The comparison of vapor chamber and conducting fin radiators in this section does not include internal fins in primary fluid ducts of the vapor chamber radiator. While these fins have some heat transfer advantages over plain ducts, they are unattractive from a fabrication standpoint.

An evaluation of several design and performance characteristics of both optimized radiator systems provides a number of interesting comparisons. A design point comparison of the two radiators is shown in Table 8-1.

Table 8-1. Design Point Summary Comparison

Design Point Summary Of Vapor Chamber Fin Radiator Characteristics			Design Point Summary Of Conduction Fin Radiator Characteristics		
	$P_o = 0.990$	0.999		$P_o = 0.990$	0.999
Requirements			Requirements		
Thermal Heat Rejection, kWt	1536	1536	Thermal Heat Rejection, kWt	1536	1536
Rad. Fluid Temperature Inlet-Outlet, °F	1200-980	1200-980	Rad. Fluid Temperature Inlet-Outlet, °F	1200-980	1200-980
Heat Rejection Rate (End-Of-Life), %	75	75	Heat Rejection Rate (End-Of-Life), %	75	75
Radiator Lifetime, Hours	20,000	43,800	Radiator Lifetime, Hours	20,000	43,800
Design Description			Design Description		
Radiator Primary Fluid	NaK78	NaK78	Radiator Primary Fluid	NaK78	NaK78
Vapor Chamber Fluid	Sodium	Sodium	Radiator Upper Diameter, In.	87.44	87.44
Radiator Upper Diameter, In.	87.44	87.44	Radiator Length (Total), In.	296.0	307.0
Radiator Length, In.	266.6	285.0	Average Number Tubes/Panel	53	43
Vapor Chamber Length (Average), In.	8.58	8.93	Fin Make-Up	50% Cu	40% Cu
Vapor Chamber Width, In.	1.24	1.24		50% SS	60% SS
Number of Vapor Chambers	9120	9851	Fin Thickness, In.	0.030	0.048
Primary Duct Inside Width, In.	2.80	2.05	Feed Line I.D., In.	2.12	2.13
Primary Ducts Per Panel	6	6	Tube I.D., In.	0.18	0.18
Duct Wall Thickness, In.	0.021	0.044	Number of Structural Frame Stiffeners	21	-
Number of Structural Frame Stiffeners	15	15	Number of Bays/Panels	2/8	2/8
Number of Bays/Panels	2/8	2/8			
Performance Data			Performance Data		
Physical Radiator Area, Ft ²	785	848	Physical Radiator Area	906	959
Primary Fluid Pressure Drop, PSI	1.0	1.1	Fluid Pressure Drop, PSI	8.7	10.4
Primary Fluid Velocity, Ft/Sec	1.5	2.0	Tube Fluid Velocity, Ft/Sec.	9.2	10.8
Temp. Drop (Primary Fluid to Rad. Surface) Average, °F	182	188	Temp. Drop (Fluid to Fin Root), °F	50	74
Weight Tabulation			Weight Tabulation		
Radiator and Fluid Inventory	2464	2734	Radiator and Fluid Inventory	2467	3975
Pump Power Penalty Weight	34	37	Pump Power Penalty Weight	294	401
Stiffeners and Frames	210	225	Stiffeners and Frames	296	359
Clamps, Splice Plates etc.	405	439	Clamps, Splice Plates etc.	83	
Total, Lb	3113	3435		3140	4735

8.3 FABRICATION FEASIBILITY

An evaluation of the fabrication processes required for each radiator indicates a decided advantage is afforded the conduction fin radiator. The rather conventional offset fin/tube geometry is not only easier to fabricate but offers relatively high reliability of fabrication compared to the fabrication of 10,000 individual liquid metal vapor chambers. Large size vacuum test and welding facilities would be required for the VCF radiator. The conduction fin radiator requires a bimetallic copper to stainless steel bonded fin. Bonding techniques such as this have been developed and should not present significant problems.

8.4 REQUIRED DEVELOPMENT EFFORT

Another important factor which must be evaluated is the present state of development of each radiator technology and the required effort involved in obtaining flight hardware. The conduction fin radiator can be considered as being state-of-the-art insofar as operation at the design point is concerned. Heat transfer performance of liquid metal conduction fin radiators has been accurately predicted in tests at temperatures below 700^oF (Reference 16), and the 1200^oF temperature regime does not appear to present any special technical problem. During these same series of tests, no flow stability or unexplained problems of coolant maldistribution were observed. It can be stipulated that a liquid metal conduction fin radiator would involve minimal development problems.

The VCF radiator design and fabrication techniques will require development. The magnitude of the development effort will depend to a large extent on the trade-off which is willing to be accepted between weight and fabrication sophistication. In addition to the actual manufacture of the VCF radiator, several other areas of investigation are necessary. These include:

1. Wick design
2. Performance predictability
3. Influences of fluid inventory.

The composite wick design used in the tests was thought to be responsible for the high condensing ΔT 's experienced. Verification of this theory as well as further investigation of other wick designs appears to be in order.

The ability to consistently predict vapor chamber performance, within certain limits, is another requirement which must be met. The large number of vapor chambers in a single radiator system makes operational uniformity and predictability especially important. To a large degree this quality will be dependent upon the ability to closely control the fabrication of each chamber.

Another area of concern which deserves attention is the fluid inventory. Theoretically, an amount of fluid which would just fill the wick pore volume is ideal. However, limitations on the ability to correctly assess this volume plus the difficulty of adding a precise amount of liquid metal to a chamber presents a problem area. The influence of variations in fluid inventory upon chamber performance should be carefully analyzed.

8.5 OPERATIONAL COMPARISON

A complete assessment between two radiator concepts cannot be performed without considering the operational requirements of each mission. Behavior of the radiator system during startup and transients are two examples of areas requiring further investigation for a specific mission before a selection between radiators can be made. A cursory analysis, presented in Section 7.4, indicates that several characteristics of the VCF radiator offer less severe startup problems.

8.6 CONCLUSIONS

The analytical design and testing performed in this study was directed towards a comprehensive evaluation of the Vapor Chamber Fin (VCF) radiator for the potassium Rankine cycle. Several conclusions concerning the characteristics of the VCF radiator and its competitiveness with the conduction fin radiator are cited here:

1. The work performed in this study has indicated that the VCF radiator is a feasible heat rejection concept for use in the potassium Rankine cycle in a zero g environment. A detailed design concept has been presented which is capable of satisfying the heat rejection and structural requirements imposed by an unmanned 300 kWe potassium Rankine power system launched aboard a two stage Saturn V. This conclusion is substantiated by the testing of a prototype sodium vapor chamber fin in the 825^o to 1600^oF temperature range.
2. A comparison of the fabrication requirements for the VCF and conduction fin radiators indicates that the VCF system is considerably more difficult to fabricate. Construction of the conduction fin concept can be considered to be state-of-the-art with the exception of the bimetallic (stainless steel and copper) fin. Although this design feature is not expected to present a large development effort, elimination of the copper would only incur a 15 to 20 percent weight penalty.
3. The construction of the optimized VCF radiator presented in this study entails the filling of approximately 10,000 separately sealed vapor chambers with alkali metal. The operation of a vapor chamber necessitates high purity filling conditions, cleanliness of the VCF walls and wick, and completely reliable individual chamber sealing. Failure to provide close quality control can lead to an overall decrease in the radiator effectiveness. It is concluded that a sizable fabrication development effort is required before a 10,000 chamber radiator can be built with predictable performance.
4. The relative attractiveness of the VCF radiator as compared to a conduction fin radiator is dependent upon the mission of interest and in particular upon the meteoroid survival probability required. At the less severe meteoroid survival probability condition considered, 0.99 for 20,000 hours, the incentive for developing a VCF radiator is minimal. However, at meteoroid survival probabilities of 0.999 for five years, a significant (for an unmanned system) weight and area savings over a conduction fin radiator can be achieved. The comparative insensitivity of the VCF radiator concept to changes in meteoroid survival probabilities is directly related to two characteristics of this concept:
 - a. Fewer primary fluid (NaK-78) ducts are required, resulting in a large reduction in the vulnerable area of the main coolant loop.
 - b. The vapor chamber fins, which comprise almost all of the radiator surface area, are redundant devices. Therefore, the armor requirements can be determined with the expectation that a percentage of chambers will eventually be punctured without a significant loss in radiator performance.

However, the weight advantage for the VCF radiator is probably negligible as compared to the modified 4π shield weight of over 50,000 pounds required for postulated manned space missions.

5. A detailed analytical investigation of four promising VCF geometries concluded that the rectangular channel configuration was optimum. This analysis included the effects of the heat transfer, heat pipe operation, meteoroid protection, vehicle and primary duct integration, structural and fabrication requirements. The finned round tube and finned rectangular chamber designs were superior to the rectangular channel from a heat transfer standpoint. Structural requirements of both finned concepts, however, increased the weight of these radiator systems significantly. The finned round tube was susceptible to tube crushing and both finned geometries were subject to fin buckling, especially when thinner (0.010 to 0.015 inch) fins were considered.
6. The honeycomb vapor chamber concept resulted in an unattractive VCF design; this is due to the poor thermal efficiency of the device caused by the interior honeycomb walls. The large radiating area required by this concept negated the effects of the inherent honeycomb structural rigidity.
7. The results of the fluid evaluation showed that sodium was a superior vapor chamber working fluid as compared to cesium and potassium. This was attributed to the high surface tension and latent heat of vaporization of sodium. Cesium was unacceptable as a vapor chamber fluid for the conditions studied.
8. The VCF tests demonstrated the ability of the rectangular channel geometry to be used as a heat rejection device with sodium as the working fluid. The VCF performed satisfactorily in the 825^o to 1600^oF temperature regime as well as under a 10 degree tilt condition and at evaporator heat fluxes up to 1.4×10^5 BTU/hr-ft². The one uncertainty surrounding the VCF tests was the condensing ΔT . Initially, observed condensing temperature drops were considerably higher than predicted. Testing of a second VCF produced lower ΔT 's which continued to decrease with time. This unexpected result was attributed to an incomplete filling of the condenser fluid return annulus. The design of composite wicks, using an annular condenser return, requires more investigation.

SECTION 9
REFERENCES

1. Whipple, F. L., "On Meteoroids and Penetration," Journal of Geophysical Research, Volume 68, Number 17, 1963.
2. Loeffler, I. J., S. Lieblein, and N. Clough, "Meteoroid Protection for Space Radiators," In "Progress in Astronautics and Aeronautics, Vol II, Power Systems for Space Flight," Academic Press, New York, 1963.
3. "A Study of Jupiter Flyby Missions," General Dynamics Report FZM-4625, May 17, 1966.
4. Volkoff, J. J., "Protection Requirements for the Resistance of Meteoroid Penetration Damage of Interplanetary Spacecraft Systems," JPL Technical Report No. 32-410, July 1, 1964.
5. Diedrich, J. H., I. J. Loeffler, and A. R. McMillan, "Hypervelocity Impact Damage Characteristics in Beryllium and Graphite Plates and Tubes," NASA TN D-3018, September, 1965.
6. Clough, N., Lieblein, S., McMillan, A. R., "Crater Characteristics of 11 Metal Alloys Under Hyper-Velocity Impact Including Effects of Projectile Density and Target Temperature", NASA TN D-5135, April 1969.
7. Cockfield, R. D., "Comparison of Load Bearing and Non-Load Bearing Radiators for Nuclear Rankine Systems." NASA CR-72307, May 6, 1967.
8. Hagen, K. G., "Integration of Large Radiators with Nuclear Electric Spacecraft Systems", Air Transport and Space Meeting, New York, N. Y., April 1964.
9. Kunz, H. R., Langston, L. S., Hilton, B. H., Wyde, S. S., and Nashick, G. H., "Vapor Chamber Fin Studies," NASA CR-812, June 1967.
10. Lieblein, S., "Analysis of Temperature Distribution and Radiant Heat Transfer Along A Rectangular Fin of Constant Thickness," NASA TN D-196.
11. Gerard G., Becker, H., "Handbook of Structural Stability Part VI - Strength of Stiffened Curved Plates and Shells," NASA-TN 3786, July 1958.
12. Cotter, L., "Theory of Heat Pipes," Los Alamos Scientific Laboratory, LA-3246 MS, March 26, 1965.

13. Sawochka, S. G. , "Thermal and Hydraulic Performance of Potassium during Condensation Inside a Single Tube," NASA CR-851, August 1967.
14. Ewing, C. T. , et al, "High Temperature Properties of Potassium," U.S. Naval Research Laboratory, NRL 6233, September 24, 1965.
15. Shanley, F. R. , "Weight-Strength Analysis of Aircraft Structures," Dover Publications, 1952.
16. Cockfield, R. D. , Killen, R. T. , "Testing of an Aluminum Radiator With Liquid Metal Coolant." Presented at AIAA Thermophysics Conference, June 1970.

APPENDIX A
NOMENCLATURE

A	-	area
a	-	meteoroid damage factor
b	-	panel width
c	-	proportionality constant
D	-	diameter
d	-	characteristic length of wick pore or radiator frame spacing
E	-	Young's modulus of elasticity
F	-	radiation view factor or stress
f	-	stress
g	-	gravitational constant
h	-	heat transfer coefficient
I	-	moment of inertia
K	-	proportionality constant or wick friction factor
k	-	thermal conductivity
L	-	fin efficiency length parameter, critical structural length or radiator length
l	-	length
M	-	bending moment or molecular weight
m	-	mass flow rate
N	-	number of chambers
n	-	number of events (or chambers)
P	-	overall meteoroid survival probability, structural load or pressure

PP	-	pumping power penalty
PSW	-	powerplant specific weight
PW	-	hydraulic pump work
p	-	individual chamber survival probability or wick porosity
Q	-	heat transfer rate
R	-	Reynolds number, ratio of compressive to critical stress or gas constant
r	-	radius
T	-	temperature
t	-	thickness
U	-	overall heat transfer coefficient
V	-	velocity
W	-	Weber number
Wt	-	weight

GREEK LETTERS

α	-	meteoroid flux parameter or vehicle half cone angle
β	-	meteoroid flux parameter
γ	-	meteoroid cratering coefficient
ΔP	-	pressure drop
ΔX	-	thickness
ϵ	-	emissivity
κ	-	fin efficiency
θ	-	contact angle between fluid and pore surface
λ	-	latent heat of vaporization

- μ - viscosity
- ν - Poissons' ratio
- ρ - density or radius of gyration
- σ - surface tension or Stephan-Boltzmann constant
- σ_c - condensation coefficient
- τ - mission time

SUBSCRIPTS

- a - armor
- c - condenser section or compressive load
- ew - evaporator wick
- f - fin
- mp - meteoroid particle
- o - overall system
- p - wick pore
- R - referenced to room temperature
- s - stiffener
- T - total
- v - vapor
- w - wick
- ND - no critical damage

APPENDIX B
TEST PLAN FOR VAPOR CHAMBER RADIATOR
SECTION 1
INTRODUCTION

1.1 SCOPE

This document presents detailed instructions for performing engineering tests on the vapor chamber radiator.

1.2 OBJECTIVE

The primary objective of this test program is to demonstrate the capability of the vapor chamber radiator as detailed in GE Drawing 47D301344.

1.3 APPLICABLE DRAWINGS

1.3.1 DRAWINGS

SK 6569JH	Vapor Chamber Radiator Bell Jar Test Assembly
47D301339	Calorimeter Tube
47D301340	Lower Insulation
47D301341	Middle Insulation
47D301342	Upper Insulation
47D301343	Electron Bombardment Heater
47D301344	Sodium Heat Pipe Vapor Chamber Radiator
47B301336	Adjustable Mounting Plate
47B301337	Channel Support
47E301338	Adjustable Mounting Support Vapor Chamber Radiator

SECTION 2
TEST CONDITIONS, FACILITIES AND EQUIPMENT

2.1 TEST CONDITIONS

2.1.1 VISUAL EXAMINATION AND TEST CONDITIONS

Visual examination and test shall be performed under the following standard conditions unless otherwise specified:

1. Temperature-- $77^{\circ}\text{F} \pm 18^{\circ}\text{F}$
2. Relative Humidity--28 to 32 inches of mercury

Vacuum conditions will be maintained at a chamber pressure of 5×10^{-5} torr or less.

2.2 TEST FACILITIES

The test facility which will be utilized for this test is the NRC 3177 Vacuum System located in Vacuum and High Temperature Technology Lab, Room 8941, CCR 8.

2.3 TEST EQUIPMENT

The following test equipment (or equivalent) is required to perform the vapor chamber heat pipe tests.

1. Vacuum Chamber System--NRC 3177
2. L&N Thermocouple Checking Furnace, Model #9009-A-3
3. L&N 3555 Type K5 Potentiometer
4. Eppley Standard Cell, Cat. #100
5. Esterline 24-point Recorder, Model #E1124E
6. Heater Power Supply (Kilovolt Corp.)

7. Variac, 120 volts at 20 amperes
8. Isolation Transformer, Sola Ca. #23-25-220
9. L&N Ice Bath
10. L&N Standard Thermocouple, platinum: platinum-rhodium, S/N AB-69-40
11. NLS Digital Voltmeter, Series 290C
12. Esterline Strip Chart Recorder, Model #11015
13. Turbine Flow Transducer Flow Technology Inc.
14. 40-Point L&N Switch
15. Weston Volt and Amp Meters
16. Flow Regulator.

SECTION 3
PRE-TEST REQUIREMENTS AND OPERATIONS

3.1 TEST SPECIMEN

The vapor chamber radiator, Drawing 47D301344, is of a rectangular cross-section, 1.25" x 0.36", and a length of 8.5". This thin-walled pipe is filled with liquid sodium and sealed. It should be noted that white gloves must be utilized in handling of the pipe and all surfaces of the pipe must be free of dirt and grease. The pipe must not be subjected to any unnecessary shock or vibration.

3.2 TEST FIXTURE SET-UP

The test fixture will be assembled in the NRC 3177 vacuum system bell jar as shown in Drawing SK-6569JH. Additional insulation may be added or removed upon approval of the test director. All instrumentation and heater leads should be routed as far away from the fixture as possible.

3.3 INSTRUMENTATION

3.3.1 THERMOCOUPLES

Forty chromel-alumel thermocouples will be calibrated and used to instrument the heat pipe as shown in Figure 1*. Thermocouples installed on the insulation will be calibrated in the 100^oF range to 400^oF range at 100^oF increments. Thermocouples installed on the calorimeter will be calibrated at their two extreme temperatures, namely, the ice point 32^oF and boiling point of water 212^oF. Thermocouples installed on the heat pipe itself will be calibrated against a L&N standard thermocouple at 900^oF, 1000^oF, 1050^oF, 1100^oF, 1150^oF, 1200^oF, 1250^oF and 1300^oF. (Minimum calibration increments).

*Not attached. Refer to Figure 6-15.

3.3.2 FLOW METER

The turbine flow transducer (Flow Tech. Inc., "Milliflow") will be placed in the output line of the calorimeter at least 10 pipe diameters from the closest up-stream and down-stream connection. This device shall be capable of metering a water flow rate of 0.02 - 0.2 gpm within $\pm 0.2\%$ of true flow. A frequency to DC converter, DVM and recorder will be used to indicate and record the flow rates as a function of time.

Flow meter readout will be made on a NLS digital voltmeter. All heater voltage and current readings will be made with 1% or better meters.

3.3.3 INSTRUMENTATION GENERAL

All thermocouples will be connected to a 32^oF reference junction and to the L&N K5 potentiometer for primary data recording for stand-by or unattended operation. Key TC's will be connected to the 24-point Esterline recorder which in turn will operate an over-temperature safety control.

A block diagram of all instrumentation will be found in Figure 2.*

*Not attached. Refer to Figure 6-12.

SECTION 4 TEST OPERATIONS

4.1 GENERAL

Vacuum conditions (5×10^{-5} torr or less) must be maintained at all times during heater operation.

At all test points steady state conditions will be held for a period of thirty minutes and sets of data taken every ten minutes. Steady state conditions will be defined as $\pm 2^{\circ}\text{F}$ change over a ten minute period.

All data shall be recorded on data sheets which will be supplied by the test conductor. Tolerance on all heat pipe test points will be $\pm 5^{\circ}\text{F}$, i. e., $900^{\circ}\text{F} \pm 5^{\circ}\text{F}$, $1000^{\circ}\text{F} \pm 5^{\circ}\text{F}$, etc.

Visual inspections will be made before start-up and after shutdown. Photographs will be taken of the heat pipe and its fixturing.

4.2 CALIBRATION AND RADIATION CONTRIBUTION

Objective--During normal operation, heat is transferred to the evaporator by radiation as well as electron bombardment. It is necessary to determine what fraction of the total heat is due to each mode of energy transfer. The procedure outlined below will make it feasible to separate these two effects.

Phase I--Determine the relationship of ac voltage and evaporator temperature during normal operation.

1. Establish a vacuum of 5×10^{-5} torr or less.
2. With heat pipe in normal position and operating mode, bring the evaporator temperature up to 900°F . Record voltage of variac setting.
3. Repeat for 1050°F , 1150°F and 1250°F .

Phase 2--Estimate the heat input due to radiation (evaporator temperatures during this part of the test will be reduced).

1. Turn off DC power supply.
2. With variac on a voltage setting corresponding to the normal 900^oF condition, record heat pipe temperature.
3. Repeat for variac voltage settings corresponding to 1050^oF, 1150^oF and 1250^oF as established in Phase 1, Step c.
4. Calculate estimates of power input to heat pipes by radiation.

Phase 3--Using a series of shrouds consisting of Dyna-Quartz blocks, measure the radiation contribution at various temperature levels.

1. Estimate the amount of shrouded area from the results of Phase 2.
2. With shrouds in place, variac voltages on settings determined in Phase 1, and DC supply off, record the evaporator temperature for the four (4) variac settings in Phase 1; 900^oF, 1050^oF, 1150^oF and 1250^oF.
3. From the recorded temperatures calculate the heat transferred versus evaporator temperature.

4.3 MEASUREMENT OF EVAPORATIVE HEAT FLUXES VERSUS ΔT 's

Objective--Measure the evaporative heat flux between 5,000 and 80,000 BTU/Hr-Ft² as a function of evaporative ΔT and condensing ΔT .

Procedure 1--Establish a vacuum of 5×10^{-5} torr or less.

Procedure 2--At a minimal power level (less than 50 watts) heat the vapor chamber until heat pipe action can be obtained. When isothermal conditions are reached, the water flow rate should be adjusted such that the water ΔT is between 10 and 20 degrees F. Record power input, all thermocouples, flow rate, etc., when steady state has been reached.

Procedure 3--Raise the evaporator temperature 50°F. When steady state has been reached, record all instrument readings in Table 1.

Procedure 4--Repeat this procedure at 50°F intervals (evaporator temperature) and also at 900°F, 1000°F, 1100°F, 1200°F and 1300°F if not previously covered.

4.4 TILTING TEST

Objective--Determine the limits of the pumping capability of the evaporator wick.

Procedure 1--Establish a vacuum of 5×10^{-5} torr or less.

Procedure 2--At 900°F tilt the pipe at a 10° angle and record all instrumentation in Table 1 when steady state has been reached.

Procedure 3--Repeat this procedure for 1000°F, 1100°F, 1200°F and 1300°F.

Procedure 4--Increase the tilt to 20° at temperatures of 900°F, 1000°F, 1100°F, 1200°F and 1300°F and finally for a 30° tilt.

CAUTION

During this procedure, it is likely that evaporative temperature runaway will occur due to insufficient capillary pumping capability. In this event the heater must be shut down and in no instance should the pipe temperature be allowed to exceed 1600°F.

4.5 LIMITING HEAT FLUX

Objective--Determine the operational limit of the heat pipe in the horizontal position

Procedure 1--Raise the temperature of the heat pipe until the evaporator temperature begins to run away from the pipe temperature.

1. Establish a vacuum of 5×10^{-5} torr or less.
2. Bring the heat pipe up to 1300°F operating temperature at steady state.
3. Raise the temperature to 1350°F .
4. If steady state is achieved, raise the power slowly. Gradually bring the operating point to 1400°F --stopping at intermediate increments of 10°F or as modified by the thermal analyst.
5. When steady state has been achieved, repeat the procedure of a gradual increase in temperature until 1600°F is attained.